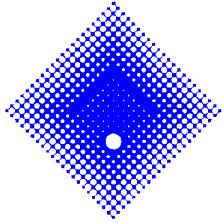


**VICTORIA
UNIVERSITY**



**O F
T E C H N O L O G Y**

Peak Power Reduction in Orthogonal Frequency Division Multiplexing Transmitters

BY

Gavin Hill

Thesis submitted in fulfilment of the
requirements for the degree of Doctor of
Philosophy

Victoria University of Technology
School of Communications & Informatics

March 2011

Abstract

Orthogonal Frequency Division Multiplexing (OFDM) is a digital transmission method developed to meet the increasing demand for higher data rates in communications which can be used in both wired and wireless environments. This thesis describes the issue of the Peak to Average Power Ratio (PAPR) in OFDM which is a major drawback, and presents new and variations to existing algorithms to reduce it.

Initially the theoretical principles behind OFDM are discussed elaborating on the advantages and disadvantages of OFDM. This is followed by analysis of the PAPR in OFDM where it is shown through theoretical analysis and simulation that the occurrence of large peaks in OFDM is actually quite rare. The effect on system performance in terms of the Bit Error Rate (BER) and Power Spectral Density (PSD) is simulated for an OFDM transceiver with a saturated High Power Amplifier. This is followed by a study of published PAPR reduction methods

The first contribution is a low complexity variation of Partial Transmit Sequences (PTS). In PTS several alternate transmit signals are seeded from the same source, each alternate transmit signal has a reversible and different phase rotation performed on the data. The transmit signal with the lowest PAPR is chosen for transmission. In novel variations, called Cyclic Shifted Sequences (CSS) and Time Inversion (TI), different shifts of the data are performed which avoid the need for complex multiplications. In certain cases a whole IFFT operation can be removed with a negligible effect on performance when CSS is combined with PTS. Furthermore it is shown that the peak regrowth of TI and CSS after pulse shaping filtering is considerably less than for PTS.

Next, new clipping techniques are presented which reduce substantially the complexity of clipping algorithms by using novel methods to calculate the magnitude, avoiding the use of multiplications. One method, called Sector clipping uses a rule base to clip the signal, dividing the clipping region into a series of sectors. When the rule base is expanded to include more sectors the performance is shown to approach

more complex existing clipping methods. This algorithm is implemented in silicon in a 3 metal layer 0.5 μ process. Another clipping scheme called *Vector Subtraction* is a variation of another low complexity magnitude estimate method which further reduces complexity by alleviating the need for a scaling operation. The performance of the new methods was ascertained through simulation of a whole OFDM transceiver chain and shown to have relative BER's. Finally *Vector Subtraction* was implemented in a previously proposed clip and filter algorithm where its low latency and accuracy proved it to be suitable for the algorithm.

Acknowledgements

First of all I wish to thank Professor Mike Faulkner for his guidance, patience, advice, and time thorough my many years of research. I owe the completion of this thesis to his efforts.

I also wish to thank Dr Reza Berangi for his mathematical and simulation knowledge and his willingness to share it. Special thanks goes to the post graduate studies committee for the numerous second chances to complete my research and to Shirley Herewyn for her omnipotent knowledge on dealing with university bureaucracy.

I would also like to acknowledge my research colleagues for the discussions on everything from communications theory to ancient history. In particular I wish to thank Abdi Waheed Mohammed, Tuan Nguyen, Andrew Mancuso, Trung Nguyen, Olivia Hu (who never really saw the significance of being Dr 'Who', even after I brought in pictures of Tom Baker and the Tardis) and Melvyn Pereira for their company and generous natures.

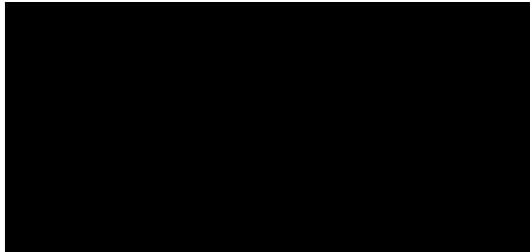
Finally I wish to thank my parents and my brother for their support, both financially and emotionally, and my best friends Dan, Spencer, and Mark for the good times and social outlet.

Gavin Hill

7 February 2006

I, Gavin Hill, declare that the PhD thesis entitled 'Peak to Average Minimisation in Orthogonal Frequency Division Multiplexing' is no more than 100,000 words in length, exclusive of tables, figures, appendices, references, and footnotes. This thesis contains no material that has been submitted previously, in whole or in part, for the award of any other academic degree or diploma. Except where otherwise indicated, this thesis is my own work.

Signature



Date 16/12/11

Contents

Abstract	i
Acknowledgements	iii
Contents	v
List of Tables	vii
List of Figures	viii
Acronyms and Symbols	xvi
Chapter 1 Introduction	1
1.1 Structure of thesis	2
1.1.1 Contributions.....	4
Chapter 2 Orthogonal Frequency Division Multiplexing	6
2.1 History of multicarrier networks	6
2.2 Multicarrier principle	8
2.3 OFDM implementation of multicarrier modulation	8
2.3.1 Use of Fourier Transform for modulation and demodulation.....	11
2.3.2 Orthogonality in OFDM	13
2.4 OFDM transmission over time varying channels	14
2.4.1 Multipath propagation.....	15
2.4.3 Frequency selective fading	17
2.4.4 Equalization	18
2.5 Limitations in OFDM	18
2.5.1 Synchronization	19
2.5.1.1 Timing errors	19
2.5.1.2 Carrier phase noise	20
2.5.1.3 Frequency errors	20
2.5.2 Non linearities	22
2.6 Applications of OFDM	22
2.6.1 COFDM	22
2.6.2 Digital Audio Broadcasting	23
2.6.3 Digital Video Broadcasting.....	24
2.6.4 HiperLan2/802.11a	24
2.6.5 ADSL	25
2.6.6 MIMO OFDM.....	26
2.7 Conclusion	26
Chapter 3 Peak to Average Power in OFDM	28
3.1 Peak to Average Power Ratio	29
3.2 Statistical distribution of OFDM samples	31
3.3 Oversampling discrete OFDM symbols to find true (continuous) peaks	35
3.4 Effect of Non Linearity on OFDM	45
3.4.1 Description of memoryless Non Linearity.....	45
3.4.2 Impact on Power Spectral Density.....	50
3.4.3 Impact on Bit Error Rate.....	51
3.5 Conclusion	53
Chapter 4 Peak to Average Power Solutions -Distortionless Techniques	55
4.1 Coding techniques	56
4.1.1 Block Codes	57
4.1.2 Bounds on PAPR	61

4.1.3 Cyclic Codes	61
4.1.4 Shapiro-Rudin codes	62
4.1.5 Golay complementary codes	63
4.1.6 Reed-Muller Codes	63
4.2 Multiple Signal Representation	66
4.2.1 Partial Transmit Signals	66
4.2.2 Oversampling PTS	72
4.2.3 Selective Mapping	77
4.3 Tone Reservation/Injection	83
4.3.1 Tone Reservation	83
4.3.2 Tone Injection	87
4.4 Conclusion	89
Chapter 5 Cyclic Shifted Sequences and Time Inversion of PTS.....	92
5.1 PTS subblock creation	92
5.2 New techniques for PTS subblock creation	93
5.2.1 Cyclic Shifted Sequences.....	93
5.2.2 PTS with CSS	96
5.2.3 Time Inversion	98
5.3 Filtering new techniques.....	99
5.4 Oversampling new techniques	104
5.5 Complexity evaluation	108
5.6 Conclusion	109
Chapter 6 Peak to Average Power Solutions -Distorted Techniques.....	111
6.1 Clipping in the Baseband	112
6.1.1 Quantisation and Clipping	121
6.2 Amplifier non linearities.....	124
6.3 Windowing.....	128
6.4 Conclusion	130
Chapter 7 Reduced Complexity Clipping Algorithms	132
7.1 Conventional clipping.....	134
7.2 New Sector Clipping method	143
7.2.1 Theoretical Analysis of Clipping Techniques.....	143
7.2.1.1 SNR Analysis.....	144
7.2.1.2 Conventional clipping.....	146
7.2.1.3 Sector Clipping	149
7.2.1.4 Square Clipping	158
7.2.1.5 Theoretical Results	158
7.2.2 Extensions of Sector Clipping	160
7.2.3 Hardware Implementation	162
7.3 New Vector Subtraction clipping method.....	167
7.3.1 Lucent Algorithm.....	167
7.3.2 Vector Subtraction	168
7.4 Comparison of new and existing clipping methods	173
7.4.1 BERF.....	173
7.4.2 PSD results.....	184
7.5 New adaptive clipping method.....	187
7.6 Conclusion	196
Chapter 8 Conclusion	198
8.1 Future Work.....	200
Bibliography	201

List of Tables

2.1: DAB parameters	23
2.2: DVB system parameters for 2K mode	24
2.3: HIPERLAN2 parameters	25
2.4: Data rates for HIPERLAN2	25
4.1: Number of complex multiplications and magnitude operations required	76
5.1: Complexity comparison of various techniques (adjacent partitioning)	109
7.1: Truth Table for 3 <i>Sector</i> clipping	155
7.2: ‘Synopsys’ reports for <i>Square</i> and 3 <i>sector</i> clipping.	164
7.3: ‘Cadence’ area utilization report on <i>Square</i> clipping	165
7.4: ‘Cadence’ area utilization report on 3 <i>Sector</i> clipping	166
7.5: Baseband clip level required to maintain a BER= 10^{-4} at varying IBO in HPA.	183

List of Figures

2.1: Block diagram of a basic multicarrier system	9
2.2: Basic OFDM transmitter and receiver. Occupied frequency band shown in between.	10
2.3: Basic OFDM transmitter and receiver pair utilizing Fourier transform.	12
2.4: Frequency spectrum of 5 orthogonal subcarriers of an OFDM transmit signal .	14
2.5: OFDM symbol a) without cyclic prefix, and b) with cyclic prefix.	16
2.6: Time and frequency properties of single carrier and OFDM techniques.	19
2.7: Effects of frequency offset ϵ_f : reduction of signal amplitude (star), and ICI (circle).	21
3.1: Simulated envelope for OFDM system (N=64) normalized by average power.	33
3.2: Simulated (solid line) and theoretical (3.13, dashed line) OFDM symbol CCDF for N=32, 64, 128, and 256 subcarriers. QPSK, 30000 runs.	33
3.3: Simulated OFDM sample CCDF for N=32, 64, 128, and 256 subcarriers. QPSK, 30000 runs.	34
3.4: Simulated OFDM CCDF for M=4, 16, and 64 constellation mapping. N=64, 30000 runs.	36
3.5: Simulated OFDM symbol with no oversampling (dashed) with it's oversampled version (solid) overlaid on top. The solid circle represents the 6dB level with respect to the average power. N=64, oversampling factors are 1 and 8.	36
3.6: Simulated OFDM CCDF for oversampling rates of 1, 2, 4, and 8. N=64, QPSK, 15000 runs.	37
3.7: Theoretical OFDM CCDF from (3.15) and (3.21) for N=64, 512 with simulated results: QPSK, oversampling factor rate of 16, 20000 runs, N=64, 512.	40
3.8: Theoretical OFDM CCDF from (3.22) for N=64, 512 with simulated results: QPSK, oversampling factor rate of 16, 20000 runs, N=64, 512.	41
3.9: Simulated OFDM CCDF QPSK, 64 point IFFT, 256 tap RRCF, $\alpha=0.15$. Clipped at 3dB after IFFT, then filtered (solid line). No clipping, then filtered (dashed line).	43
3.10: Zero padding of the IFFT, null carriers are set in the middle of the input.	44
3.11: Simulated OFDM CCDF after IFFT (os=1 and 2) and after filtering (os=1 and 2). QPSK, N=64, 256 tap RRCF, $\alpha=0.15$, 15000 runs.	44

3.12: AM/AM properties of a Soft Limiter (SL).47
3.13: AM/AM properties of a Traveling Wave Tube Amplifier (TWTA).48
3.14: AM/AM properties of a Solid State Amplifier (SSPA) for different values of P, and ideal amplifier.49
3.15: PSD of 64 subcarrier OFDM signal with 64 point IFFT, RRCF with excess bandwidth of 0.15. A SSPA with P=3 and various backoffs is used.	51
3.16: Signal constellation at the output of the HPA, P=3 after non linear amplification a) 4 QAM, 6dB IBO; b) 4 QAM, 0dB IBO; c) 16 QAM 6dB IBO; and d) 16 QAM 0dB IBO.	52
3.17: BER of 64 subcarrier OFDM signal with 64 point IFFT, RRCF with excess bandwidth of 0.15 for 4, 16, and 64 QAM constellations. A SSPA with P=3 and various backoffs is used.	53
4.1: Block diagram of OFDM transmitter showing PAPR coding.	56
4.2: Block diagram of PAPR reduction using the PTS approach.	68
4.3: An example of the 3 main PTS structures: (a) Interleaved (b) Adjacent (c) Pseudo-random.	70
4.4: Simulated CCDF for PTS-OFDM with V=2 and varying W. N=64, adjacent subblock partitioning.	71
4.5: Simulated CCDF for PTS-OFDM with W=4 and varying V. N=64, adjacent subblock partitioning.	71
4.6: Generation of subblocks for PTS using Concatenated Pseudo Random Sub Block Partition Scheme (CPR SPS).	73
4.7: Block diagram of OLS-PTS transmitter.	76
4.8: Block diagram of an SLM OFDM transmitter.	78
4.9: Simulated CCDF for SLM-OFDM for varying values of U. N=64, $os=1$	79
4.10: Simulated CCDF for SLM-OFDM. U=1, 3, and 8. Oversampling rates are 1, 2, and 4, and 8.	80
4.11: SLM transmitter block diagram employing technique to avoid explicit transmission of side information, a) serial form, b) parallel form.	81
4.12: Scrambler polynomial for new SLM technique.	81
4.13: a) Receiver structure of the proposed SLM system, b) Descrambler polynomial at the receiver.	82
4.14: Block diagram of a Tone Reservation (TR) OFDM transceiver.	84
4.15: Block diagram of a Tone Injection (TI) OFDM transceiver.	87

4.16: Example of possible expansions of constellation in TI for 16 QAM.88
5.1: Block diagram showing the simulation model of Section 5.2.93
5.2: Block diagram of PTS, CSS and TI transceiver.95
5.3: Simulated CCDF for PTS (V=2, W=8; V=4, W=4; V=4, W=8), CSS (V=2, S=8; V=4, S=4; V=4, S=8) and uncoded OFDM. N=64, adjacent partitioning, with no oversampling in IFFT, (os=1).96
5.4: Simulated CCDF for PTS (V=2, W=8; V=3, W=4), PTS/CSS (V=2, W=4, S=2; V=2, W=4, S=4), and uncoded OFDM. N=64, adjacent partitioning, with no oversampling in IFFT, (os=1).98
5.5: Simulated CCDF for PTS (V=2, W=8), PTS/TI (V=2, W=4, S=2) and uncoded OFDM. N=64, adjacent partitioning, with no oversampling in the IFFT, (os=1).99
5.6: Block diagram showing the simulation model of Section 5.2.	100
5.7: Simulated CCDF of discrete and filtered PTS (V=4, W=4), CSS (V=4, S=4), and uncoded OFDM. N=64, adjacent partitioning, with no oversampling in IFFT (os=1), interpolated by 8, filtered with RCF ($\alpha=0.15$).	101
5.8: Simulated CCDF of discrete and filtered PTS (V=4, W=8), CSS (V=4, S=8), and uncoded OFDM. N=64, adjacent partitioning, with no oversampling in IFFT (os=1), interpolated by 8, filtered with RCF ($\alpha=0.15$).	102
5.9: Simulated CCDF of discrete and filtered PTS (V=2, W=8), PTS/CSS (V=2, W=4, S=2), and PTS/TI (V=2, W=4, S=2), and uncoded OFDM. N=64, adjacent partitioning, with no oversampling in IFFT (os=1), interpolated by 8, filtered with RCF ($\alpha=0.15$).	103
5.10: Simulated CCDF of discrete and filtered PTS (V=3, W=4), PTS/CSS (V=2, W=4, S=4), and uncoded OFDM. N=64, adjacent partitioning, with no oversampling in the IFFT (os=1), interpolated by 8, filtered with RCF ($\alpha=0.15$).	104
5.11: Simulated CCDF for PTS/CSS (V=2, W=4, S=4), and Uncoded OFDM. Discrete oversampled curves (dashed) move from left to right and oversampled (solid) filtered curves move from right to left. N=64, adjacent partitioning, with oversampling rates in the IFFT of 1, 2, 4, and 8, interpolated by 8, and filtered with RCF ($\alpha=0.15$).	105

5.12: Simulated CCDF for PTS (V=3, W=4), and Uncoded OFDM. Discrete oversampled (dashed) curves move from left to right and oversampled (solid) filtered curves move from right to left. N=64, adjacent partitioning, with oversampling rates in the IFFT of 1, 2, 4, and 8, interpolated by 8, and filtered with RCF ($\alpha=0.15$).	106
5.13: Simulated CCDF for PTS (V=2, W=8), and Uncoded OFDM. Discrete oversampled curves (dashed) move from left to right and filtered (solid) oversampled curves move from right to left. N=64, adjacent partitioning, with oversampling rates in the IFFT of 1, 2, and 4, interpolated by 8, and filtered with RCF ($\alpha=0.15$).	107
5.14: Simulated CCDF for PTS/CSS (V=2, W=4, S=2), and Uncoded OFDM. Discrete oversampled curves (dashed) move from left to right and filtered (solid) oversampled curves move from right to left. N=64, adjacent partitioning, with oversampling rates in the IFFT of 1, 2, and 4, interpolated by 8, and filtered with RCF ($\alpha=0.15$).	107
5.15: Simulated CCDF for PTS/TI (V=2, W=4, S=2), and Uncoded OFDM. Discrete oversampled curves (dashed) move from left to right and filtered (solid) oversampled curves move from right to left. N=64, adjacent partitioning, with oversampling rates in the IFFT of 1, 2, and 4, interpolated by 8, and filtered with RCF ($\alpha=0.15$).	108
6.1: Analytical symbol error probability from (6.10) and (6.12) for 64 QAM and N=64.	117
6.2: Probability of clipping DMT signal as a function of μ for p=1,2,3. N=64 subcarriers.	123
7.1: Average noise in the channel vs. BER for 4, 16, and 64 QAM	133
7.2: IQ diagram showing conventional clipping region.	134
7.3: Block diagram of simulation model used for clipping models.	135
7.4: Baseband clip level vs the BERF for varying RRCF parameters. 64 QAM symbols, 64 point IFFT, LPA, no channel impairments. AWGN=0	136
7.5a: Demapped constellation, M=64, with no clipping or channel impairments. 64 filter taps in RRCF, $\alpha=0.15$.	137
7.5b: Demapped constellation, M=64, with no clipping or channel impairments. 128 filter taps in RRCF, $\alpha=0.15$.	137
7.6: Baseband clip level vs the BERF with varying IBO in HPA. 64 QAM	

symbols, 64 point IFFT (os=1), RRCF with 128 taps and $\alpha=0.15$	139
7.7: Baseband clip level vs. the BERF with varying IBO in HPA. 64 QAM symbols, 128 point IFFT (os=2), RRCF with 128 taps and $\alpha=0.15$	139
7.8: CCDF clipped in baseband at 5dB, HPA backoff set to 8dB for 64 and 128 IFFT.	140
7.9: Baseband clip level vs the BERF with varying M-ary constellations. 128 point IFFT (os=2), RRCF with 128 taps and $\alpha=0.15$. AWGN=0.	141
7.10: Baseband clip level vs the BERF with varying p in the SSPA. 128 point IFFT (os=2), RRCF with 128 taps and $\alpha=0.15$. HPA backoff set equal to baseband clipping level.	142
7.11: I Q diagram showing different sector clipping regions and the direction of data reduction for 3 <i>Sector</i> Clipping.	144
7.12: Input output relationship of clipping operation.	144
7.13: I Q diagram of 1st quadrant of a 3 <i>Sector</i> clipping system showing the vector of an unclipped and clipped sample.	150
7.14: Block diagram of 3 <i>Sector</i> clipping.	156
7.15: Flowchart for the LUT in Figure 7.14 (3 <i>Sector</i> clipping)	157
7.16: Theoretical Clip level vs. SNR for Conventional (Standard), 3 <i>Sector</i> , and Square clipping. Theoretical (dashed), simulated (solid)	159
7.17: Clipping angle, θ , vs. the SNR for 3 <i>Sector</i> clipping, based on (7.41).	160
7.18: I Q diagram showing the 1st quadrant Sector clipping regions of a) 4 Sector clipping and b) 5 <i>Sector</i> clipping.	161
7.19: Simulated clip level vs. SNR for Conventional, Square, 3, 4, and 5 <i>Sector</i> Clipping.	162
7.20: Design flow for silicon implementation of 3 <i>Sector</i> clipping.	163
7.21: Block diagram of 3 <i>Sector</i> clipping implemented in VHDL.	163
7.22: <u>A</u> pplication <u>S</u> pecific <u>I</u> ntegrated <u>C</u> ircuit (ASIC) view of 3 <i>Sector</i> clipping algorithm implemented in Silicon using ‘Cadence Silicon Ensemble’. 0.5 μ process, 3 metal layers.	166
7.23: Block diagram of new <i>Vector Subtraction</i> scaling operation.	169
7.24: IQ plane for Vector Subtraction showing vector of sample being clipped.	170
7.25: Simulated CCDF for Lucent patent [101] for various iterations clipped	

at 5dB showing the leakage of under clipped samples.	171
7.26: Simulated CCDF for <i>Vector Subtraction</i> for various iterations clipped at 5dB showing the leakage of under clipped samples.	171
7.27: Simulated clip level vs. SNR for <i>Lucent</i> clipping technique with varying iterations, as well as <i>Conventional</i> and <i>Square</i> clipping.	172
7.28: Simulated clip level vs. SNR for <i>Vector Subtraction</i> clipping with varying iterations, as well as <i>Conventional</i> and <i>Square</i> clipping.	173
7.29: Simulated 3, 4, and 5 <i>Sector</i> , <i>Conventional</i> and <i>Square</i> clipping vs. BERF with a LPA. 64 QAM symbols, 128 point IFFT (os=2), RRCF with 128 taps, and $\alpha=0.15$, AWGN=0	174
7.30: Simulated <i>Vector Subtraction</i> (1, 2, 3, and 4 iterations), <i>Conventional</i> and <i>Square</i> clipping vs. BERF with a LPA. 64 QAM symbols, 128 point IFFT (os=2), RRCF with 128 taps, and $\alpha=0.15$, AWGN=0	175
7.31: Simulated <i>Lucent</i> [101] clipping (1, 2, 3, and 4 iterations), <i>Conventional</i> and <i>Square</i> clipping vs. BERF with a LPA. 64 QAM symbols, 128 point IFFT (os=2), RRCF with 128 taps, and $\alpha=0.15$. AWGN=0	176
7.32: Simulated 3 <i>Sector</i> clipping, vs. BERF with varying IBO in HPA, 64 QAM symbols, 128 point IFFT (os=2), RRCF with 128 taps and $\alpha=0.15$. AWGN=0	177
7.33: Simulated 4 <i>Sector</i> clipping, vs. BERF with varying IBO in HPA 64 QAM symbols, 128 point IFFT (os=2), RRCF with 128 taps and $\alpha=0.15$. AWGN=0	177
7.34: Simulated 5 <i>Sector</i> clipping, vs. BERF with varying IBO in HPA, 16 QAM symbols, 128 point IFFT (os=2), RRCF with 128 taps and $\alpha=0.15$. AWGN=0.	178
7.35: Simulated <i>Vector Subtraction</i> (1 iteration), vs. BERF with varying IBO in HPA. 64 QAM symbols, 128 point IFFT (os=2), RRCF with 128 taps and $\alpha=0.15$. AWGN=0.	179
7.36: Simulated <i>Vector Subtraction</i> (4 iterations), vs. BERF with varying IBO in HPA. 64 QAM symbols, 128 point IFFT (os=2), RRCF with 128 taps and $\alpha=0.15$. AWGN=0	179
7.37: Simulated <i>Lucent</i> clipping (1 iteration), vs. BERF with varying IBO in HPA. 64 QAM symbols, 128 point IFFT (os=2), RRCF with 128 taps, and $\alpha=0.15$. AWGN=0.	181

7.38: Simulated <i>Lucent</i> clipping (4 iterations), vs. BERF with varying IBO in HPA. 64 QAM symbols, 128 point IFFT ($os=2$), RRCF with 128 taps, and $\alpha=0.15$. AWGN=0.	181
7.39: Simulated <i>Square</i> clipping vs. BERF with varying IBO in HPA. 64 QAM symbols, 128 point IFFT ($os=2$), RRCF with 128 taps, and $\alpha=0.15$. AWGN=0.	182
7.40: PSD 0dB clipping in baseband with increasing amplifier backoffs (HPA=CL, CL+1,CL+2,CL+3,CL+4, LPA). RRCF, $\alpha=0.15$, 128 taps.	185
7.41: PSD 5dB clipping in baseband with increasing amplifier backoffs (HPA=CL, CL+1,CL+2,CL+3,CL+4, LPA). RRCF, $\alpha=0.15$, 128 taps.	185
7.42: PSD after 0dB clipping in baseband and receiver filtering, with increasing amplifier backoffs (HPA=CL, CL+1,CL+2,CL+3, CL+4, LPA). RRCF, $\alpha=0.15$, 128 taps.	186
7.43: PSD after 5dB clipping in baseband and receiver filtering, with increasing amplifier backoffs (HPA=CL, CL+1,CL+2,CL+3,CL+4, LPA). RRCF, $\alpha=0.15$, 128 taps.	186
7.44: Block diagram of the <i>Level Detection Algorithm (LDA)</i>	189
7.45: Detailed block diagram of the <i>LDA</i>	189
7.46: a) Amplitude of zero padded input to filter b) amplitude of filtered output c) <i>LDA</i> correction vectors.	190
7.47: Vector representation of filtering with 3 active taps and the required correction vector to bring the output back to CL.	191
7.48: Block diagram of the simulation model used to evaluate <i>LDA</i>	192
7.49: In band distortion for <i>Conventional</i> and <i>Vector Subtraction</i> (2 iter) with 64 and 128 taps in compensation filter. ACL=5dB.	193
7.50: In band distortion for <i>Conventional</i> and <i>Vector Subtraction</i> (2 iter) with 64 and 128 taps in compensation filter. ACL=8dB.	193
7.51: Clipping error vs. in-band distortion. Performance curves for <i>LDA</i> using <i>Conventional</i> clipping and <i>Vector Subtraction</i> with 2 iterations. Compensation filter has 64 and 128 taps. ACL=5dB. . . .	195
7.52: Clipping error vs. in-band distortion. Performance curves for <i>LDA</i> using <i>Conventional</i> clipping and <i>Vector Subtraction</i> with 2	

iterations. Compensation filter has 64 and 128 taps. ACL=8dB. . . . 195

Acronyms and Symbols

ADC	Analog to Digital Converter
ACI	Adjacent Channel Interference
ADSL	Asymmetric Digital Subscriber Line
AGC	Automatic Gain Control
AM/AM	Amplitude Modulation to Amplitude Modulation
AM/PM	Amplitude Modulation to Phase Modulation
AWGN	Additive White Gaussian Noise
BER	Bit Error Rate
BPSK	Binary Phase Shift Keying
BSLM	Blind Selected Mapping
BW	Bandwidth
CCDF	Complementary Cumulative Density Function
CCOFDM	Combined Coded OFDM
CDF	Cumulative Density Function
CDMA	Code Division Multiple Access
CF	Crest Factor
CL	Clip Level
COFDM	Coded Orthogonal Division Multiplexing
CP	Cyclic Prefix
CPR-SPS	Concatenated Pseudo Random Subblock Partition Scheme
CSS	Cyclic Shifted Sequences
DAB	Digital Audio Broadcasting
DAC	Digital to Analog Conversion
DAR	Decision Aided Reconstruction
DFT	Discrete Fourier Transform
DMT	Discrete MultiTone
DQSK	Differential Quadrature Phase Shift Keying
DRL	Data Rate Loss
DSP	Digital Signal Processing
DVB	Digital Video Broadcasting
EDGE	Enhanced Data rates for Global Evolution

FEC	Forward Error Correction
FDM	Frequency Division Multiplexing
FFT	Fast Fourier Transform
FPGA	Field Programmable Gate Array
GSM	Global System Mobile
HD-DIVINE	High Definition-Digital Video Narrowband Emission
HIPERLAN2	HiPERformance Local Area Network version 2
HF	High Frequency
HPA	High Power Amplifier
IBO	Input BackOff
ICI	Inter Channel Interference
IDFT	Inverse Discrete Fourier Transform
IEEE	Institute of Electrical and Electronic Engineering
IFFT	Inverse Fast Fourier Transform
ISI	Inter Symbol Interference
LAN	Local Area Network
LDA	Level Detection Algorithm
LP	Linear program
LPA	Linear Power Amplifier
LUT	Look Up Table
MIMO	Multiple Input Multiple Output
MLD	Maximum Likelihood Detection
MMSE	Minimum Mean Squared Error
MSE	Mean Squared Error
MSR	Multiple Signal Representation
MQAM	M-ary Quadrature Amplitude Modulation
OBO	Output BackOff
OBR	Out of Band Radiation
OLS	Optimal Limited Search
PAP	Peak to Average Power
PAPR	Peak to Average Power Ratio
PDF	Power Density Function
PEP	Peak Envelope Power
PICR	Peak-Intercarrier-to Carrier Interference

PMEPR	Peak to Mean Envelope Power Ratio
PRT	Peak Reduction Tones
PSD	Power Spectral Density
PSK	Phase Shift Keying
P/S	Parallel to Serial
PTS	Partial Transmit Sequences
QAM	Quadrature Amplitude Modulation
QCQP	Quadratically Constrained Quadratic Program
QPSK	Quadrature Phase Shift Keying
RF	Radio Frequency
RMS	Root Mean Square
RRCF	Root Raised Cosine Filter
RS	Reed-Solomon
SBC	Sub Block Coding
SC	Single Carrier
SER	Symbol Error Rate
SES	Suboptimal Exhaustive Search
SL	Soft Limiter
SLM	Selected Mapping
SNR	Signal to Noise Ratio
S/P	Serial to Parallel
SSPA	Solid State Power Amplifier
STERNE	System de Television En Radiodiffusion Numerique
SVD	Singular Value Decomposition
TCM	Trellis Coded Modulation
TI	Time Inversion
TR	Tone Reservation
TWTA	Travelling Wave Tube Amplifier
VHDL	Visual Hardware Design Language
VLSI	Very Large Scale Integration
WCDMA	Wide Band Code Division Multiplexing
WLAN	Wireless Local Area Network
N	Number of subcarriers
<i>n</i>	<i>n</i> th subcarrier in OFDM symbol

$x_m(t)$	m^{th} continuous OFDM symbol
$x_{m,n}$	n^{th} discrete sample of m^{th} OFDM symbol
W	Total occupied frequency bandwidth of OFDM symbol
Δf	Frequency separation between subcarriers
T	Total OFDM symbol duration
T_s	Duration of one sample in OFDM symbol
$X_{m,k}$	k^{th} mapped transmit sample of m^{th} OFDM symbol
$Y_{m,k}$	k^{th} mapped received sample of m^{th} OFDM symbol
N_g	Length of Cyclic Prefix
T_E	Number of taps in equalization algorithm
P	Mean envelope power
P_{av}	Average Power of an OFDM symbol
ζ	Peak to Average Power Ratio of OFDM
ζ_{CF}	Crest Factor of OFDM
x_{mPB}	m^{th} passband OFDM symbol
$P_{\zeta_n}(\zeta)$	Probability density function of an OFDM symbol
$F[\rho]$	Transfer properties of HPA
d_{\min}	Minimum code distance
$d(C_i, C_j)$	Code distance
Rc	Code rate
RM(2, m)	2^{nd} order Reed-Muller codes
$p_{m,k}$	Phase rotation of PTS subblock
W	Number of phase rotations in PTS
V	Number of Subblocks
os	Oversampling rate in IFFT
U	Number of alternate SLM transmit symbols
∂^v	Cyclic shift in time domain for TI
R_{xx}	Autocorrelation of the input
R_{xy}	Cross correlation
R_{yy}	Autocorrelation of the output
α	Roll off factor of pulse shaping filter

R	Clip level
SNR_{conv}	SNR of conventional clipping
$SNR_{3\text{sec}}$	SNR of 3 Sector clipping
d	data stream

Chapter 1

"We are all interested in the future, for that is where you and I are going to spend the rest of our lives. And remember my friend, future events such as these will affect you in the future."

---Criswell, Intro to "Plan 9 From Outer Space" (1958)

Introduction

With the advance of communications technology comes the demand for higher data rate services such as multimedia, voice, and data over both wired and wireless links. New modulation schemes are required to transfer the large amounts of data which existing 3rd generation schemes such as Global System Mobile (GSM), its enhanced version Enhanced Data Rates for Global Evolution (EDGE), and Wideband Code Division Multiple Access (WCDMA) cannot support. These new modulation schemes must be able to act over point to point links and in broadcast mode, support bi-directional communications, and be able to adapt to different requirements of individual services in terms of their data rate, allowable Bit Error Rate (BER), and maximum delay.

One new modulation scheme which has received significant attention over the last few years is a form of multicarrier modulation called Orthogonal Frequency Division Multiplexing (OFDM). OFDM has been used for Digital Audio Broadcasting (DAB) and Digital Video Broadcasting (DVB) in Europe, and for Asymmetric Digital Subscriber Line (ADSL) high data rate wired links. OFDM has also been standardized as the physical layer for the wireless networking standard 'HIPERLAN2' in Europe and as the IEEE 802.11a, g standard in the US, promising raw data rates of between 6 and 54Mbps.

OFDM has various properties that make it desirable over existing single carrier systems, the main advantage is OFDM's immunity to frequency selective fading.

Single carrier systems can increase their data rate by shortening the symbol time, thereby increasing the occupied bandwidth. Wideband channels are sensitive to frequency selective fading which require complex equalizers in the receiver to recover the original signal. OFDM overcomes this problem by dividing the wideband channel into a series of narrowband channels which each experience flat fading. Therefore only 1 tap equalizers are required in the receiver, reducing complexity greatly.

Other factors such as advances in silicon and Digital Signal Processing (DSP) allow the use of efficient Fourier transforms in the transmitter and receiver to perform the modulation, demodulation respectively. Due to the orthogonality of the subcarriers the transmission bandwidth is used efficiently as the subcarriers are allowed to overlap each other and still be decoded at the receiver.

Despite the many advantages of OFDM it still suffers from some limitations such as sensitivity to carrier frequency offset and a large Peak to Average Power Ratio (PAPR). The large PAPR is due to the superposition of N independent equally spaced subcarriers at the output of the Inverse Fast Fourier Transform (IFFT) in the transmitter. A large PAPR is a problem as it requires increased complexity in the wordlength at the output of the IFFT and the Digital to Analog Converter (DAC). Perhaps the most serious problem is the reduced efficiency of the High Power Amplifier (HPA) which must cater for these low probability large peaks.

If the high PAPR is allowed to saturate the HPA out of band radiation is produced affecting adjacent channels and degrading the BER at the receiver. As portable devices have a finite battery life it is important to find ways of reducing the PAPR allowing for a smaller more efficient HPA, which in turn will mean a longer lasting battery life.

1.1 Structure of thesis

This thesis analyses the principles of OFDM concentrating on the PAPR problem in OFDM. The thesis is structured as follows:

- Chapter 2 provides an initial overview of OFDM starting with a brief history of multicarrier networks and their evolution towards OFDM. The multicarrier principle is explained mathematically encompassing the use of the Fourier transform and the principle of orthogonality. OFDM in time varying channels is discussed, its advantages in terms of multipath propagation, the use of a cyclic prefix, frequency selective fading, and equalization. Problems with OFDM are also discussed such as synchronization, which includes timing errors, carrier phase noise, and frequency errors. The issue of the PAPR is also briefly presented. The chapter concludes with a discussion on the applications of OFDM in society.
- Chapter 3 explores the issue of the PAPR in more detail starting with a mathematical definition of the PAPR. Theoretical Cumulative Complementary Distribution Function (CCDF) results are compared to simulated CCDF results identifying the processes which influence large peaks such as the number of subcarriers and oversampling. Non linearities are treated with a description of various models for the HPA, and finally the effect of saturation of the HPA is analyzed in terms of the PSD and the BER.
- Chapter 4 begins the literature review for PAPR reduction techniques reviewing distortionless techniques. Distortionless techniques do not corrupt the data and encode it in such a way that it can be completely recovered at the receiver. Initially the family of coding techniques such as block codes, cyclic codes, Shapiro-Rudin Sequences, Golay complementary sequences, and Reed Muller codes are presented. Multiple representation techniques such as Selective Mapping (SLM), Partial Transmit Sequences (PTS) are reviewed with and without oversampling. Finally modified constellation techniques Tone Reservation (TR) and Tone Insertion (TI) are examined.
- Chapter 5 introduces several new alterations to PTS called Cyclic Shifted Sequences (CSS) and Time Inversion (TI). PTS produces alternative transmit signals by dividing the bit source into a V sub-blocks which each have an IFFT performed on them. Sub-blocks are then rotated by a set phase rotation

(which must be sent as side information to the receiver) and combined to produce a possible transmit symbol, after a number of set phase rotations the transmit symbol with the lowest PAPR is chosen for transmission. CSS and TI reduce complexity and improve performance of PTS by using time shifts of the data instead of phase rotations which can be combined with standard PTS to reduce complexity and in some cases allow for the removal of a whole IFFT operation without degrading performance. It is further shown that CSS and TI perform better after oversampling and filtering than PTS. This work is published in [1, 2].

- Chapter 6 continues the literature review for distorted PAPR reduction techniques which do not attempt to create a transmit signal with a low crest factor, instead they take the output of the IFFT and then limit the amplitude of large samples which invariably causes distortion degrading the BER. Methods reviewed are pulse shaping (or windowing), and clipping at every stage from the output of the IFFT to limited backoffs in the amplifier. Results are analyzed in terms of their BER and affect on the PSD.
- Chapter 7 introduces new low complexity clipping techniques starting with a comprehensive analysis of an OFDM transceiver with clipping at various points in the transmission chain and under other variable conditions such as the amount of oversampling in the IFFT, pulse shaping taps and roll off, and the HPA parameters. New low complexity clipping methods are introduced which avoid complex hardware operations while maintaining similar performance to conventional clipping. The new clipping algorithms called Sector clipping and Vector Subtraction are then implemented in a new clip and filter algorithm which is much less susceptible to peak regrowth after baseband filtering. This work is published in [3].

1.1.1 Contributions

The contribution that this research work has made to the wireless communications field is summarized as follows:

- A thorough analysis of the theory, principles, and techniques of OFDM based wireless systems including a detailed analysis of PAPR reduction techniques are presented (Chapters 2, 3, 4, and 6).
- A new method for producing Partial Transmit Sequences (PTS) signals and their performance under oversampling conditions is proposed (Chapter 5).
- A detailed analysis of the effect of clipping on an OFDM transceiver under various system conditions (Chapter 7).
- Several new low complexity clipping algorithms are proposed (Chapter 7).
- Implementation and analysis of a proposed clip and filter algorithm utilizing one of the new low latency clipping algorithms (Chapter 7).

Chapter 2

Orthogonal Frequency Division Multiplexing

This chapter provides an initial overview of Orthogonal Frequency Division Multiplexing (OFDM). Section 2.1 provides a brief history of multicarrier networks and their evolution towards OFDM. Section 2.2 explains the multicarrier principle and Section 2.3 explains how it is applied to OFDM, detailing the use of the Fourier transform, and the importance of orthogonality. Section 2.4 explores OFDM in time varying channels describing its advantages in terms of multipath propagation, the use of a cyclic prefix, frequency selective fading, and equalization. Limitations of OFDM, such as synchronization, which includes timing errors, carrier phase noise, and frequency errors are discussed in Section 2.5. Non linearities are also introduced as a major hindrance to a practical OFDM system in this section. Section 2.6 looks at applications of OFDM in society and discusses where this new communications technology will be used. Finally Section 2.7 summarizes the chapter with a brief recap of the chapter.

2.1 History of multicarrier networks

Multicarrier networks such as Frequency Division Multiplexing (FDM) have been around since the late 1950's [4], however due to their implementational complexity and inefficient use of the frequency band they were restricted to military applications. A multicarrier system is basically a number of information bearing carriers

transmitted in parallel. Multicarrier systems in wireless applications are less susceptible to channel induced distortions than single carrier systems at corresponding data rates.

Chang [5] and Saltzberg [6] further developed FDM in the mid 60's by introducing multiple carriers which overlap in the frequency domain without interfering with each other, utilizing the frequency spectrum more efficiently, hence OFDM. However the complexity issue still remained.

In the 1970's Weinstein and Ebert [7] used an Inverse Discrete Fourier Transform (IDFT) and Discrete Fourier Transform (DFT) to perform the modulation and demodulation respectively, exploiting the sinusoidal nature of the Fourier Transform and significantly reducing the complexity of an OFDM system.

In the last 10 years more advances in practical OFDM systems have been made, particularly in Europe where various projects and prototypes were initiated such as Digital Video Narrowband Emission (HD-DIVINE), System de Television En Radiodiffusion Numerique (STERNE), and digital Terrestrial Television broadcasting (dTTb). This has led to the adoption of OFDM in many European standards.

OFDM has progressed to the point where it has now been used for various communication applications such as Digital Audio Broadcasting (DAB) and Digital Video Broadcasting (DVB) in Europe. It has also been adopted as the physical layer modulation scheme for wireless networking standards such as Hiperlan2 in Europe and the Institute of Electrical and Electronic Engineers (IEEE) 802.11a, g standards in the United States.

However while OFDM successfully alleviates the problem of dispersive channels there are still some problems which need to be addressed such as time and frequency synchronization, frequency selective fading, and the Peak to Average Power Ratio (PAPR).

2.2 Multicarrier principle

An early form of a multicarrier system is shown in Figure 2.1. The basic principle of multicarrier modulation is to divide the data stream, d , into N parallel data streams with a reduced data rate of d/N . Each low rate data stream is then modulated on a separate narrow band subcarrier and summed together for transmission, thereby providing the same data rate as an equivalent single carrier system. At the receiver a set of filter banks separate the wideband signal into the original narrowband subcarriers for demodulation. *The advantage of this structure over single carrier systems is that the extended symbol time (due to lower data rate) makes the signal less susceptible to effects of the channel such as multipath propagation which introduces Inter Symbol Interference (ISI). Each subchannel will therefore experience flat fading reducing the equalization complexity in the receiver dramatically.* This issue will be explored in more depth in Section 2.4.

A disadvantage of the method shown in Figure 2.1 is the implementation complexity due to the large number of filter banks required in the transmitter and receiver as well as the inefficient use of the available frequency band [8]. The spectra of the different carriers cannot overlap as this would introduce distortion degrading system performance.

2.3 OFDM implementation of multicarrier modulation

A more spectrally efficient implementation of the aforementioned multicarrier system is OFDM (Figure 2.2). In OFDM the transmit signals are constructed in such a way that the frequency spectra of the individual subchannels are allowed to overlap thereby utilising the frequency spectrum much more efficiently.

Mathematically the continuous time representation of the OFDM transmit signal depicted in Figure 2.2 is

$$x_m(t) = \frac{1}{\sqrt{N}} \sum_{k=-N/2+1}^{N/2} X_{m,k} \cdot e^{j2\pi k \Delta f t} \cdot w_k(t-mT) \quad 0 > t > T \quad (2.1)$$

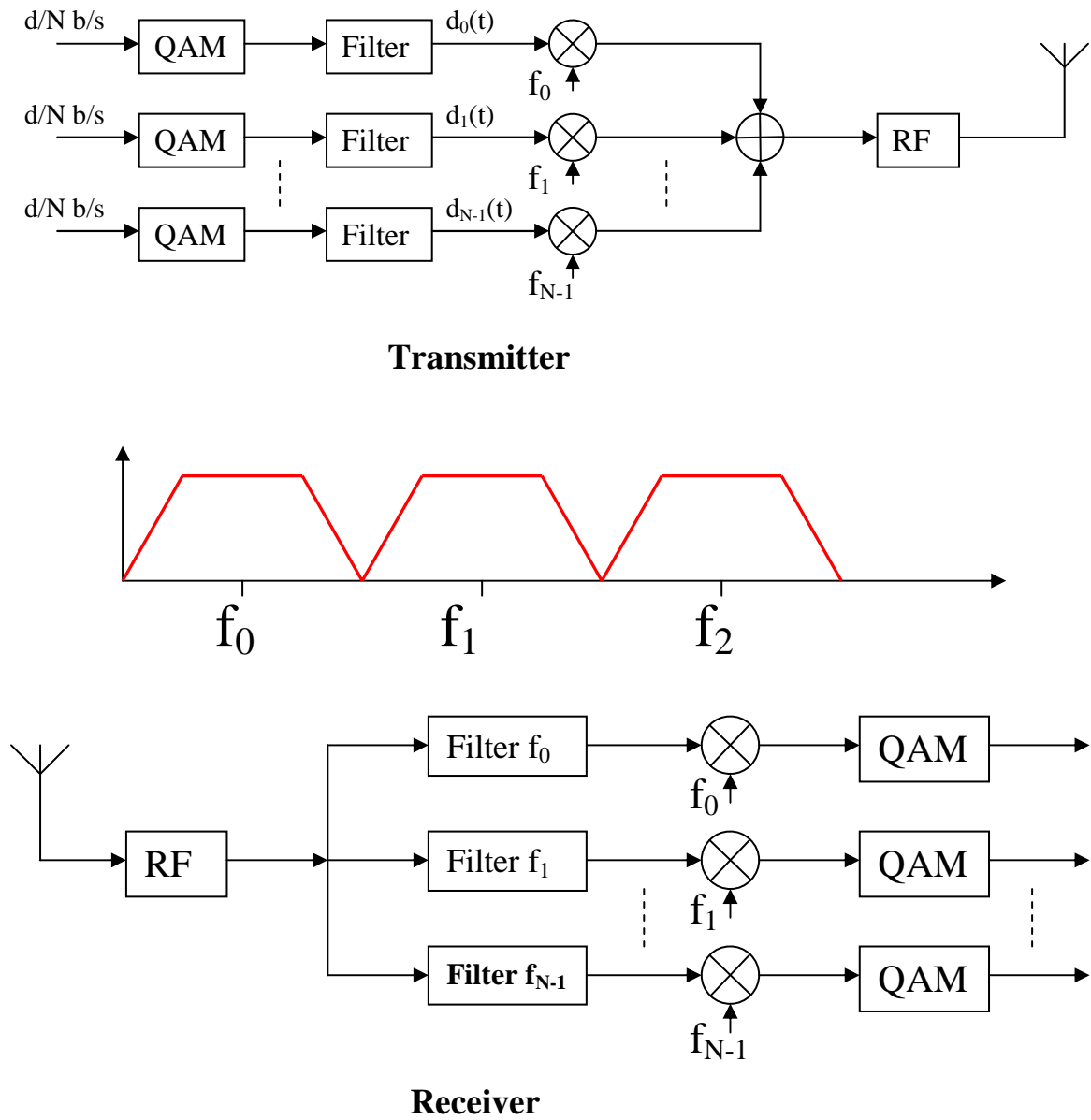


Figure 2.1: Block diagram of a basic multicarrier system.

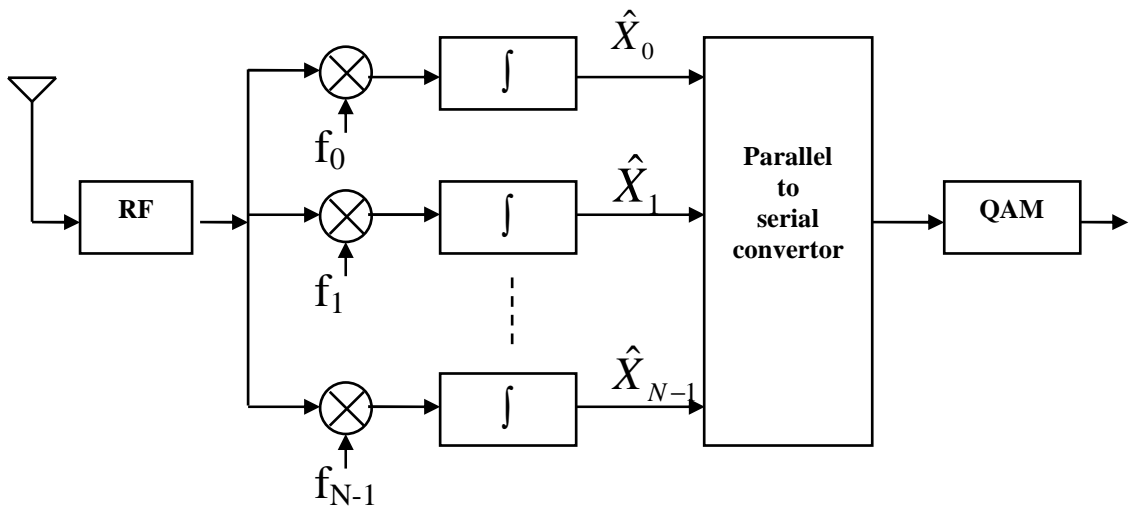
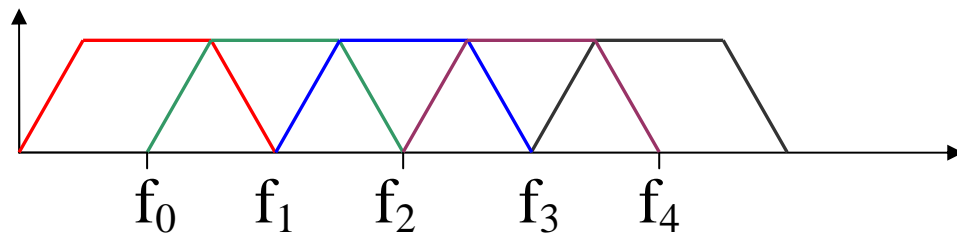
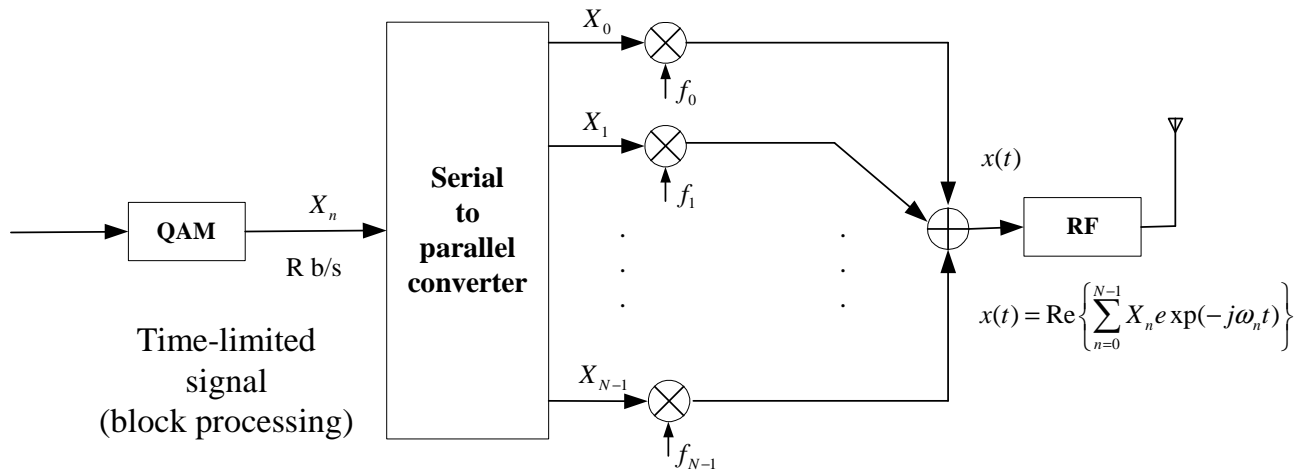


Figure 2.2: Basic OFDM transmitter and receiver. Occupied frequency band shown in between.

where $X_{m,k}$ is the mapped (QAM, PSK, etc) data to be transmitted on the k^{th} subcarrier of the m^{th} transmitted symbol, $e^{j2\pi k\Delta f t}$ is the k^{th} subcarrier, Δf is the frequency spacing between subcarriers, and $w_k(t-mT)$ is a rectangular window applied to each subcarrier, N is the number of subcarriers, and T is the total time of the transmit symbol. To ensure the orthogonal relationship between subcarriers Δf is set as $\frac{W}{N} = \frac{1}{T}$ (W is the total bandwidth of the signal).

In the receiver an integrate and dump operation is performed over time T to recover the data.

2.3.1 Use of Fourier Transform for modulation and demodulation

In order to make multicarrier systems a more practical technology an IDFT and DFT are used for the baseband modulation and demodulation respectively, as first suggested in reference [7], where the sinusoidal nature of the Fourier transform basic functions is exploited. Advances in silicon technology have made the production of the DFT more cost efficient [9-11]. Figure 2.3 shows a block diagram of a basic OFDM system in the baseband utilising the IDFT, DFT pair.

A discrete time representation of (2.1) can be obtained by sampling the continuous signal. Under the condition that $W = N\Delta f$ and $\Delta f = \frac{1}{T}$ the signal can be determined by its samples if sampled at $t = \frac{T}{N}$. Under this condition (2.1) then becomes (2.2)

$$x_{m,n} = \frac{1}{\sqrt{N}} \sum_{k=0}^{N-1} X_{m,k} \cdot e^{j2\pi nk/N} = \text{IDFT} \{X_{m,k}\} \quad 0 \leq n \leq N-1 \quad (2.2)$$

where ‘ n ’ are the discrete sampling points. This equation describes exactly the IDFT operation. In hardware the more efficient form of the IDFT and DFT, the Inverse Fast Fourier Transform (IFFT) and Fast Fourier Transform (FFT) is used for the modulation, demodulation respectively, where N is set to be a power of 2.

Figure 2.3 shows a baseband transceiver structure for OFDM utilising the Fourier transform for modulation and demodulation. Here the serial data stream is mapped to complex data symbols (PSK, QAM, etc) with a symbol rate of $\frac{1}{T_s}$. The data is then demultiplexed by a serial to parallel converter resulting in a block of N complex symbols, X_0 to X_{N-1} . The parallel samples are then passed through an N point IFFT (in this case no oversampling is assumed) with a rectangular window of length $N.T_s$, resulting in complex samples x_0 to x_{N-1} . Assuming the incoming complex data is random it follows that the IFFT is a set of N independent random complex sinusoids summed together. The samples, x_0 to x_{N-1} are then converted back into a serial data stream producing a baseband OFDM transmit symbol of length $T=N.T_s$.

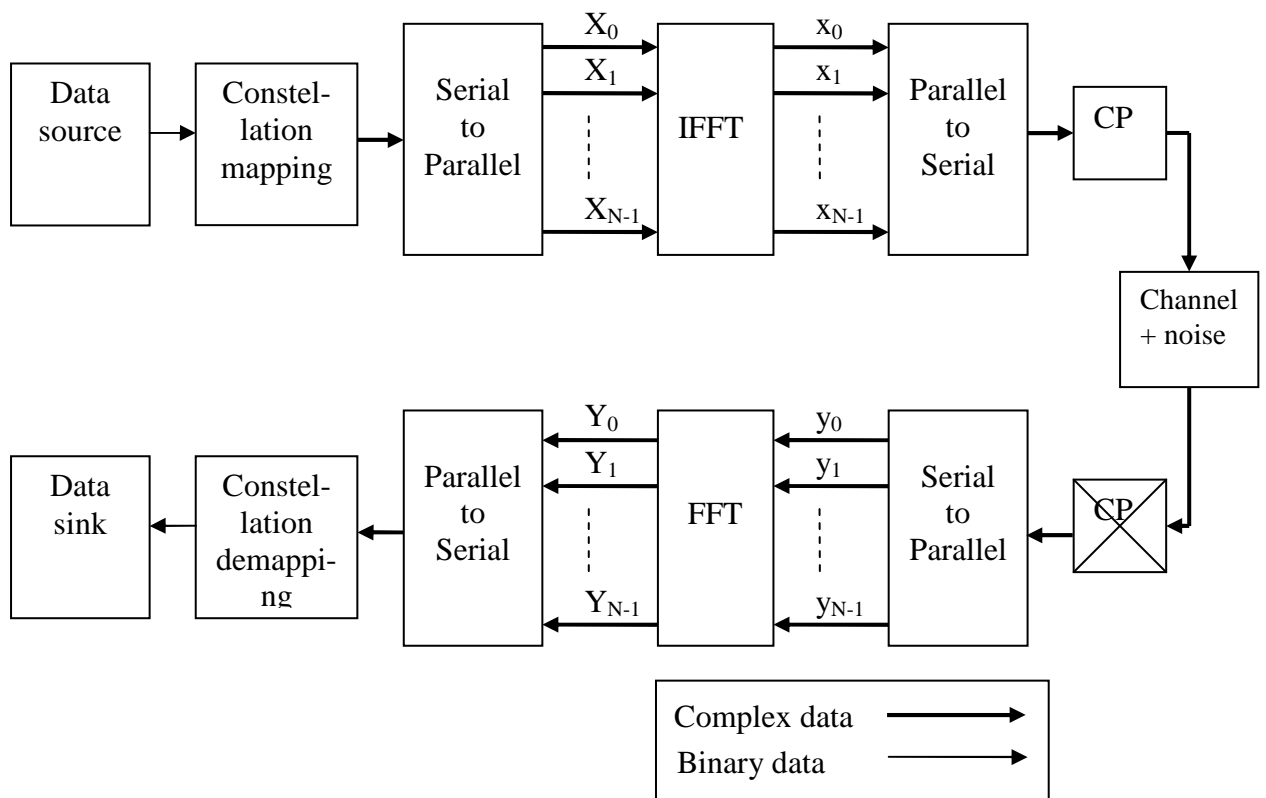


Figure 2.3: Basic OFDM transmitter and receiver pair utilizing Fourier transform.

A Cyclic Prefix (CP), which is a copy of the last part of the samples is appended to the front of the serial data stream before Radio Frequency (RF) up conversion and

transmission. The CP combats the disrupting effects of the channel which introduce Inter Symbol Interference (ISI) and is discussed in more detail in section 2.4.2.

In the receiver the whole process is reversed to recover the transmitted data, the CP is removed prior to the FFT which reverses the effect of the IFFT. The complex symbols at the output of the FFT, $Y_0 \dots Y_{N-1}$ are then decoded and the original bit stream recovered.

Mathematically the demodulation process (assuming no CP and no channel impairments) using the FFT is (2.3)

$$\begin{aligned}
 Y_{m,k} &= FFT\{x_{m,n}\} \\
 &= \frac{1}{N} \sum_{n=0}^{N-1} x_{m,n} e^{-j2\pi nk/N} \\
 &= \frac{1}{N} \sum_{n=0}^{N-1} \sum_{d=0}^{N-1} X_{m,d} e^{j2\pi n(d-k)/N} \\
 &= \frac{1}{N} \sum_{d=0}^{N-1} X_{m,d} \sum_{n=0}^{N-1} e^{j2\pi n(d-k)/N} \\
 &= \frac{1}{N} \sum_{d=0}^{N-1} X_{m,d} N\delta[d-k] \\
 &= X_{m,k}
 \end{aligned} \tag{2.3}$$

2.3.2 Orthogonality in OFDM

One of the key advantages of OFDM is its efficient use of the frequency band as the subcarriers are allowed to overlap each other in the frequency domain. The N equally spaced subcarriers will be orthogonal if the frequency separation between subcarriers is $\Delta f = \frac{1}{N \cdot T_s} = \frac{1}{T}$, where $N \cdot T_s$ is symbol duration, and rectangular windowing of the IFFT is performed. Under these conditions the subcarriers will have a sinc waveform frequency response. Figure 2.4 shows the frequency response of a 5 carrier system where it is seen that because of the orthogonal relationship the maximum of a particular sample corresponds to a null in all other carriers, therefore eliminating the effects of interference. Smoother window functions (eg. Raised Cosine Filter) reduce

the out of band emissions and Inter Carrier Interference (ICI) susceptibility to system imperfections (e.g. frequency offset) but they increase the symbol period.

Mathematically, orthogonality of two signals, $\psi_k(t)$ and $\psi_l(t)$ over time period $N.T_s$ is described in reference [12] and expressed here as (2.4)

$$\int_0^{NT_s} \psi_k(t) \psi_l^*(t) dt = \begin{cases} 0, & k \neq l \\ C, & k = l \end{cases} \quad (2.4)$$

where C is a constant.

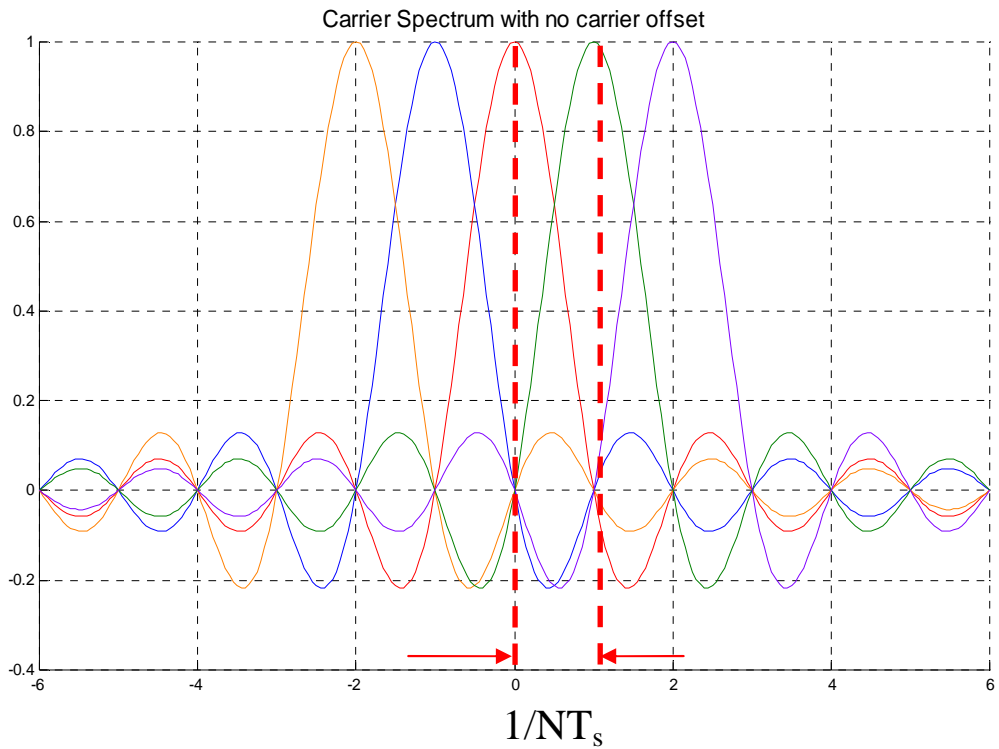


Figure 2.4: Frequency spectrum of 5 orthogonal subcarriers of an OFDM transmit signal

2.4 OFDM transmission over time varying channels

OFDM is being primarily deployed in the wireless environment. This section describes properties of the wireless channel and describes the advantages and disadvantages of OFDM in this environment.

2.4.1 Multipath propagation

The wireless channel is a harsh one, electromagnetic signals travelling through this medium are fraught with disruptive and warping effects. The transmitted signal does not only have a direct path to the receiver (in the case of line of sight). The signal is reflected off buildings and mountains and other obstacles so that multiple delayed copies of the same transmitted signal arrive at the receiver affecting other symbols. This causes ISI which degrades the Bit Error Rate (BER). The longer the delay of the paths the greater the ISI, a measure of the delay is given by the root-mean-square (rms) delay spread which is a measure of the delay experienced by a single pulse.

It is this effect which restricts single carrier systems from achieving high data rates. The data rate in a single carrier system can be increased by shortening the symbol time of the transmitted pulses, but they will be even more affected by the rms delay spread and require more complex equalisation in the receiver. As the rms delay spread is a result of the physical channel it cannot be changed and systems must be designed to accommodate it. This phenomenon has prompted the use of multicarrier techniques where the transmitted bandwidth is divided into many narrow band channels which are then transmitted in parallel. Each subcarrier is modulated at a sufficiently low data rate so that it is not affected by the delay spread.

2.4.2 Use of a Cyclic Prefix

In order to protect successive OFDM symbols from multipath a CP of length N_g is used which is a copy of the last part of the samples of a OFDM transmit block appended to the front before transmission as depicted in Figure 2.5. The transmitted signal is therefore $N+N_g$ samples. Provided that the length of the CP is chosen so that it is longer than the longest expected delay path successive OFDM symbols will be free of ISI [13].

At the receiver a window of N samples is chosen from the $N+N_g$ length block for maximum power, the rest of the repeated samples are discarded. After cyclic shifting to get the samples back into the original order a FFT is performed to demodulate the data.

Obviously the use of a CP decreases the data rate by a factor of

$$\frac{N}{N + N_g} \quad (2.5)$$

as the repeated samples are discarded in the receiver so it is important to keep the length of the CP as short as possible with respect to the rms delay spread. A loss in the SNR of the received signal is also incurred due to the lost energy in the CP. However there are techniques which use the CP for both frequency offset estimation and symbol synchronization [14]. Also when filtering the signal there is a delay before the filter is at full power, by using a CP the delay will occur in CP so that N of the samples will be at full power. The CP (with repeated samples) retains the cyclic nature of the symbol by creating a periodic received signal for processing, eliminating ICI.

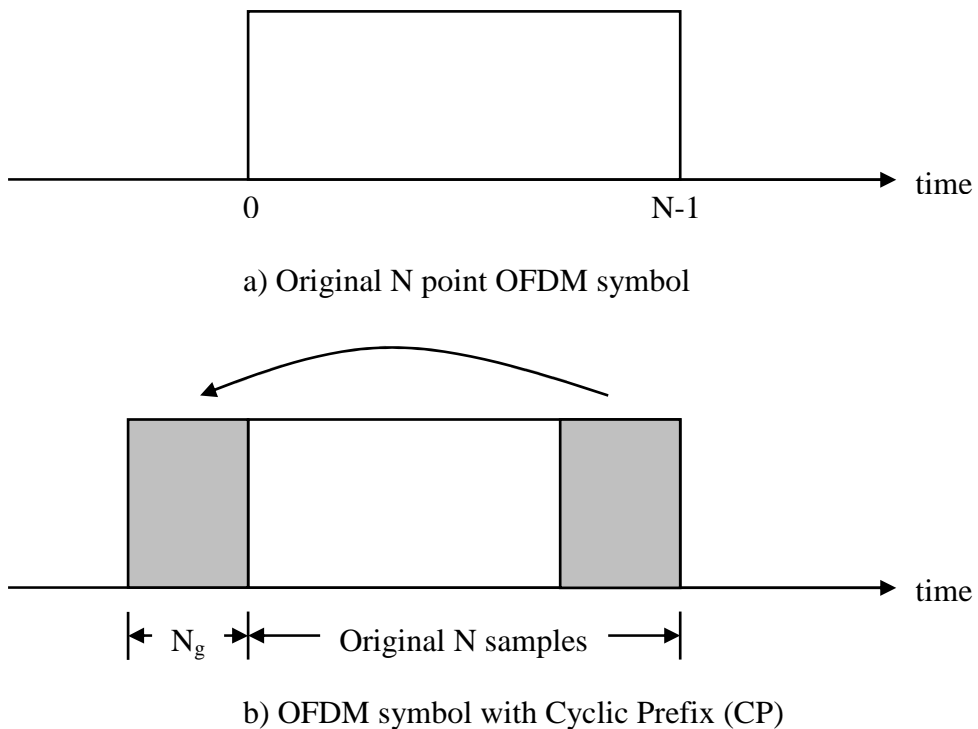


Figure 2.5: OFDM symbol a) without cyclic prefix, and b) with cyclic prefix.

More recent work has shown that it is possible to use null values for the CP provided additional processing is done at the receiver. The received signal in the null sample positions is wrapped around and added to the samples at the start of the symbol to restore orthogonality and eliminate ICI. This is one of the proposals for the new IEEE 802.15.3a ultra wideband standard.

Other forms of the CP have also been investigated, in particular reference [15] examines the effect that using null values in the CP will have. It was concluded that null samples have a detrimental effect through loss of orthogonality increasing ICI.

2.4.3 Frequency selective fading

Multipath propagation as discussed in the previous section can be combated successfully through the use of a cyclic prefix. Frequency selective fading is the reciprocal effect of multipath propagation in the time domain and can be defined thus. If the channel has a constant magnitude and phase response over a bandwidth that is *smaller* than the bandwidth of the transmitted signal the channel creates frequency selective fading [16]. Under this condition the signal experiences multipath introducing ISI, this effect shows itself in the frequency domain where certain frequency components in the received spectrum have greater or less power than the transmitted spectrum.

Narrow pulses in time (such as high data rate single carrier transmission) occupy a wide frequency bandwidth, conversely pulses with a long duration (such as OFDM) occupy a relatively narrow frequency band. Figure 2.6 compares a single and multicarrier signal in the time and corresponding frequency domain with equivalent data rates. Here we see that the many narrowband channels of the OFDM signal experience fading, however each subchannel has a constant gain within its own frequency band. Constant fading over the occupied bandwidth is known as frequency flat fading and is a much easier effect to correct in the receiver than frequency selective fading.

2.4.4 Equalization

In order for the receiver to correct the effect of fading equalization is performed in the receiver which is the process of measuring the channel response and using this information to correct the received signal. Several methods have been suggested, one of the more popular methods utilize pilot tones [17-19] which are certain (usually evenly spaced) subcarriers with a known amplitude and phase at the receiver. By measuring the difference between the received and the transmitted value a picture of the channel can be extrapolated. Other methods use blind estimation techniques [20, 21] which do not require pilot tones. The equalization technique depends on the modulation scheme and the channel properties. Equalization algorithms are usually implemented as tapped delay lines. The relation between the number of taps required, T_E and the occupied bandwidth, W , of the signal is [22].

$$T_E = (BW)^2 \quad (2.6)$$

Signals which experience frequency selective fading such as single carrier systems require complex equalization (i.e. more taps) where the complexity is directly proportional the bandwidth of the signal. Signals such as OFDM which experience frequency flat fading only require a 1 tap equalizer. This reduction in equalization complexity is a driving force for the use of OFDM.

2.5 Limitations in OFDM

Previous sections have detailed the advantages of OFDM, however the advantages are offset by some problems that are unique to OFDM, namely time and frequency synchronization problems and non linearities.

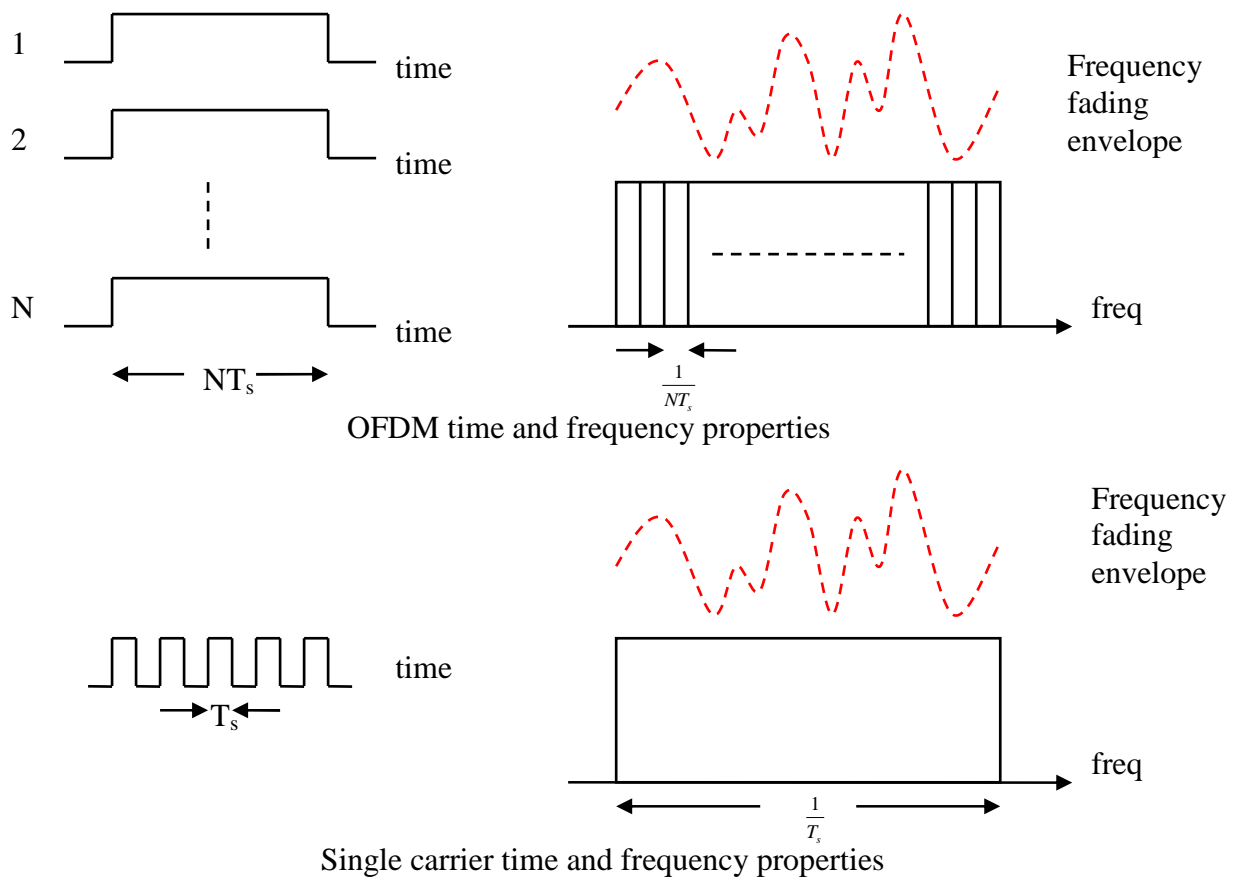


Figure 2.6: Time and frequency properties of single carrier and OFDM techniques.

2.5.1 Synchronization

Both time and frequency synchronization are a major drawback in OFDM, the following sections detail the problem and provide a basic introduction into solutions for these problems.

2.5.1.1 Timing errors

Timing synchronization is the process of finding the start of a symbol in the receiver. If the timing mismatch is within the CP the demodulation produces a linear phase rotation at the output of the FFT which can be corrected with a channel estimator.

$$\tilde{x}_b(t) = \sum_{k=0}^{N-1} a[k] e^{j2\pi[k\Delta f t + (f_c + k\Delta f)\delta t]} \quad (2.7)$$

where

$$\hat{a}_{\delta t}[k] = a[k] e^{j2\pi(f_c + n\Delta f)\delta t} \quad (2.8)$$

is the phase shift.

If the timing mismatch is not corrected additional interference (ISI) is generated. Therefore a sufficient length of the CP needs to be chosen. An alternative approach is to use pilot based methods [13] which uses certain carriers with a known amplitude and phase at the receiver. By analyzing the phase rotation and amplitude change, an estimate of the channel can be made.

2.5.1.2 Carrier phase noise

Carrier phase noise is caused by a mismatch in the RF oscillators in the transmitter and receiver and manifests itself in the baseband as additional phase rotation and amplitude attenuation [13]. No distinction can be made between phase rotations introduced by timing errors and carrier phase offset [14]. The effect of phase noise is more pronounced in differential detection schemes than coherent detection schemes [13]. Several references [23, 24] have analyzed the effect of carrier phase noise on the performance of OFDM schemes.

2.5.1.3 Frequency errors

Frequency offset errors are caused by mismatch between the RF oscillators, Doppler shifts, and phase noise introduced by non linear channels [14]. Frequency offset causes the received signal to not be sampled at the peak, this means that the sample under consideration is not at maximum power. Power from adjacent subcarriers is also sampled as well. A simplistic representation of this effect in the frequency domain is visualized in Figure 2.7.

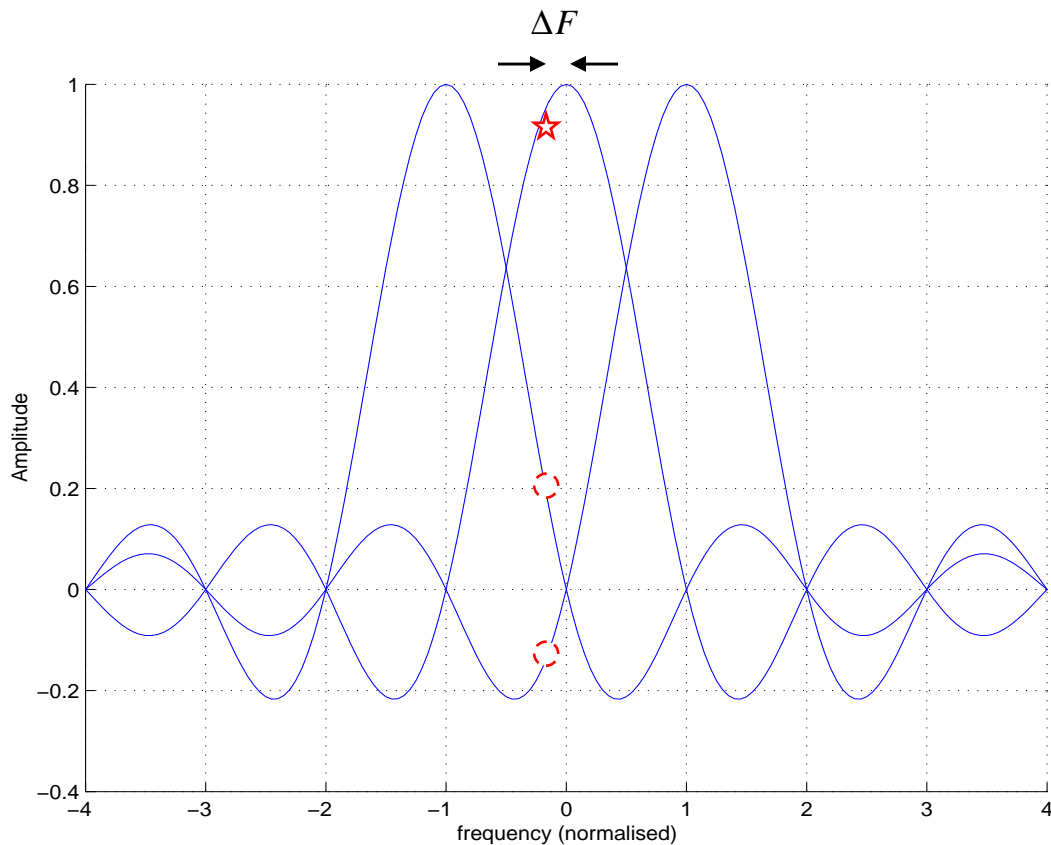


Figure 2.7: Effects of frequency offset ΔF : reduction of signal amplitude (star), and ICI (circle).

OFDM is more sensitive to frequency offset than single carrier systems due to the tight orthogonal packing of the subcarriers. Reference [14] concludes that to avoid severe degradation the frequency accuracy should be better than 2%.

Suggested solutions to frequency synchronization (like symbol synchronization) are based on pilot symbols and the cyclic prefix are used in reference [14] where it is noted that time and frequency synchronization are closely related. Frequency sensitivity can be made more robust by reducing the number of subcarriers within a set bandwidth thereby increasing the frequency distance between subcarriers. However this shortens the symbol time which increases the demands on timing synchronization, therefore a trade off must be made.

2.5.2 Non linearities

Another limiting aspect of multicarrier and OFDM modulation is the high instantaneous signal peak with respect to the signals average power. Large peaks are due to the superposition of N random phase sine waves in the IFFT. Hardware components such as the Digital-to-Analog Converter (DAC), IFFT/FFT with limited word length and most importantly the High Power Amplifier (HPA) will be driven into saturation unless they are designed to operate over large dynamic ranges. If the signal is allowed to go into saturation both in band noise which degrades the BER and out of band radiation introducing ICI will result.

Therefore many papers (refer to Chapters 4, 5, 6, and 7) have been published on ways to overcome the PAPR and can be divided into two methods: distortionless techniques which attempt to create a transmit signal with a low PAPR without affecting BER of the data, and distorted techniques which deliberately reduce peaks but increase distortion and therefore the BER. *This problem is the area of research of this thesis and will be treated with more detail in the following chapters.*

2.6 Applications of OFDM

The previous section detailed some of the problems with OFDM, it should be noted that depending on the application and medium different design issues take precedence. This section identifies some of the current and future applications of OFDM. OFDM takes its place in the next generation of communication systems because of its high data rates and low complexity.

2.6.1 COFDM

Coded OFDM (COFDM) is a practical form of OFDM where redundant bits are inserted into the bit stream at the transmitter. These specially chosen bits allow powerful error correction codes in the receiver to reduce the BER. The more bits used for error correction the better the error correction properties, however the useful data rate is decreased.

Types of error correction codes used for example DAB-OFDM are Trellis Coded Modulation (TCM) combined with frequency and time interleaving. In practice all the following technologies use some form of COFDM.

2.6.2 Digital Audio Broadcasting

Digital Audio Broadcasting (DAB) using OFDM has been standardized in Europe [25] and is the next step in evolution beyond FM radio broadcasting providing interference free transmission. The standard for DAB is known as Eureka-147 [26] and is a multi-service digital broadcasting method transmitting at around 1.5Mbps in the 1.536MHz band. In DAB between 192 and 1536 carriers are used with Differential Quadrature Phase Shift Keying (DQPSK), which allows the system to avoid channel estimation techniques. The very long symbol time means that large echoes can be tolerated and that the redundancy due to the CP is not that great. Large echoes are expected as the broadcasting is over large distances so that long delay paths will be present. The PAPR is a problem but as DAB only uses DQPSK modulation it is more impervious to noise generated through saturation of the amplifier. The DAB data payload contains audio, data associated with audio, and other optional data services. Table 2.1 displays system parameters for DAB.

Table 2.1: DAB parameters.

Parameters	Mode		
	I	II	III
Application	SFN	Terrestrial	Satellite
Modulation	DQPSK	DQPSK	DQPSK
Total number of subcarriers	1536	384	192
OFDM symbol duration	1246 μ S	312 μ S	156 μ S
Guard interval	246 μ S	62 μ S	31 μ S
Frequency range	≤ 375 MHz	≤ 1.5 GHz	≤ 3 GHz

2.6.3 Digital Video Broadcasting

Digital Video Broadcasting (DVB) [27, 28] is also using OFDM as the carrier modulation scheme. DVB promises to deliver full multimedia in digital form in a broadcast format. DVB adapts the baseband TV signal from the output of the MPEG-2 [29] transport multiplexer to the terrestrial channel characteristics. Maximum spectral efficiency within the VHF and UHF bands is achieved by utilizing Single Frequency Network (SFN) operation. There are two modes defined in DVB: 1/ 2K mode, and 2/ 8K mode. The 2K mode is used for single transmitters and small SFN's where the distance for transmission is limited. The 8K mode encompasses the 2K mode as well as larger SFN's. One of the many advantages of OFDM is that different mapping types can be used on different subcarriers, this aspect is taken advantage of in DVB so that the data rate on a channel mirrors its quality. Table 2.2 shows the system parameters for DVB in 2K mode [28].

Table 2.2: DVB system parameters for 2K mode.

Parameters	Value
Information data rate	5-30 Mbps
Modulation	QPSK, 16 QAM, 64 QAM
FEC code	Reed Solomon outer code Convolutional inner code
Code Rates	$\frac{1}{2}$, $\frac{2}{3}$, $\frac{3}{4}$
Total number of subcarriers	1705 (2K mode)
OFDM symbol duration	303 μ S
Guard interval	75.9 μ S
Signal bandwidth	5.62MHz

2.6.4 HiperLan2/802.11a

Wireless networking standards such as HIPERLAN2 and 802.11a use OFDM as the physical layer modulation scheme and operate in the unlicensed 5GHz frequency band. Hiperlan2 promises to deliver raw data rates of up to 56Mbps which puts them in the ballpark of wired LANs which have data rates of up to 100Mbps. Wireless

LANs applications are for home and office networking over short distances (<50 metres) as well as community spaces such as Starbucks which operates the 802.11b wireless standard free of charge for customers and provides data rates up to 11Mbps [52]. Tables 2.3 and 2.4 list Hiperlan2/802.11a specifications and data rates respectively.

Table 2.3: HIPERLAN2 parameters

Parameter	Value	
Sampling Rate $f_s=1/T$	20MHz	
Useful symbol part duration T_U	$64 \times T$ 3.2 μ S	
Cyclic Prefix duration T_{CP}	$16 \times T$ 0.8 μ S (mandatory)	$8 \times T$ 0.4 μ S
Symbol Interval T_S	$80 \times T$ 4.0 μ S (T_U+T_{CP})	$72 \times T$ 3.6 μ S (T_U+T_{CP})
Number of data sub-carriers N_{SD}	48	
Number of pilot sub-carriers N_{SP}	4	
Total number of sub-carriers N_{ST}	52 ($N_{SD}+N_{SP}$)	
Subcarrier spacing Δf	0.3125MHz ($1/T_U$)	
Spacing between two outmost sub-carriers N_{ST}	16.25MHz ($N_{ST} \times \Delta f$)	

Table 2.4: Data rates for HIPERLAN2

Modulation	Coding rate R	Nominal bit rate (Mbps)
BPSK	1/2	6
BPSK	3/4	9
QPSK	1/2	12
QPSK	3/4	18
16QAM	9/16	27
16QAM	3/4	36
64QAM	3/4	54 (optional)

2.6.5 ADSL

Asynchronous Digital Subscriber Lines (ADSL) utilize OFDM over wired links [30]. Data rates for ADSL standard [14] are 1.54Mbps to 6.1Mbps in the downlink and 9.6 to 192Kbps in the uplink over several kilometers of ordinary twisted pair telephone line, while still supporting the standard telephone. The unbalanced data rates make

ADSL particularly applicable to internet type applications where the downlink rate is typically much larger than the uplink rate.

Stationary channels like wireless links do not change over time, therefore a technique called bit loading is used. Bit loading assigns a mapping type to sub-carriers depending on its quality, using the available bandwidth efficiently. Bit loading used in conjunction with OFDM over wired links is usually called Discrete MultiTone (DMT).

2.6.6 MIMO OFDM

Multiple In Multiple Out (MIMO) [31] OFDM combines OFDM with multiple antennas at the transmitter and receiver. This structure allows greater diversity when techniques such as Singular Value Decomposition (SVD) are used. This process, called spatial multiplexing, proportionally boosts the data-transmission speed by a factor equal to the number of transmitting antennas. In addition, since all data is transmitted both in the same frequency band and with separate spatial signatures, this technique utilizes spectrum very efficiently.

2.7 Conclusion

This chapter introduced fundamental properties of OFDM, identifying its advantages and discussing its limitations. Specifically the history of multicarrier networks was discussed and its evolution towards OFDM. The introduction of the Fourier transform, advances in silicon technology, and the efficient use of the frequency spectrum with orthogonally spaced subcarriers were shown to make OFDM a practical technology for the next generation of digital communications.

OFDM transmission over wireless channels was discussed focusing on multipath propagation and the advantages of OFDM in this medium. The use of the cyclic prefix in OFDM was shown to reduce the equalizer complexity dramatically down to one tap per subcarrier. This is one of the great advantages of OFDM over single

carrier networks which require prohibitively high complexity equalizer structures as the carrier frequency is increased to cater for higher data rates. Frequency selective fading was also introduced as a major advantage of OFDM where due to the long effective symbol time OFDM subcarriers experience flat fading.

Limitations of OFDM were analyzed next, with the two main disadvantages; synchronization errors and non linearities treated. Synchronization errors were shown to include timing errors, carrier phase noise, and frequency errors. Non linearities due to the Rayleigh distributed samples at the output of the IFFT were also briefly introduced and shown to have a degrading affect on the quality of OFDM systems.

Finally applications of OFDM were presented detailing where this new technology has manifested itself in society. Areas of application in the wireless field were shown to be COFDM, DAB, DVB where OFDM is used in a broadcast mode, Hiperlan2/802.11a for wireless networking potentially taking the place of large wired networks. OFDM in DMT form is being used in wired networks for ADSL. Extensions of OFDM such as MIMO OFDM were also shown to expand the reach of OFDM systems.

Chapter 3

Peak to Average Power in OFDM

Chapter 2 discussed fundamental principles of OFDM and showed how it is a practical technology for the next generation of high data rate communication systems. However several design issues need to be addressed, one of the most important being the Peak to Average Power Ratio (PAPR) of the highly fluctuating transmit signal envelope.

Due to the nature of the IFFT which, as described in Section 2.3, sums N sinusoids through superposition, some combinations of the sinusoids create large peaks. The drawback of a large dynamic range is that it places pressure on the design of components such as the word length of the IFFT/FFT pair, DAC and ADC, mixer stages, and most importantly the HPA which must be designed to handle irregularly occurring large peaks. Failure to design components with a sufficiently large linear range results in saturation of the HPA. Saturation creates both in band distortion, increasing the BER and out of band distortion, or spectral splatter, which causes ACI.

One obvious solution is to design the components to operate within large linear regions, however this is impractical as the components will be operating inefficiently and the cost becomes prohibitively high. This is especially apparent in the HPA where much of the cost and ~50% of the size of a transmitter lies.

This chapter provides a mathematical definition of the PAPR and identifies the processes which contribute to large peaks. Specifically section 3.1 gives a

mathematical definition of the PAPR, section 3.2 provides a statistical analysis of PAPR and identifies contributing factors to large peaks. Section 3.3 introduces oversampling of OFDM signals while section 3.4 investigates the effect of non linearities on OFDM, finally section 3.5 summarizes the chapter reiterating the main points of this section. Note that the terms subcarrier, tones, and N will be used interchangeably to signify the number of subcarriers in an OFDM symbol.

3.1 Peak to Average Power Ratio

The PAPR is the relation between the maximum power of a sample in a given OFDM transmit symbol divided by the average power of that OFDM symbol. The mean envelope power of the baseband expression (assuming same constellation on each subcarrier) is defined as (3.1)

$$P = \frac{1}{T} \int_{t=0}^T |x_m(t)|^2 dt = \frac{1}{N} \sum_{k=0}^{N-1} |X_{m,k}|^2 \quad (3.1)$$

where $x_m(t)$ is defined in (2.1), $X_{m,k}$ are assumed to be complex Quadrate Amplitude Modulated (QAM) data which are statistically independent, identically distributed (i.i.d) random variables with 0 mean and variance $\sigma^2 \triangleq E[|X_{m,k}|^2]$. The average power is defined as (3.2)

$$P_{av} = E[P] = E[|x_m(t)|^2] \quad (3.2)$$

The PAPR can then be defined

$$\zeta = \frac{\max_{0 \leq t \leq T} |x_m(t)|^2}{P_{av}} \quad (3.3)$$

where $\max_{0 \leq t \leq T} |x_m(t)|^2$ is the maximum instantaneous power within the period $0 \leq t \leq T$.

Another definition for the PAPR is *crest factor*, defined in reference [32] as (3.4)

$$\xi_{CF} = \frac{\max_{0 \leq t \leq T} |x_m(t)|^2}{\sqrt{P_{av}}} \quad (3.4)$$

and results in a 3dB shift in results compared to (3.3). Throughout this thesis the definition of the PAPR given in (3.3) will be used unless specified otherwise.

For passband transmission the OFDM symbol is modulated onto a carrier frequency, f_c ,

$$\begin{aligned} x_{mPB} &= \Re\{x_m(t) e^{j2\pi f_c t}\} \\ &= \Re\{x_m(t)\} \cos(2\pi f_c t) - j\Im\{x_m(t)\} \sin(2\pi f_c t) \\ &= x_{mI}(t) \cos(j2\pi f_c t) - jx_{mQ}(t) \sin(j2\pi f_c t) \end{aligned} \quad (3.5)$$

The carrier frequency is usually much higher than the signal bandwidth, i.e. $f_c \gg \Delta f$, therefore the maximum of the passband signal is approximately equal to the baseband expression, i.e.

$$\max |x_{mPB}(t)| \approx \max |x_m(t)| \quad (3.6)$$

Most OFDM schemes usually employ QAM mapping for the modulation where

$|x_{mI}(t)|^2 = |x_{mQ}(t)|^2$ therefore

$$E\{|x_m(t)|^2\} = 2E\{|x_{mI}(t)|^2\} = 2E\{|x_{mQ}(t)|^2\} \quad (3.7)$$

The average RF power of the passband signal can be derived as

$$\begin{aligned} E\{|x_{mPB}(t)|^2\} &= E\{|x_{mI}(t) \cos(2\pi f_c t) - jx_{mQ}(t) \sin(2\pi f_c t)|^2\} \\ &= E\{|x_{mI}(t) \cos(2\pi f_c t)|^2\} + E\{|x_{mQ}(t) \sin(2\pi f_c t)|^2\} \end{aligned}$$

$$\begin{aligned}
 &= \frac{1}{2} E\{|x_{mI}(t)|^2\} + \frac{1}{2} E\{|x_{mQ}(t)|^2\} \\
 &= \frac{1}{2} E\{|x_m(t)|^2\} \\
 &= P_{av}/2
 \end{aligned} \tag{3.8}$$

Substituting (3.8) back into (3.3) gives the PAPR in the passband.

$$\begin{aligned}
 \zeta_{PB} &= \frac{\max_{0 \leq t \leq T} |x_{mPB}(t)|^2}{E\{|x_{mPB}(t)|^2\}} \\
 &= \frac{\max_{0 \leq t \leq T} |x_{mPB}(t)|^2}{P_{av}/2}
 \end{aligned} \tag{3.9}$$

The problem with OFDM is that theoretically the PAPR can be up to $\log_2(N)$, which is huge. But as will be shown in the next section the general distribution of samples is much lower.

3.2 Statistical distribution of OFDM samples

Section 3.1 provided a worst case scenario or upper bound of the PAPR, but only a few combinations of input data sequences produce large peaks, therefore it is more pertinent to define the statistical distribution of the PAPR in OFDM. (2.2) describes a Nyquist sampled baseband OFDM symbol with N subcarriers, from the central limit theorem [33] the sum of these elements are zero mean complex random near Gaussian (provided $N > 64$) distributed variables with variance, σ^2 , of $1/2$. It then follows that the amplitude, a_n , of the OFDM symbol has a Rayleigh distribution [13] with a Probability Density Function (PDF) of

$$p_{\zeta_n}(\zeta) = \frac{\zeta}{\sigma^2} e^{-\zeta^2/2\sigma^2} \tag{3.10}$$

Substituting $\sigma^2 = 1/2$

$$p_{\zeta_n}(\zeta) = 2\zeta e^{-\zeta^2} \quad (3.11)$$

Figure 3.1 shows the simulated envelope ($N=64$) of a baseband OFDM system which as expected follows a Rayleigh distribution. It is seen here that the probability of any given sample having a magnitude above 3dB decays rapidly. The probability that the magnitude of a sample is below a certain threshold, ζ_0 , is given by the Cumulative Distribution Function (CDF)

$$\Pr\{\zeta \leq \zeta_0\} = \int_{-\infty}^{\infty} p_{\zeta_n}(\zeta) d\zeta = \int_0^{\zeta_0} 2\zeta e^{-\zeta^2} d\zeta = 1 - e^{-\zeta_0^2} \quad (3.12)$$

Under the assumption of statistically independent samples the Complementary Cumulative Distribution Function (CCDF) can be found for the case where at least one sample in an OFDM symbol exceeds the magnitude, ζ_0 .

$$\begin{aligned} \Pr\left\{\max_{0 \leq n < N} \zeta > \zeta_0\right\} &= 1 - \Pr\left\{\max_{0 \leq n < N} \zeta \leq \zeta_0\right\} \\ &= 1 - (\Pr\{\zeta \leq \zeta_0\})^N \\ &= 1 - \left(1 - e^{-\zeta_0^2}\right)^N \end{aligned} \quad (3.13)$$

Figure 3.2 displays simulated and theoretical results of (3.13) with varying N . The simulation model passes N QPSK symbols through a N point IFFT, the maximum sample of each OFDM symbol is stored and plotted. As in Figure 3.1 the probability that large peaks occur is very irregular, doubling the number of subcarriers results in a modest increase in the PAPR leading to the assumption that using a large number of subcarriers makes sense as this will allow for greater data throughput (provided the CP length is constant). However a larger number of subcarriers leads to increased sensitivity to carrier and sampling frequency offsets as described in section 2.5.1.2 and 2.5.1.3. Therefore, balance must be met between these design constraints. Comparing the theoretical and simulated results we see that the results only converge

at $N=128$, the theoretical results for $N < 128$ are slightly more pessimistic at higher PAPR levels.

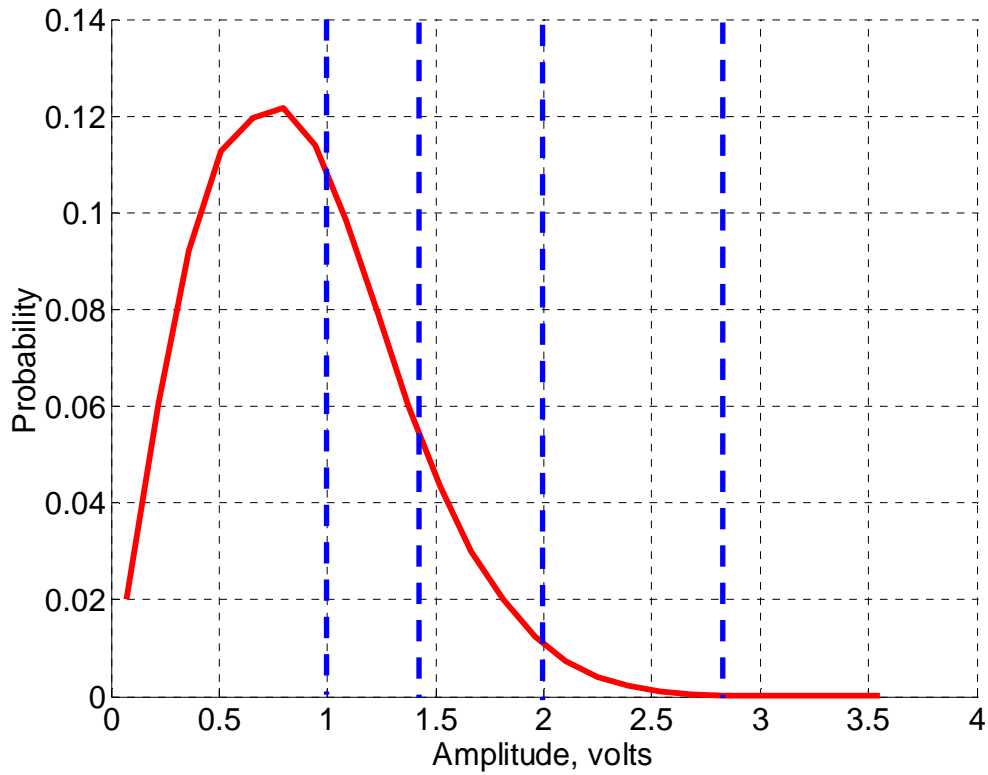


Figure 3.1: Simulated envelope for OFDM system ($N=64$) normalized by average power.

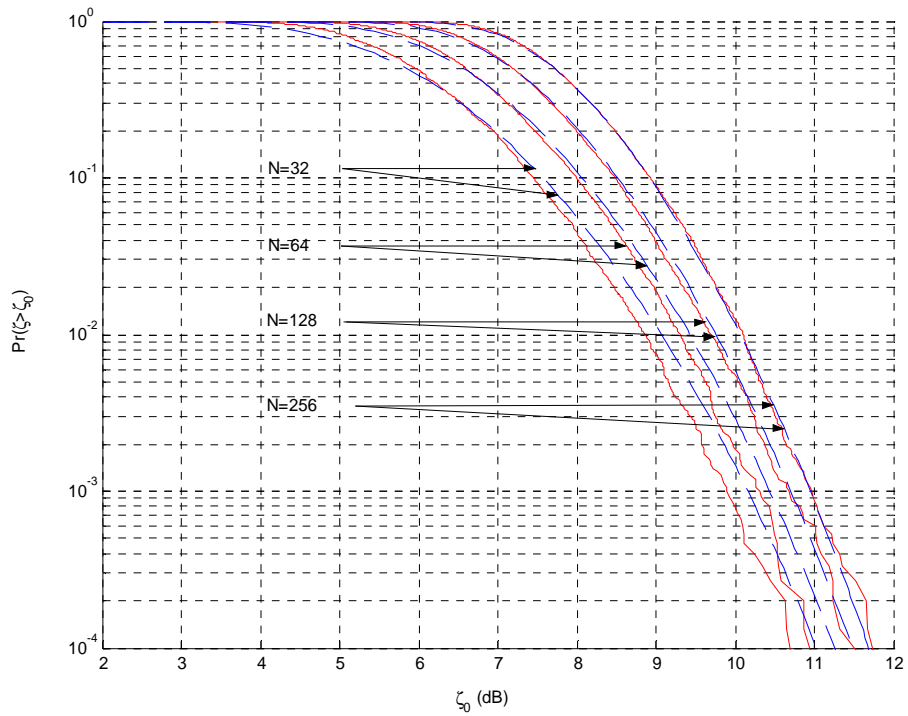


Figure 3.2: Simulated (solid line) and theoretical (3.13, dashed line) OFDM **symbol** CCDF for $N=32$, 64, 128, and 256 subcarriers. QPSK, 30000 runs

To provide further insight into the total distribution of the PAPR Figure 3.3 plots all simulated OFDM samples for the same case as Figure 3.2. Here it is seen that the sample distribution is lower than the symbol distribution as is predicted by (3.13).

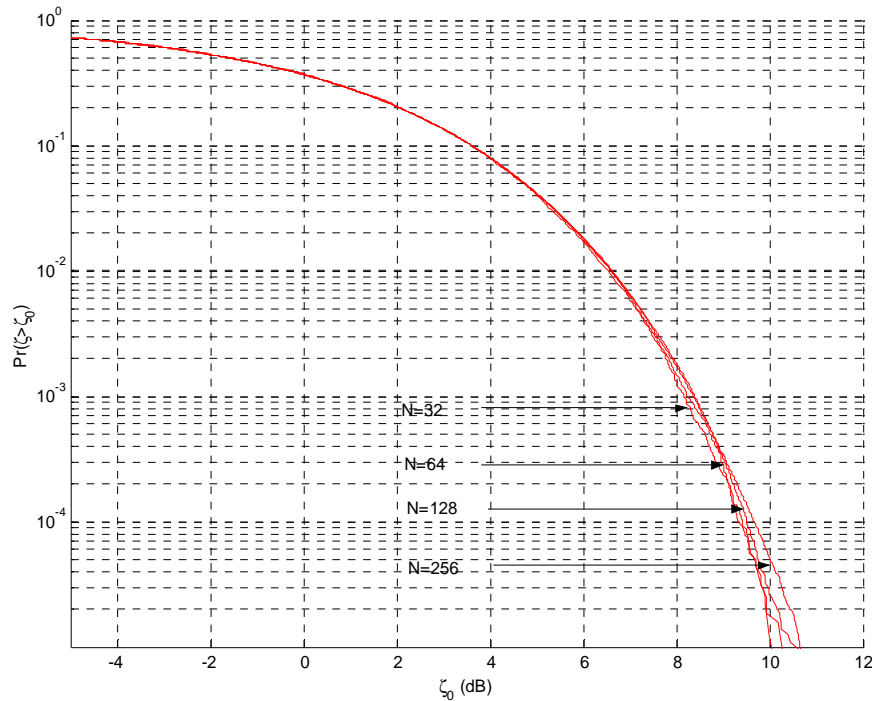


Figure 3.3: Simulated OFDM **sample** CCDF for $N=32$, 64, 128, and 256 subcarriers. QPSK, 30000 runs.

The effect of various QAM mapping constellations is simulated in Figure 3.4 where it is seen that changing the constellation has a minimum affect on the PAPR which is to be expected considering the M-ary constellations are normalized to have the same average power. This same principle applies to non active subcarriers which also do not influence the PAPR as the average power decreases in line with a reduction in the number of active subcarriers. However null subcarriers have the advantageous side effect of increasing the resolution of the OFDM symbol due to the oversampling effect.

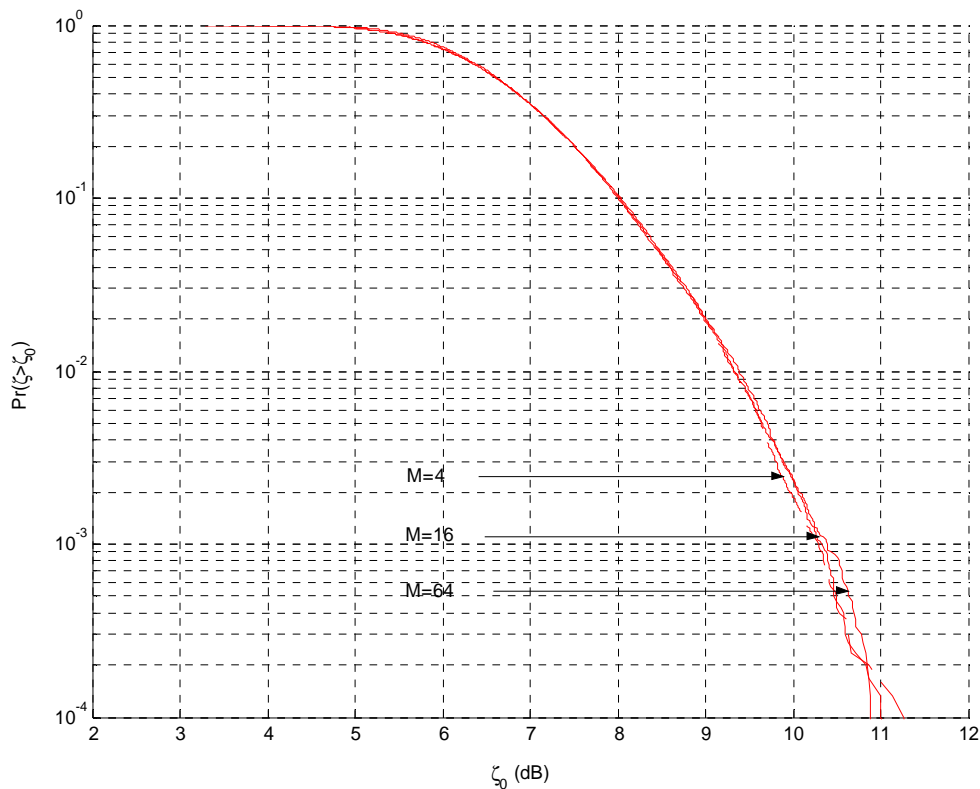


Figure 3.4: Simulated OFDM CCDF for $M=4, 16,$ and 64 constellation mapping. $N=64, 30000$ runs.

This section has shown that the PAPR per symbol is only a function of the length, N , of the IFFT. The constellation type and number of active subcarriers have a negligible affect on the PAPR after modulation with the IFFT.

3.3 Oversampling discrete OFDM symbols to find true (continuous) peaks

Section 3.2 provided an analysis of the PAPR for critically sampled baseband OFDM symbols. However this analysis does not reveal the peak of the band limited OFDM signal. Oversampling the data in the IFFT increases the resolution of the OFDM symbol giving a closer approximation to the band limited signal after filtering. This is best explained in Figure 3.5 where the complex components of one OFDM symbol with no oversampling is overlaid with the same symbol oversampled at the IFFT by a factor of 8 (to approximate the continuous filtered signal). Note the parabolic trajectory from one discrete sample to another, the growth in new peaks occurs in between the discretely sampled peaks.

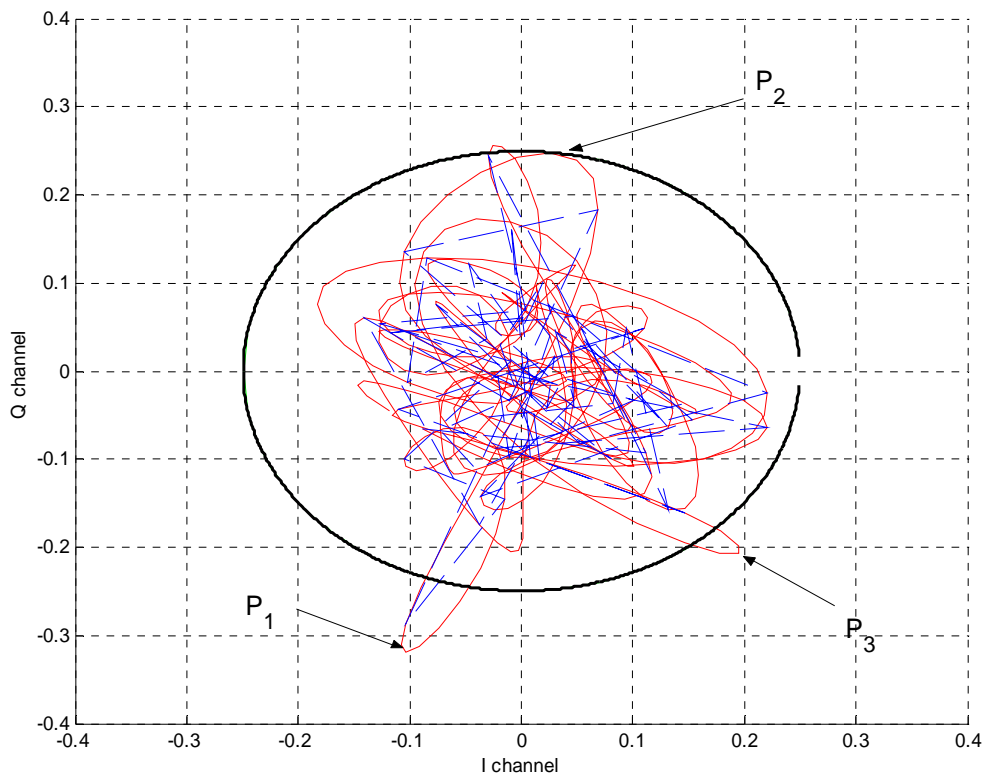


Figure 3.5: Simulated OFDM symbol with no oversampling (dashed) with its oversampled version (solid) overlaid on top. The solid circle represents the 6dB level with respect to the average power. $N=64$, oversampling factors are 1 and 8.

Some interesting observations that can be made viewing Figure 3.5 are at P_1 where the only sample of the critically sampled OFDM symbol is above 6dB, when oversampled the true peak grows slightly larger still. At P_2 it is seen that the two critical samples that make up its end points are well under 6dB, but after oversampling a peak is produced in between the 2 critical samples. At P_3 we see that the second largest peak in the oversampled case occurs at a position where no peak existed in the critically sampled symbol. These results show how the critically sampled OFDM symbol and its oversampled version can diverge greatly in PAPR.

The CCDF for various oversampling rates at the IFFT is shown in Figure 3.6, here it is seen that an oversampling factor of 8 is sufficient to represent the continuous signal and results in around 0.5dB increase in the PAPR.

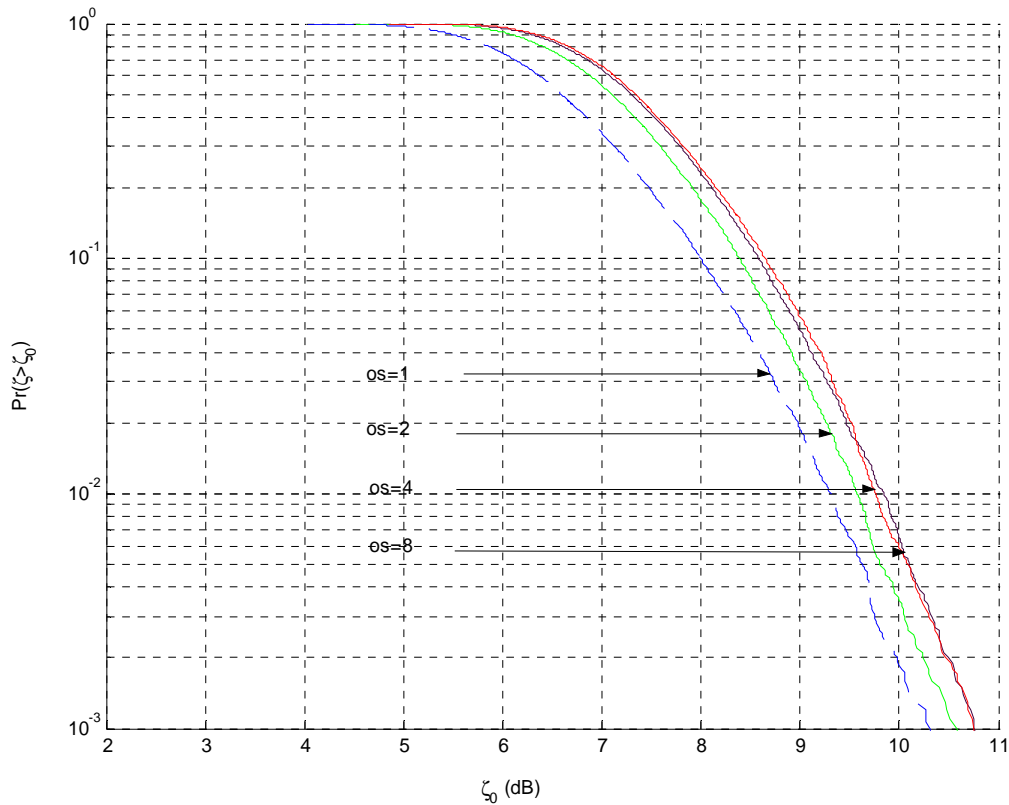


Figure 3.6: Simulated OFDM CCDF for oversampling rates of 1, 2, 4, and 8. $N=64$, QPSK, 15000 runs.

Equation (3.13) assumes that samples are mutually independent and uncorrelated, however Parseval's theorem states that

$$\sum_{m=0}^{N-1} |x_m|^2 = N \quad (3.14)$$

Therefore the independent assumption of (3.13) is not true, especially in the oversampling case where adjacent samples are highly correlated to each other. Various papers [34-36] have been published which address the issue of oversampling.

Reference [37] suggests that adding a number of extra independent samples to (3.13) will give a closer approximation to the oversampled signal, (3.15)

$$\Pr \left\{ \max_{0 \leq n < N} \zeta > \zeta_0 \right\} = 1 - \left(1 - e^{-\zeta_0^2} \right)^{\alpha N} \quad (3.15)$$

where $\alpha=2.8$ gives a good approximation to oversampled signals. Reference [35] takes exception to this non theoretical approximation of the over sampled signal and states that the bound is not close to the theoretical bound for large numbers of N.

Reference [35] developed a method for finding the exact peak distribution of band limited Rayleigh processes giving an expression for the CCDF of the PAPR as (3.16)

$$\begin{aligned} \Pr(\zeta < \zeta_0)^{\bar{N}_p(0)} &= (1 - \Pr(\zeta > \zeta_0))^{\bar{N}_p(0)} \\ &= \left(1 - \frac{\bar{N}_p(\zeta_0)}{\bar{N}_p(0)}\right)^{\bar{N}_p(0)} \end{aligned} \quad (3.16)$$

where

$$\bar{N}_p(\zeta_0) = \frac{4N}{\sqrt{15\pi}} \int_{a_0}^{\infty} u^2 \int_0^{\infty} e^{-(\phi^2+1)u^2} \left\{ e^{\frac{-5}{4}(\phi^2-1)^2 u^2} - \frac{\sqrt{5\pi}}{2}(\phi^2-1) \text{uerfc}\left(\frac{\sqrt{5}}{2}(\phi^2-1)u\right) \right\} d\phi du$$

which is the mean number of peaks above the level ζ_0 in one OFDM symbol, and

$$\bar{N}_p(0) \approx 0.64N \quad (3.17)$$

which is the mean number of total peaks.

As this method is numerically cumbersome to solve due to the double integration in (3.16) a simpler approximation of the distribution is developed which is as accurate as the previous method for a large number of N.

The simpler method derives the peak distribution of the band limited Rayleigh process based on the level crossing rate approximation and then applies the result to the derivation of the distribution of the CF in OFDM signals. This is made under the assumption that 1) the complex components of the signal, $x(t)$ are ideally band limited Gaussian processes (i.e. $N>64$) and 2) the peaks are statistically uncorrelated. Also a suitiably high level for a_0 must be chosen well above 0 to make the assumption valid,

i.e. each positive crossing of the level $\bar{\zeta}_0$ has a single positive peak that is above the level $\bar{\zeta}_0$. The CDF of the CF is given as (3.18)

$$F_C(\zeta | C > \bar{\zeta}_0) = \Pr(\zeta < \bar{\zeta}_0 | \zeta > \bar{\zeta}_0)^{\bar{N}_p(\bar{\zeta}_0)} \quad (3.18)$$

where $\bar{N}_p(\bar{\zeta}_0)$ is the mean number of peaks above $\bar{\zeta}_0$, and can be approximated for high $\bar{\zeta}_0$ by (3.19)

$$\bar{N}_p(\bar{\zeta}_0) = \sqrt{\frac{\pi}{3}} N \bar{\zeta}_0 e^{-\bar{\zeta}_0^2} \quad (3.19)$$

An expression for the CDF, $F_C(\zeta_0)$ is then obtained:

$$F_C(\zeta_0) \approx F_C(\zeta_0 | C > \bar{\zeta}_0) = \begin{cases} \left(1 - \frac{\zeta_0 e^{-\zeta_0^2}}{\bar{\zeta}_0 e^{-\bar{\zeta}_0^2}}\right)^{\sqrt{\frac{\pi}{3}} N \bar{\zeta}_0 e^{-\bar{\zeta}_0^2}} & \text{for } \zeta_0 > \bar{\zeta}_0 \\ 0 & \text{for } \zeta_0 \leq \bar{\zeta}_0 \end{cases} \quad (3.20)$$

The CCDF can then be expressed as

$$1 - F_C(\zeta_0) \quad (3.21)$$

[35] suggests $\bar{\zeta}_0 = \sqrt{\pi}$ for QPSK modulation and a marginally lower value for 16 QAM. Figure 3.7 plots simulated CCDF of the PAPR for QPSK with $N=64$ and 512 with an oversampling factor of 16, and 20000 OFDM symbols against (3.15) and (3.21). Here we see that the bound from (3.15) is closer to the simulated results for $N=64$ as a small number of subcarriers does not have a completely Gaussian distribution. On the other hand (3.21) is an excellent bound for $N=512$ where the Gaussian assumption is true.

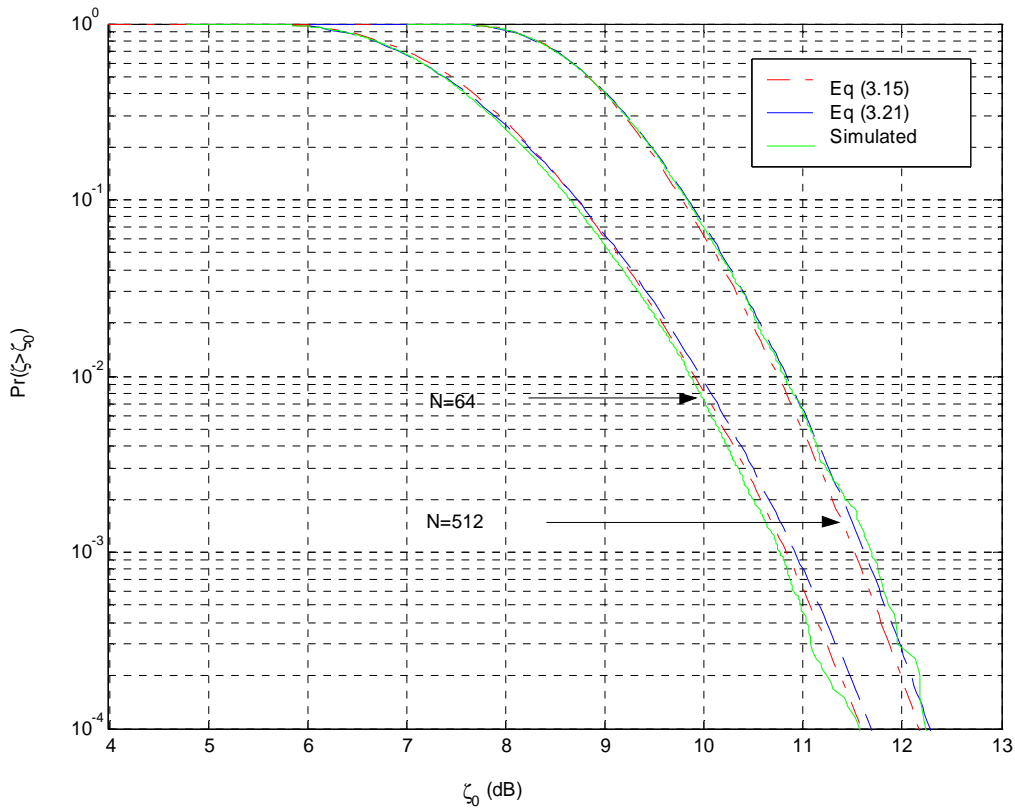


Figure 3.7: Theoretical OFDM CCDF from (3.15) and (3.21) for $N=64, 512$ with simulated results: QPSK, oversampling factor rate of 16, 20000 runs, $N=64, 512$.

Reference [36] finds bounds for the peak of the continuous envelope based on the maximum of the oversampled sequence. This bound is used to derive a closed form expression for the upper bound of the CCDF in an uncoded OFDM system with large N . Unlike [35] where the PMEPR is derived under the assumption that OFDM signals behave as band limited Gaussian processes, only the Gaussian assumption for each sample is used, there is no assumption on the joint distribution of the samples. The CCDF is given as

$$\Pr\{PMEPR > \zeta_0\} < kNe^{-\lambda\left(1 - \frac{\pi^2}{2k^2}\right)} \quad (3.22)$$

where k is the oversampling factor, N is the number of subcarriers, and ζ_0 is the clip value. Note that k must be $> \pi/\sqrt{2}$. Figure 3.8 plots the simulated results (QPSK, $os=16$) against the theoretical results of (3.22). This method predicts a much higher distribution of the peaks than is seen in simulation and is therefore very pessimistic.

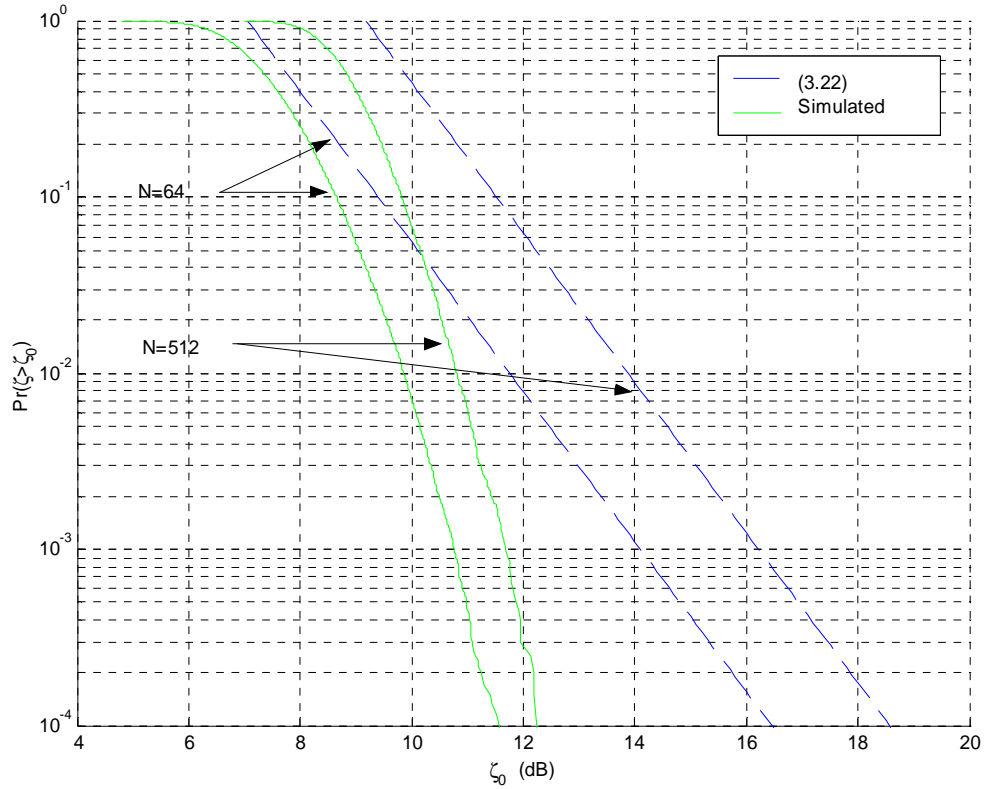


Figure 3.8: Theoretical OFDM CCDF from (3.22) for $N=64, 512$ with simulated results: QPSK, oversampling factor rate of 16, 20000 runs, $N=64, 512$.

Reference [38] extends the theory of [37], [35], and [36] to find new upper bounds for different constellation types such as QAM and PSK, rather than just QPSK. The theoretical results are useful at low probability regions where simulations are time consuming. The upper bound on the CDF for QAM constellations is given as

$$F(\zeta_0) \leq \min_{L, K \in \mathbb{N}; L > 1, K > 2} \left\{ KLN e^{\frac{-4(M^2-1)a_0^2}{3(4\gamma+M^2)C_k^2 C_L^2}} \right\} \quad (3.23)$$

$$\zeta_0 \geq 0$$

where

$$C_L = \frac{1}{\cos\left(\frac{\pi}{2L}\right)} \quad L > 1 \quad (3.24)$$

$$C_k = \begin{cases} \frac{1}{\cos\left(\frac{\pi}{K}\right)} & K > 3 \quad \text{Keven} \\ \frac{3 - \cos\left(\frac{\pi}{K}\right)}{1 + \cos\left(\frac{\pi}{K}\right)} & K \geq 3 \quad \text{Kodd} \end{cases} \quad (3.25)$$

where ζ_0 is the clip level, L is the oversampling factor, N is the number of subcarriers, M is the constellation type: M=2 (4 QAM), 4 (16 QAM), or 8 (64 QAM), $\gamma=0$ (4QAM), 1 (16 QAM), or 5 (64 QAM).

For BPSK constellation the CDF is given by

$$F(\zeta_0) \leq 4B(\zeta_0) + \min_{L, K \in \mathbb{N}; L > 1, K > 2} \left\{ \sum_{l_1=1}^{\frac{LN-1}{2}} \sum_{l_2=0}^{K-1} e^{-\frac{N\zeta_0^2}{2C_1\left(N, \frac{l_1}{LN} - 2\pi, \frac{l_2}{K} 2\pi\right) C_K^2 C_L^2}} \right\} \quad \zeta_0 \geq 0 \quad (3.26)$$

where

$$C_1(N, \theta, \alpha) = \frac{N}{2} + \frac{1}{2} \frac{\sin(N\theta)}{\sin(\theta)} \cos((N-1)\theta + 2\alpha) \quad (3.27)$$

and

$$B(\zeta_0) = \frac{1}{2^N} \sum_{k=\lceil \zeta_0 \sqrt{N/C_L} \rceil}^N \binom{N}{(N-k)/2} \quad (3.28)$$

Results comparing the new CDF calculation against the Gaussian model of (3.13) show that for BPSK the new bound is tighter below 10^{-4} probability for large N. Interestingly the Gaussian approximation provides better results than the new bound for all N. For 16 QAM and 64 QAM the Gaussian bound again looks better.

The CCDF results from Figure 3.6 imply that using an oversampling factor of 1 predicts the PAPR within 0.5dB, *however this is not true when PAPR reduction*

techniques are applied to the OFDM symbol [30],[39]. Figure 3.9 shows the CCDF of a 64 point IFFT OFDM modulator clipped at 3dB, interpolated by 8 and then filtered with a 256 tap RRCCF, as well as the same OFDM data set left unclipped at the IFFT and then interpolated and filtered with the RRCCF.

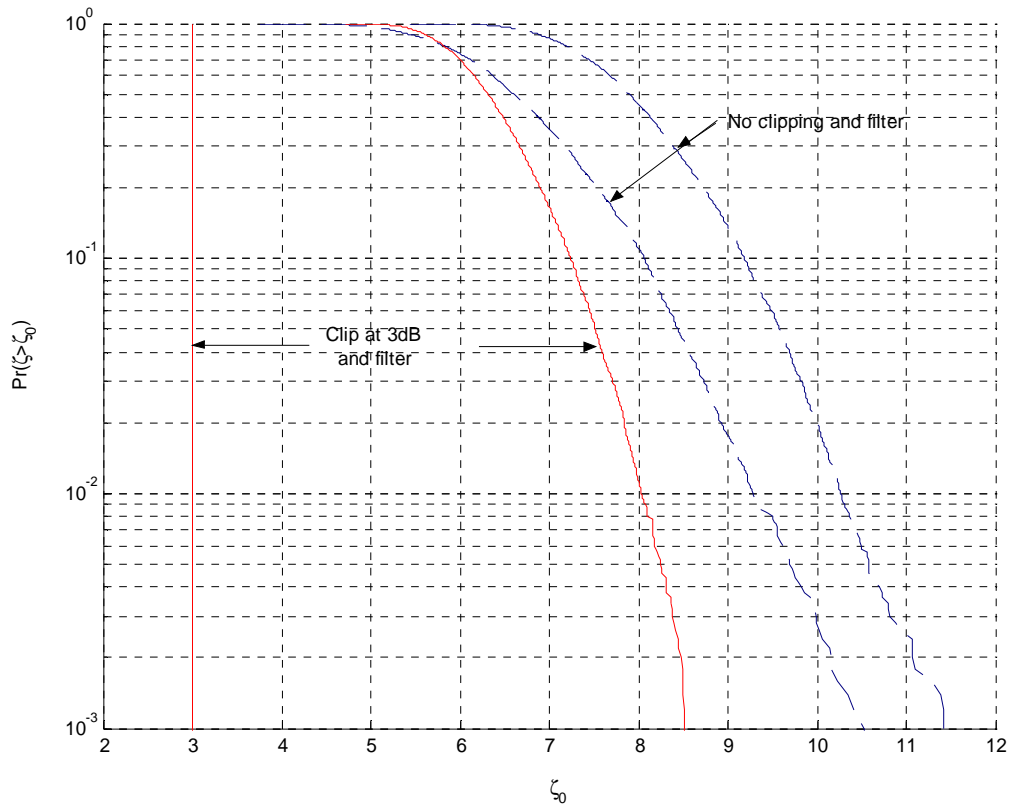


Figure 3.9: Simulated OFDM CCDF QPSK, 64 point IFFT, 256 tap RRCCF, $\alpha=0.15$. Clipped at 3dB after IFFT, then filtered (solid line). No clipping, then filtered (dashed line).

Peak regrowth after clipping and filtering is dramatic, much worse than without clipping and filtering. The degree of peak regrowth is determined by the sequence of the filtered data, the value of the excess bandwidth, α , of the RRCCF (smaller α greater peak regrowth), the length of zero padding in the IFFT, and the degree of clipping (harder the clipping the greater the regrowth). Oversampling means the introduction of null samples at the input of the IFFT as shown in Figure 3.10. The null samples are introduced in the centre of the IFFT input to ensure that they occupy the outer samples in the frequency spectrum.

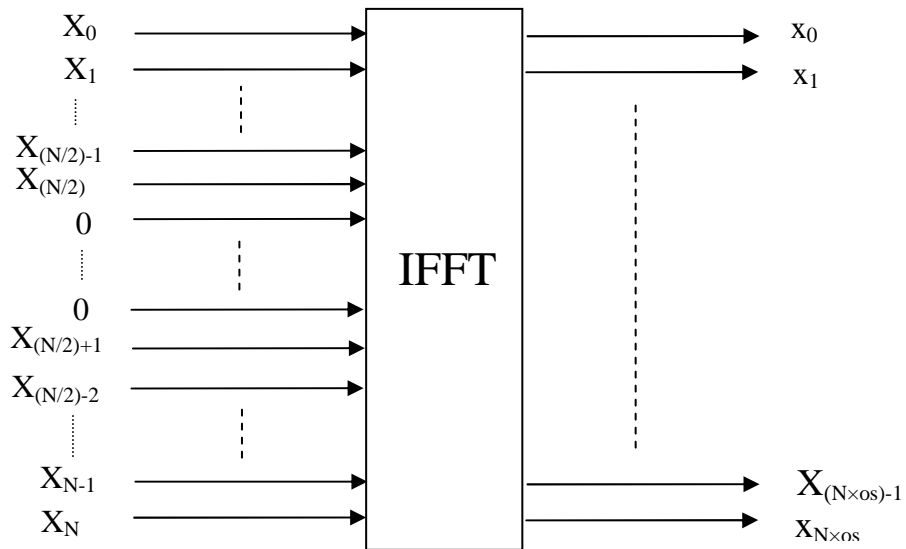


Figure 3.10: Zero padding of the IFFT, null carriers are set in the middle of the input

Figure 3.11 shows the simulated CCDF for a non oversampled IFFT compared to a 2 times oversampled IFFT, both of which are interpolated by a factor of 8 and filtered with a RRCF.

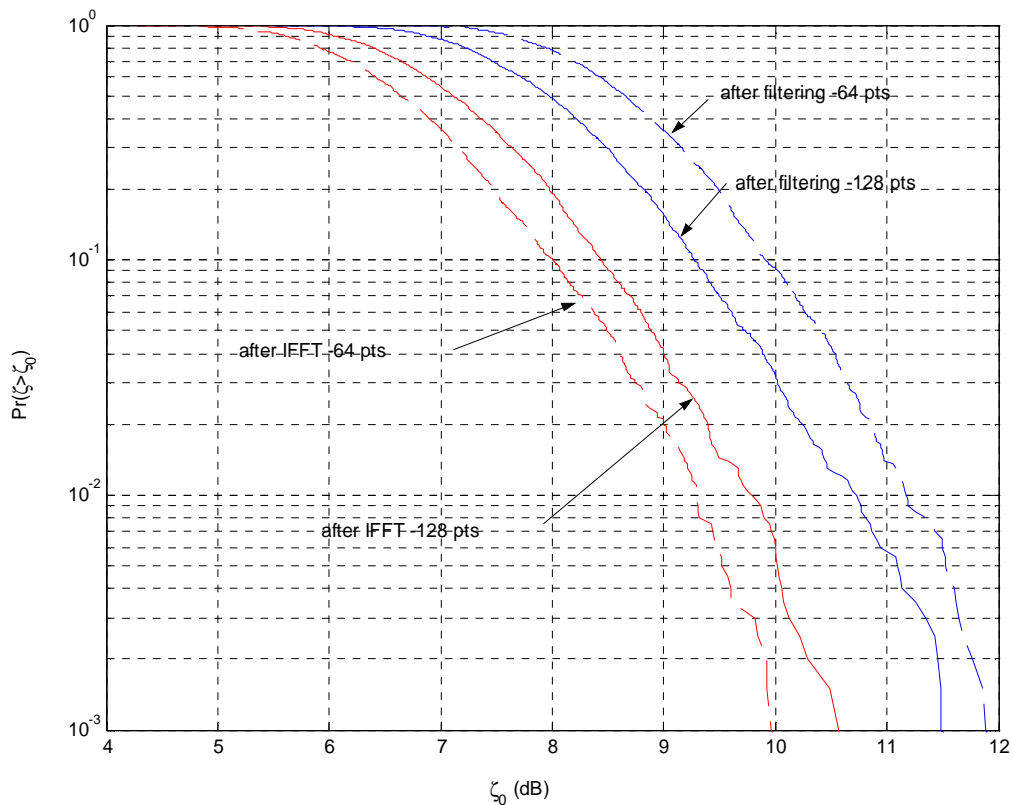


Figure 3.11: Simulated OFDM CCDF after IFFT (os=1 and 2) and after filtering (os=1 and 2). QPSK, N=64, 256 tap RRCF, $\alpha=0.15$, 15000 runs.

This time we notice that the oversampled IFFT has a slightly higher PAPR distribution, but what is of most importance is that the PAPR distribution after filtering has less peak regrowth and is below the critically sampled IFFT. We can conclude that oversampling of the data at the IFFT is an effective way to counter the peak regrowth after filtering. Oversampling beyond a factor of 2 provides a law of diminishing returns in terms of peak regrowth (see Figure 4.10: $U=1$).

3.4 Effect of Non Linearity on OFDM

The previous sections described the causes of large PAPR and the problems of non linearity, this section describes common models for HPA's which are used in wireless communications and the effect they have on the OFDM signal in terms of the Power Spectral Density (PSD) and the increase in the BER. Section 3.4.1 describes commonly used HPA models, section 3.4.2 details the corruption of the frequency spectrum due to changing backoffs in the HPA, and finally section 3.4.3 describes the degradation in BER due to changing backoffs in the HPA.

3.4.1 Description of memoryless Non Linearity

Non linearities provide the greatest obstacle to OFDM as a practical system due to their distorting effect on the quality of the system. Here we concentrate on the most common form of non linearity, distortion in the RF amplifier due to a limited linear range in the amplifier. Papers [40-44] tend to focus on the distortion due to the RF amplifier stage as this is the most expensive component in a transmitter and takes up to 50% of the cost and space in a unit. The RF amplifier must be driven as close as possible to the maximum signal in the linear region to make it efficient, however when operating near the saturation point it exhibits non linear behavior distorting the transmitted signal. This distortion causes spectral regrowth in the transmitter which can adversely affect adjacent frequency bands, and an increased BER at the receiver. A balance must be met between allowable distortion and the linear region of an amplifier. Therefore it is pertinent to evaluate the performance of OFDM signals through different non linear devices.

A convenient form of expression for non linear devices is in polar coordinates reference [45]. The input can be expressed as (3.29)

$$x = |x|e^{j\arg(x)} = \rho e^{j\phi} \quad (3.29)$$

Therefore the complex envelope of the output signal can be expressed as (3.30)

$$g(x) = F[\rho]e^{j(\phi+\psi[\rho])} \quad (3.30)$$

where $F[\rho]$ and $\psi[\rho]$ represent the AM/AM and AM/PM conversion characteristics of the memoryless non linear amplifier respectively. Some commonly used models follow.

Soft Limiter (SL)

The Amplitude Modulation to Amplitude Modulation (AM/AM) and Amplitude Modulation to Phase Modulation (AM/PM) characteristics of a SL can be expressed as [43]

$$F[\rho] = \begin{cases} -A & \text{if } \rho < -A \\ \rho & \text{if } -A \leq \rho \leq A \\ A & \text{if } \rho > A \end{cases} \quad (3.31)$$

and $\psi[\rho] = 0$.

There is no phase distortion in this model, only amplitude distortion, A is the clipping level of the amplifier. The AM/AM characteristics of a SL are plotted in Figure 3.12.

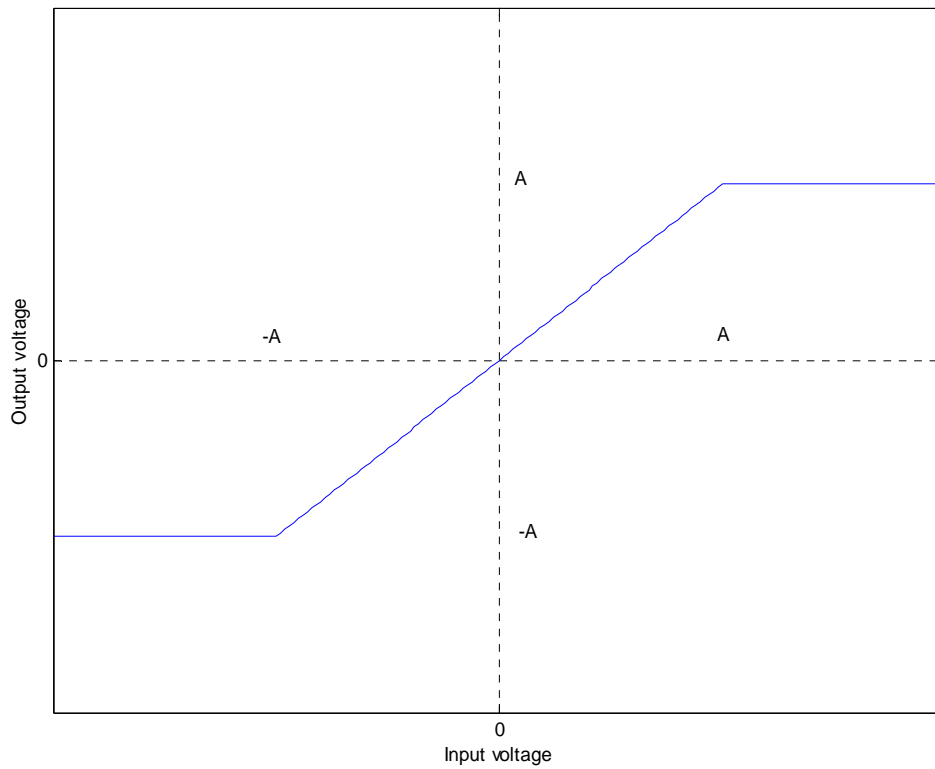


Figure 3.12: AM/AM properties of a Soft Limiter (SL)

Travelling Wave Tube Amplifier (TWTA)

According to reference [40] the AM/AM and AM/PM functions are

$$F[\rho] = \frac{\rho}{(1 + \beta_a \rho^2)} \quad (3.32)$$

and

$$\psi[\rho] = \frac{\alpha_\phi \rho^2}{(1 + \beta_\phi \rho^2)} \quad (3.33)$$

A common choice for the above parameters is $\beta_a = 0.25$, $\alpha_\phi = \pi/12$, and $\beta_\phi = 0.25$.

The AM/AM characteristics of a TWTA are plotted in Figure 3.13.

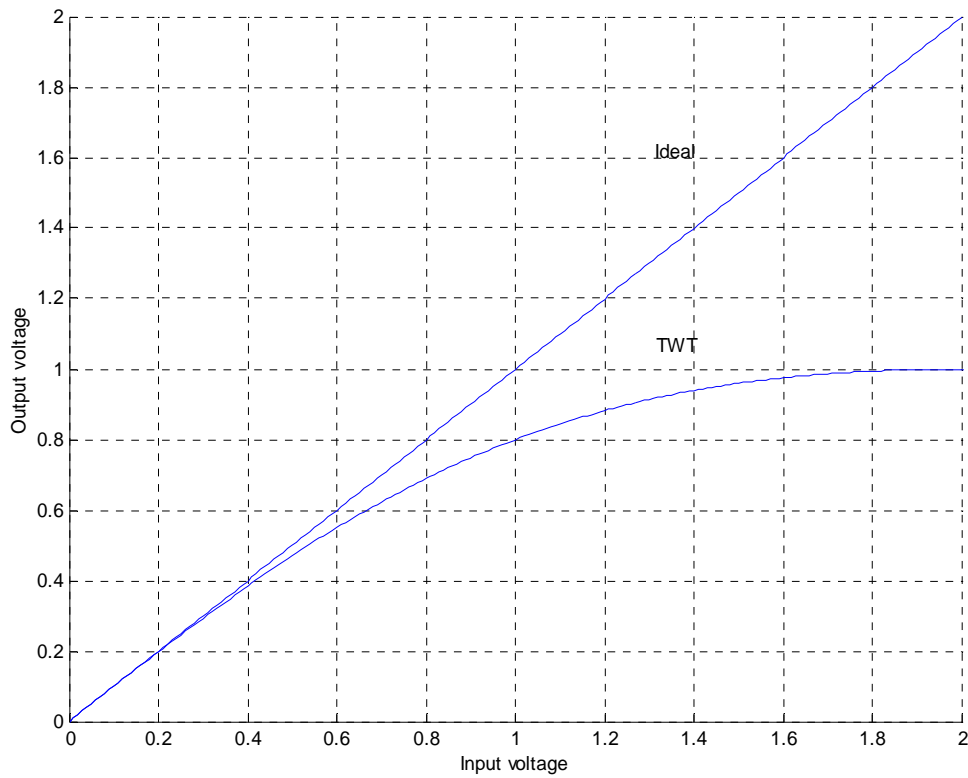


Figure 3.13: AM/AM properties of a Traveling Wave Tube Amplifier (TWTA)

Solid State Power Amplifier (SSPA)

Probably the most common and practical model for amplifiers is the SSPA [40]. The AM/AM and AM/PM transfer characteristics can be modeled as

$$F[\rho] = \frac{\rho}{\left[1 + \left(\frac{\rho}{A}\right)^{2P}\right]^{\frac{1}{2P}}} \quad (3.34)$$

and

$$\psi[\rho] = 0 \quad (3.35)$$

The parameter P controls the smoothness of the transition from the linear region into the saturation region. When $P \rightarrow \infty$ the SSPA acts as a SL, P=3 is a good

approximation of a practical amplifier. The AM/AM characteristics of a SSPA and an ideal amplifier are plotted in Figure 3.14.

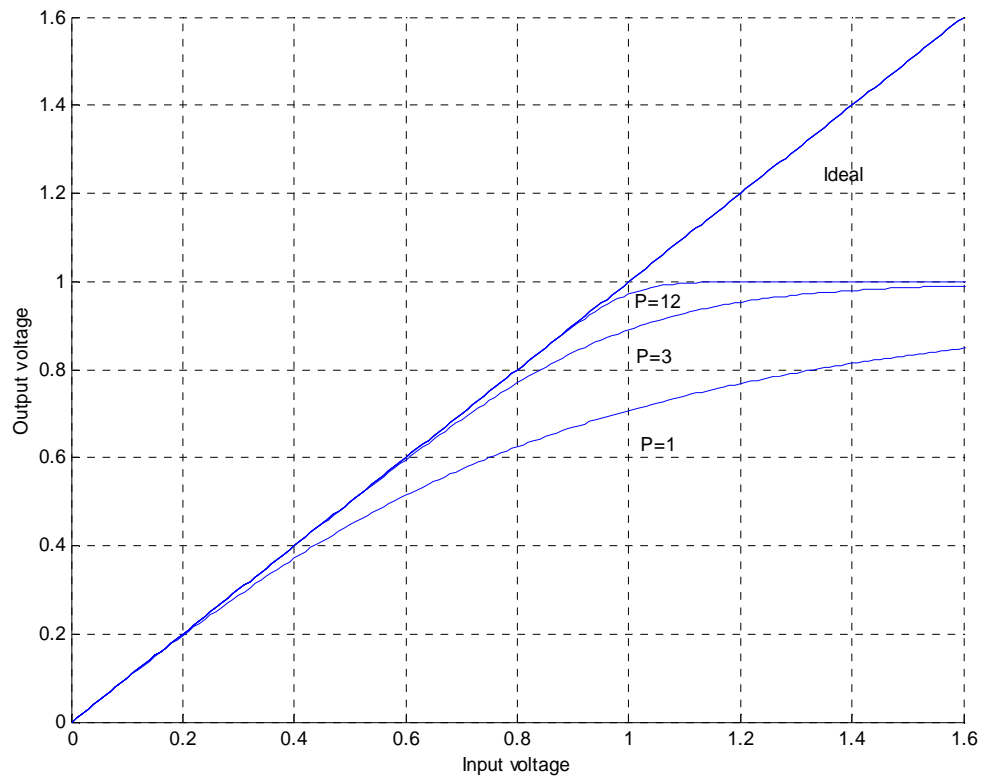


Figure 3.14: AM/AM properties of a Solid State Amplifier (SSPA) for different values of P, and ideal amplifier.

In all amplifiers discussed in this section ‘A’ represents the saturating amplitude of the amplifier. The non linear distortion depends on the backoff of the amplifier and can be calculated as either the Input BackOff (IBO) or the Output BackOff (OBO), and is defined as

$$IBO \triangleq 10 \log_{10} \frac{A_s^2}{P_{IN}} \quad (3.36)$$

$$OBO \triangleq 10 \log_{10} \frac{A^2}{P_{OUT}} \quad (3.37)$$

where A_s is the amplifier input saturation voltage, P_{IN} is the average power at the input, A is the saturating amplitude at the output, and P_{OUT} is the average power at the output.

3.4.2 Impact on Power Spectral Density

The simulated spectrum for $N=64$ subcarriers is shown in Figure 3.15. The PSD is measured for each OFDM block then averaged over 2000 blocks to eliminate the effect of

the rectangular time window [46]. Blocks of 4 QAM data were mapped to a 64 point IFFT for modulation, the data is then interpolated by a factor of 8 and filtered. A RRCF was used for pulse shaping with 128 taps and an excess bandwidth of 0.15. The low rolloff factor of the filter results in a fast drop off of the spectral splatter outside the normalised FFT bandwidth. A SSPA with $P=3$ is used as the amplifier model. The frequency axis is normalized.

Changing the IBO of the SSPA results in inband distortion and spectral regrowth, or splatter outside the normalized frequency bandwidth of the filter. An amplifier backoff of 0dB results in noise power that is only 16dB lower than signal power. With a backoff of 3dB the noise power is 19.5dB below the signal power. A 6dB amplifier backoff results in a slight amount of spectral splatter 23dB below the signal power and an almost indistinguishable amount of in band distortion. With an infinite amplifier backoff the PSD matches exactly the PSD after transmit filtering.

OFDM standards such as Hiperlan2 and 802.11a require adjacent OFDM carriers to be closely packed in the frequency domain with overlapping spectrums. This is achieved by

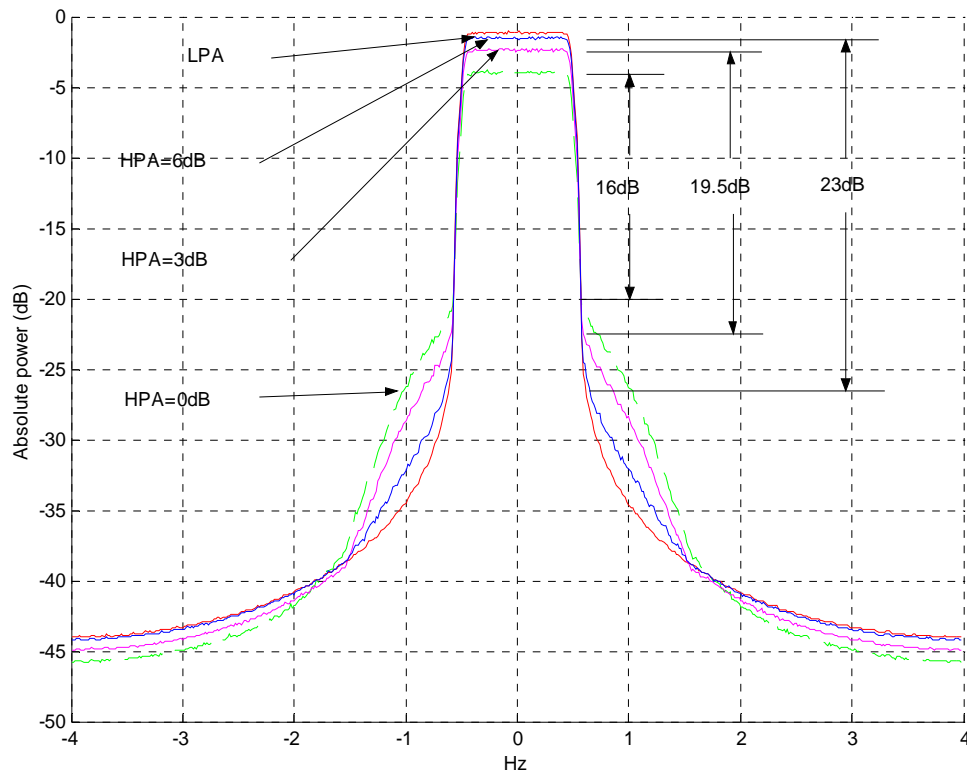


Figure 3.15: PSD of 64 subcarrier OFDM signal with 64 point IFFT, RRCF with excess bandwidth of 0.15. A SSPA (HPA in figure) with $P=3$ and various backoffs is used.

setting null subcarriers at the edge of the spectrum, where the rolloff of the filters occurs in the unused subcarriers, easing the design constraints on the filters.

Filtering after the SSPA to reduce spectral splattering is complex, therefore reference [46] proposed clipping in the baseband after the IFFT followed by filtering. This successfully reduces the out of band distortion but the BER due to the in band distortion remains. Also peak regrowth after filtering remains a problem. These issues are explored in more depth in chapters 5, 7.

3.4.3 Impact on Bit Error Rate

The inband distortion due to non linear amplification at the transmitter results in ISI when filtered with the matched filter at the receiver, resulting in an increase in the BER when the data is decoded. Two observed effects of clipping (whether due to the amplifier non linearity or baseband clipping) are a Gaussian like spreading of the

decoded constellation points and a compaction of the whole received constellation, shown in Figure 3.16 where the two constellation types (4 and 16 QAM) are normalized to have the same average power.

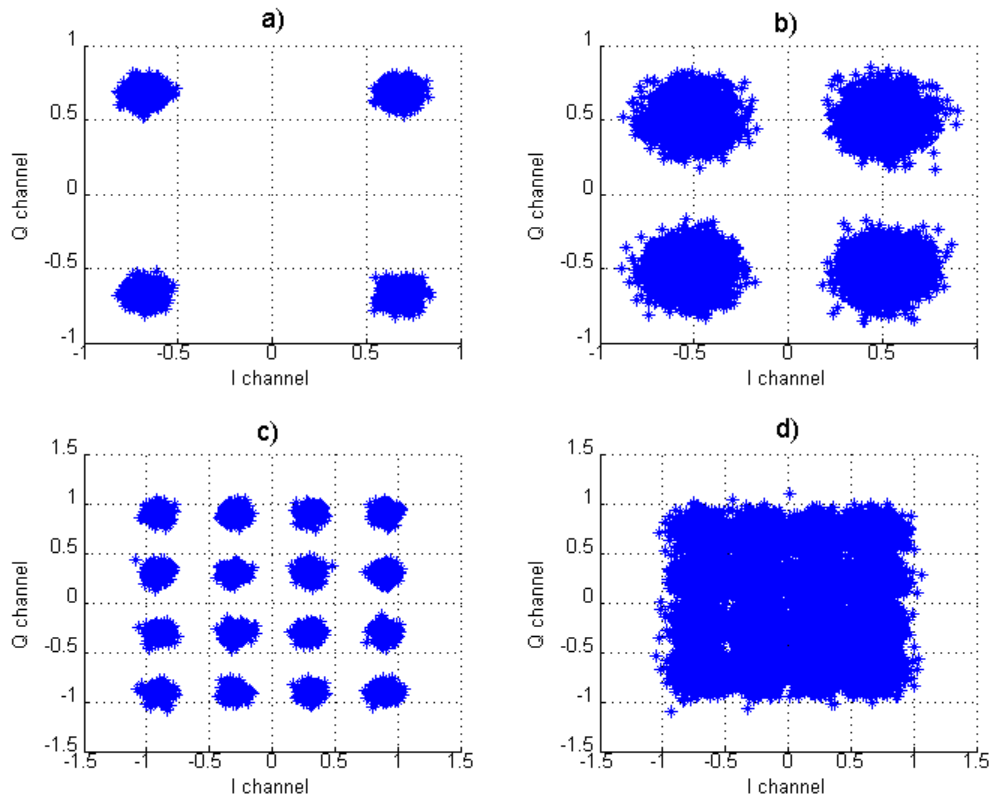


Figure 3.16: Signal constellation at the output of the SSPA, $P=3$ after non linear amplification a) 4 QAM, 6dB IBO; b) 4 QAM, 0dB IBO; c) 16 QAM 6dB IBO; and d) 16 QAM 0dB IBO.

The noise due to clipping is evenly spread across all subcarriers [47], this is because each sample that is clipped is a conglomeration of all the input samples to the IFFT. Therefore the BER is nearly equal on all subcarriers.

Figure 3.17 shows the BER due to a non linearity in the HPA for 3 M-ary constellation types. 4 QAM is very impervious to clipping noise as there is a greater Euclidean distance between constellation points. Indeed 4 QAM has a very acceptable BER performance without any coding or PAPR correction. Mapping types 16 and 64 QAM are much more susceptible to clipping in the amplifier. The BER of Figure 3.17 could be improved with Automatic Gain Control (AGC) in the receiver which would expand the constellation to the correct size before decoding [48].

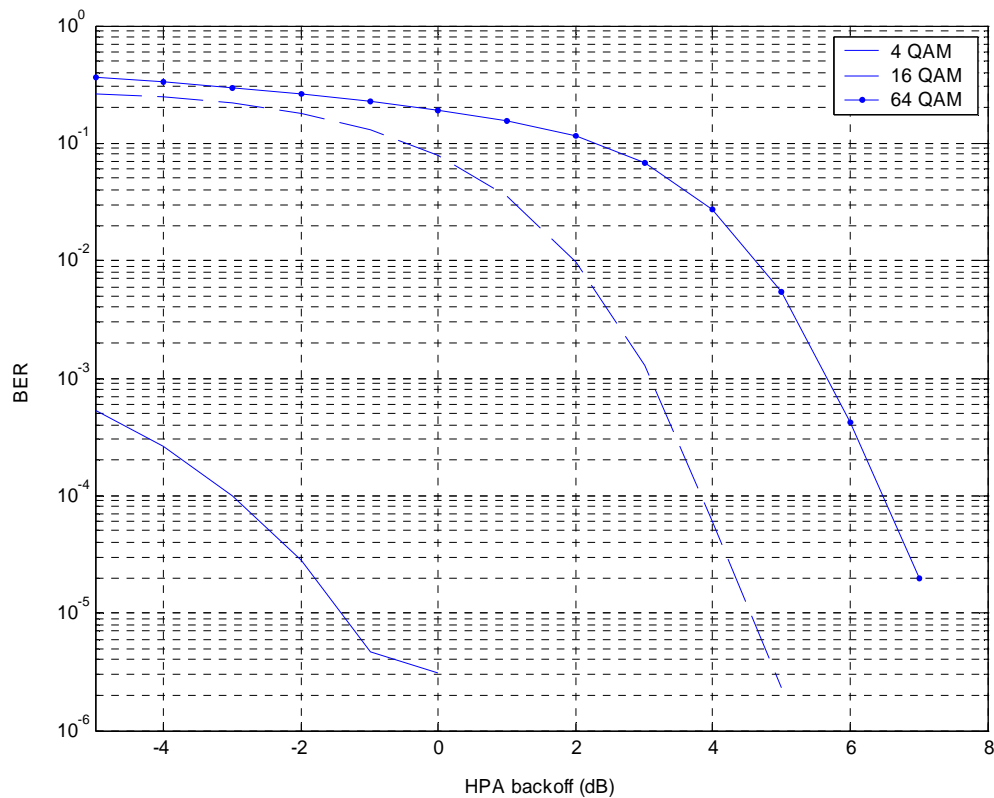


Figure 3.17: BER of 64 subcarrier OFDM signal with 64 point IFFT, RRCF with excess bandwidth of 0.15 for 4, 16, and 64 QAM constellations. A SSPA (HPA on x-axis) with $P=3$ and various backoffs is used.

3.5 Conclusion

This chapter defined the problem of PAPR in OFDM beginning with a mathematical analysis of the PAPR in both the baseband and passband. Next the stochastic distribution of OFDM samples was shown through analytical and simulated means to only be a function of the number of subcarriers. It was also shown that the general distribution of samples is quite low and that the transmit envelope follows a Rayleigh distribution.

Oversampling of the IFFT was also introduced as an important issue, it was shown that oversampling the IFFT increased the CCDF by ~ 0.5 dB. These results were supported analytically by various papers which analysed the issue of oversampling.

Furthermore, it was shown through simulation that filtering has a dramatic affect on the CCDF when combined with PAPR reduction techniques such as clipping. The peak regrowth is much worse than when no PAPR reduction techniques are used. Oversampling at the IFFT was shown to both increase the discrete CCDF and reduce the continuous, filtered CCDF.

Non linearities were also examined with models of the most common form of non linearity, the SSPA, described mathematically. The impact of non linearity on the PSD and BER was simulated. It was shown that reducing the IBO of the SSPA causes both spectral spreading, affecting the adjacent channels, and in band distortion corrupting the BER at the receiver. Higher order constellations were shown to be more susceptible to lower backoffs in the SSPA.

Chapter 4

Peak to Average Power Solutions - Distortionless Techniques

The previous chapter outlined the disruptive effects of an uncontrolled OFDM signal envelope on system performance. This chapter and chapter 6 provide an analysis of solutions to the PAPR problem, each solution has advantages and disadvantages in terms of PAPR reduction, distortion of data, and complexity. This chapter reviews distortionless PAPR reduction techniques. Distortionless techniques do not corrupt the data and encode it in such a way that it can be completely recovered at the receiver, however they are usually more complex. Specifically Section 4.1 explains the family of coding techniques for PAPR reduction, Section 4.2 elaborates on Multiple Signal Representation (MSR) and phase rotating techniques, Section 4.3 details modified constellation techniques, and finally Section 4.4 summarizes the chapter and provides a comparison in terms of complexity and performance of the detailed techniques.

The other side of PAPR reduction are distortion introducing techniques, these techniques deliberately attenuate the envelope of the signal corrupting the BER as described in Section 3.4, however things can be done to lessen the effect of the introduced distortion. These techniques will be explored in Chapter 6.

4.1 Coding techniques

Many early papers considered how standard coding techniques could be applied to OFDM. The basic premise of coding is to insert redundant bits into the data stream which can be used for error correction at the receiver. Their application to PAPR reduction is in creating sequences of bits which will exhibit low PAPR after the IFFT. There are 2 types of error detection and correction codes, *block codes* and *convolutional codes*. Most papers relate to the block coding family for PAPR reduction. During the encoding process k information bits are encoded into n code bits, therefore $(n-k)$ redundant non information bits are added to the k information bits [16]. The block code is referred to as an (n,k) code, and the rate of the code as $R_c=k/n$. Figure 4.1 is a block diagram showing where coding for PAPR reduction is located in an OFDM transmitter.

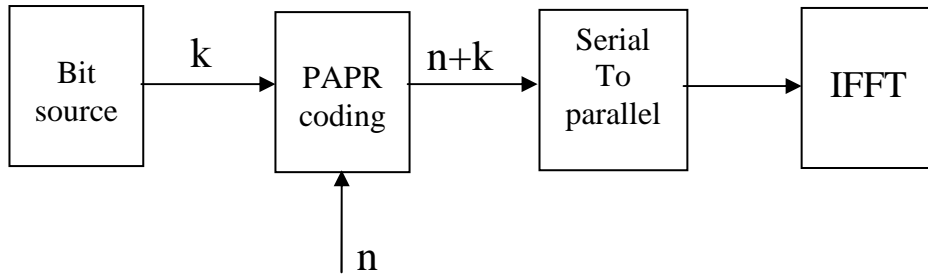


Figure 4.1: Block diagram of OFDM transmitter showing PAPR coding

The ability of a code to correct errors is a function of the *code distance*, (4.1)

$$d(C_i, C_j) = \sum_{l=1}^N C_{i,l} \oplus C_{j,l} \pmod{q} \quad (4.1)$$

where d is the distance of the codeword and q is the number of possible values of C_j and C_i . The smallest distance d_{\min} is the minimum distance for a given set, (4.2)

$$d_{\min} = \text{Min}\{d(C_i, C_j)\} \quad (4.2)$$

Different codes exhibit different degrees of error correction ability. Another important property of codes is the *weight* of the code, which is the number of non zero elements in the codeword. Types of block codes are Hamming, Golay, and Reed-Solomon, some of which are used for PAPR reduction.

4.1.1 Block Codes

The first paper to apply coding techniques for PAPR reduction in OFDM was reference [49]. The basic premise of this paper was to determine which combinations of data at the IFFT input produced large peaks at the output and to avoid transmitting these sequences by adding redundant bits to the input. Initially a simple (impractical) OFDM system with 4 subcarriers and BPSK modulation is considered. A 3 bit data word is mapped on to a 4 bit code word, ie (3,4) block code, so that the set of allowable code words does not create excessive envelope spikes. They identify the code as an odd parity code and state that the PEP is reduced from 6.02dB to 2.48dB, a reduction of 3.54dB.

An 8 subcarrier system with BPSK constellation is also evaluated to illustrate how block coding can be traded off against PAPR reduction. The permissible number of codewords CW_{perm} is traded off against the total possible number of codewords, CW_{poss} . With no block coding the PAPR is 9.03dB. If half the code words are allowed, i.e. a (7,8) rate code, the resultant PAPR is 4.45dB. If a quarter of the code words are allowed, a (3,4) rate code the PAPR is 3.01dB.

The PAPR reduction comes at the cost of an increase of bandwidth for the same data rate and a reduction of the energy per transmitted bit for the same transmit power. However the increase in bandwidth is small and is offset by the high spectral efficiency of OFDM, as is the reduction in energy per transmitted bit which is offset by the *possible* error detection/correction potential of block coding. No results on the minimum distance of the code are given but the authors indicate that a large number of the codes found are Golay complementary sequences. These codes are explored in greater depth in later papers. Practical OFDM systems employ at least 64 subcarriers and higher order mapping types which make the complexity of a block coding scheme

grow exponentially as the coding must be done in combinational logic or a Look Up Table (LUT).

Aware of the limitations of the previous paper Jones and Wilkinson extended the block coding principle in reference [50]. 4 and 8 subcarrier systems are evaluated using QPSK mapping. They prove that the code rate is unaffected by changing the number of carriers and mapping types. 3 areas are identified to make coding techniques more practical

- Selection of suitable code words for any number of carriers and any M-ary mapping type.
- Selection of code words that allow efficient implementation of the coding/decoding.
- Selection of code words that also offer error detection/correction properties.

The authors review a set of papers published in the 80's which addressed a similar problem for multitone test signals with low PAPR. Although certain parameters differ much of this work can be applied to the OFDM case.

The reverse of a code word will result in the same PAPR, i.e. for the 4 subcarrier BPSK case '1000' will give the same PAPR as '0001'. Codes such as these are derived from Shapiro-Rudin sequences which are a subset of Golay complementary sequences. A definition of Golay complementary sequences is given in the paper as "a pair of equally long, finite sequences whose aperiodic autocorrelations sum to zero for all non-zero displacements". Analysis of the code words that exhibited low PAPR's for 4 and 8 subcarriers revealed them to be Golay complementary sequences, however they did not give the optimum minimum solution, but they are amenable to mathematical encoding and decoding and the authors note that they may have error correction properties.

For an 8 subcarrier BPSK OFDM signal based on Golay complementary sequences a (5,8) rate code can give a PAPR of 3.01dB. Larger code sets can be found by rewriting the definition of an OFDM signal (4.3)

$$s(t) = \sum_{n=1}^{n=N} d_n(t) e^{j(2\pi f_n t + \phi_n)} \quad (4.3)$$

as (4.4)

$$x(t) = \sum_{n=1}^{n=N/2} \left[d_n(t) e^{+j(2n-1)\pi f_s t} + d_{-n}(t) e^{-j(2n-1)\pi f_s t} \right] \quad (4.4)$$

This form gives a term in the summation as 2 carriers that are equidistant from and on either side of the centre frequency of the complex envelope representation. If the d_n data words are chosen so that the resultant vector lie on one of two orthogonal lines, then the PAPR is less than or equal to $N/2$. The principle of these sequences can be extended to give polyphase sequences suitable for multilevel phase modulation. The search for better sets of code words with error detection/correction properties is addressed in later papers.

The authors of [49, 50] presented another paper, [51], in which they describe Combined Coded OFDM (CCOFDM). CCOFDM attempts to exploit the error detection/correction properties presented in reference [50] while still maintaining the PAPR suppression. Polyphase weighting codes are applied to the encoded data (chosen from a low PAPR set) which are known at the receiver. Thus they can be compensated for without affecting the distance properties of the code. The BER in a non linear channel for CCOFDM is compared to the COFDM channel and significant improvement in the BER is seen in a highly non linear channel. Still, the work is limited to 8 subcarriers.

Reference [52] expanded on the work of reference [51] by developing an algorithm to compute the phases that minimize the PAPR for larger sets of data of practical interest. The authors found sets of phase values (calculated offline) which are known at both the transmitter and receiver that reduce the PAPR without affecting the error correction properties. These phase shifts that calculated for various coding rates in the Hiperlan2 [53] standard where there are 48 information bearing subcarriers. For $\frac{1}{2}$ rate BPSK with 90° phase shifts a reduction of 4.09dB is reported. The reduction

can be improved slightly by using smaller phase shifts such as 8PSK and 16PSK. The authors elaborated on the results given in [52] in [54] where the computation of the PAPR is given in a rigorous mathematical proof.

Going back in time another early paper [55] extended the work in reference [49] by identifying Quadature Phase Shift Keying (QPSK) message structures which produce high PAPR. They are grouped into *equivalence classes* where messages which have the same PAPR are in the same *equivalence class*. Up to $N=5$ subcarriers are analyzed with different coding rates. They show that that a small amount of redundancy can significantly reduce the PAPR.

The authors of reference [55] developed their results in references [55, 56] to provide bounds for the PEP of OFDM using basic coding techniques as described in reference [49] for up to 16 subcarriers. They prove through analytic and simulated results that only 4 bits of redundancy are required to reduce the PEP to within 10% of its optimum value as the number of subcarriers is increased. They show that further redundancy provides little benefit in terms of PAPR reduction.

Reference [57] presented an idea again based on reference [49] where vectors or messages of data which exhibit a high PAPR are attenuated. The amplitude of subcarriers which are above a given threshold are uniformly reduced to achieve equality between the maximum of the envelope power and the threshold level. Also where the envelope power is below the threshold these subcarriers are increased to obtain equality. This allows the PAPR to be reduced without affecting the net bit rate. Results are given for a BPSK and QPSK with less than 20 subcarriers. The PAPR is reduced significantly however this comes at the cost of a reduction in the SNR which becomes more pronounced as the number of subcarriers is increased.

Reference [58] is another early paper which draws a link between the number of subcarriers and the mapping type used (4 Phase Shift Keying (PSK), 8 PSK, etc). It is stated that if sub carriers in the same group (where a group is a set of subcarrier frequencies sharing some relation) are phase shifted by the same amount, then the envelope remains unchanged. This concept is used to create code sets with low PAPR properties. Reed-Solomon codes are examined with parameters $N=16$ and $M=4$.

They also note that the constraints on the code can be loosened up if at least some variation in the envelope is allowed.

4.1.2 Bounds on PAPR

Reference [52] provided an efficient computational method for finding offsets which can be used with coding in OFDM, which could allow large reductions in the PAPR, but no concrete level on the PAPR has been proven. Reference [59] addressed this issue by providing bounds for the PAPR for different error correction coding schemes coined *trace codes*. Duals of primitive BCH codes are identified as good error correction codes.

Reference [60] presented an interesting paper which clarified the relation between the PAPR and the out of phase aperiodic autocorrelation of the message or data sequence. The PAPR as defined in (3.3) can be bounded as (4.5)

$$\zeta \leq 1 + \frac{2}{N} \sum_{k=1}^{N-1} |\rho(k)| \quad (4.5)$$

where

$$\rho(k) = \sum_{n=1}^{N-k} a_{n+k} a_n^* \quad \text{for } k=0, \dots, N-1 \quad (4.6)$$

and a_n is the input data sequence to the IFFT. (4.6) shows that binary or polyphase sequences with low out of phase aperiodic correlation values can be used to construct low PAPR signals. The problem remains to find sequences that reduce the PAPR. (4.6) is useful as it is a much less complex process to calculate than (3.3).

4.1.3 Cyclic Codes

Reference [61] developed a simple method based on $\frac{3}{4}$ rate code rate cyclic coding which can reduce the PAPR by 3dB when the number of subcarriers is a multiple of 4.

The phase of every 4th subcarrier is calculated so as to minimize the amplitude giving a $\frac{3}{4}$ rate code. The method is simple to implement.

Reference [62] achieves the same results as [61] but with reduced complexity. The authors also introduced Sub Block Coding (SBC) where systems with a large number of subcarriers are divided into sub-blocks with the last bit of each subblock altered according to the method described in [49]. By dividing the OFDM frame into sub-blocks larger number of subcarriers can be used while still maintaining a reduced PAPR, which is a problem with other earlier coding schemes. The idea is developed to optimize the positions of the odd parity checking bits for further PAPR reduction at the cost of the introduction of side information to inform the receiver of the positions of odd parity checking bits.

4.1.4 Shapiro-Rudin codes

A very early paper [63] applied Shapiro-Rudin and Newman phases to multitone frequency response testing. Although the application was not for multicarrier applications the theory still holds with multicarrier signals. Reference [63] stated that a multitone signal can achieve a CF under 6dB for Shapiro-Rudin phases and around 4.6dB using Newman phases for an arbitrarily large number of subcarriers. Many definitions which were to become convention in later papers as far as the statement of the problem of large PAPR, as well as identifying some very pertinent parameters in the makeup of multitone signals. It was also noted that the set of tones needs to be a power of 2 (which is the case in all OFDM standards) in order for the codes to be optimum. Reference [63] closes the paper with an open question as to whether the CF can be reduced lower than 3dB. The authors also state that Newman phases which vary quadratically exhibit a lower CF than Shapiro-Rudin sequences which vary linearly for all N.

Eleven years later reference [64] revisited the application of Shapiro-Rudin sequences to reduce the PAPR in OFDM. In [64] a $\frac{1}{2}$ rate code is employed for QPSK signals with 16 information carriers giving 32 subcarriers in total. 4 bit input messages are concatenated to 4 bit codewords which are determined according to the message data. A simple digital circuit using eight two input XOR gates can be used for the encoder.

Results taken from a limited subset of possible messages suggest that the coded signal will reduce the PAPR to $\frac{1}{4}$ of the original uncoded message.

4.1.5 Golay complementary codes

Golay codes are linear binary block codes which are the only non trivial example of a perfect code. As every codeword lies within distance 3 of any codeword they can be used in conjunction with maximum likelihood detection [16] for decoding which is not overly complex to implement.

In reference [65] the use of Golay complementary codes is examined. Golay sequences were first recognized to have good PAPR properties for application in OFDM in reference [50]. An algorithm was developed where certain subsets of codes up to length 16 have a minimum distance of half the code length and have a PAPR of 3dB. Existing Forward Error Correction (FEC) codes are incorporated into PAPR techniques with a new decoding algorithm developed which utilizes the efficient inverse Walsh-Hadamard transform. However the new decoding algorithm has 3dB worse performance than the optimum maximum likelihood detection.

The author notes that the scheme may be unfeasible for a large number of subcarriers as the length of the codes is the same as the number of subcarriers. However reference [65] proposed ways to nullify this effect at the cost of the PAPR reduction made and error correction capability by breaking the total number of subchannels into smaller groups and applying a complementary code to each group.

4.1.6 Reed-Muller Codes

Golay complementary sequences were further developed for PAPR reduction in reference [66] where again the PMEPR is found to be at most 2 (3dB) when the data sequence is constrained to be a member of a Golay complementary pair. However Golay pairs have a high overhead in terms of redundancy and may not be a practical coding solution for OFDM. Therefore the authors developed a more suitable coding method by recognizing the relation between Golay complementary sequences and

second order Reed-Muller codes (RM(2,m)), i.e. in the binary case Golay sequences occur as cosets of the first order Reed-Muller code within the second order Reed-Muller code. Standard decoders can be used in the receiver for the RM(2,m). RM(2,m) allow the code rate to be improved by allowing a slight increase in the PMEPR. RM(2,m) further developed the theory of reference [65] by allowing a trade off to be made between the Hamming distance, PMEPR reduction made, code rate, and the number of phases allowed in the PSK mapping type.

The authors of reference [66] advanced their work further in reference [67] providing many mathematical proofs for Golay sequences, Reed-Muller codes, decoding using fast Hadamard transforms. Basically this paper formalized the results given in reference [66] and extended the results for larger sets of variables such as an increase in the PSK mapping type. However a limitation which the authors note is that the codes are limited to 32 subcarriers where the resulting code rate will be high.

Reference [68] examined the Reed-Muller coding scheme presented in reference [67] through simulation of an end to end system with various non linearity's and 16 subcarriers. It was shown that at -40dB ACI the new coding scheme had around a 12dB gain in IBO over an uncoded system in experimental results, however this gain drops to 4dB for the simulated results.

Reference [69] also uses Reed-Muller codes in a simulation environment to test their performance in the presence of AWGN to determine the BER with QPSK, and 8 PSK mapping types, and different code lengths, m. The number of subcarriers is chosen such that $N=2^m$, the length of the code. Results indicated that increasing the code length improves error correction capabilities for high SNR values, but at low values of SNR the uncoded system has better performance. As the code rate decreases performance is improved. QPSK and 8PSK are compared in terms of their BER, and it was shown that to maintain the same BER the code length for 8PSK must be increased.

Reference [70] also enlarged on the work of [67] by developing new decoding algorithms with generalized fast Hadamard transforms. The complexity and performance of their decoding algorithm is compared to the standard maximum

likelihood method. Suboptimal algorithms are also presented with reduced complexity which were shown to have minimal degradation over optimal methods.

Another paper to address decoding issues is [71] which used soft decision decoding methods for block codes. The performance is evaluated in an AWGN channel with PSK modulation and 8 and 16 subcarriers. The authors point out the inherent problem with coding schemes i.e. the decrease in coding rate with the increase in the number of subcarriers but state as others have that the PAPR reduction gained can be traded off for reduction in complexity and code length. The new block coding method coined Ordered Statistic Codewords (OSD). BERs for (8,4) and (16,5) block codes utilizing 8 and 16 PSK show that with partial order decoding almost optimum results are achieved compared to the union bound. Complexity compared to MLD methods is greatly reduced at the expense of a minor error increase.

A limitation of references [67, 68] is that PSK mapping types are used. Most practical OFDM standards use QAM mapping [53]. Reference [72] addresses this limitation by combining QPSK constellations to form any M-ary QAM constellation. This is achieved by using shift and rotation operations as defined in (4.7)

$$QAM_M = \sum_{i=0}^{\frac{n}{2}-1} (2^i) \left(\frac{\sqrt{2}}{2} \right) (j^{x_i}) \exp\left(\frac{\pi j}{4}\right) \quad (4.7)$$

where the QPSK constellations can be expressed as j^{x_i} , where $x_i \in Z_4 = \{0,1,2,3\}$. Any QPSK sequence $\mathbf{a} = (a_0 a_1 \dots a_{N-1})$ can be associated with another sequence $\mathbf{x}_i = (x_i^0 x_i^1 \dots x_i^{N-1})$ where the elements of \mathbf{x}_i are in Z_4 . Golay and Reed-Muller sequences can now be created using the theory developed in reference [67].

Reference [73] extended on the coding theory of references [49, 50] by finding codes that simultaneously reduce both the PAPR and the ICI which is introduced by frequency offset between the transmitter and receiver. They define a new measurement term, Peak-Intercarrier-to-Carrier Interference (PICR) to quantify their results. As minimum PICR and PAPR do not occur in the same code word, a balance

is found where both are at an acceptable level. Simulations performed on a rudimentary system with 16 subcarriers and BPSK modulation in AWGN show that the PAPR is reduced by 3dB with a decrease in the PICR. The authors note that finding codes for higher mapping types and more subcarriers is difficult.

Coding techniques while popular in early OFDM papers have since fallen out of favour. Their performance would be largely negated in a practical communications system due to the interleaving stage which follows the coding. It is also worth noting that none of the papers referenced consider the effect of over sampling.

4.2 Multiple Signal Representation

Multiple Signal Representation (MSR) techniques are another distortionless method for PAPR reduction. The basic premise of MSR is to produce a set of alternative transmit signals seeded from the same data source. Various techniques are used to encode the alternative sets of transmit signals, which are encoded in such a way so that they will have different PAPR properties. The transmit signal with the lowest PAPR is chosen for transmission.

4.2.1 Partial Transmit Signals

Reference [74] first proposed Partial Transmit Sequences (PTS). PTS generates a signal with a low PAPR through the addition of appropriately phase rotated signal parts. The original signal is given by (2.2) and is reproduced in (4.8)

$$x_m = \frac{1}{\sqrt{N}} \sum_{k=0}^{N-1} X_m \cdot e^{j2\pi nk/N} \quad \text{where } 0 \leq n \leq N-1 \quad (4.8)$$

The signal to be transmitted is broken up into several sub blocks, $X_{m,k}$, of length N/V (where N is the number of sub carriers and V is the number of sub blocks). All subcarrier positions which are occupied in another block are set to 0, i.e.

$X_m = \sum_{k=1}^V X_{m,k}$ Next a *constant* phase rotation, $p_{m,k} = e^{+j\phi_{m,k}}$, $\phi_{m,k} \in [0, 2\pi)$ $1 < k < V$ is

performed on each subblock except for the first one which is kept constant, giving (4.9)

$$\tilde{X}_m = \sum_{k=1}^V p_{m,k} \cdot X_{m,k} \quad (4.9)$$

The information in \tilde{X}_m is the same as X_m but with an added phase rotation, which must be known at the receiver. An IFFT is performed on each subblock which are then all summed together to create a possible transmit symbol, (4.10)

$$\tilde{x}_m = \sum_{k=1}^V p_{m,k} \cdot \text{IFFT}\{X_{m,k}\} = \sum_{k=1}^V p_{m,k} \cdot x_{m,k} \quad (4.10)$$

The process is repeated again with a different phase rotation, $p_{m,k}$, to produce another alternative transmit signal. The optimum parameters for the transmit symbol are (4.11)

$$\{\tilde{p}_{m,1} \cdots \tilde{p}_{m,V}\} = \arg \min_{\{\tilde{p}_{m,1} \cdots \tilde{p}_{m,V}\}} \left(\max_{0 \leq n < N-1} \left| \sum_{k=1}^V p_{m,k} \cdot x_{m,k} \right| \right) \quad (4.11)$$

The optimum phase angle, $\tilde{p}_{m,k}$, is obviously the one where the PAPR is minimized. Therefore the actual transmit signal is given as (4.12)

$$\tilde{x}_m = \sum_{k=1}^V \tilde{p}_{m,k} \cdot x_{m,k} \quad (4.12)$$

Figure 4.2 shows a block diagram of a PTS transmitter.

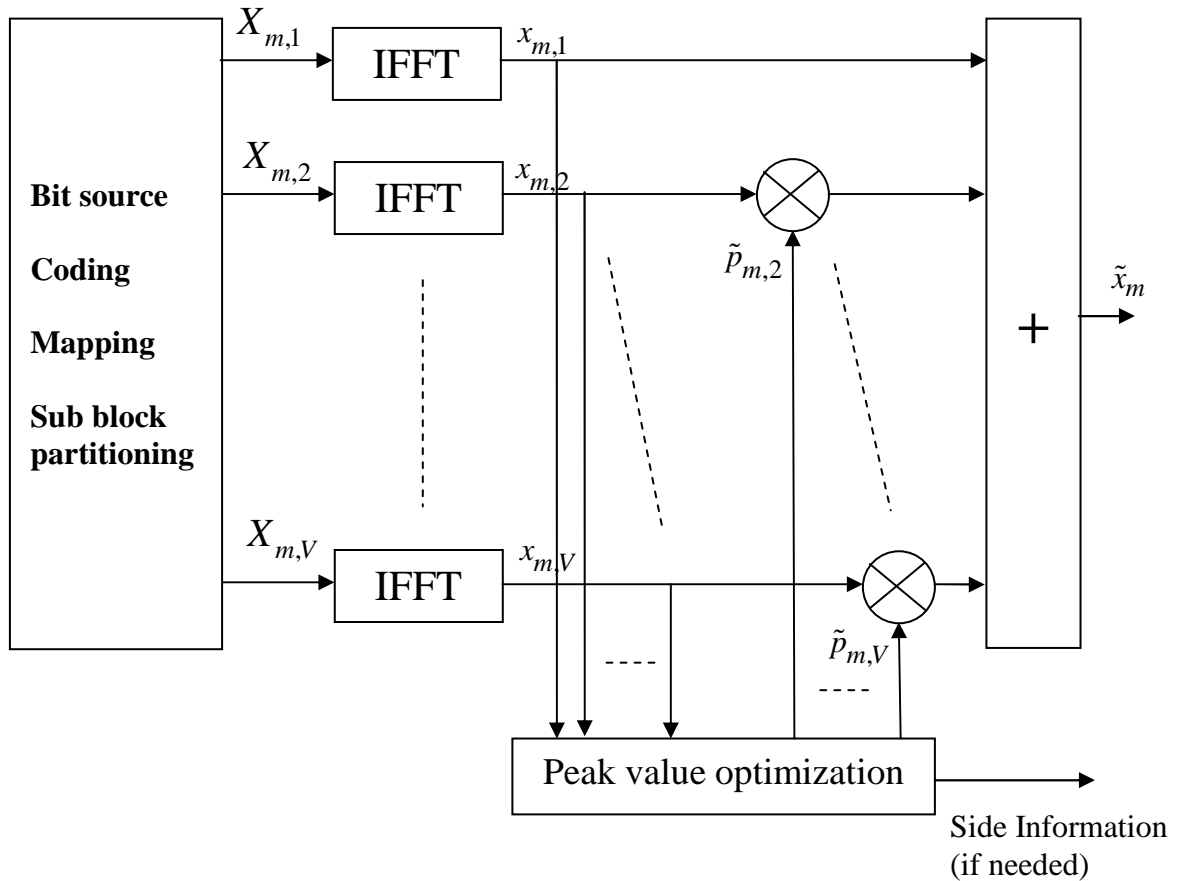


Figure 4.2: Block diagram of PAPR reduction using the PTS approach.

PTS requires side information to be sent to the receiver to inform it of the phase rotation used so the data can be decoded. Reference [74] noted that the number of angles should be kept low to keep the side information to a minimum. If each phase rotation is chosen from a set of W admissible angles then the required number of bits for side information is, $R_{ap} = (V-1)\log_2 W$ bits per OFDM symbol. In order to reduce complexity the phase angles should be restricted to $\{\pm 1, \pm j\}$, i.e. $W=4$, this allows multiplications to be performed with sign changes. Simulations shown in Chapter 5 reveal that increasing the number of allowed phase angles has a minimum impact of PAPR reduction. Reference [75] noted that explicit side information can be avoided if differential encoding is used for the modulation across the subcarriers within each subblock. In this case only the block partitioning need to be known at the receiver and one subcarrier in each subblock must be left unmodulated as a reference carrier.

PTS is flexible as the number of blocks and phase rotations can be increased providing more alternative transmit signals to choose from. The disadvantage of this scheme is the complexity, especially with an increase in V and W . Also, a large amount of memory is required to store the alternative transmit signals (if check performed in parallel) in order to compare them to find the one with the lowest peak value. Alternatively the optimisation can be performed in an iterative fashion where the current best transmit signal is stored until a better one is found, at the cost of increased latency.

It should also be noted that the data can be divided into sub blocks in different ways as noted in reference [76] and shown in Figure 4.3. Different PTS sub block structures have varying performance with pseudo random having the best and interleaving having the worst. Of course there is a trade off with complexity, interleaved sub blocks are the least complex PTS structure to implement (The size of the IFFT's can be halved by interleaving the input data to the IFFT and performing the last stage of the IFFT operation at the IFFT output [77].) and pseudo random PTS is the most complex (random sequences require more hardware complexity to implement in this case). Also computationally efficient IFFT's can be used to exploit the number of zero's in the PTS sub-blocks. Results from reference [74] indicate that pseudo-random partitioning is 0.5 to 0.9dB better than adjacent partitioning.

It should be noted that no guaranteed level of PAPR reduction can be provided with MSR techniques, all they can do is reduce the probability of large peaks. Figures 4.4 and 4.5 show CCDF results with varying factors of V and W , N is set at 64. The simulation model is described in Figure 5.1.

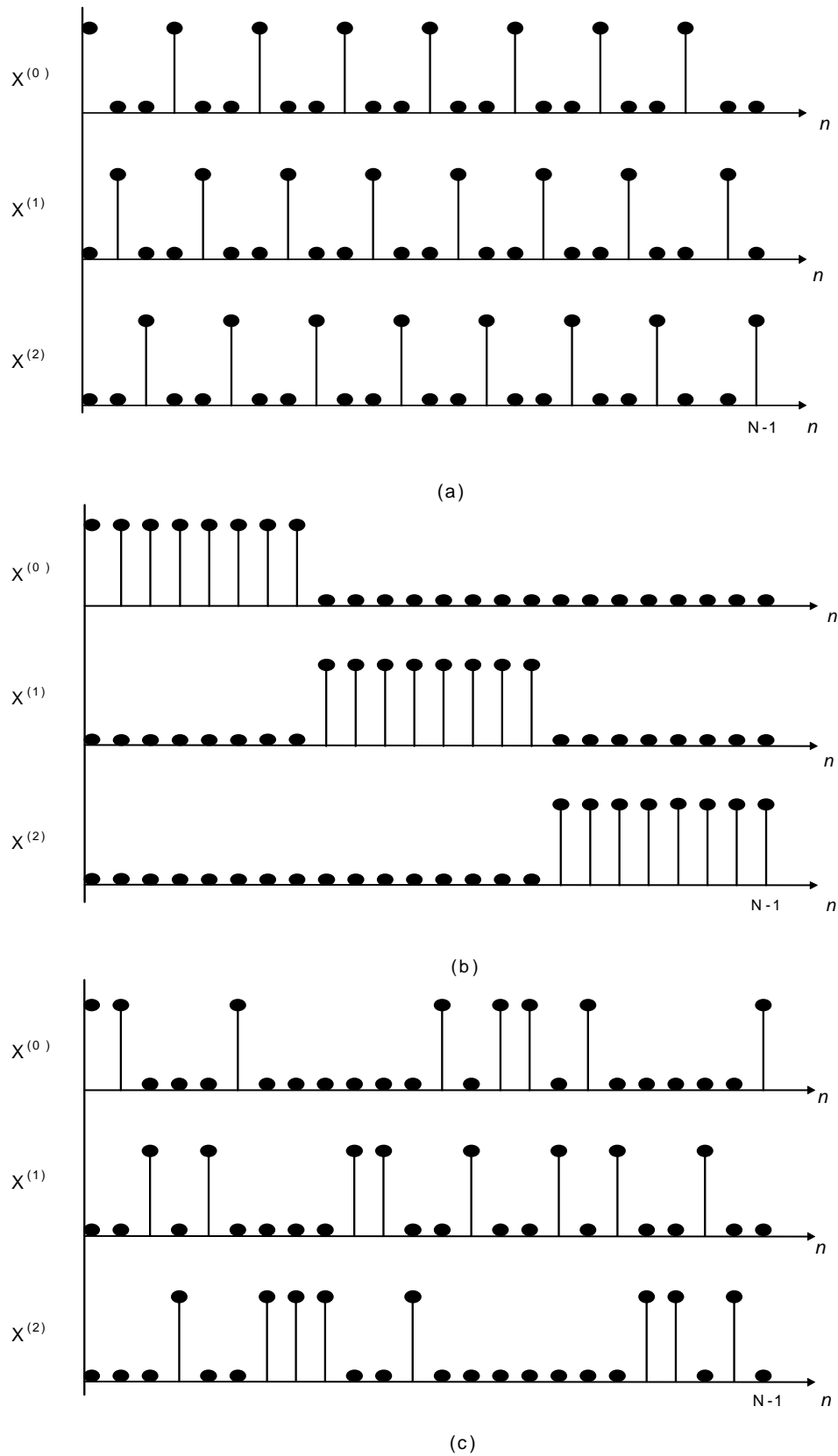


Figure 4.3: An example of the 3 main PTS structures: (a) Interleaved (b) Adjacent (c) Pseudo-random.

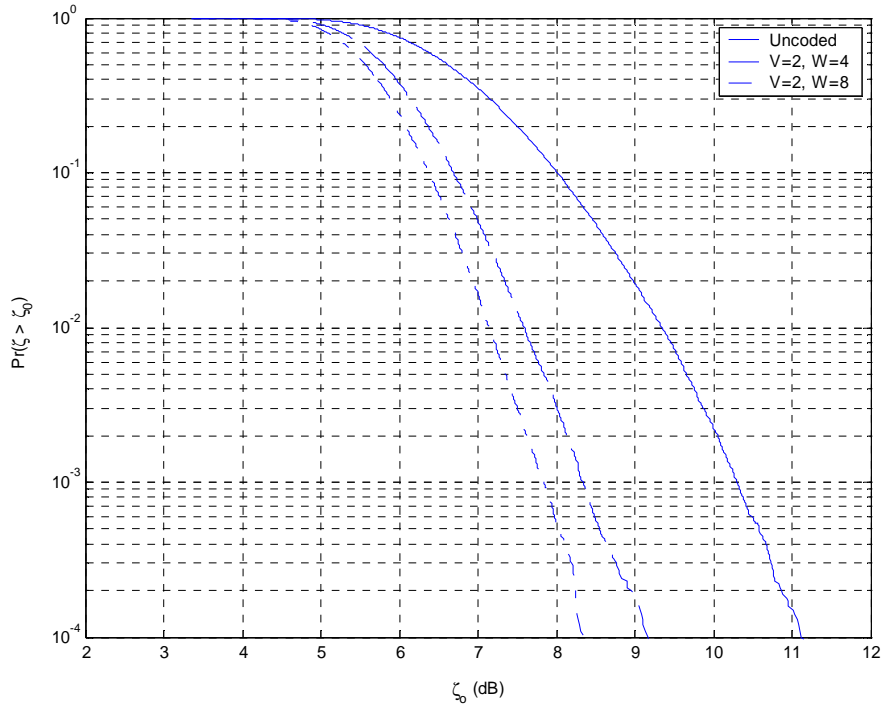


Figure 4.4: Simulated CCDF for PTS-OFDM with $V=2$ and varying W . $N=64$, adjacent subblock partitioning.

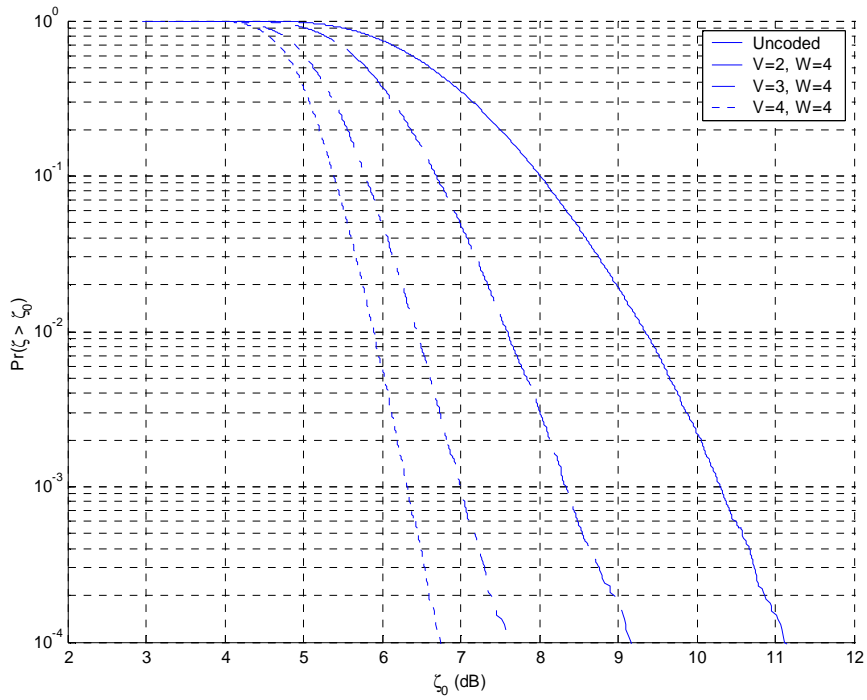


Figure 4.5: Simulated CCDF for PTS-OFDM with $W=4$ and varying V . $N=64$, adjacent subblock partitioning.

4.2.2 Oversampling PTS

Early on in the development of PTS a problem was identified which skewed the true gains of the proposed technique. As already mentioned in section 3.3 oversampling at the IFFT is important to get a true reflection of PAPR reduction. Reference [34] first identified this issue and showed that for a PTS system with $V=4$, $W=4$ the PAPR reduction gained using the T r u e P e a k F a c t o r (TPF) i.e. oversampled signal is only 1dB better than the uncoded case. In reference [34] it is shown that the true peak will move away from the discrete sampled points. There is a 3dB difference in the reduction between TPF and L o w e r P e a k F a c t o r (LPF), i.e. the discrete PAPR. Reference [34] goes on to suggest a new optimisation technique based on the aperiodic autocorrelation of $x_{m,k}$, λ_k .

$$\{\tilde{P}_{m,1} \cdots \tilde{P}_{m,V}\} = \arg \min_{\{\tilde{P}_{m,1} \cdots \tilde{P}_{m,V}\}} \left(\sum_{k=1}^{N-1} |\lambda_k| \right) \quad (4.10)$$

A reduction of 2.5dB can be achieved when using the optimisation criteria of (4.10) at $\Pr(\zeta > \zeta_0) = 10^{-5}$. However this process is complex, for QPSK the calculation of λ_k can be achieved with less multiplications and replaced with integer additions giving a total complexity of $O(4^{V-1}N^2)$.

Reference [39] acknowledges the limitations of discrete sampled PTS and notes that the mismatch between discrete and continuous CCDF's occurs due to DSP filtering after the IFFT, peak regrowth becomes more pronounced with a sharper rolloff, α , of the filter. Reference [39] suggests that oversampling the IFFT by a factor of 2 (zero padding) will reduce the peak regrowth affects after filtering. Oversampling of PTS is explored in more depth in Chapter 5.

Another paper, [78], to explore the PTS approach looked at alternative ways to create sub-blocks. The new method coined C o n c a t e n a t e d P s e d o r a n d S u b b l o c k P a r t i t i o n S c h e m (CPR SPS) divides the OFDM symbol into multiple disjoint sub-blocks and assigns signals randomly in each subblock. The partial sub band is then

duplicated and assigned to the rest of the subbands repetitively to form a complete sub block. This procedure is depicted in Figure 4.6 for 3 subcarriers.

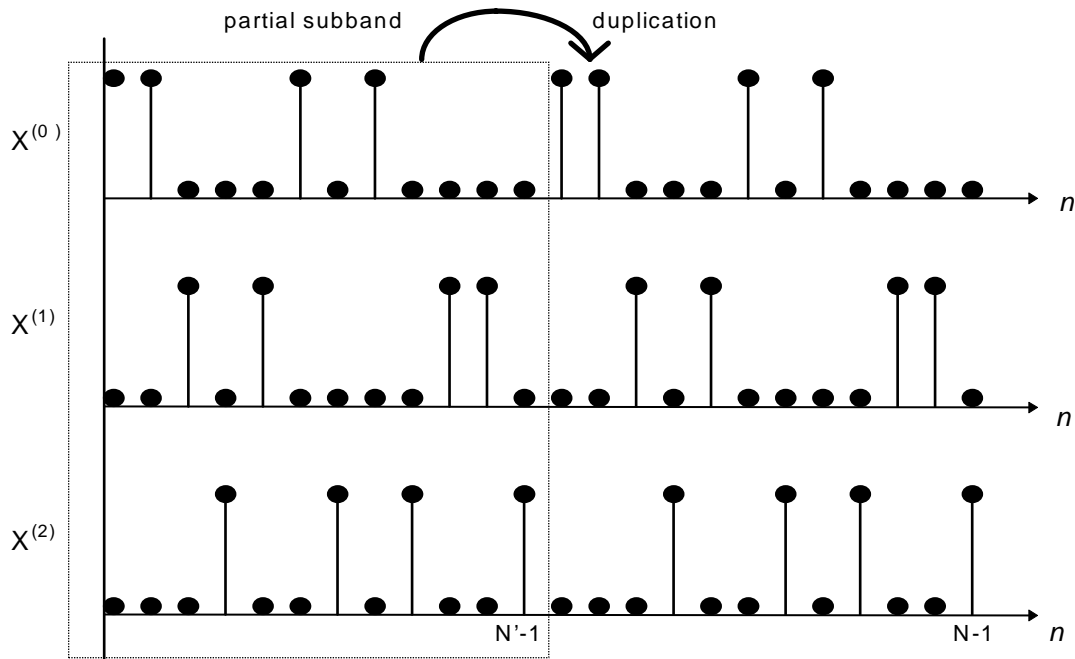


Figure 4.6: Generation of sub-blocks for PTS using Concatenated Pseudo Random Sub Block Partition Scheme (CPR SPS).

C is the concatenation factor, i.e. the number of sub-blocks. $C=1$ is equivalent to pseudo random PTS. Results indicate that CPR SPS can achieve similar results to the optimum pseudo random block allocation method but with a decrease in complexity, especially when efficient FFT structures such as the Cooley-Tukey algorithm are used. Best results are obtained with low values of C (2 or 4) which results in a marginal decrease in complexity compared to pseudo random PTS. For a significant reduction in complexity $C=16$ has similar performance to the adjacent subblock allocation method.

References [79, 80] also examined the PTS complexity reduction. The basic principle of these papers is to produce a suboptimal iterative algorithm which uses a similar structure to PTS but with reduced complexity. This method is coined Suboptimal Exhaustive Search (SES) algorithm and exhibits good performance with a minimal number of trials. One of the problems of PTS is that in order to work out which

transmit signal has the largest peak, every sample in each possible signal has to be checked to work out its peak value. The process of finding large peaks contributes significantly to the complexity of PTS. If the time domain signal is given as (4.9) then the phase optimization values are restricted to $p_{m,k} = [\pm 1]$. The SES algorithm works as follows:

- 1/ Assume $p_{m,k}=1$ for all k and compute the PAPR of the combined signal (ie. no optimisation).
- 2/ Next, invert the first phase factor ($p_{m,k}=-1$) and recompute the resulting PAP for the first value in each sub block, V . If the new PAP is lower than the previous value use b_1 as part of the final phase sequence, otherwise use the original value for $p_{m,1}$ (ie. 1).
- 3/ The algorithm continues until all V points have been given this treatment.

Simulations for $V=16$ sub blocks, and $N=256$ subcarriers exhibited around a 1dB degradation compared to standard PTS with adjacent subblock partitioning at $\Pr(\zeta > \zeta_0) = 10^{-3}$. However the optimisation process has been reduced to N^2 additions, a considerable saving in terms of hardware operations. Note that in the simulations an oversampling factor of 4 is used, which is sufficient to catch all peaks.

Various parameters were varied in the simulation such as a) the number of sub blocks, V . b) number of allowed phases, $p_{m,k}$ for optimization and c) data constellation size. It was concluded that the performance improves with an increase in V . However as V is increased the performance improvement becomes less pronounced. Increasing the number of phases to four $[\pm 1, \pm j]$ provides a minor improvement for higher values of V and up to a 1dB improvement at low values of V . The data constellation size has a minimal effect on performance.

The SES algorithm has similar performance to traditional PTS with optimum phase selection (within 1dB of optimum solution at $\Pr(\zeta > \zeta_0) = 10^{-4}$) but with reduced complexity. However complexity increases substantially with an increase in V .

Reference [81] again looked at developing optimum phase factors for PTS with reduced complexity. The new method called Optimal Limited Search (OLS) also

addresses the oversampling issue by including an oversampling factor, L . The output of the PTS algorithm can be written as (4.11)

$$S = \begin{bmatrix} A_{11} & A_{21} & \dots & A_{M1} \\ A_{12} & A_{22} & \dots & A_{M2} \\ \dots & \dots & \dots & \dots \\ A_{1LN} & A_{2LN} & \dots & A_{MLN} \end{bmatrix} \begin{bmatrix} e^{j\phi_1} \\ e^{j\phi_2} \\ \dots \\ e^{j\phi_M} \end{bmatrix} \quad (4.11)$$

where

$$S = [S_1(\phi), \dots, S_{LN}(\phi)]^T \quad (4.12)$$

contains the optimized signal samples. Figure 4.7 shows a block diagram of an OLS-PTS transmitter. OLS sorts same subcarrier positions over V IFFTs in order of magnitude as depicted in (4.13)

$$|A_{r1i}| > |A_{r2i}| > \dots > |A_{rMi}| \quad (4.13)$$

then chooses

$$\phi_{rl} = \begin{cases} -\angle A_{rli} & l = 1, 3, \dots \\ \pi - \angle A_{rli} & l = 2, 4, \dots \end{cases} \quad (4.14)$$

The minimum amplitude sum for one IFFT point is then given by (4.15)

$$S_i(\phi) = |A_{r1i}| - |A_{r2i}| + |A_{r3i}| - \dots \quad (4.15)$$

The phase selection (4.14) nearly always yields the maximum amount of amplitude cancellation for the i^{th} signal sample. Next all LN solutions are calculated and the one that minimises the maximum signal samples is chosen.

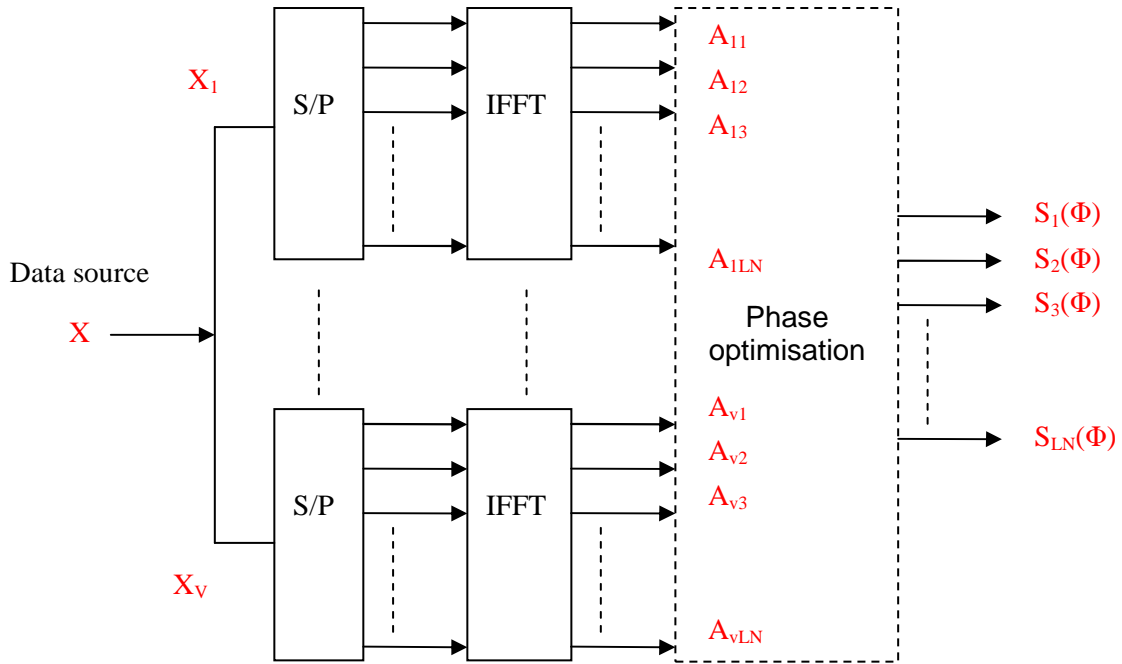


Figure 4.7: Block diagram of OLS-PTS transmitter.

The effect of quantization and the PSD is also examined for OLS. Quantization is shown to have a negligible effect on performance and the out of band radiation is also shown to be better than the OBPS case.

OLS out performs the methods of references [79, 80] for larger values of V (>8), also the number of iterations is independent of V . Simulations (QPSK $N=256$) show OLS to be slightly better than the OBPS of reference [74] for $V>4$ and much better for $V<4$. The complexity of the 3 preceding methods is summarized in Table 4.1.

Table 4.1: Number of complex multiplications and magnitude operations required.

L=4; N=256; W=2		
	V=2	V=16
OBPS (Huber et al)	33,554,432	$5.52 \cdot 10^{70}$
SES (Cimini, et al)	2048	33,554,432
OLS (Tellambura et al)	1,048,576	1,048,576

Reference [82] developed another scheme to find optimal phases based on orthogonal vectors called Orthogonal Projection-based PTS (OP-PTS). The authors state that OP-PTS can reduce the PAPR within 0.4-0.8dB (using adjacent partitioning) of OBPS using pseudo random partitioning and is suitable for a large number of subcarriers.

The complexity of OP-PTS is better than OBPS when a large number of subcarriers and sub-blocks are used ($N=128$, $W=4$, $V \leq 5$), but improvement using OP-PTS reduces with an increase in V . The complexity of OP-PTS is also slightly lower than SES for high N and V . Note that no oversampling is used in OP-PTS. A suboptimum solution for OP-PTS approach to find near optimum phases with negligible affect on performance is also presented. The optimum phases are chosen from a set of 32 selected phases.

4.2.3 Selective Mapping

In reference [83] another multiple signal representation method is presented called SeLected Mapping (SLM). The basic idea of SLM is to produce U alternative transmit sequences seeded from the same data source and then to select the transmit signal exhibiting the lowest PAPR. The idea stems from the fact that as the PAPR is determined by the sequence of the transmit data vectors, X_m , multiplying the data vectors by some random phase will change the PAPR properties after the IFFT.

Mathematically, a set of U markedly different, pseudo random fixed vectors are generated, $P^{(u)} = [P_0^{(u)}, \dots, P_{D-1}^{(u)}]$, $P_k^{(u)} = e^{+j\varphi_k^{(u)}}$, $\varphi_k^{(u)} \in [0, 2\pi)$, $0 \leq k < N, 1 \leq u < U$.

The data, X_m , is multiplied subcarrier wise with each one of the U vectors, $P^{(u)}$, resulting in a set of U different possible transmit symbols, $X_m^{(u)}$ as depicted in (4.16)

$$X_{m,k}^{(u)} = X_{m,k} \cdot P_k^{(u)}, \quad 0 \leq k < N, 1 \leq u < U \quad (4.16)$$

Next, all U possible transmit vectors are transferred to the to the time domain via the IFFT, $x_m^{(u)} = IFFT\{X_m^{(u)}\}$, and the transmit symbol with the lowest PAPR, \tilde{x}_m , is chosen for transmission. A SLM transmitter block structure is depicted in Figure 4.8.

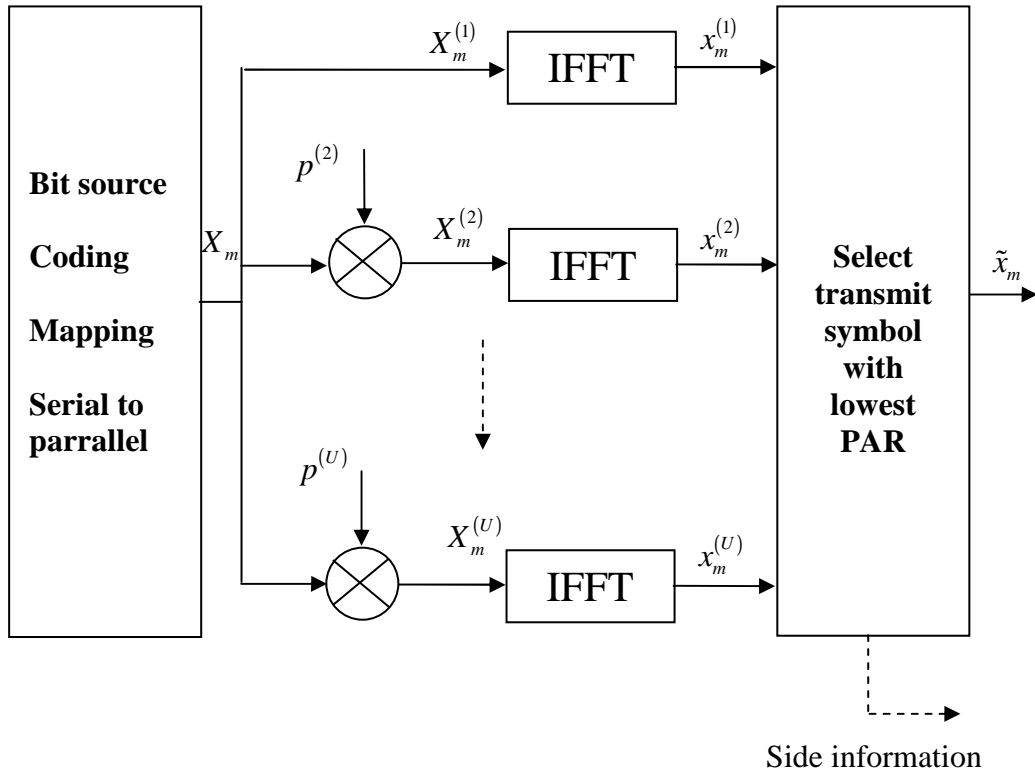


Figure 4.8: Block diagram of an SLM OFDM transmitter.

Simulations performed with $N=128$ and 4-PSK mapping indicate that at $\Pr(\zeta > \zeta_0) = 10^{-4}$, with $U=4$ a PAPR reduction of $\sim 3\text{dB}$ is gained compared to the uncoded case. Complexity reduction can also be achieved by restricting the random generated data to $P_m^{(u)} \in \{\pm 1, \pm j\}$ avoiding complex multiplications.

Figure 4.9 shows the CCDF of SLM with $N=64$, $os=1$, and $U=1$ to 32. At $\Pr(\zeta > \zeta_0) = 10^{-4}$ the PAPR is reduced from 2 to 4.5dB for $U=1$ to $U=32$ respectively. Figure 4.10 shows the CCDF of SLM with $N=64$ and $U=1$ (uncoded) 3, and 8. The oversampling rate is set at 1, 2, and 4, and 8. Here it is seen that oversampling has a minimal affect on the PAPR, only increasing it by $\sim 0.5\text{dB}$. An oversampling rate of 4 is sufficient. This is due to all the alternative transmit signals being uncorrelated as shown in Figure 3.6. This is one of the main advantages of SLM, i.e. that oversampling and filtering does not increase the PAPR dramatically as it does in PTS (shown in Chapter 5). Again oversampling is seen to have a negligible affect on the PAPR, the purpose of this plot is to show that oversampling still has a minimal affect at higher values of U .

Side information is also an important issue in SLM as the receiver needs to be informed which vector, $P^{(u)}$, was used. $\log_2(U)$ bits are required to send this information increasing redundancy. As loss of this information (in a fading channel) means the complete loss of the transmit symbol channel coding is required to ensure correct recovery of the data at the receiver, increasing redundancy further.

In reference [74] SLM is compared to PTS for various combinations of V , W (PTS) and U (SLM). In terms of redundancy (side information) SLM with $U=1..5$ outperforms PTS using pseudo-random subblock partitioning ($W=4$, $V=1..5$) at the cost of greater system complexity. In terms of performance PTS has better PAPR reduction if the number of IFFT's is fixed as PTS can vary W with no additional IFFT's. 4 alternative signals produced with PTS require 3 IFFT's while the same performance with SLM can only be achieved with 4 IFFT's.

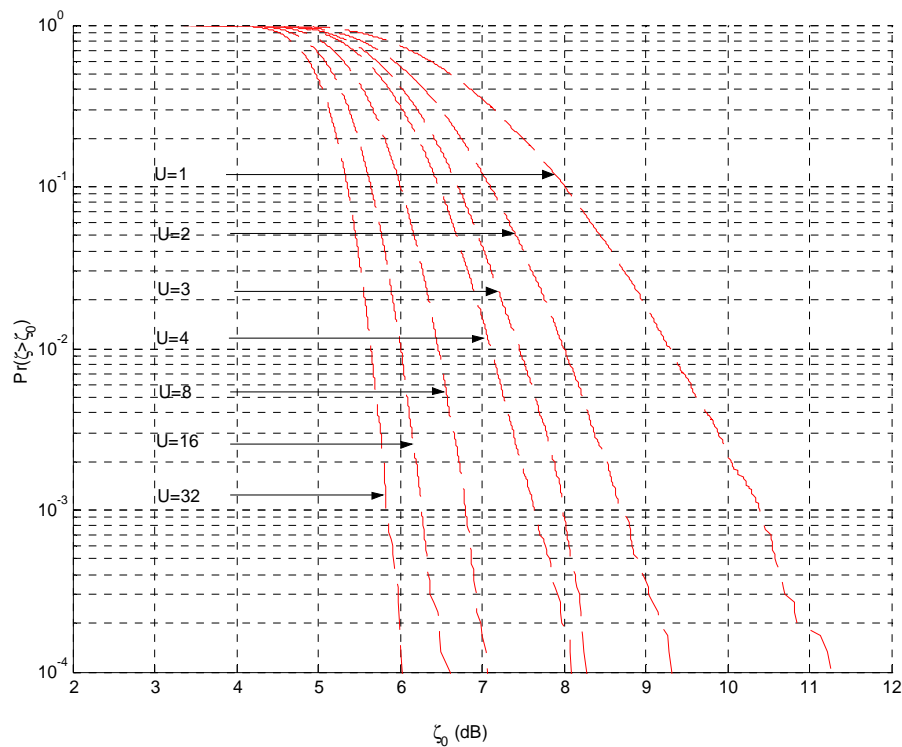


Figure 4.9: Simulated CCDF for SLM-OFDM for varying values of U . $N=64$, $os=1$.

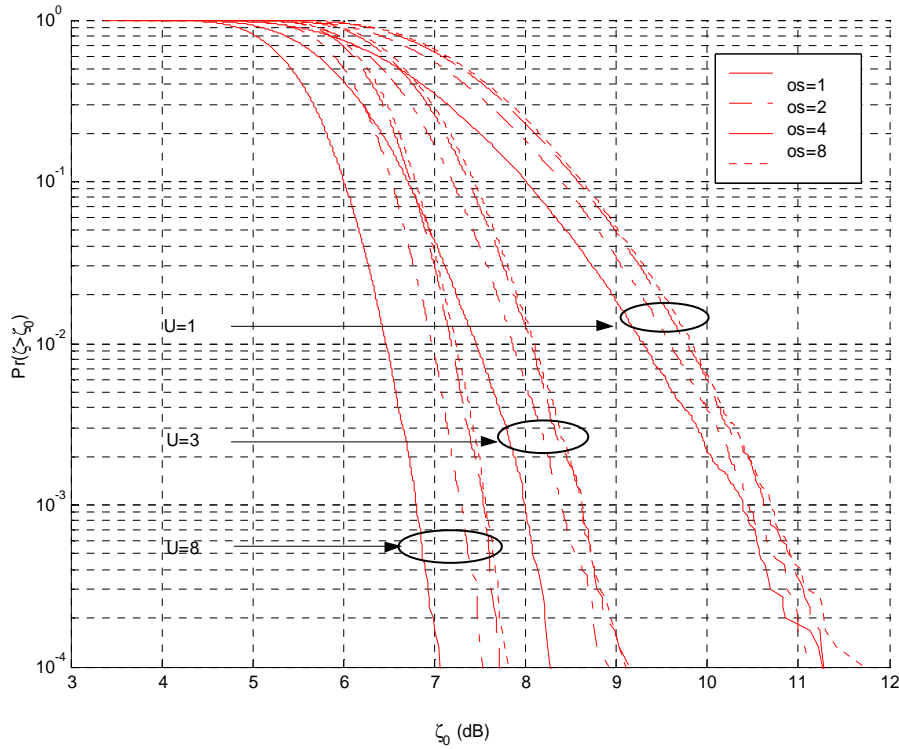


Figure 4.10: Simulated CCDF for SLM-OFDM. $U=1, 3,$ and 8 . Oversampling rates are $1, 2,$ and $4,$ and 8 .

The issue of side information for SLM is further explored in [84] where the need for explicitly sent side information is avoided. The new technique employs a scrambling sequence and inserts U different ‘labels’, $b^{(u)}$, of length $\log_2 U$ as a prefix to the data sequence as shown in Figure 4.11a. The data with prefix is then fed into a scrambler polynomial as shown in Figure 4.12. The labels drive the scrambler into one of U different states before scrambling the data itself. The scrambled data is then processed as usual. The process is repeated with the other different U labels to produce U alternative transmit sequences as in standard SLM.

Figure 4.11b is a variation where the linearity of the scrambler is exploited, here only a single codeword $\tilde{q}^{(0)}$ needs to be generated. U different subcarrier vectors can then be generated by applying U different vector mappings to $\tilde{q}^{(0)}$. The advantage of this structure is that u^{th} calculated vector mapping can be calculated once from the label $b^{(u)}$ and can be stored in memory. The receiver structure complexity is hardly

increased at all, only the label needs to be removed after descrambling. The complexity of the new scheme is increased by around U compared to standard SLM.

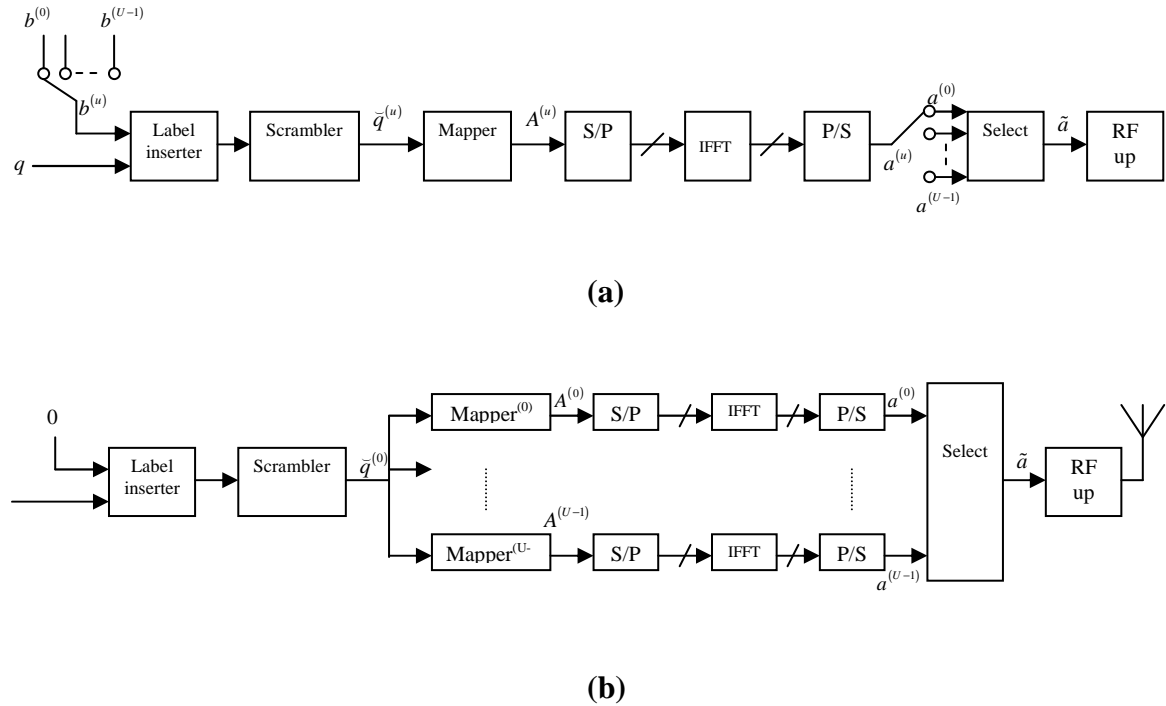


Figure 4.11: SLM transmitter block diagram employing technique to avoid explicit transmission of side information, a) serial form, b) parallel form.

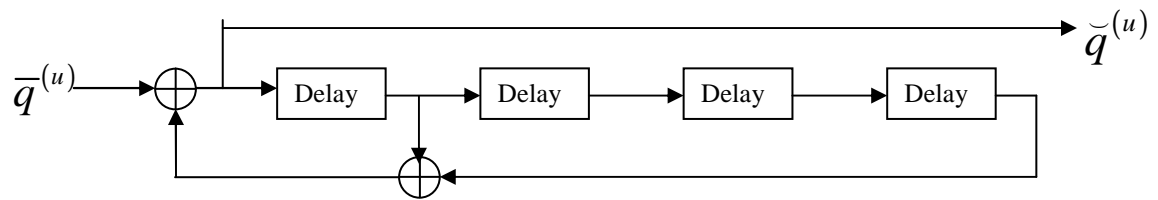


Figure 4.12: Scrambler polynomial for new SLM technique.

Simulations were performed with $N=256$ carriers, 219 of which are active (to decrease the design constraints of the transmit filter), 16 QAM mapping is used. The IFFT was oversampled by a factor of 2 yielding more accurate results. The data was then interpolated by a factor of 8 and a RRCF with a rolloff of 0.12 was used, results were shown after the transmit filter. At $\Pr(\zeta > \zeta_0) = 10^{-5}$ the new SLM algorithm can

reduce the PAPR by 1.8 and 2.5dB for U=4 and 8 respectively. Figure 4.13 shows the receiver structure of the new SLM technique.

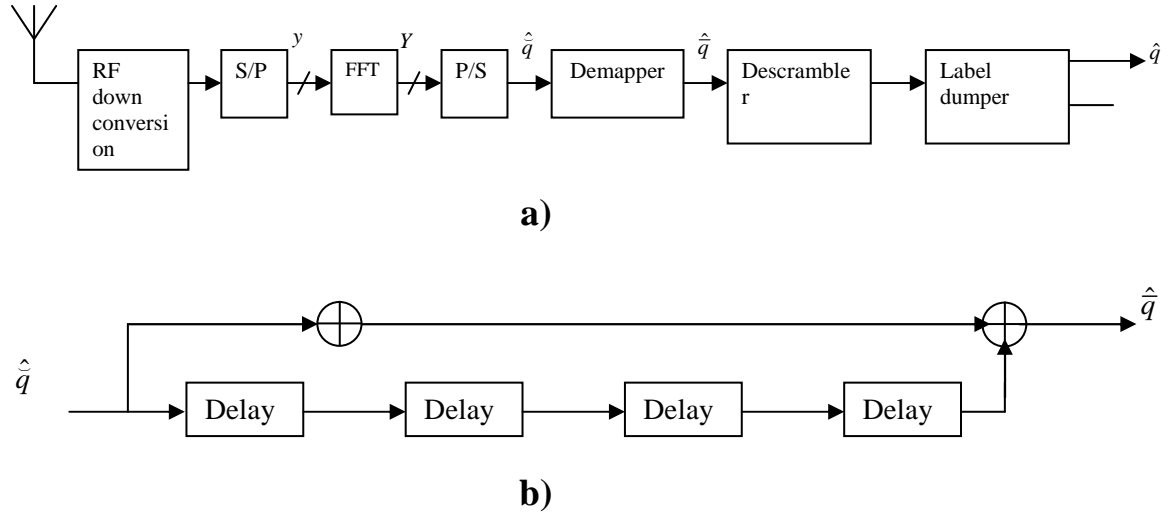


Figure 4.13: a) Receiver structure of the proposed SLM system, b) Descrambler polynomial at the receiver.

The impact on the BER is also analyzed where perfect knowledge of the channel and noise is assumed. The descrambler can multiply errors in receiver, but the effect is negligible as the BER is degraded by 0.2dB. PSD plots showed that between 1 and 2dB can be saved in power backoff of the LPA with 4 bits redundancy per OFDM symbol.

Reference [85] again looks at the issue of side information in SLM and proposes a variation of reference [84] called Blind SLM (BSLM) which does not require the labels to be sent with the data for descrambling in the receiver. The U sets pseudo scrambling noise vectors are restricted to a known set at the receiver and all U sets are sufficiently different. In order for the method to work $c_n e^{j\phi_n^u} \in Q$, where Q is the constellation mapping type.

At the receiver the decision metric is (4.17)

$$D = \min_{\substack{[\hat{c}_0, \hat{c}_1, \dots, \hat{c}_{N-1}] \in C \\ P_u, u \in \{0, 1, \dots, U-1\}}} \sum_{n=0}^{N-1} \left| r_n e^{-j\theta_n^a} - H_n \hat{c}_n \right|^2 \quad (4.17)$$

is performed for P_1, P_2, \dots, P_{U-1} , the global minimum-distance solution provides the best estimate for the transmitted data. A suboptimal metric is also presented to reduce complexity in the receiver.

Simulations of the BER revealed that the new technique has almost the same performance as SLM with perfect side information available with a infinite backoff in the LPA. When a SL is employed with varying backoffs, BSLM slightly outperforms the standard SLM approach. However there is a slight degradation when the new algorithm is used in a fading channel.

4.3 Tone Reservation/Injection

Tone Reservation (TR) and Tone Injection (TI) were first introduced in reference [86] and further detailed in reference [30]. These methods use an iterative algorithm to provide increasingly better CCDF results.

4.3.1 Tone Reservation

In TR subcarriers, called Peak Reduction Tones (PRT's), are set aside for PAPR reduction as shown in the transceiver block diagram in Figure 4.14.

The signal plus Peak Reduction Tones (PRTs) are represented in (4.18)

$$x + c = Q(X + C) \quad (4.18)$$

where Q is the IFFT matrix, X is the transmit data before the IFFT, and C are the PRT's.

$$X_k^m + C_k^m = \begin{cases} C_k^m, & k \in \mathfrak{R} \\ X_k^m, & k \notin \mathfrak{R}^c \end{cases} \quad (4.19)$$

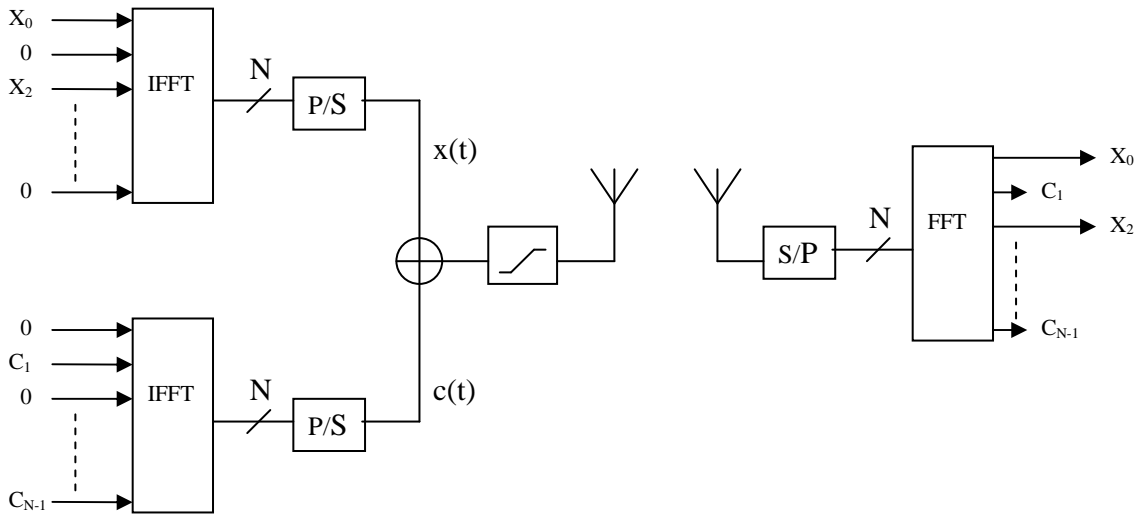


Figure 4.14: Block diagram of a Tone Reservation (TR) OFDM transceiver.

where

$$X_k = 0, k \in \{i_1, \dots, i_L\} \quad \text{and} \\ C_k = 0, k \notin \{i_1, \dots, i_L\}$$

Coefficients for C_k can be found with a reduced complexity iterative algorithm which achieves a solution close to the optimum in a few steps to reduce the PAPR. This method is distortionless as the data lies in disjoint frequency bins, i.e. $X_k^m C_k^m = 0$, which introduces redundancy. The new transmit signal has PAPR defined as (4.21)

$$PAR\{x+c\} = \frac{\|x+c\|^2}{\mathcal{E}[\|x\|^2]/N} \quad (4.21)$$

Vector c is computed so that the maximum peak value is reduced as (4.22)

$$\min_c \|x+c\|_\infty = \min_{\hat{C}} \left\| x + \hat{Q} \hat{C} \right\|_\infty \quad (4.22)$$

Solving $\|x+c\|^2$ is a convex problem, where the optimum solution lies at the bottom of the parabola. When the terms are expanded out it can be solved as a Quadratically Constrained Quadratic Program (QCQP), which can also be solved as a Linear Program (LP). The complexity of the LP is $O(N \log N)$.

L/N is the ratio of redundancy where L is the number of PRT's and N is the total number of data tones or subcarriers. To reduce the bit redundancy, PRTs can be assigned to subcarriers which have a small number of bits assigned to them (in the case of ADSL), i.e. QPSK as opposed to 16 QAM subchannels. The Data Rate Loss (DRL) can be given as (4.23)

$$DRL = \frac{\sum_{k=1}^L b_{i_k}}{\sum_{k=0}^{N-1} b_k} \quad (4.23)$$

Simulation results indicated that for a L/N ratio of 5%, the clip probability is reduced from 15dB to 9dB at $\Pr(\zeta > \zeta_0) = 10^{-5}$. For a L/N ratio of 20% the clip probability is reduced from 15dB to 5dB at $\Pr(\zeta > \zeta_0) = 10^{-5}$. Basically an increase in the number of PRT's improves the PAPR reduction made. All simulations are based on $N=512$ subcarriers.

The performance of TR is influenced by the position of the peak reduction tones. As with PTS it was found that random positions of PRC gave the best peak reduction results of 6.2dB at $\Pr(\zeta > \zeta_0) = 10^{-5}$ probability. Adjacent PRTs on the other hand only had a peak reduction of 3.4dB.

The number of iterations required to achieve various peak reduction values for random PRT also has a pronounced affect on the performance of TR. For example with $L/N = 5\%$, 1 iteration gives a 2dB reduction at $\Pr(\zeta > \zeta_0) = 10^{-5}$, 5 iterations provides a 3.8dB reduction at $\Pr(\zeta > \zeta_0) = 10^{-5}$, which is 2.1dB away from optimum solution. Note that law of diminishing returns applies in that the more iterations performed the less the PAPR reduction achieved, i.e. after 40 iterations the new peak value is still 0.5dB away from optimum solution.

These results are for the optimum solution where the complexity is quite high. The complexity can be reduced using general purpose iterative algorithms which find sub-optimal solutions such as the gradient algorithm.

Gradient algorithm for computing c

Reference [86] uses gradient algorithms with reduced complexity, to reduce the hardware requirements while still providing a good approximation to the optimum solution.

By taking the gradient of the clipping noise Mean Square Error (MSE), simple iterative algorithms were produced which achieved a solution close to the optimum in a few steps. The gradient algorithm searches for the largest terms in $x+c$ and subtracts scaled replicas of them to cancel large peaks. The complexity of this algorithm is $O(N)$ per iteration compared to $O(N\log N)$ in the optimum case.

The clipping noise of the gradient algorithm is defined as (4.24)

$$\|x - clip_A(x)\|^2 = \sum_{n=0}^{N-1} (x_n - clip_A(x_n))^2 \quad (4.24)$$

Including the PRT's in the transmitted time signal $x+c$, the Signal to Clipping noise Ratio (SCR) is given by (4.25)

$$SCR = \frac{\|x\|^2}{\|x+c - clip_A(x+c)\|^2} \quad (4.25)$$

In order to maximize the SCR the denominator is minimized. Instead of solving for c ($c=QC$) [30] solves for the gradient of c giving (4.26)

$$c^{(k+1)} = c^{(k)} - \mu \sum_{|x_i+c_i^{(k)}|>A} \alpha_n^{(k)} \hat{Q} \hat{q}_{row}^n \quad (4.26)$$

where $\alpha_n^{(k)} = sign(x_n + c_n^{(k)}) (|x_n + c_n^{(k)}| - A)$. As is seen in (4.26), each iteration requires an IFFT to be performed. Basically the algorithm searches for the largest terms in $x+c^{(k)}$ and subtracts scaled, circularly shifted replicas of the vector p^0 to cancel large peaks ($p^0 = \hat{Q}\hat{q}_{row}^0$).

4.3.2 Tone Injection

Another method developed in reference [86] called TI maps data that cause large peaks to new positions which will not produce peaks when the IFFT is performed. The data can then be easily decoded correctly with a modulo D operation in the receiver as shown in the block diagram in Figure 4.15.

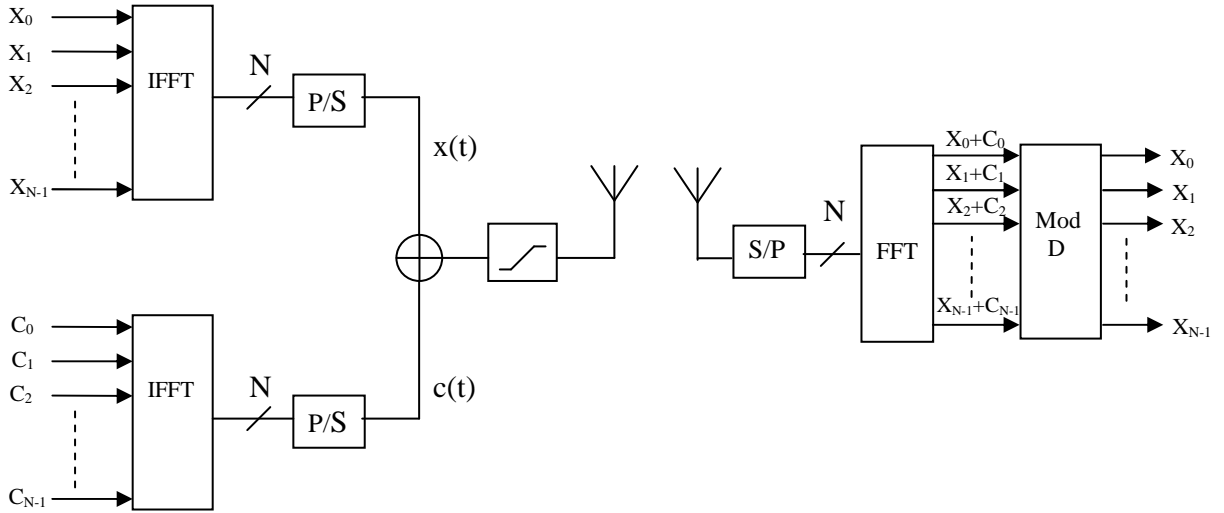


Figure 4.15: Block diagram of a Tone Injection (TI) OFDM transceiver.

If

$$X_k = A = \frac{d_k}{2} + j\frac{3d_k}{2} \quad (4.27)$$

and A is changed so that

$$\hat{A} = A + pD + jqD \quad (4.28)$$

where p and q are any integer values and D is a positive real number known at the receiver. This process effectively increases the size of the constellation, as well as the average power of the transmit symbol. Reference [30] indicated that careful selection \hat{A} can reduce the PAPR by over 5dB with only a 2% increases in the average power.

The possible expansions of the selected tone for a 16QAM constellation are shown in Figure 4.16. The new transmitted signal can be given as (4.29)

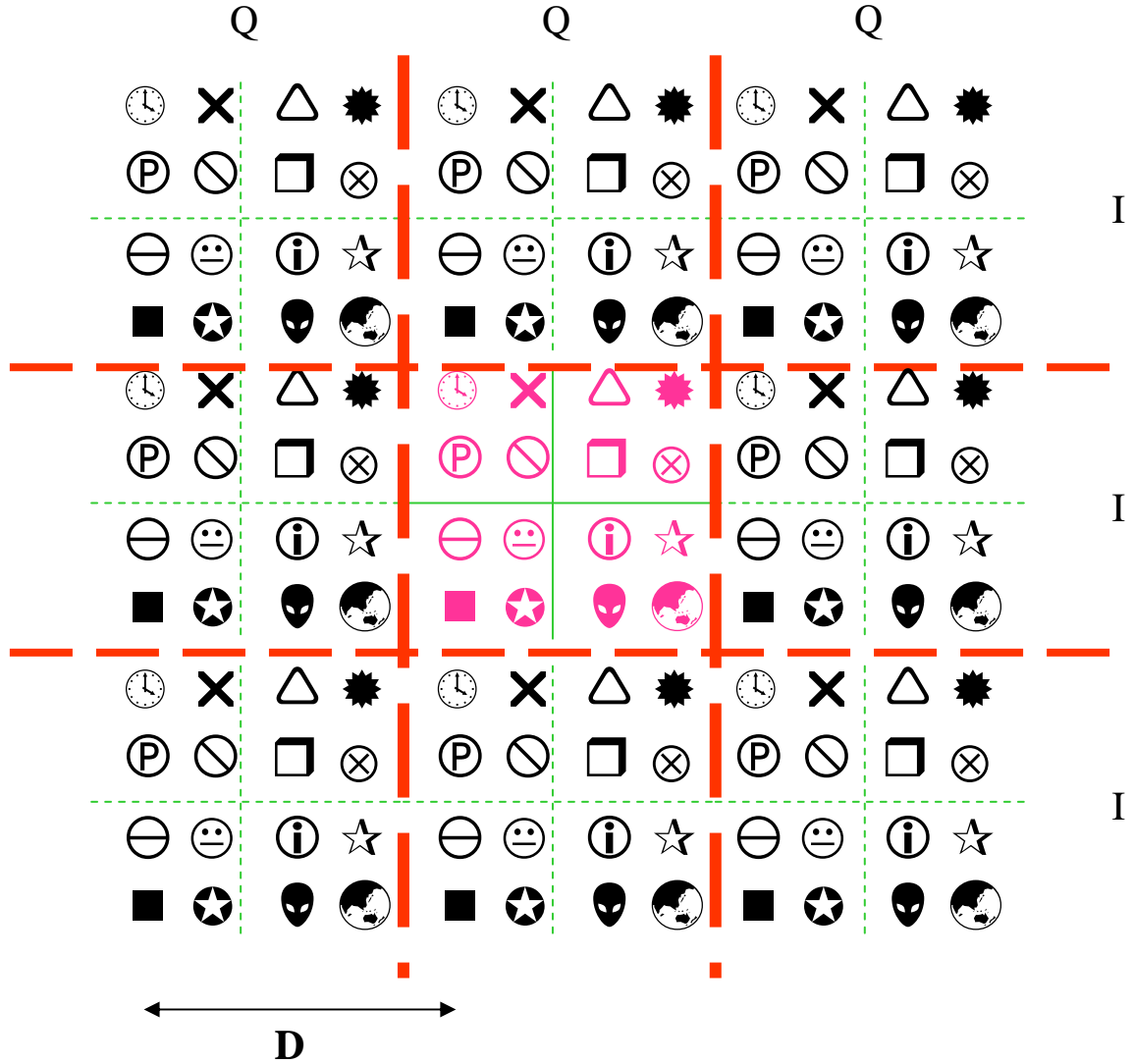


Figure 4.16: Example of possible expansions of constellation in TI for 16 QAM.

$$\hat{x}_n = \frac{1}{\sqrt{N}} \sum_{k=0}^{N-1} (X_k + p_k D_k + j q_k D_k) e^{j2\pi k n / N} \quad (4.29)$$

The maximum peak reduction per tone shift is (4.30)

$$\delta = \sqrt{\frac{6M_{k_0}^2}{M_{k_0}^2 - 1} \frac{2\rho}{\sqrt{N}}} \quad (4.30)$$

where $\sqrt{M_k}$ is the number of levels per dimension. The maximum peak reduction factor (assuming normalized data) is $K\delta$, where K is the number of real/imaginary dimensions. The peak reduction factor δ decreases as N increases, so to keep the peak reduction factor constant K must be increased.

There is no redundancy in TI as the receiver uses a modulo D operation to decode information, thereby separating the original constellation point from the expanded one. The complexity in TI comes from finding values of p_k and q_k which produce low PAPR which in turn require (as in TR) the solving of an integer programming problem, which has exponential complexity.

Assuming L duplicate points per constellation, if K dimensions are to be modified, the algorithm must search over $(NL)^K$ combinations for vectors p_k and q_k , where L is the oversampling factor. Low complexity iterative algorithms are used to find approximations close to the optimum solution.

The algorithm starts with the original multicarrier symbol ($p_k=0, q_k=0$). After the maximum sample, n_0 , is located, the tone, k_0 , is found (4.29) is updated. If more than 1 value of \hat{x}_n is large, a new value for k_0 that reduces as many peaks of possible is found. This procedure can be repeated several times until the desired PAPR is met or the maximum of iterations is reached. Each iteration decreases the PAPR by around 1 dB up to a max of 6dB of reduction.

4.4 Conclusion

This chapter introduced distortionless techniques for PAPR reduction in OFDM. Distortionless techniques have the advantage of not corrupting the data thereby maintaining a low BER but come at the cost of increased complexity and bandwidth.

Coding techniques for PAPR reduction were first discussed in Section 4.1 where redundant bits are added to the bit stream before the IFFT. Properly chosen, these codewords ensure that the PAPR after the IFFT is kept low. These codes can be

combined with existing COFDM to reduce the redundancy and complexity inherent in coding. A disadvantage of coding is that the complexity becomes prohibitively high with an increase in the number of subcarriers (>32). Various codewords were presented such as cyclic codes, Shapiro-Rudin Sequences, Golay Complementary codes, and Reed-Muller codes. Golay codes and their subset, second order Reed Muller codes were found to have excellent PAPR properties restricting the PAPR to 3dB. This reduction could be traded off with reductions in complexity and the code length. Still complexity remains a restrictive issue in coding.

Section 5.2 introduced MSR methods, where a set of alternative transmit signals are seeded from the same data source. Various techniques are used to encode the alternative sets of transmit signals, which are constructed in such a way so that they will have different PAPR properties. The transmit signal with the lowest PAPR is chosen for transmission.

The effect of MSR OFDM is to shift the CCDF curve from the right to left, i.e. reduce the amplitude peaks in a uniform manner to lower PAPR's. Both PTS and SLM require side information to be sent with the chosen transmit signal. This information must be protected as loss of the side information means loss of the whole transmit symbol. The redundancy required for PTS is $(V-1)\log_2 W$ while SLM requires $\log_2 U$ bits per OFDM symbol. Variations of SLM and PTS have also been presented which alleviate the need for explicit side information. Increasing the number of alternative transmit symbols reduces the PAPR but also increases the complexity, reductions in the PAPR also become less pronounced with larger numbers of alternative transmit symbols. The number of alternative transmit symbols that can be produced for 1 OFDM symbol is W^{V-1} for PTS and U for SLM.

An advantage of MSR over coding techniques is that the reductions are independent of the constellation type, and only marginally affected by the number of subcarriers. However unlike coding no specific level of PAPR can be guaranteed with MSR methods, only a shift to lower PAPR as shown in the CCDF curves.

The effect of oversampling PTS is examined in the next chapter where filtering is shown to degrade the gains made with PTS by 'regrowing' peaks. Oversampling at

the IFFT is required to maintain the reductions gained. SLM is much more robust to filtering due to the greater independence of the alternative transmit symbols. Generally SLM outperforms PTS in terms of reduction versus redundancy, but PTS is much better in terms of PAPR reduction versus additional system complexity.

Section 4.3 described TR and TI for PAPR reduction, both methods prevent distortion by reducing the PAPR before the HPA. In TR the additional complexity is only in the transmitter. Suboptimal solutions to the PAPR minimization problem were presented which successfully reduced the complexity without sacrificing the amount of PAPR reduction to a great degree.

In TI a similar method to TR is presented where most of the complexity is in the transmitter with some additional complexity in the receiver which is a simple modulo operation of the demodulated complex vectors. Again suboptimal solutions were proposed with similar performance to the optimal case.

Chapter 5

Cyclic Shifted Sequences and Time Inversion of PTS

This chapter introduces new techniques to produce alternative transmit signals in PTS. Section 5.1 reviews standard PTS subblock creation methods. Two new techniques for subblock creation in PTS are described in section 5.2. Section 5.2.1 describes Cyclic Shifted Sequences (CSS) where shifts in the data are used in place of phase rotations. Section 5.2.2 looks at a combination of traditional PTS using phase rotations and CSS to produce alternative transmit signals. Section 5.2.3 describes Time Inversion (TI) where the data sequence is reversed to provide an alternative transmit signal. Section 5.3 analyses the effect of filtering on traditional phase rotated PTS as well as CSS and TI. Section 5.4 provides results for the aforementioned techniques when oversampling of the IFFT is done before filtering. Section 5.5 compares the complexity of standard PTS and the new techniques and Section 5.6 closes the chapter with a conclusion.

5.1 PTS subblock creation

As was shown in section 4.2.1 PTS can provide promising reductions in the PAPR. However issues such as complexity and filtering after PTS limit the techniques usefulness. In traditional PTS alternative sub-blocks are created by increasing V , the number of IFFT's, and W , the number of allowable phase rotations. Increasing the

number of phase rotations provides increasingly less PAPR reduction for a set V . In addition the hardware operations are non trivial for $W > 4$. This limitation in PTS is the impetus for finding alternatives to phase rotations in order to create unique transmit sequences. Note that all simulations use adjacent block partitioning.

5.2 New techniques for PTS subblock creation

Of all the MSR techniques PTS suffers the most after filtering [39] as the alternative sequences are not necessarily independent of each other as in the case of SLM. The following sections propose new techniques to create alternative sequences for PTS and shows through simulation that the peak regrowth of the proposed techniques after filtering is not as severe as in traditional PTS. This advantage is combined with a reduction in complexity of the new algorithms.

Figure 5.1 shows a block diagram of the simulation model, note that the CCDF is measured after the nyquist sampled IFFT.

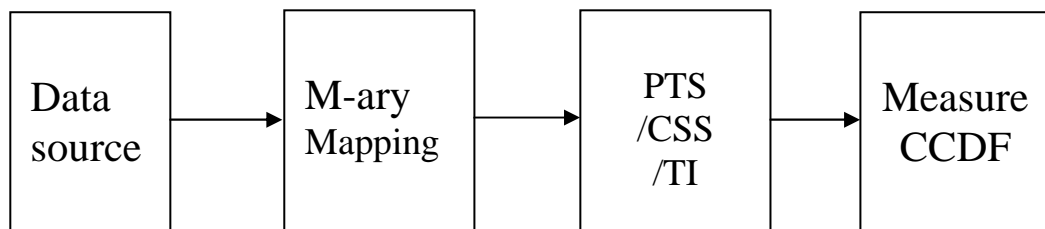


Figure 5.1: Block diagram showing the simulation model of Section 5.2.

5.2.1 Cyclic Shifted Sequences

As detailed in Section 4.2.1 PTS produces alternative signals by breaking up the transmit bit stream and phase rotating whole parts before performing the IFFT. These phase rotations can be kept trivial if W is restricted to 4 or less. In other words for phase rotations of 90, 180, and 270 degrees only the sign of the I or Q value needs to be changed, making them trivial hardware operations. If the number of phase

rotations, W , is greater than four, then the rotation becomes non trivial as the I and Q values have to be manipulated requiring a more complex circuit. CSS does not suffer from this limitation, the number of positions that can be shifted to provide alternative transmit signals can be up to $N/2$ (before identical signals are produced) where N is the number of subcarriers.

Figure 5.2 shows a block diagram of a PTS system depicting PTS, CSS, and TI which is introduced in the next section. The system represents a PTS/CSS/TI system with $V=2$ sub-blocks and $W/S=4$ rotations/shifts.

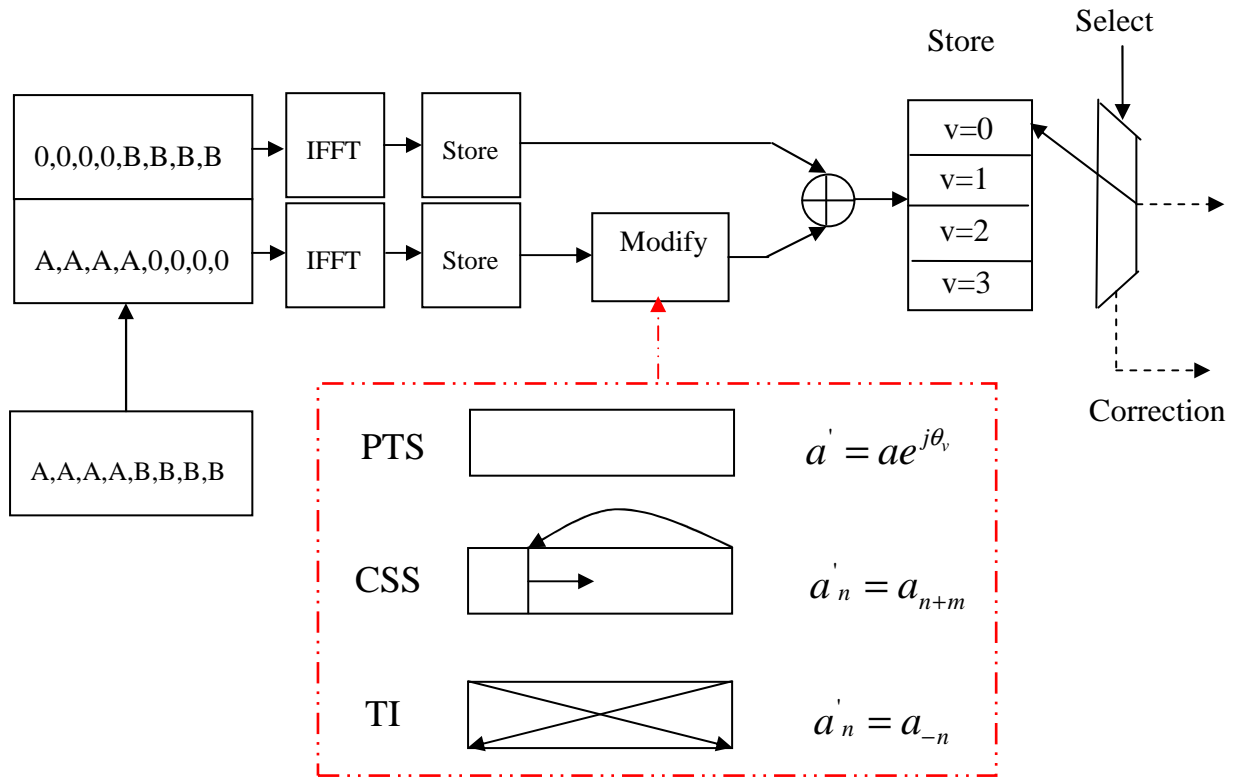
Figure 5.3 compares the CCDF of CSS to PTS where the phase shifts are replaced with cyclic shifts, they are equivalent in all other aspects. Unless otherwise stated all simulations use $N=64$ subcarriers with QPSK mapping. No oversampling is performed. Here we see that CSS outperforms PTS in all cases, also the complexity of CSS when $W>4$ is reduced. CSS: $V=2, S=8$ performs 0.4dB better at $\Pr(\zeta>\zeta_0)=10^{-4}$ than PTS: $V=2, W=8$. CSS: $V=4, S=4$ has a minor improvement of 0.2dB over PTS: $V=4, W=4$ at $\Pr(\zeta>\zeta_0)=10^{-4}$. CSS: $V=4, S=8$ has 0.6dB better performance than PTS: $V=4, S=8$ at $\Pr(\zeta>\zeta_0)=10^{-4}$. CSS has a PAPR reduction of 3dB, 4.5dB, and 5.5dB compared to the uncoded conventional case for CSS: $V=2, S=8$; $V=4, S=4$; and $V=4, S=8$ respectively at $\Pr(\zeta>\zeta_0)=10^{-4}$.

Mathematically CSS can be expressed as (5.1):

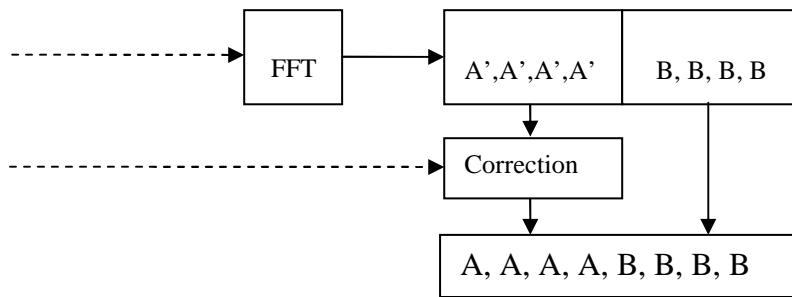
$$\tilde{a}_n = \sum_{v=1}^V \tilde{a}_{n+\delta^{(v)}} \quad (5.1)$$

Where $\delta^{(v)}$ is a cyclic shift in the time domain.

It seems that with CSS not only is complexity reduced but the independence of the generated alternative signals is greater thereby giving better PAPR reduction. The performance of CSS at lower probability regions should be increasingly better than PTS due to the steeper slope of the curve, especially for $V=4, S=8$.



a) Transmitter



b) Receiver

Figure 5.2: Block diagram of PTS, CSS and TI transceiver.

For a CSS structured OFDM transmitter with $V=2$ and 64 subcarriers, 32 alternative transmit signals can be created. In a PTS transmitter, with $V=3$ and $W=4$ only 16 alternative transmit signals with trivial phase rotations can be produced. Increasing the number of subcarriers in CSS allows for more alternative transmit signals to be produced with trivial operations. The effect of double shifts has also been analysed

where it was found that large shifts produce better results. This comes at the cost of reducing the possible number of transmit signals that can be constructed.

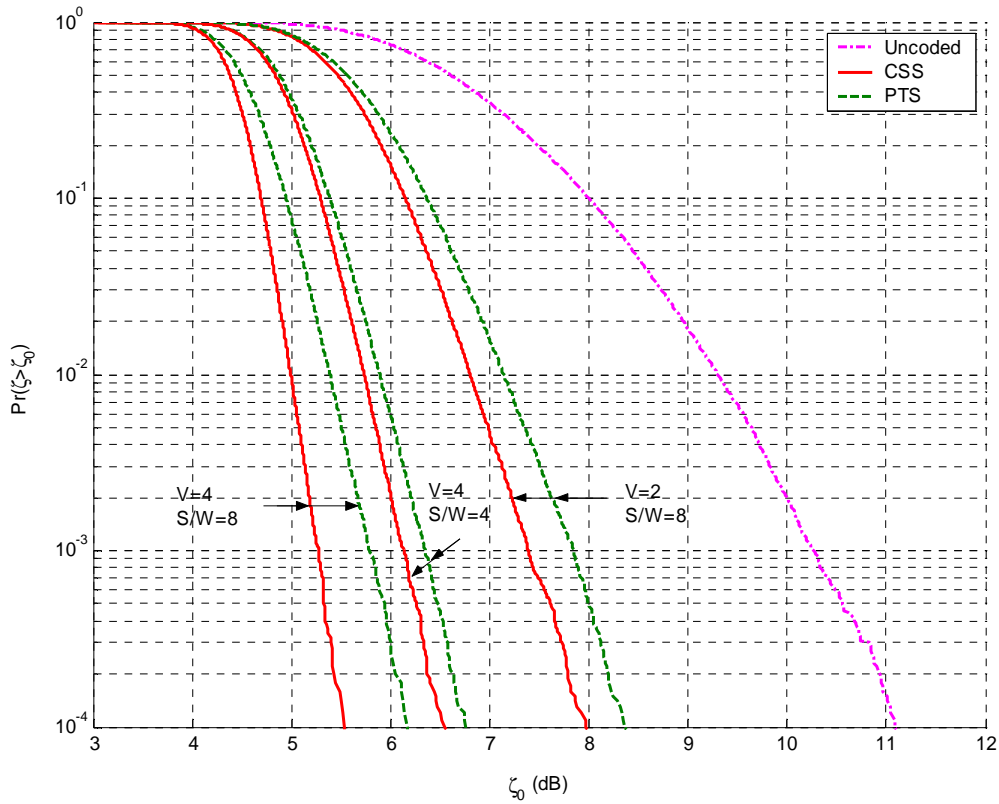


Figure 5.3: Simulated CCDF for PTS ($V=2, W=8$; $V=4, W=4$; $V=4, W=8$), CSS ($V=2, S=8$; $V=4, S=4$; $V=4, S=8$) and uncoded OFDM. $N=64$, adjacent partitioning, with no oversampling in IFFT, ($os=1$).

5.2.2 PTS with CSS

Another variation of CSS combining the trivial phase rotations ($W=4$) in standard PTS with CSS shifts to create more alternative transmit sequences was first presented in [1].

The PTS signal can be expressed as (5.2)

$$\tilde{\mathbf{a}}_n = \sum_{v=1}^V \tilde{\mathbf{a}}_n^{(v)} \cdot e^{j\phi^{(v)}} \quad (5.2)$$

Adding cyclic shifts to PTS gives (5.3)

$$\tilde{\mathbf{a}}_n = \sum_{v=1}^V \tilde{\mathbf{a}}_{n+\delta^{(v)}} \cdot e^{j\phi^{(v)}} \quad (5.3)$$

Where $\delta^{(v)}$ is a cyclic shift in the time domain. The number of alternative transmit signals is now WS , where S is the number of cyclic shifting options. Cyclic shifting generates a linear phase shift at the output of the FFT in the receiver. This linear phase component must be removed prior to demodulation and requires one complex multiplication for each data symbol. This process can be made trivial if the linear phase shift is constrained to $\frac{g\pi}{2}$ radians per frequency bin ($g=0,1,2,\text{or }3$). This corresponds to a signal shift of $\delta^{(v)} = \frac{N \cdot g}{4}$ samples ($g=0,1,2,\text{ or }3$). Therefore for each of the W different phase rotations, $S=4$ additional signals can be produced by cyclic shifting with trivial operations in the transmitter and receiver.

Figure 5.4 shows CCDF plots comparing standard PTS to PTS/CSS. There is a negligible performance difference in the two methods. The advantage here is that for 8 alternative transmit sequences (PTS: $V=2, W=8$; PTS/CSS: $V=2, W=4, S=2$) 4 complex multiplications per sample are avoided in the transmitter. For 16 alternative transmit sequences (PTS: $V=3, W=4$; PTS/CSS: $V=2, W=4, S=4$) a whole IFFT can be avoided, reducing complexity significantly. The reduction in PAPR from the uncoded case is $\sim 2.5\text{dB}$ and $\sim 3.5\text{dB}$ for (PTS: $V=2, W=8$; PTS/CSS: $V=2, W=4, S=2$) and (PTS: $V=3, W=4$; PTS/CSS: $V=2, W=4, S=4$) respectively at $\Pr(\zeta > \zeta_0) = 10^{-4}$.

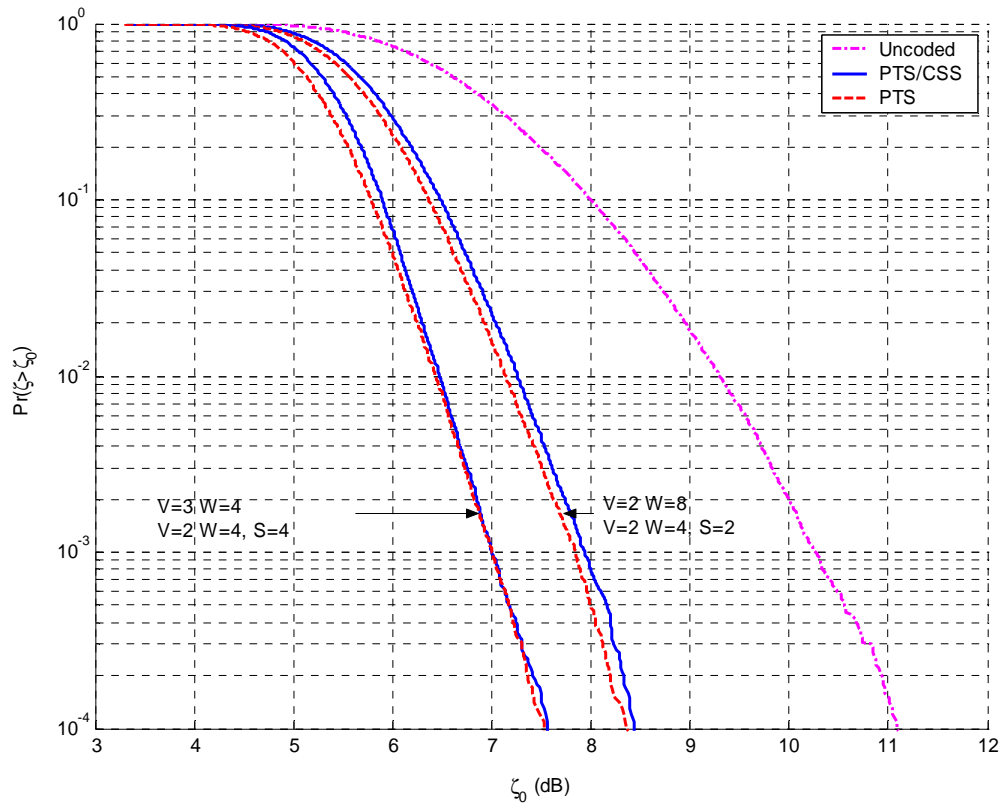


Figure 5.4: Simulated CCDF for PTS ($V=2$, $W=8$; $V=3$, $W=4$), PTS/CSS ($V=2$, $W=4$, $S=2$; $V=2$, $W=4$, $S=4$), and uncoded OFDM. $N=64$, adjacent partitioning, with no oversampling in IFFT, ($os=1$).

5.2.3 Time Inversion

Another new proposed PAPR technique based on a variation of PTS first presented in [2] is Time Inversion (TI), a block diagram description of which is shown in Figure 5.2. TI involves reversing the output sequence of the IFFT sub block before addition and transmission of the sub blocks. Mathematically TI can be expressed as (5.4)

$$\tilde{a}_n = \sum_{v=1}^V \text{conj}^{i^{(v)}} \left(a_{(-1)^{i^{(v)}}(n+\delta^{(v)})}^{(v)} \cdot e^{-j\phi^{(v)}} \right) \quad (5.4)$$

where i takes the value 0 or 1 for a time inversion of the V^{th} sub block in the time domain. TI of a sub-block must be accompanied by conjugation of its elements to stop the information from jumping into image sub-channels after the demodulation process. The effect that this has on the demodulated sub-channels can be reversed by

taking the conjugate of the output after the FFT process in the receiver circuit. No extra multiply operations are required in the transmitter or receiver.

Simulation results for PTS with TI are shown in Figure 5.5 where it is seen that TI has slightly worse performance than PTS with an equivalent number of alternative transmit sequences. TI has $\sim 0.5\text{dB}$ degradation compared to PTS at $\Pr(\zeta > \zeta_0) = 10^{-4}$. TI reduces the PAPR by $\sim 2.2\text{dB}$ over the uncoded case while PTS has a reduction of $\sim 2.7\text{dB}$ at $\Pr(\zeta > \zeta_0) = 10^{-4}$.

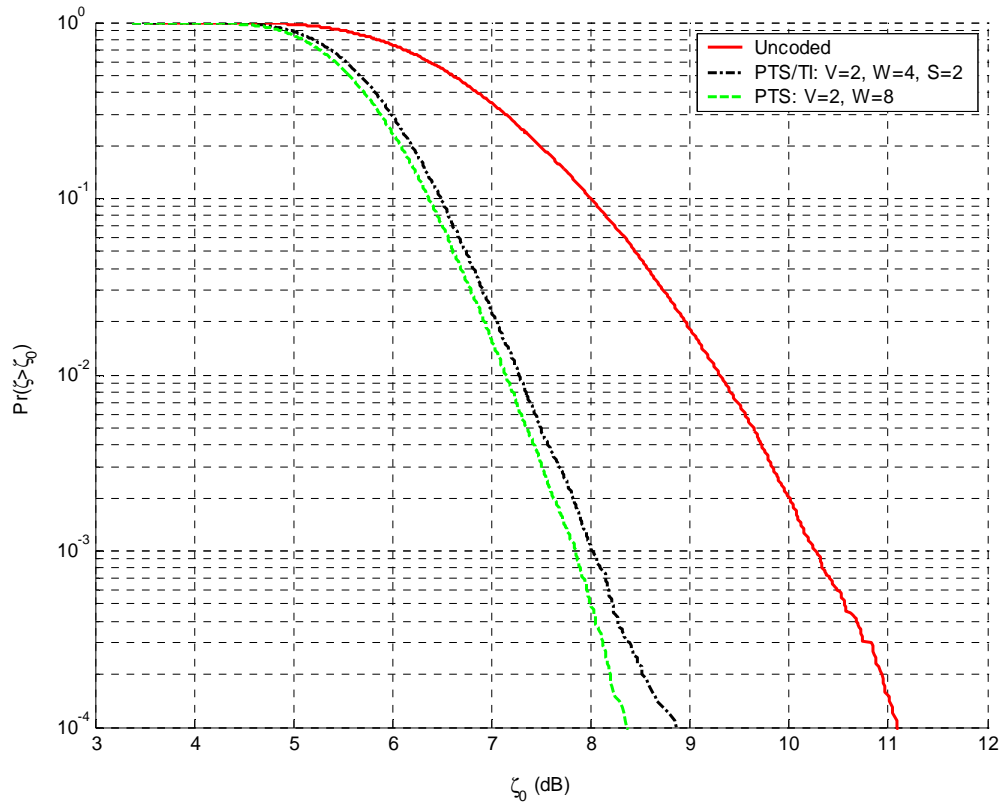


Figure 5.5: Simulated CCDF for PTS ($V=2$, $W=8$), PTS/TI ($V=2$, $W=4$, $S=2$) and uncoded OFDM. $N=64$, adjacent partitioning, with no oversampling in the IFFT, ($os=1$).

5.3 Filtering new techniques

As noted in [34, 39] the reductions made with PTS are drastically reduced when passed through a pulse shaping filter due to peak regrowth. Furthermore as shown in Figure 3.10 peak regrowth after some form of PAPR reduction is more severe than when no PAPR reduction is performed. Certain PAPR reduction schemes such as

PTS and clipping display greater peak regrowth after interpolation and filtering than coding and SLM (Figure 4.11). This section analyses the effect of interpolation and pulse shaping filtering on CSS and TI, comparing them to standard PTS through simulation.

Simulations performed in this section use $N=64$ subcarriers with no oversampling in the IFFT (i.e. $os=1$) and adjacent partitioning. As shown in reference [39] the partitioning type has a minimal effect on the peak regrowth after filtering. A RCF is used with a rolloff factor of 0.15 and 128 filter taps with a normalized sampling rate. The data is interpolated by a factor of 8 before filtering. The simulation model is represented in Figure 5.6.

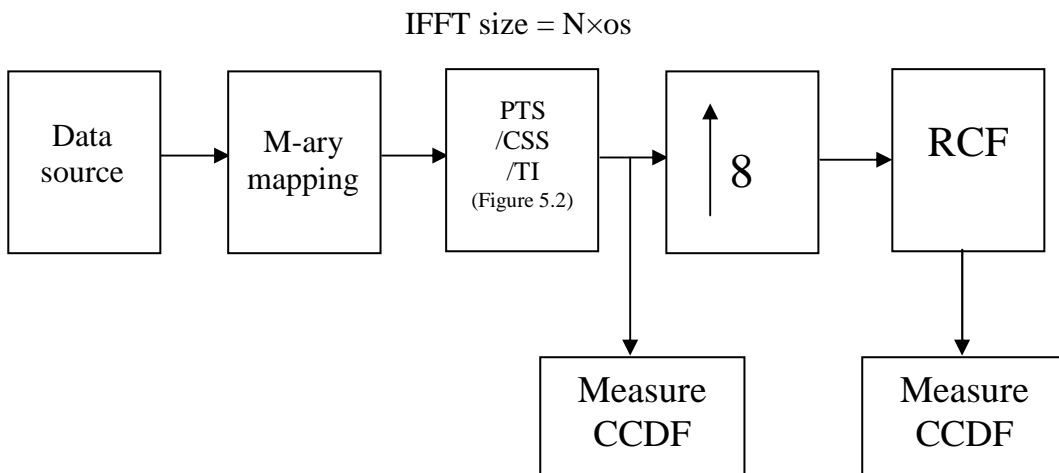


Figure 5.6: Block diagram showing the simulation model of Section 5.2.

In Figure 5.7 the discrete CCDF after the IFFT is plotted with the CCDF after filtering for PTS and CSS. Both PTS and CSS have 16 alternative transmit symbols. CSS has a peak regrowth of ~ 3.5 dB from the discrete level and PTS has a peak regrowth of ~ 4 dB at $\Pr(\zeta > \zeta_0) = 10^{-4}$. This is contrasted with only 1dB of peak regrowth in the uncoded case at $\Pr(\zeta > \zeta_0) = 10^{-4}$. So the PAPR reduction after filtering is only ~ 1.5 dB and ~ 2 dB for PTS and CSS respectively at $\Pr(\zeta > \zeta_0) = 10^{-4}$. It is also worth noting that CSS has a steeper rolloff than PTS leading to the increasingly better performance than PTS at low probability levels.

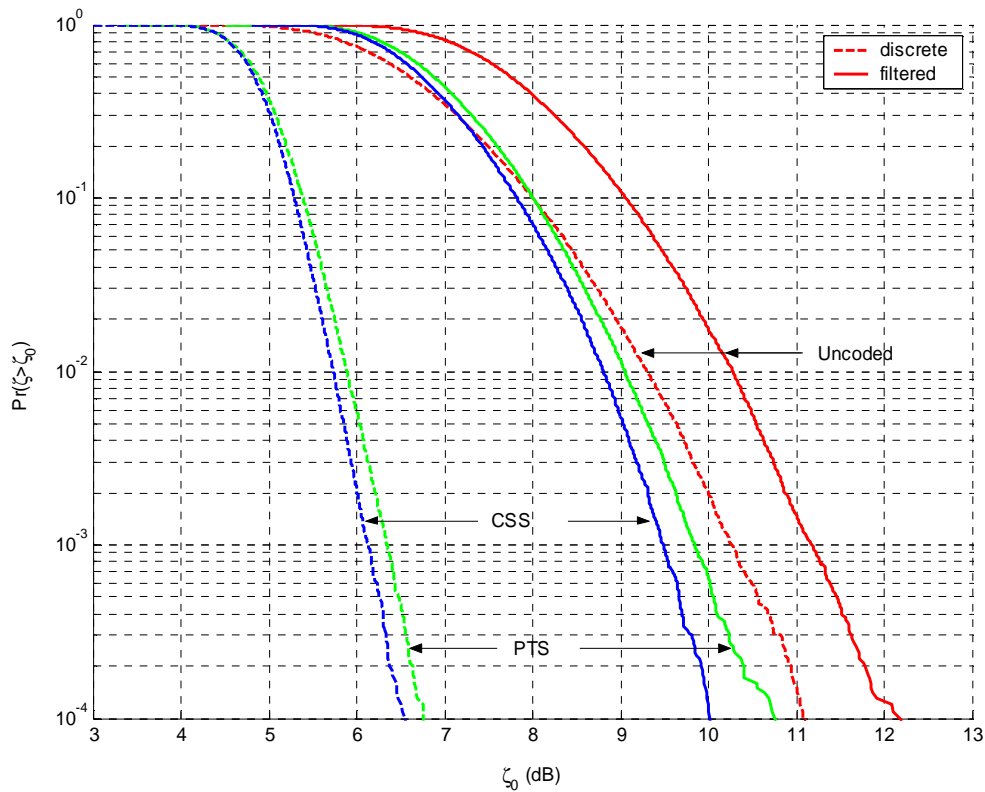


Figure 5.7: Simulated CCDF of discrete and filtered PTS ($V=4$, $W=4$), CSS ($V=4$, $S=4$), and uncoded OFDM. $N=64$, adjacent partitioning, with no oversampling in IFFT ($os=1$), interpolated by 8, filtered with RCF ($\alpha=0.15$).

Figure 5.8 maintains the same number of IFFT's ($V=4$) as Figure 5.7 while increasing the number of phase rotations/shifts from 4 to 8. The peak regrowth of CSS above the discrete level after filtering is 4.3dB while PTS peak regrowth is 4.1dB at $\Pr(\zeta > \zeta_0)=10^{-4}$. The peak power reduction after filtering is only ~ 1.7 dB and ~ 2.2 dB for PTS and CSS. Comparing these results with Figure 5.7 it is seen that increasing the number of phase rotations/shifts to 8 provides only a further 0.2dB PAPR reduction for both PTS and CSS after filtering.

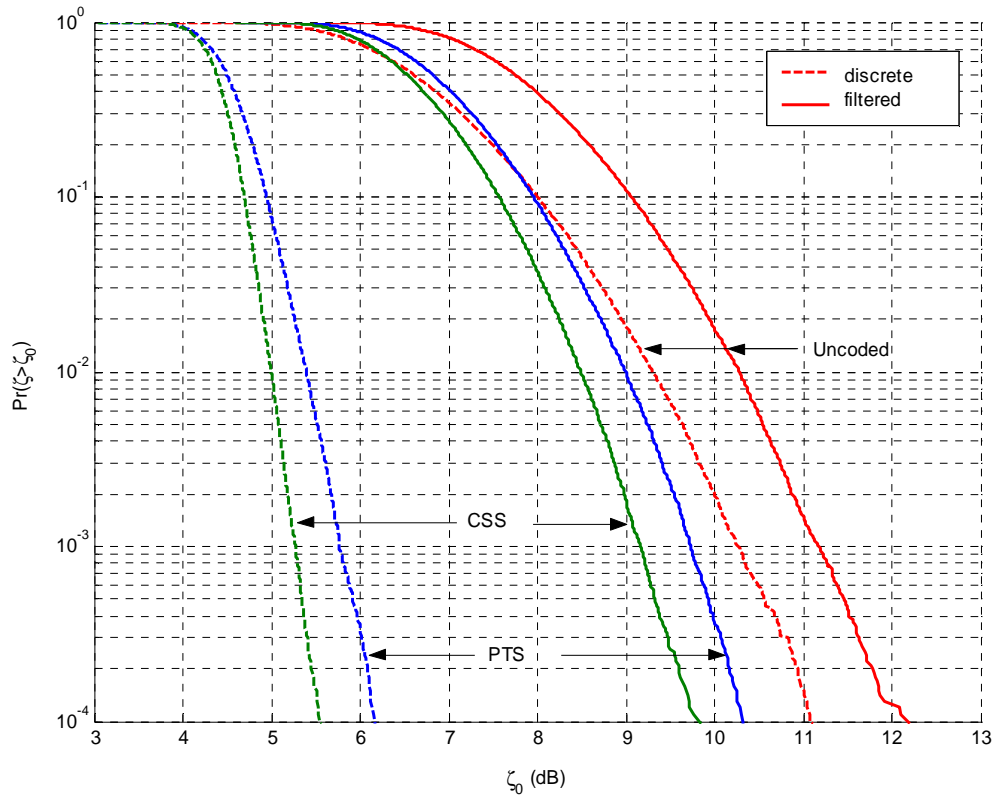


Figure 5.8: Simulated CCDF of discrete and filtered PTS ($V=4$, $W=8$), CSS ($V=4$, $S=8$), and uncoded OFDM. $N=64$, adjacent partitioning, with no oversampling in IFFT ($os=1$), interpolated by 8, filtered with RCF ($\alpha=0.15$).

Figure 5.9 compares combined PTS/CSS and PTS/TI with standard PTS, with 8 alternative transmit signals. Both PTS/CSS and PTS/TI have very similar performance after filtering with a peak regrowth of ~ 2.5 dB and 2.1dB respectively from the discrete level, while standard PTS is ~ 0.4 dB worse with a peak regrowth of ~ 3 dB at $\Pr(\zeta > \zeta_0) = 10^{-4}$. Note that again the slope at $\Pr(\zeta > \zeta_0) = 10^{-4}$ is slightly steeper for the new techniques after filtering implying further PAPR improvement over PTS at lower probability levels. The PAPR reduction after filtering is very poor in all cases, only ~ 1 dB for the new techniques and 0.6dB for standard PTS at $\Pr(\zeta > \zeta_0) = 10^{-4}$.

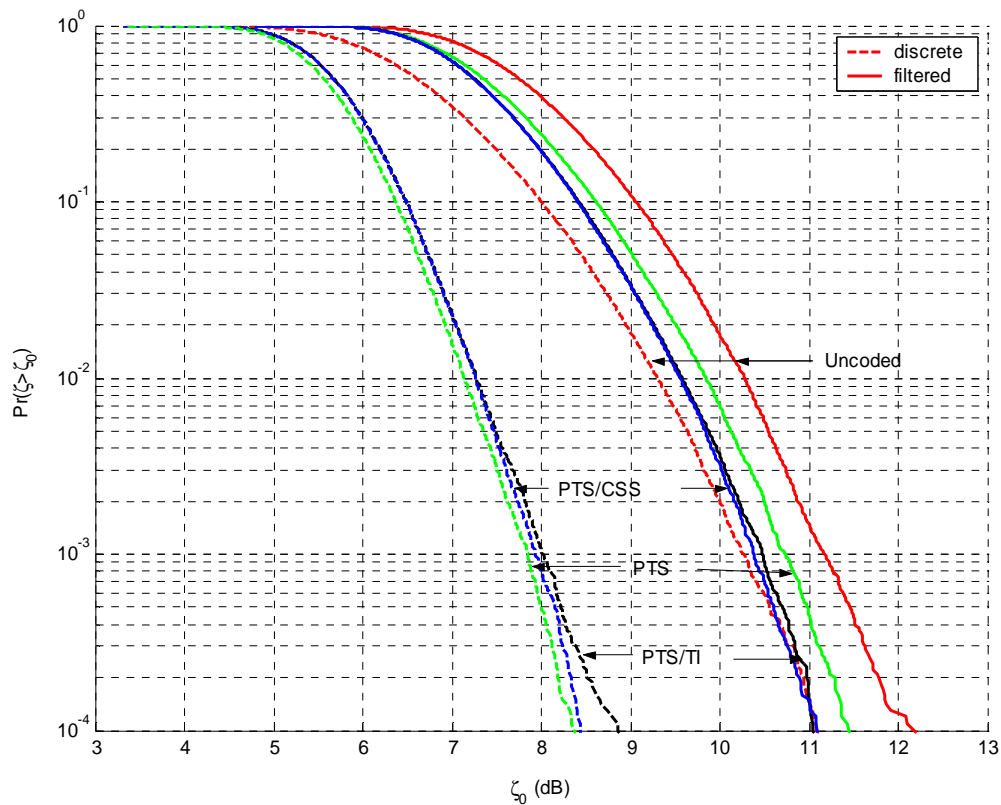


Figure 5.9: Simulated CCDF of discrete and filtered PTS ($V=2$, $W=8$), PTS/CSS ($V=2$, $W=4$, $S=2$), and PTS/II ($V=2$, $W=4$, $S=2$), and uncoded OFDM. $N=64$, adjacent partitioning, with no oversampling in IFFT ($os=1$), interpolated by 8, filtered with RCF ($\alpha=0.15$).

In Figure 5.10 the CCDF of PTS and PTS/CSS is compared, where 16 alternative transmit sequences produced. The peak regrowth is $\sim 2.8\text{dB}$ and $\sim 3.1\text{dB}$ above the discrete level for PTS and PTS/CSS respectively at $\Pr(\zeta > \zeta_0) = 10^{-4}$. Again the PAPR reduction after filtering is heavily penalized with only $\sim 1.8\text{dB}$ and $\sim 1.5\text{dB}$ gained in PAPR reduction at $\Pr(\zeta > \zeta_0) = 10^{-4}$ for PTS and PTS/CSS respectively. As stated earlier the advantage of PTS/CSS in this case is the removal of 1 IFFT operation per transmit symbol.

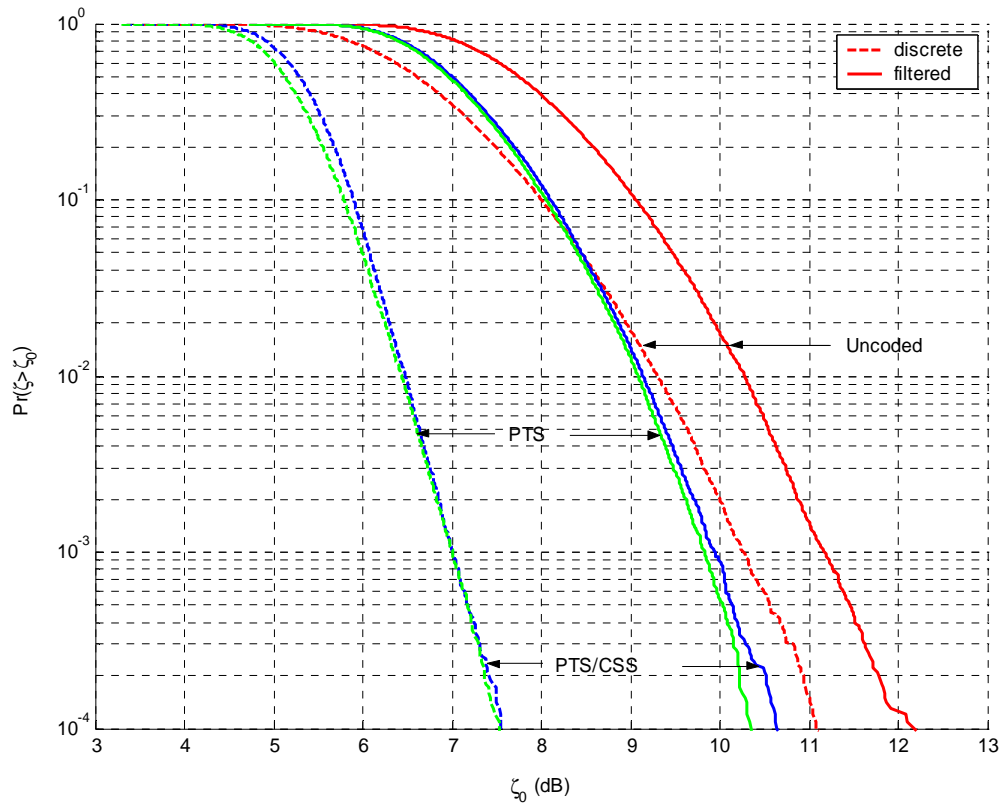


Figure 5.10: Simulated CCDF of discrete and filtered PTS ($V=3$, $W=4$), PTS/CSS ($V=2$, $W=4$, $S=4$), and uncoded OFDM. $N=64$, adjacent partitioning, with no oversampling in the IFFT ($os=1$), interpolated by 8, filtered with RCF ($\alpha=0.15$).

5.4 Oversampling new techniques

Oversampling [39] is required to improve the performance of PTS techniques. Oversampling the IFFT increases the convergence between the discrete PAPR and the filtered PAPR. Oversampling increases the PAPR in the discrete domain, while reducing the PAPR after filtering. The simulation model here is the same as Figure 5.6 except that oversampling is performed at the IFFT before filtering, i.e. $os=1, 2, 4$, or 8. Again $N=64$ subcarriers, and adjacent partitioning is used. The data is interpolated by 8 before filtering with a RCF with 128 taps and a rolloff factor of 0.15.

Figure 5.11 and 5.12 shows PTS/CSS ($V=2$, $W=4$, $S=4$) and PTS ($V=3$, $W=4$) under oversampled and filtered conditions respectively, with 16 alternative transmit signals. It is seen that oversampling by 2 brings the discrete and filtered CCDF curves to

within 1dB of each other at $\Pr(\zeta > \zeta_0) = 10^{-4}$. Furthermore oversampling by a factor of 8 brings them almost to convergence with PTS/CSS slightly closer (~ 0.1 dB) than PTS (~ 0.3 dB) at $\Pr(\zeta > \zeta_0) = 10^{-4}$. The PAPR reduction for PTS/CSS and PTS after filtering is 3.3dB and 3dB respectively at $\Pr(\zeta > \zeta_0) = 10^{-4}$. As oversampling the IFFT by a factor of 8 provides minimal improvement over 4, all further simulations will use oversampling rates of $os=1, 2,$ and 4 .

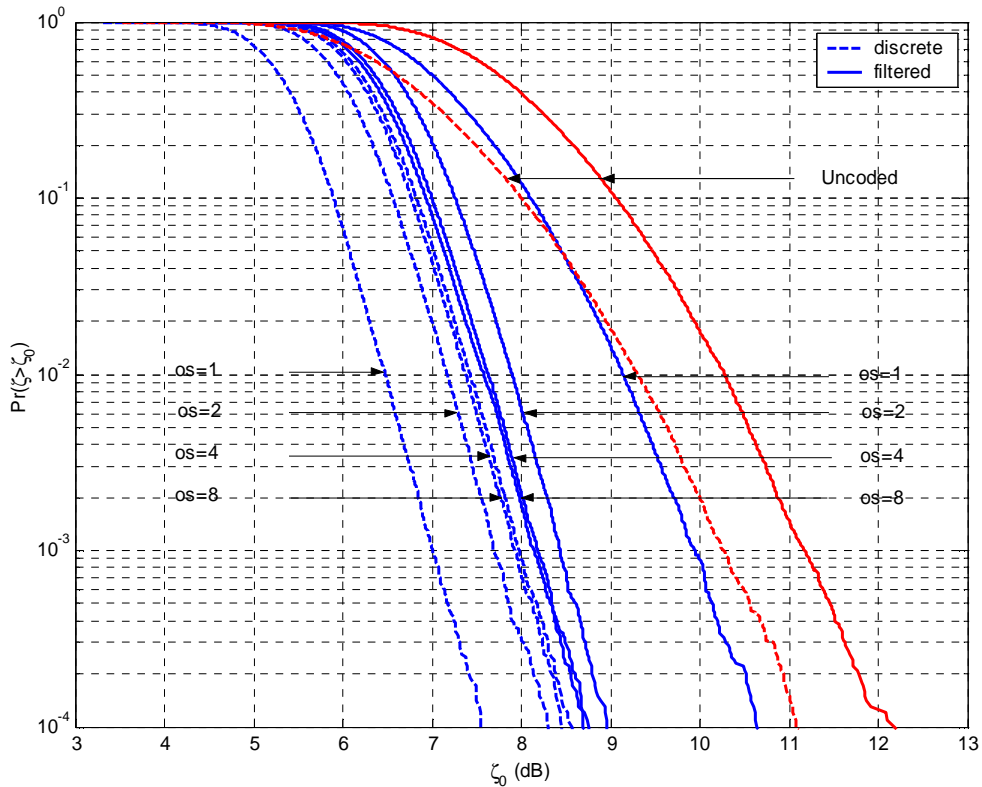


Figure 5.11: Simulated CCDF for PTS/CSS ($V=2, W=4, S=4$), and Uncoded OFDM. Discrete oversampled curves (dashed) move from left to right and oversampled (solid) filtered curves move from right to left. $N=64$, adjacent partitioning, with oversampling rates in the IFFT of 1, 2, 4, and 8, interpolated by 8, and filtered with RCF ($\alpha=0.15$).

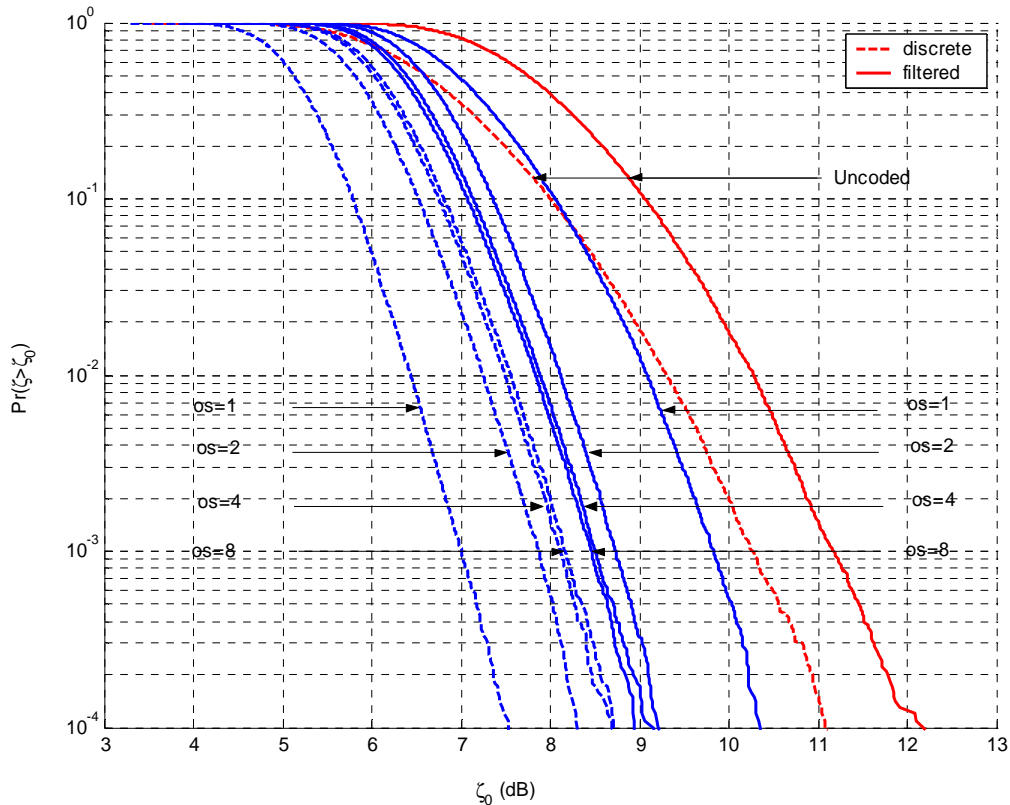


Figure 5.12: Simulated CCDF for PTS ($V=3$, $W=4$), and Uncoded OFDM. Discrete oversampled (dashed) curves move from left to right and oversampled (solid) filtered curves move from right to left. $N=64$, adjacent partitioning, with oversampling rates in the IFFT of 1, 2, 4, and 8, interpolated by 8, and filtered with RCF ($\alpha=0.15$).

Figures 5.13, 5.14, and 5.15 compare PTS ($V=2$, $W=8$), PTS/CSS ($V=2$, $W=4$, $S=2$), and PTS/TI ($V=2$, $W=4$, $S=2$) under oversampled and filtered conditions respectively, with 8 alternative transmit signals. Oversampling by a factor of 2 brings the discrete and filtered CCDF curves to within 0.8dB of each other at $\Pr(\zeta > \zeta_0) = 10^{-4}$. Oversampling by a factor of 4 brings them almost to convergence (0.2dB). PTS/CSS and PTS/TI have slightly better performance at any given oversampling rate. For example, with an oversampling factor of 2 PTS has a PAPR of 10.2dB at $\Pr(\zeta > \zeta_0) = 10^{-4}$, while PTS/CSS and PTS/TI has a PAPR of 9.9dB and 10dB respectively at $\Pr(\zeta > \zeta_0) = 10^{-4}$. The PAPR reduction for PTS, PTS/CSS, and PTS/TI after filtering ($os=4$) is 2.2dB, 2.5dB, and 2.3dB respectively at $\Pr(\zeta > \zeta_0) = 10^{-4}$.

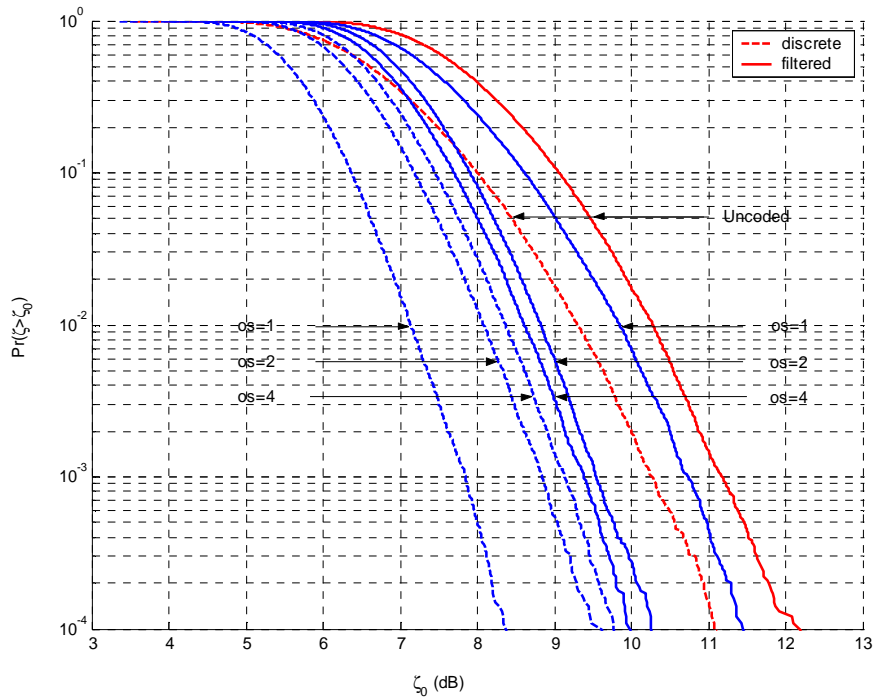


Figure 5.13: Simulated CCDF for PTS ($V=2$, $W=8$), and Uncoded OFDM. Discrete oversampled curves (dashed) move from left to right and filtered (solid) oversampled curves move from right to left. $N=64$, adjacent partitioning, with oversampling rates in the IFFT of 1, 2, and 4, interpolated by 8, and filtered with RCF ($\alpha=0.15$).

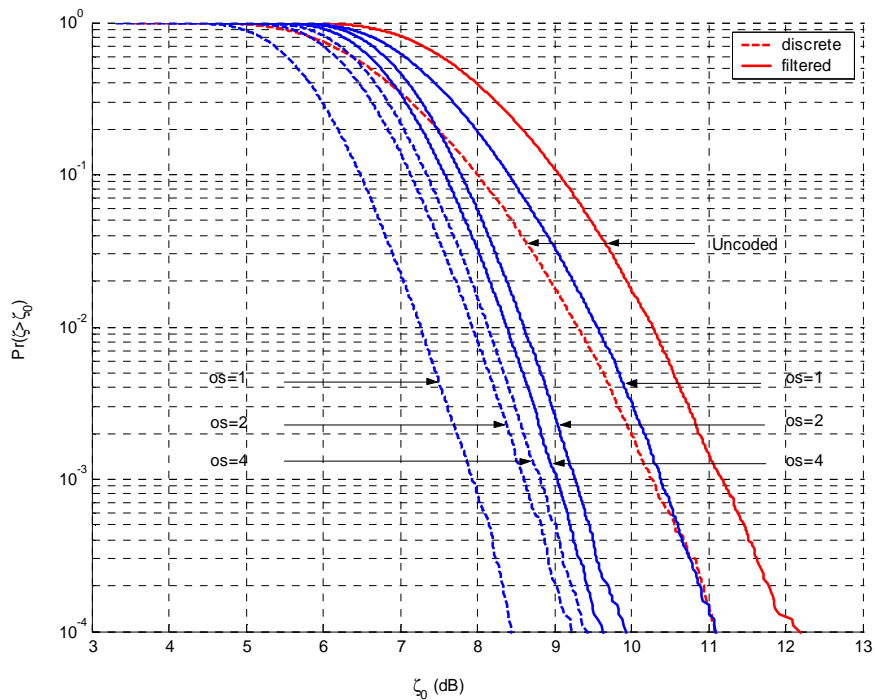


Figure 5.14: Simulated CCDF for PTS/CSS ($V=2$, $W=4$, $S=2$), and Uncoded OFDM. Discrete oversampled curves (dashed) move from left to right and filtered (solid) oversampled curves move from right to left. $N=64$, adjacent partitioning, with oversampling rates in the IFFT of 1, 2, and 4, interpolated by 8, and filtered with RCF ($\alpha=0.15$).

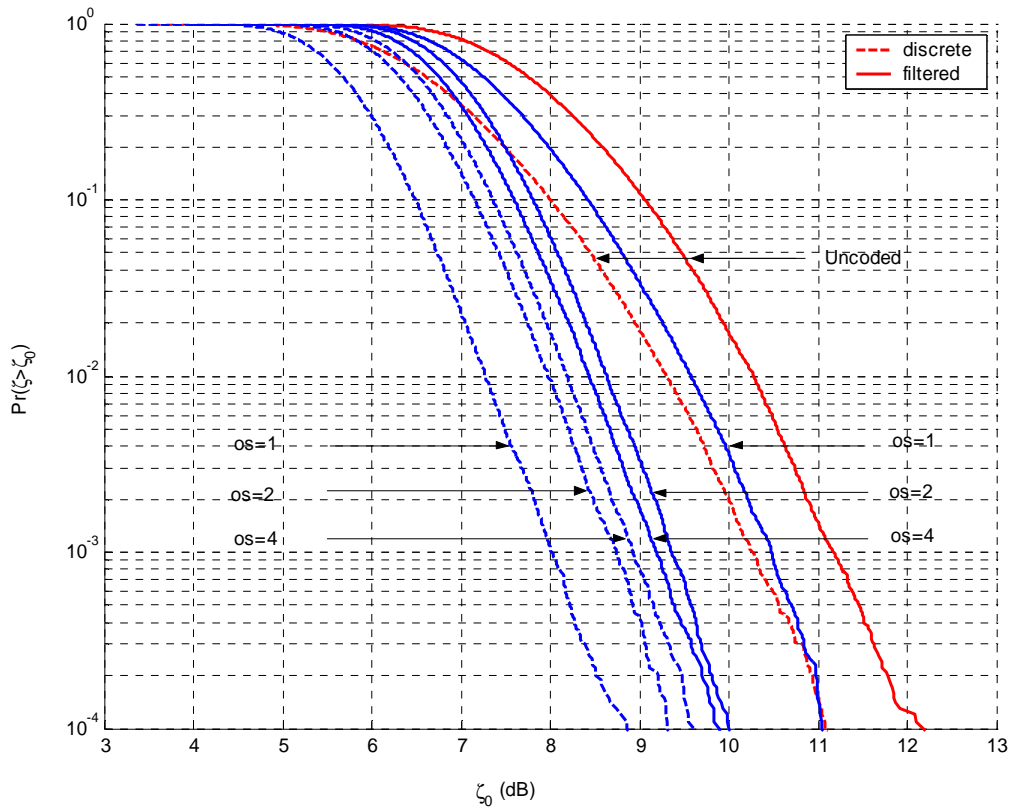


Figure 5.15: Simulated CCDF for PTS/TI ($V=2$, $W=4$, $S=2$), and Uncoded OFDM. Discrete oversampled curves (dashed) move from left to right and filtered (solid) oversampled curves move from right to left. $N=64$, adjacent partitioning, with oversampling rates in the IFFT of 1, 2, and 4, interpolated by 8, and filtered with RCF ($\alpha=0.15$).

5.5 Complexity evaluation

The performance in terms of the CCDF and PSD of CSS, PTS/CSS, and PTS/TI has been established. Table 5.1 compares them in terms of hardware operations where it is seen that multiplications are avoided when appropriate values of V , W , and S are chosen.

For example with a PTS system ($N=64$, $V=3$, $W=4$) 85 non complex multiplications, 170 squaring operations, and 178 compares are required. The equivalent PTS/CSS system ($N=64$, $V=2$, $W=4$, $S=2$) requires no multiplications in exchange for an increase in 512 squaring operations, and 528 comparisons as well as the removal of a whole IFFT operation. A PTS system ($N=64$, $V=2$, $W=8$) requires 256 multiplications, half of which

Table 5.1: Complexity comparison of various techniques (adjacent partitioning)

Type	Comments	Operations
PTS	<ul style="list-style-type: none"> - V blocks - W rotations 	<ul style="list-style-type: none"> - $(N/V)W$ multiplications (trivial if $W < 4$) - $(N/V)W(V-1)$ squaring - $(N/V+1)W(V-1)$ comparisons - $V^*(N/V)$ IFFT'S
PTS/CSS	<ul style="list-style-type: none"> - V blocks - W rotations - S shifts 	<ul style="list-style-type: none"> - $(N/V)WS(V-1)$ squaring - $(N/V+1)WS(V-1)$ comparisons - $V^*(N/V)$ IFFT'S
PTS/TI	<ul style="list-style-type: none"> - V blocks - W rotations - T(=2) inversion 	<ul style="list-style-type: none"> - $(N/V)TW(V-1)$ squaring - $(N/V+1)TW(V-1)$ comparisons - $V^*(N/V)$ IFFT'S

are complex, 256 squaring operations, and 264 comparisons. The equivalent PTS/CSS system ($V=2$, $W=4$, $S=2$) requires no multiplications, and has the same number of squaring and comparison operations as the PTS system.

5.6 Conclusion

This chapter introduced new techniques for the creation of PTS OFDM signals. In section 5.2 it was shown through simulation of the CCDF that CSS has better performance (up to 1dB) than PTS for the same number of alternative signals over various combinations of V and W . Combining PTS with CSS and TI was shown to provide similar performance to standard PTS but with the advantage of a reduction in complexity. PTS ($V=3$, $W=4$) was shown to have the same performance as PTS/CSS ($V=2$, $W=4$, $S=4$) but with the added advantage of the removal of one whole IFFT operation.

The performance after filtering was examined in Section 5.3 where it was shown that the gains made with PTS techniques are dramatically affected when passed through a pulse shaping filter. In the simulations a RCF with 128 taps and a roll off factor of 0.15 was used. The resultant reduction in PAPR after filtering was between 1 and 2dB for various combinations of V , W , and S with the new techniques having up to

0.7dB better PAPR for all combinations. The only exception is PTS/CSS ($V=2$, $W=4$, $S=4$) where the performance was slightly worse than PTS ($V=3$, $W=4$) for the same number of alternative signals. This small degradation is a trade off for removing 1 of the IFFT's.

The effect of oversampling on PTS and the new techniques was also examined, where it was seen that an oversampling factor of 2 was sufficient to bring the discrete PAPR to within 1dB of the filtered PAPR. The effect of oversampling was to increase the PAPR of the discrete CCDF while reducing the CCDF of the filtered CCDF. Oversampling by a factor of 8 (implying IFFT sizes of $N \times 8$) was necessary to bring both curves almost to convergence. However in a practical system an oversampling factor of 2 was shown to be sufficient bringing the discrete and filtered CCDF curves to within 1dB of each other.

The avoidance of multiplications and in some cases IFFT operations, as well as a modest performance gain combine to make the new techniques viable alternatives to standard PTS OFDM. Two publications resulted from this chapter.

Chapter 6

Peak to Average Power Solutions - Distorted Techniques

This chapter details another approach to PAPR reduction, distortion introducing techniques. These methods do not attempt to create a transmit signal with a low crest factor, instead they take the output of the IFFT and then limit the amplitude of large samples which invariably causes distortion. These methods include approaches such as pulse shaping (or windowing), and clipping at every stage from the output of the IFFT to limited backoffs in the amplifier.

The advantages of clipping are a reduction in complexity and ease of implementation, the disadvantages are the inband distortion (increasing BER) and spectral splatter, affecting adjacent channels by increasing out of band distortion.

Section 6.1 describes the most common form of clipping in the baseband and reviews papers which seek to quantify the effect of clipping on the BER and PSD under different OFDM system conditions. Section 6.1.1 looks at the relation between clipping and quantization. Section 6.2 looks at amplifier limiting where the unconstrained OFDM signal is allowed to saturate the amplifier introducing spectral regrowth. Section 6.3 analyses windowing and pulse shaping techniques.

6.1 Clipping in the Baseband

Reference [46] is an early paper looking at the effect of clipping and filtering on OFDM. The authors note that clipping causes both inband distortion, deteriorating the BER and out of band noise which reduces the spectral efficiency. Filtering after clipping was noted to reduce the spectral splatter but at the cost of peak regrowth.

The simulation model used $N=128$ subcarriers with a guard interval, T_g , of 32 samples. QPSK modulation was applied to the data samples before modulation with an IFFT. As direct clipping of the samples will cause all the noise to fall in band the OFDM symbol is oversampled by a factor of 8 before clipping. The complex baseband samples were modulated up to a carrier frequency 1/4 of the sampling frequency in order to reduce the complexity of the simulation model. The real valued bandpass samples, x , are then clipped at amplitude, A , according to (6.1)

$$y = \begin{cases} -A, & \text{if } x < -A \\ x, & \text{if } -A \leq x \leq A \\ A & \text{if } x > A \end{cases} \quad (6.1)$$

where the clipping level A is determined as $CL = A/\sigma$, where σ is the rms level of the OFDM signal. Filtering is performed with an equiripple bandpass Finite Impulse Response (FIR) filter with 103 taps, a stopband of 40dB, and 1dB ripple in the passband. PSD results for clipping ($CL=0.8$ to 1.6) with no filtering displayed both in band distortion and spectral splatter. For a $CL=1.4$ the out of band noise was only 16dB lower than the signal power. This demonstrated the need for filtering to suppress the sidelobes. When the filter was applied the sidelobes were suppressed to ~50dB below the signal power for the same CL .

Results also indicated that the peak regrowth after filtering was significant. For example, for a $CL=1.4$ (3dB) the clipped and filtered signal had a CF of ~9dB at the 99.999 percentile, i.e. 6dB of peak regrowth. The unclipped signal at the same percentile had a CF of 13dB. Finally the BER was examined after clipping and filtering in an AWGN channel. For reasonable clipping levels ($CL>1.4$) it was shown

that less than 1dB of degradation at the 10^{-2} BER level is encountered. However it should be noted as shown in Figure 3.17 that QPSK, unlike higher modulation types is inherently impervious to clipping.

Reference [87] presented a theoretical analysis of both cartesian and envelope clipping for various oversampling rates. Cartesian clipping is where the I and Q values of the complex sample are clipped independently. As the magnitude is not required this method is much less complex to implement than envelope clipping, however it introduces more distortion than envelope clipping at a set clipping level. Considering z as the I or Q component of the complex OFDM signal the output of the Cartesian clipper is expressed as (6.2)

$$y = g(z) = \begin{cases} -y_0 & , z < z_0 \\ (y_0/z_0)z & , -z_0 < z < +z_0 \\ +y_0 & , z > z_0 \end{cases} \quad (6.2)$$

Under the assumption of a Gaussian like nature of the samples (i.e. high number of subcarriers) the impact of non linear distortion was analytically derived , and included the effects of AWGN as well as clipping noise.

The analytical results were compared to a simulated system with $N=128$ subcarriers and QPSK modulation. Square, or Cartesian clipping was shown to have worse performance by around 1dB than envelope clipping (as expected). An oversampling factor of 2 was shown to be enough to have the same performance as an infinitely oversampled signal. A moderate deterioration was seen when the oversampling factor was set at 1 for both square and envelope clipping. Optimum clipping levels were shown to be $A_{clip}/\sigma = 2.5$ for square clippers and $A_{clip}/\sigma = 2.0$ for magnitude clippers.

Another reference [88] to analyze the performance of Cartesian clipping developed analytical expressions for the PSD and SER for any M-ary constellation with various clipping backoffs. Clipping is performed according to the rule set in (6.2)

Clipping is defined as

$$ibo = 20 \log_{10} \left(\frac{x_0}{\sigma} \right) \quad (6.3)$$

The SER was found to be

$$SER = p_s = 1 - (1 - p_e)^2 \quad (6.4)$$

where

$$p_e = 2 \frac{\sqrt{M-1}}{\sqrt{M}} \Pr \left\{ r > \alpha \sigma \sqrt{\frac{3}{M-1}} \right\} \quad (6.5)$$

and $\alpha = \frac{y_0}{x_0} \left(1 - 2Q \left(\frac{x_0}{\sigma} \right) \right)$, Q is the Gaussian error function, σ is the variance of the input signal, and M is the M -ary constellation mapping type.

A simple simulation model was created where an IFFT was used to modulate the complex samples, which were then clipped using the Cartesian method. A FFT was used to demodulate the data.

Many interesting aspects of clipping were revealed analytically and supported through simulation, namely

- The BER is not uniform across all the subcarriers, some subcarriers have slightly worse performance.
- Increasing the number of subcarriers (which increases the CF) distributes the clipping noise over more subcarriers improving the BER, especially in higher order M -ary constellation ($M > 64$).
- The authors note the limitation of a Gaussian assumption of noise as identified in reference [89]. The Gaussian assumption only holds for hard clipping, at higher IBO backoffs, the noise tends to have an impulsive distribution.

Reference [89] also analytically examined clipping in the baseband focusing on magnitude clipping and derived an expression for the SER and BER versus the clip level, as well as performance in both AWGN and Rayleigh fading channels. Bounds on the probability of error due to clipping are derived for both the transmitter and the receiver. The analysis treats clipping noise differently to the standard AWGN assumption which is sufficient if the clipping level is set low enough so that there are a number of clips per symbol. In practice, the clipping level is set higher so that a low probability of error is maintained making clipping a rare event. Under this condition the clipping noise is of an impulsive nature as identified in reference [88] leading to a different type of error mechanism.

Clipping is performed as (6.6)

$$y = h(x) = \begin{cases} -l & x \leq -l \\ x & |x| < l \\ l & x \geq l \end{cases} \quad (6.6)$$

where $x(t)$ is a continuous time baseband multicarrier signal, $y(t)$ is the clipped output, and l is the clipping level.

Reference [89] identified from the distortion spectrum analysis that the probability of error varies across the subcarriers with the lower subcarriers dominating the errors, (assuming a constant constellation size on all subcarriers). The probability of symbol error for a discretely sampled signal is given as (6.7)

$$\Pr(\text{error}) = \frac{8N(L-1)}{L} Q(l) \cdot Q \left(\left[\frac{3\pi l^2}{\sqrt{8(L^2-1)}} \right]^{\frac{1}{3}} \right) \quad (6.7)$$

where N is the number of subcarriers, L is the constellation type (eg: $L=2$ is 4 QAM; $L=8$ is 64 QAM), and $Q(\cdot)$ is the Gaussian error function. An expression for the BER is given as (6.8)

$$\Pr_b(\text{error}) = \frac{4N(L-1)}{L \log_2 L} Q(l) \cdot Q \left(\left[\frac{3\pi l^2}{\sqrt{8(L^2-1)}} \right]^{\frac{1}{3}} \right) \quad (6.8)$$

The AWGN approach is also presented for comparison and is given as (6.9)

$$\Pr(\text{error}) = 4 \frac{L-1}{L} Q \left(\frac{\sqrt{3}}{\sigma_c \sqrt{L^2-1}} \right) \quad (6.9)$$

where

$$\sigma_c^2 = -\sqrt{\frac{2}{\pi}} l \exp\left(-\frac{l^2}{2}\right) + 2(1+l^2)Q(l) \quad (6.10)$$

Reference [89] noted that the Gaussian model is pessimistic as it does not take into account that some of the noise power will fall out of band, and will therefore not contribute to the in band distortion.

Comparing the two analytical methods in Figure 6.1 it is seen that even with the pessimistic assumption of (6.9) the error probability is much lower than (6.7). *This is because instead of being spread uniformly over time, as is assumed in (6.9), clipping noise is actually concentrated in time as impulses, which leads to a greater error probability.* The AWGN model is appropriate for hard clipping levels but it underestimates the error probability by several magnitudes at higher clipping levels. It should be noted that the y-axis in Figure 6.1 exaggerates the difference between the 2 equations. A probability of error of 10^{-6} is probably sufficient.

The advantage of (6.7) is that the error probabilities for high clipping levels can be calculated analytically avoiding laborious simulations times which would be required to get accurate results at these levels.

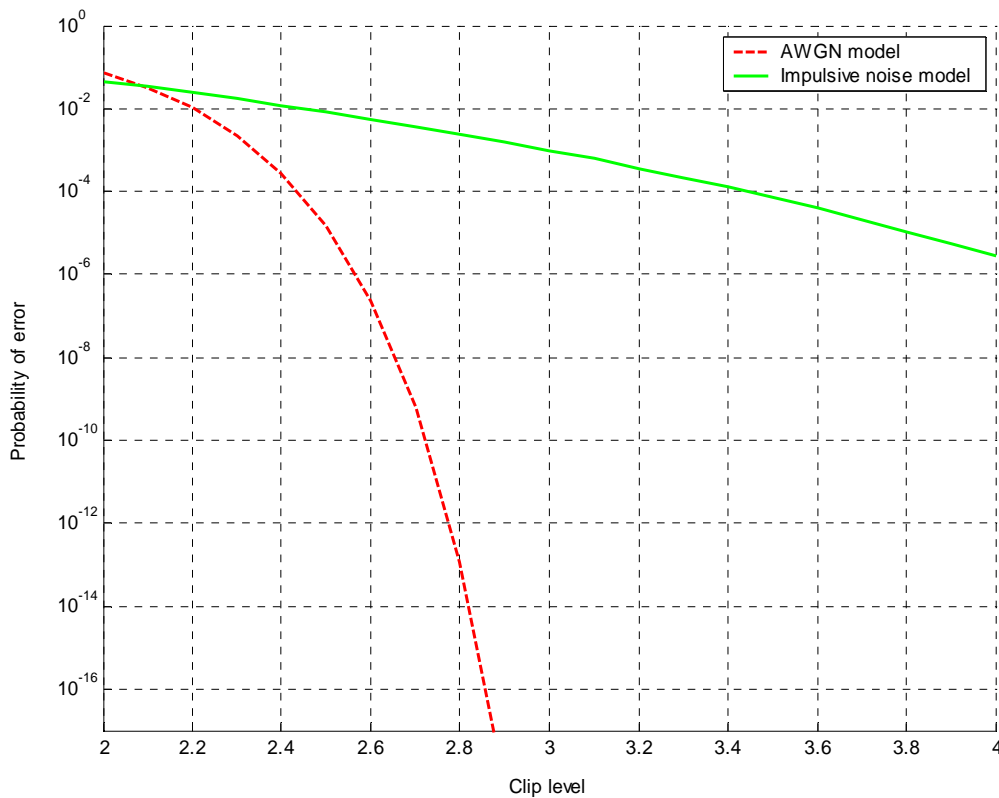


Figure 6.1: Analytical symbol error probability from (6.7) and (6.9) for 64 QAM and $N=64$.

The affect of clipping in the presence of channel impairments is also analyzed both through analytical methods and simulation to observe the effect at the receiver. The simulation model uses the Hiperlan2 [52] specification with a guard interval length of 16 samples, perfect synchronization and a 1 tap equalizer. Analytical analysis revealed that the error probability is further degraded in the presence of channel fades, together with clipping at the receiver. The BER performance was degraded by 1 to 1.5dB on the lower subcarriers. The analytical model is within an order of magnitude of the simulated results.

Reference [90] presented another analytical derivation of the SER resulting from clipping in the baseband extending on the impulsive nature of noise at higher clip levels first presented in reference [89]. Reference [90] claims that the SER curves of reference [89] are too pessimistic and that their claim that approximations become tight in the higher OBO region is unsubstantiated.

Reference [90] proposed a different technique to limit the upper bound by using the Chernoff bounding technique. The expression for the average SER due to clipping is given as (6.11)

$$SER(\lambda) \leq 4 \min_{\varepsilon > 0} \left\{ e^{-d\sqrt{N}\varepsilon} \left(b(\lambda) + \int_0^\infty J_0(\varepsilon r) p(r + \lambda) dr \right)^N \right\} \quad (6.11)$$

where $J_0(x) := \frac{1}{2\pi} \int_0^{2\pi} e^{x \cos \varphi} d\varphi$ is the modified Bessel function of the first kind. Unfortunately no closed form solution is provided, however the computational effort is much less compared to long simulation times required for smooth curves below 10^{-6} probability. Due to the Gaussian assumption of the non linearity the results are only within an order of magnitude of simulated results provided $N > 256$ and the clip level, λ , is greater than 7dB.

Further expressions for the SER in AWGN and Rayleigh fading channels using the previously described Chernoff method are provided. Oversampling at both the transmitter and receiver is also treated, resulting in the realization that the side lobes generated by the transmitting non linearity are suppressed at the receiver by the filter. Furthermore, reference [90] claimed that the average SER is the same for the nyquist and oversampling case, only the out of band radiation is reduced by oversampling. An interesting claim which is not supported by simulations of the BER in the next chapter. The asymptotic behavior is treated and it was found that for $N \rightarrow \infty$, $\lambda_N \rightarrow \infty$ the Gaussian model matches the Chernoff bound of this paper in that the $SER \rightarrow 0$.

Reference [91] looked at the out of band radiation produced by clipping and presented correcting functions which limit the signal while avoiding out of band radiation, and keeping the in band interference to a minimum. This is relevant when oversampling is performed at the IFFT as out of band radiation is created by the clipping process. Filtering after clipping reduces the out of band radiation but regrows previously clipped peaks.

Two correction functions were suggested, the first is a Gaussian correcting function $k(t)$ which is an additive correction of the OFDM signal. If the signal exceeds the amplitude threshold A_0 at times t_n , then the corrected signal is (6.12)

$$c(t) = s(t) + k(t) \quad (6.12)$$

where $k(t) = \sum_n A_n g(t - t_n)$, $g(t) = e^{-t^2/2\sigma^2}$, and $A_n = -(|s(t_n)| - A_0) \frac{s(t_n)}{|s(t_n)|}$. The

correcting function must be normalized so that $g(0)=1$, which limits the signal $s(t)$ to A_0 at the positions t_n . However, the correction function may cause peaks in other positions, but this consequence is shown to have a minor effect. Other functions for $g(t)$ are developed which cause no out of band interference and keep the in band interference to a minimum. A Gaussian function is defined as (6.13)

$$g(t) = \sum_{k=0}^{N-1} G_k e^{j2\pi k \Delta f t} \quad (6.13)$$

$$g(0) = \sum_{k=0}^{N-1} G_k = 1$$

And a sinc correcting function is defined as (6.14)

$$g(t) = \frac{1}{N} \sum_{k=0}^{N-1} e^{j2\pi k \Delta f t}$$

$$\approx \text{sinc}(\pi B t) e^{j\pi B t} \quad (6.14)$$

The correcting function (6.14) can correct an amplitude peak in an OFDM signal with minimal in band distortion and no out of band radiation. Note that if the signal is not oversampled then the correction scheme is the same as normal clipping.

Simulations with the correcting functions were performed with $N=128$ subcarriers and an oversampling rate of 4. The signal is corrected with $k(t)$ and any peak regrowth after the correction is clipped at A_0 . An IBO level of 4dB was used and the algorithm was tested in both an AWGN and fading environment. It was shown that the

correction functions introduce more inband noise than standard clipping, however the slight increase in inband noise is offset by the alleviation of out of band interference. For example, at an IBO of 4dB standard clipping has a Signal to Interference Ratio (SIR) of 21dB, Gaussian 13dB, and Sinc 16dB. The BER vs IBO in an AWGN channel with SNR of 18dB shows a magnitude greater degradation for the sinc correction function at 4dB IBO, but in the fading channel the BER degradation is negligible for the sinc case and only marginally worse for the Gaussian case.

Clipping and filtering issues were addressed in reference [92] where an oversampled (LN- where L is the oversampling factor) IFFT zero padded in the middle is used to modulate the OFDM symbol. The resultant samples are then clipped by a SL in the normal way, as this results in out of band radiation as described section 3.4.2 the data is filtered by a FFT/IFFT pair of size LN. The filter passes the wanted in band samples while nulling out the out of band components. The advantage of this technique is twofold, firstly out of band radiation is greatly attenuated and secondly, by oversampling peak regrowth after filtering is greatly reduced (refer to Figure 3.11).

Simulations were performed with 4QAM data and N=64 subcarriers. CCDF results for a CR of 6dB compared the new algorithm (L=2, N=64) with standard non oversampled clipping (L=1, N=64) where it is seen that the L=2 case has 1dB less peak regrowth than the L=1 case at 10^{-5} probability region. It was noted that increasing the oversampling rate (L>2) at the IFFT provided minimal further improvement. Out of band radiation is also analyzed in the form of the PSD where a perfectly linear amplifier with a CR 1dB higher than the baseband clipping level is used after modulation with a carrier frequency. Out of band radiation was reduced down to 65dB using the new technique (L=2), compared to 55dB for clipping before interpolation (L=1) and 45dB with no clipping before amplification. In band distortion is also an affect of clipping, reference [92] stated that clipping adds a noise like component and a reduction in the constellation size (refer to Figure 3.16) which can be corrected at the receiver with AGC. Also as the noise from clipping is created at the transmitter it will lessen its effect in a fading channel. These properties will improve the BER. This technique can be implemented in existing OFDM systems and requires no redesign at the receiver only replacing the IFFT at the transmitter.

Another technique to lessen the effects of clipping [93] called Decision Aided Reconstruction (DAR) reduces clipping noise with an algorithm in the baseband at the receiver. Like the method of [92] it uses a FFT/IFFT pair in an iterative algorithm at the receiver to try to estimate which samples were clipped at the transmitter. When the clipping noise is large compared to the AWGN in the channel, performance is limited by the clipping noise. Using the FFT/IFFT pair to make decisions in the frequency domain regrows samples that were clipped at the transmitter, and although they are still distorted decisions made on the new symbols are much less affected by clipping noise. However much of the gain from DAR may be achieved by simply correcting the constellation shrinkage which clipping causes (refer to Figure 3.16).

The algorithm can predict false clipped peaks when the clipping level is set too low (<2dB) worsening performance more than standard clipping. Through simulation reference [92] found that DAR worked best when a small number of samples were clipped, and that it worked better with higher order constellations with a clip level >4dB. For example in a 64QAM OFDM system with a CL of 5dB in an AWGN channel the improvement was quite dramatic being only ~1dB lower than the theoretical lower bound. It was also noted that a slight further improvement is seen as N is increased. The number of iterations required for good performance was shown to be around 3. The problem with the methods of references [92, 93] is the latency and complexity of performing extra FFT/IFFT operations.

6.1.1 Quantisation and Clipping

An early paper to investigate the relation between clipping and quantization in DMT transceivers is reference [94] where an analytical expression was developed to find the minimum number of bits required in the A/D, D/A converters when the signal is clipped to a predefined level. Due to the Rayleigh nature of the envelope of the DMT envelope 2 to 3 bits can be saved in the A/D, D/A operation without changing the SNR. An expression to calculate the number of bits that can be saved is (6.15)

$$\Delta = \frac{1}{2} \cdot \log_2 \left\{ \frac{v^2 - 3\sqrt{(8/\pi) \cdot 2^{2R_1} \cdot \mu^{-3} \cdot e^{-\mu^2/2}}}{\mu^2} \right\} \quad (6.15)$$

where $\Delta = R_1 - R_2$ is the number of bits saved, R_1 is the number of bits required for the A/D-D/A when no clipping is performed, R_2 is the number of bits required for the A/D-D/A with clipping to keep the same SNR as when no clipping is performed, $v = \frac{1+\sqrt{2}}{2} \cdot \sqrt{(3N)} \cdot \sqrt{\left(\frac{L-1}{L+1}\right)}$ is a parameter set by the number of subcarriers, N , the QAM constellation size L^2 , ($L=4$ equates to 16 QAM), and $\mu = \frac{A_{\max}}{\sigma}$ is the clip level. A_{\max} is the clip level in volts and σ is the rms voltage of the DMT transmit symbol. It was assumed in the paper that all subcarriers have the same constellation type, however the authors claim that different mapping types on subchannels would have a minimum effect.

Clipping and quantization are further explored in reference [95] for DMT based transceivers where a improved clipping technique allows for up to an 8dB improvement in the SNR over standard clipping. The new method analyzed the samples after the IFFT, if a sample is above the clipping threshold, A_{clip} , then the phase of each QAM modulated carrier is changed by means of a fixed phasor rotation, and a new DMT symbol is generated by the IFFT. By careful selection of the phasor rotation, the probability of the new symbol requiring clipping at A_{clip} will be reduced. Otherwise the symbol is sent on to further processing unmolested.

The overall probability of clipping for the 2 pass method described above is (6.16)

$$P_{\text{Clip/Total}} = P_{\text{clip/1}} \cdot P_{\text{clip/2}} = P_{\text{clip}}^2 \quad (6.16)$$

which is determined to be

$$P_{\text{Clip/Total}} = \left[1 - \text{erf}^{2N} \left(\frac{\mu}{\sqrt{2}} \right) \right]^2 \quad (6.17)$$

where $\mu = A_{clip} / \sigma$.

Recalculating the IFFT can create a bottleneck slowing down system performance, but does not necessarily require a factor 2 increase of the IFFT as not every symbol will require clipping, especially at higher levels of A_{clip} . Side information is also required to inform the receiver of the number of passes, p , used (if any) of $\log_2 p$ bits per transmitted symbol.

As seen in Figure 6.2, the clipping probability drops with an increase in the number of passes. At $\mu=4$ the 2 pass and 3 pass methods reduce the probability of clipping down to $\sim 10^{-4}$ and $\sim 10^{-6}$ respectively.

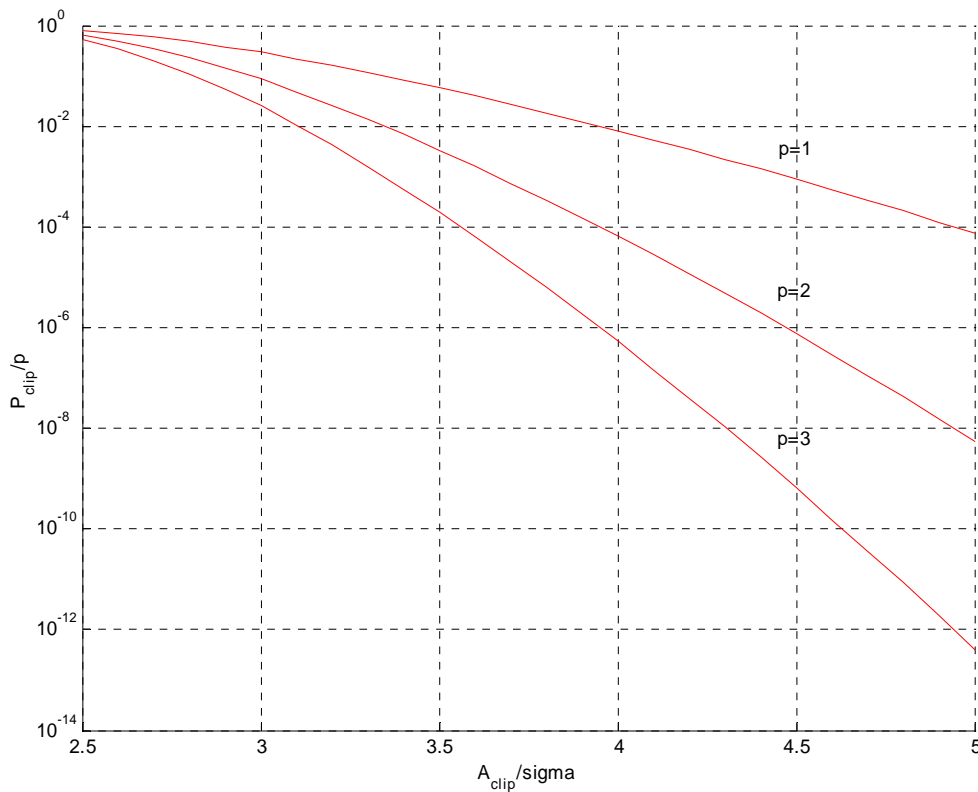


Figure 6.2: Probability of clipping DMT signal as a function of μ for $p=1,2,3$. $N=64$ subcarriers.

Quantization effects are also examined in terms of noise from the DAC and ADC in the transmitter and receiver respectively for various wordlengths, b . For 16 QAM,

$N=256$, $b=12$, $\mu \geq 3.7$ with $p=1$ and $\mu \geq 3.4$ with $p=2$ an improvement of 3 and 8dB can be achieved.

Another reference [96] analyzed quantization effects on OFDM used a simulation model with Hiperlan2 [53] specifications. Clipping is performed on the I and Q outputs of the IFFT. As the wordlength at the IFFT output is decreased, the power consumption and complexity of the DAC/ADC decreases at the expense of quantization noise, which increases the BER. However as noted in reference [94] the wordlength can be reduced with minimal affect on the BER. Also clipping at the IFFT output increases the resolution giving a better average signal/quantization noise power ratio, of course this is at the expense of clipping noise.

In a nutshell, lowering the clipping level increases the clipping noise while at the same time reducing the quantization noise. Results from reference [96] indicated that the optimum clipping level for wordlengths between 6 and 9 bits occurs at around 4σ (slightly lower for smaller wordlengths). An 8 bit wordlength is also recommended with an extra 2 bits for the receiver ADC to compensate for peak regrowth affects after transmit filtering (upsampled by 4 before filtering) and imperfect AGC in the receiver.

Reference [97] examined the effect of rounding and saturation in fixed-point DSP implementation of the IFFT and FFT where optimum trade-offs are found between saturation and rounding. Results from simulation revealed that performance for fixed point FFT's is improved when overflow is allowed to occur with low probability. The distribution of error was shown to depend on the ratio of the maximum quantization level to the RMS power of the random variable. For 16-bit arithmetic the headroom was shown to be around 15dB. Doubling the size of the FFT resulted in an improvement in the new scaling method of 3dB.

6.2 Amplifier non linearities

As shown in Section 3.4 if no attempt is made to control the peak excursions of an OFDM symbol the HPA will saturate causing spectral regrowth and an increase in the

BER at the receiver. This section reviews papers which analyze the effect of an uncontrolled OFDM symbol on the HPA.

An early reference [42] to look at the effect of a non linearity on QPSK OFDM compared analytically derived and simulated results for the BER versus SNR. Specifically they assumed that the intermodulation products were generated by non linearities in the receiver IF module. These results are stated to be applicable to the transmitter amplifier, and that only 3rd order distortion will affect the system.

The BER is calculated under the assumption that the intermodulation products cause an additive Gaussian interference and that the BER is approximately equal on all subcarriers. The non linearity is set at the 1dB compression point of the in band output and is related to the output signal, V_o , by $V_{1dB} = 0.27V_o$. The simulated results for the amplifier which is linear up to 3dB, with 1dB backoff show that even with a 1dB backoff the BER is within 1 order of magnitude of the linear amplifier at SNR=10dB. The simulated results were shown to be in good agreement with theoretical results.

Reference [98] focused on simulation comparing Single Carrier (SC) and OFDM systems with clipping in the baseband and RF amplifier non linearities. The simulation model used N=2K and 8K (DVB, DVA) subcarriers with QPSK and 16 QAM mapping to produce SER versus clipping and AWGN plots in a Monte Carlo simulation. It was shown that the SER versus SNR is almost the same for both systems with OFDM having slightly better performance due to the frequency guard interval used in OFDM which reduces the equivalent noise bandwidth. The number of subcarriers has a negligible effect on OFDM due to the Gaussian distribution of samples.

The baseband clipping effect was simulated with the SNR set at 16dB for 16 QAM and the backoff was defined as $BO = A^2 / 2\sigma^2$. Again the number of subcarriers was shown to have a negligible effect on the BER. The performance of the SC and OFDM system converges at a baseband clipping of BO=6dB for OFDM when 16

QAM mapping was used, a backoff of 3dB was only required for QPSK due to the larger Euclidean distance of QPSK constellation points.

For the RF amplifier the low pass equivalent was used, where the signal is of the form $A(t)e^{j\theta(t)}$, the HPA output can then be expressed as (6.18)

$$y(t) = f[A(t)]e^{j(\theta(t)+g[A(t)])} \quad (6.18)$$

Where $f[A]$ is the AM/AM characteristic of the amplifier and $g[A]$ is the AM/PM characteristic of the HPA. The phase distortion was considered to be linear. Performance for 16 QAM OFDM under different amplifier backoffs is almost identical to the baseband clipping effects with a 6dB BO required to bring performance in line with its equivalent SC counterpart. It was also shown that the degradation increases as the third order interception point approaches the 1dB compression point. QPSK was again shown to be more robust to amplifier non linearity.

Reference [40] both analytically derived and simulated an OFDM system in a AWGN channel with and without equalization (1 tap) to produce BER versus SNR plots. Amplifier non linearity (using TWT as described in Section 3.4.1) is stated to cause two effects on the detected samples:

- constellation warping (amplitude and phase distortion)
- non linear distortion which generates a Gaussian spread like cluster of received values around each constellation point (refer to Figure 3.16)

For 16 QAM OFDM system it was shown that at high IBO (25dB) equalization had no effect on the BER. As the IBO is reduced (14dB) the equalized BER degraded only a little, however the non equalized OFDM model lost a further 7dB of SNR. At 12dB IBO the non equalized system lost so much SNR that its error floor became 10^{-3} . For all cases a good agreement is shown between analytical and simulated results.

Reference [47] provided an analytical analysis of smooth non linear distortion on the SER as a function of third order distortion (the most dominant distortion for smooth non linearities) in a memoryless non linear power amplifier. The analysis was performed on a matched filter pair. Initially the spectrum of the distorted OFDM signal is examined, which is then used to determine the detection error for the matched filter detection. It was found through analytical means that the variance is approximately equal on all subcarriers with the middle subcarriers experiencing the most noise, this means that the SER is similar on all subcarriers, a result supported by reference [88].

Simulated results are compared to analytical results for QPSK and 16 QAM OFDM. The simulation model used an equivalent low pass representation to avoid RF up and down conversion, $N=1024$ subcarriers were processed by an IFFT at which point the non linearity was performed. The data was demodulated with an FFT and the transmit symbols were compared to the received samples. The difference was squared and stored and then averaged to find the noise variance. The simulation results for 16 QAM were found to better fit the analytical results than QPSK, the tails in both cases fall off quicker in the simulated case because they are not exactly Gaussian. However a good agreement is seen between the analytical and simulated curves.

Reference [41] extended on earlier work presented in reference [40] to theoretically analyze the effect of non linear amplifiers in conjunction with phase noise on M-QAM OFDM. Phase noise is caused by the oscillators in the RF stage and becomes a more dominant source of noise at higher carrier frequencies (up to 40GHz). The theoretical expressions were supported by simulations using SSPA and TWTA with different values of phase noise. Under the assumption of modeling the phase and amplifier distortions as additive Gaussian noise, the computed variances are used to get an estimate of the BER in an AWGN channel.

Results indicated that while QPSK is rather impervious to both amplifier non linearity and phase noise, the performance of 16 and 64 QAM is greatly diminished in terms of the BER even with a large OBO in the amplifier. A SSPA with $p=2$ introduced 4th order distortions which further diminished the performance of 16 and 64 QAM. In

general it was shown that the joint effects of amplifier non linearity and phase noise have two major effects. Amplifier non linearity generates a uniform amplitude attenuation and phase rotation which can be corrected at the receiver by AGC. Phase noise introduced a constant phase rotation within 1 OFDM symbol which can be estimated and corrected using the pilot tones. The second effect is constellation clustering due to the interference produced by the HPA to the ICI caused by the phase noise.

Finally it was shown that the phase noise impairment was dependant on the relationship between the phase noise rate and the OFDM symbol period. It was shown that the phase noise can become a limiting factor if a large number of subcarriers and a high frequency carrier are used.

6.3 Windowing

Windowing or pulse shaping are similar to clipping in that they attenuate large peaks. However in windowing a corrective window is multiplied with the data so that not only the peak cancelled but surrounding samples are also affected. The advantage of this process is to keep the OBR lower than in standard clipping. Windows should be as narrowband as possible in the frequency spectrum domain, so as to have good OBR properties. However narrowband windows have the reciprocal affect of being long in the time domain which implies many signal samples being affected, which increases the BER.

Reference [99] uses window types such as cosine, Kaiser, and Hamming, comparing their use to standard clipping in terms of the frequency spectrum and BER. The simulation model uses Hiperlan2 [53] specifications with a $\frac{1}{2}$ rate convolutional code and 16 QAM where it is shown that clipping the signal at 5dB has a minor affect on the BER with a 0.2dB loss in SNR. Windowing is shown to have almost identical affect on the BER above 5dB clipping but interestingly has worse performance at harder clipping levels.

To simulate the affect of the required backoff in the HPA a SSPA with $p=3$ as described in Section 3.4.1 is used. In order to keep the OBR to below 30dB for 64 subcarriers a backoff of 6.3dB was required, which could be reduced by 1 dB to 5.3dB when peak windowing is used. When 256 subcarriers are used the backoff of 6.3dB can be reduced by 0.8dB to 5.5dB with peak windowing, showing that windowing is independent of N.

A later reference [100] uses broadband pulse shaping on individual subcarriers as a way to reduce the PAPR. By making the cross correlation between samples in the same block close an OFDM signal with a low PAPR can be created. The new OFDM signal is given as

$$x(t) = \sum X_n(m) p_m(t) e^{j2\pi m t/T} \quad nT \leq t \leq (n+1)T \quad (6.19)$$

Where $X_n(m)$ is the modulated data symbol of subcarrier m, T is the duration of the OFDM block, and the waveform $p_m(t)$ is a pulse shape of duration T, on subcarrier m which has a bandwidth less than or equal to the bandwidth of the OFDM signal $x(t)$.

Unique RRC waveforms are multiplied with each sample, which are cyclic shifts of each other within the same time interval $0 \leq t < T$. As each RRC pulse is seeded from the same source they are easy to create, the RRC pulse for each subcarrier is defined as

$$p_m(t) = \sum_{k=-L}^{N+L-1} C(k) e^{-j2\pi \frac{mk}{N}} e^{-j2\pi \frac{k-m}{N} t} \quad 0 \leq t < T \quad (6.20)$$

where

$$C(k) = \frac{1}{T} \int_0^T p(t) e^{-j2\pi \frac{k}{N} t} dt = \frac{1}{T} P\left(\frac{m}{T}\right) \quad (6.21)$$

is the Fourier series of $p(t)$ and

$$p(t) = \begin{cases} p_{rc}(t-T/2), & 0 \leq t < T \\ 0, & \text{elsewhere} \end{cases} \quad (6.22)$$

where $p_{rc}(t-T/2)$ are the samples of the time domain RRC pulse.

When the rolloff factor is increased to 0.5 the reduction in the CCDF at $\Pr(\zeta > \zeta_0) = 10^{-3}$ is around 6.5dB. However the effect of oversampling and the frequency spectrum is not treated. I anticipate that the spectrum is at least 50% larger than normal OFDM because the spectrum of the broadband pulse would have to be convolved with the basic OFDM linear spectrum.

Note that reference [100] is actually mathematically equivalent to clipping and filtering with a linear time invariant filter.

6.4 Conclusion

This chapter presented distorted techniques for the reduction of PAPR in OFDM. Clipping in the baseband was first introduced as this is the simplest and most widely examined area in distorted PAPR reduction techniques. Clipping was shown both analytically and through simulated means to have a minor effect on the BER when QPSK modulation was used due to the large Euclidean distance between constellation points. Higher order mapping types such as 16 and 64 QAM were much more susceptible to clipping. The BER on individual subcarriers was also treated where it was shown that the probability of error was almost equal on all subcarriers. Increasing the number of subcarriers was shown to have a beneficial affect as the noise introduced by clipping would be spread over more subcarriers.

The Gaussian like assumption of the noise which is assumed in most analysis of clipping noise was also shown to be unsubstantiated resulting in optimistic error probabilities. Clipping noise was shown to have an impulsive nature at higher clip levels resulting in a much smoother decay in error probability as the clip level was increased.

Clipping at the nyquist rate (no oversampling) does not cause out of band radiation as all the noise was shown to fall in band. Oversampling before clipping was shown [46] to produce less in band noise but to increase the out of band noise, requiring filtering.

Quantization in hardware and clipping was also treated where it was shown that some bits could be saved after clipping, due to the Rayleigh distribution of samples without degrading system performance. This also improves the resolution of the clipped samples.

Furthermore it was shown that several steps could be taken to mitigate the errors caused by clipping. As clipping noise caused shrinking in the constellation size as well as a Gaussian like spreading the AGC in the receiver could be used to correct this depending on the clip level. Also, the noise due to clipping will also experience fading along with the signal further lessening its effect.

Early windowing and pulse shaping techniques displayed little improvement and sometimes a further degradation in the BER while attempting to reduce the OBR. Later work in this area produced a markedly greater improvement in the PAPR by the selection of appropriate pulse shapes which were applied to individual subcarriers rather than the whole transmit signal.

Chapter 7

Reduced Complexity Clipping Algorithms

The previous chapter covered distorted techniques for PAPR reduction. As described clipping suffers after filtering as clipped peaks can regrow resulting in saturation of the HPA. Also, although clipping is less complex in terms of hardware operations than distortionless techniques, estimates of the magnitude still need to be made in order to decide whether a sample needs to be clipped or not and multiplications have to be made to correct the signal. This chapter presents new low complexity clipping techniques which avoid complex hardware operations while maintaining similar performance to conventional clipping. The new clipping algorithms are then implemented in a new clip and filter algorithm which is much less susceptible to peak regrowth after baseband filtering.

Section 7.1 describes conventional clipping and a simulation model is developed to quantify the effects that various transceiver components have on the BER¹. This model is then used to test the new clipping algorithms. Section 7.2 details a new technique coined *Sector Clipping* and provides theoretical and simulated analysis of the new method. Section 7.3 presents another new technique which is similar to the CORDIC algorithm but with reduced complexity called *Vector Subtraction*. Section

¹ In this work the BER will be plotted against clipping level with the noise set to zero. All the errors are therefore caused by clipping noise. The BER's in these plots therefore represent the 'error floor' of the more commonly used BER vs. SNR plots.

7.4 compares the new and existing clipping methods in terms of their baseband Clipping Level (CL) vs. the BER. Section 7.5 implements the new algorithms in a new clip and filter algorithm which is less susceptible to peak regrowth. Finally section 7.6 concludes the chapter with a review of the advantages of the proposed clipping techniques.

Note that the results in Sections 7.1 and 7.4.1 show the Bit Error Rate Floor (BERF), i.e. the BER due to clipping as that is the focus of this chapter. For comparison Figure 7.1 shows the BER with Additive White Gaussian Noise (AWGN) in the channel and the CL set at 3, 5dB and no clipping. 4, 16, and 64 M-ary QAM symbols are modulated with a 64 point IFFT and then pulse shape filtered with a Root Raised Cosine Filter (RRCF) with $\alpha=0.35$, and 128 taps. It can be observed that 16 and 64 QAM mapping is much more susceptible to clipping noise than 4 QAM. The error floors for 64 QAM can be cross referenced with figure 7.4. The OFDM transceiver system is shown in Figure 7.3.

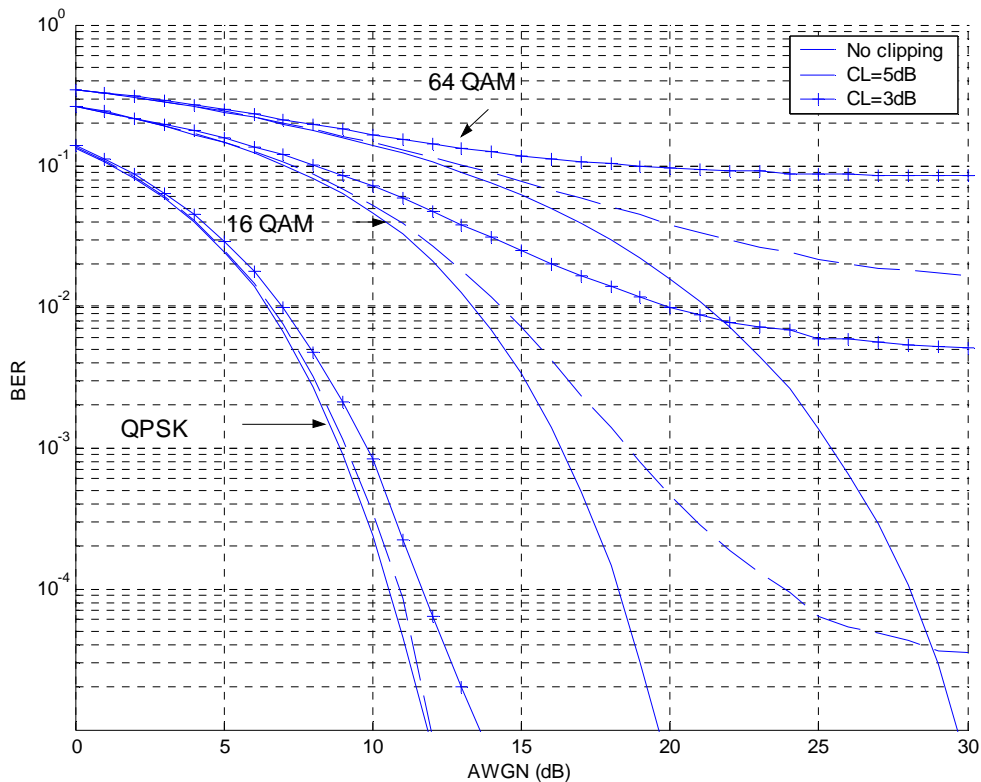


Figure 7.1: Average noise in the channel vs. BER for 4, 16, and 64 QAM.

7.1 Conventional clipping

Conventional clipping is defined here as any hardware method which reduces the amplitude of the signal to a predefined level in line with the origin as shown in Figure 7.2.

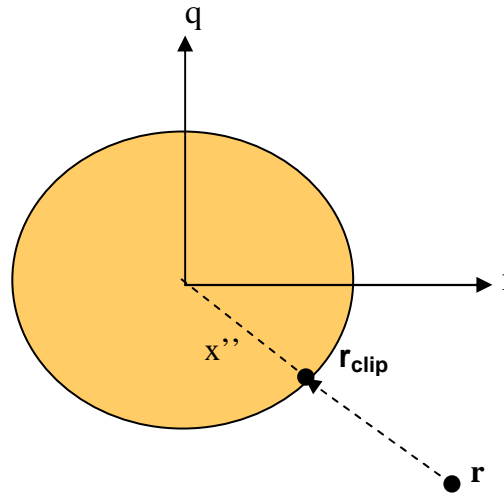


Figure 7.2: IQ diagram showing conventional clipping region. The vector r is reduced to r_{clip} .

Clipping in this way only introduces amplitude distortion, the phase is unaffected. This method is the most hardware intensive of all methods described in the following sections. Some of the operations require iterative techniques when implemented in fixed point processes (e.g. Division and square roots) and therefore take a number of clock cycles. Other methods require vast LUT's which consume chip area or memory space. Mathematically conventional clipping can be described as

$$x'' = \begin{cases} r & |r| \leq r_{clip} \\ r_{clip} e^{j\angle(r)} & |r| > r_{clip} \end{cases} \quad (7.1)$$

In order to analyze the performance of conventional clipping it is useful to quantify the effects of the different system components involved, i.e. the mapping type, IFFT size, number of filter taps, filter rolloff factor, and IBO of the HPA. A block diagram of the simulation model used is shown in Figure 7.3.

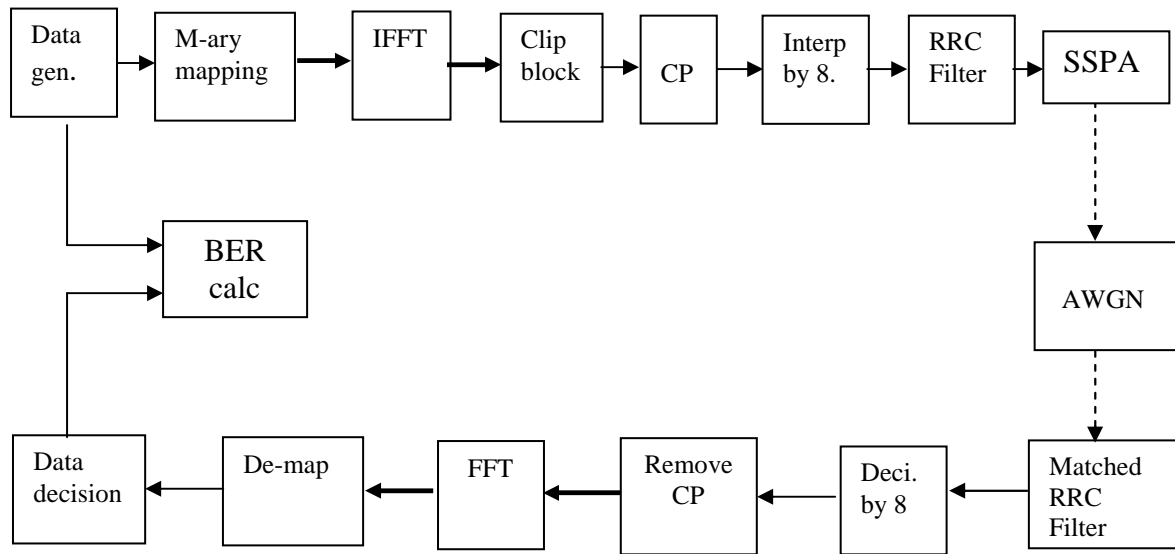


Figure 7.3 Block diagram of simulation model used for clipping models.

The baseband Monte Carlo simulation model of Figure 7.3 randomly generates M-ary mapped data and then modulates the signal with the IFFT. Note the data is buffered at the input to the IFFT so that N samples are fed into the IFFT, after modulation the data is converted back into serial form and sent to the baseband clipping block. After clipping to a predefined level relative to the mean power of the transmit symbol a cyclic prefix can be added to the data. The data is then interpolated by a factor of 8 before being filtered by a matched Root Raised Cosine Filter (RRCF). A SSPA (as described in Section 3.4.1) models the HPA. AWGN and multipath delayed versions of the signal can then be added in the channel.

At the receiver side the process is reversed, a matched RRCF filters the received samples which are then decimated by 8 to retrieve the transmitted samples. The cyclic prefix (if used) is removed prior to demodulation with the FFT. Again note that the data is buffered at the input to the FFT until all N samples are ready. Finally, a simple Least Square (LS) algorithm is used to make decisions on the decoded data. A comparison between the gray encoded transmitted bits and the received bits is made to determine the BER.

In the results that follow the conventional baseband clipping algorithm is used as described in Figure 7.2. Note that 64 QAM mapping is used unless otherwise stated

since the more traditional QPSK has such a high tolerance to clipping excessive simulation times are required to get BER plots. In the following simulations 10,000 OFDM symbols are transmitted, each symbol has 52 information bearing subcarriers. For 64 QAM this means around 3 million bits are transmitted.

Effect of filter on the BER

Figure 7.4 shows the baseband clip level vs. the BER for a RRCF with different numbers of coefficient taps and roll off factors (named alpha in figure 7.4). There are no other sources of distortion or noise. The number of taps is set at 64, 128 and 256, and the roll off factor or excess bandwidth is set at 0.15 and 0.35.

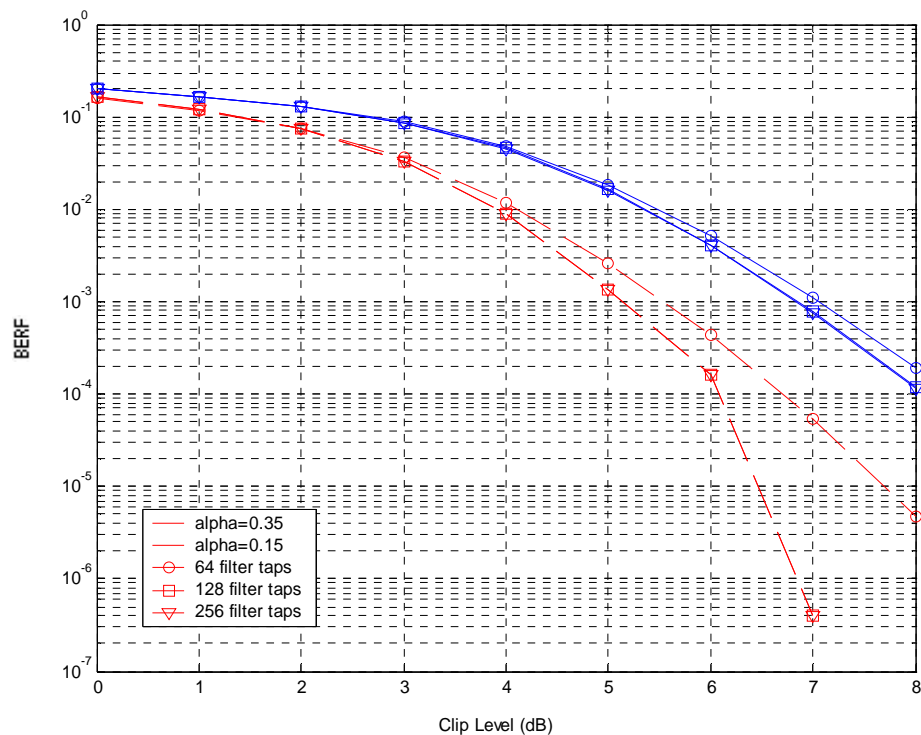


Figure 7.4: Baseband clip level vs. the BER for varying RRCF parameters. 64 QAM symbols, 64 point IFFT, LPA, no channel impairments. AWGN=0.

Two points can be made reviewing Figure 7.4, the first is that when the easier roll off or excess bandwidth of $\alpha=0.35$ is used the number of taps has little effect on the BER. The second point is that when a tighter roll off factor is used ($\alpha=0.15$) the BER is substantially affected by the number of taps. 64 filter taps has a BER almost 2 magnitudes worse than 128 taps at CL=7dB. This is due to the inband amplitude

distortion (ripple) created when insufficient taps are used with a small excess bandwidth (refer to Figures 7.5a and b). This creates a linear spreading of the demodulated samples away from the origin. In all cases $\alpha=0.35$ has worse performance than $\alpha=0.15$ for the same number of filter taps.

The 0.35 roll off factor curves will have a wide transition bandwidth in the frequency domain. The extreme subcarriers will then be effected by additional attenuation which will reduce the noise margin in the receiver decision (slicer). The 0.15 roll off curves have a steeper transition band and avoid the problem of the extreme subcarriers. However pass-band ripple will be introduced when the number of taps is low (taps=64).

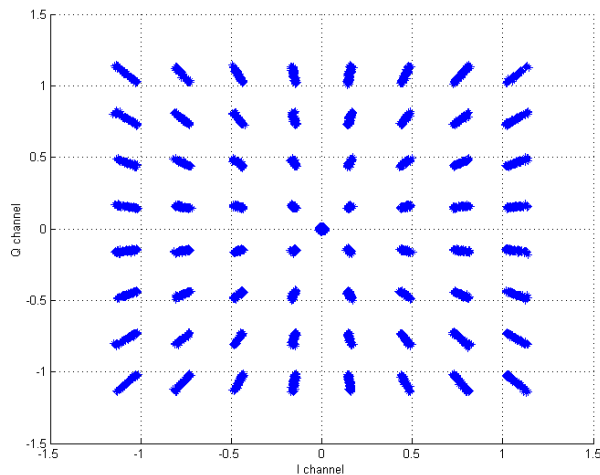


Figure 7.5a: Demapped constellation, M=64, with no clipping or channel impairments. 64 filter taps in RRCF, $\alpha=0.15$.

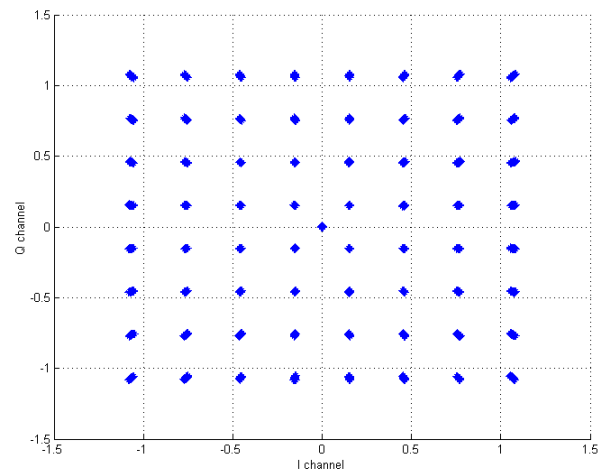


Figure 7.5b: Demapped constellation, M=64, with no clipping or channel impairments. 128 filter taps in RRCF, $\alpha=0.15$.

The Hiperlan2/802.11a physical layer specification requires a tight roll off, ($\alpha \approx 0.15$) so that the filter skirts occur in the null subcarriers. In all further simulations 128 filter taps with a roll off of $\alpha=0.15$ will be used unless stated otherwise.

Effect of HPA amplifier backoff and IFFT on the BERF

Figure 7.6 and Figure 7.7 again shows the clip level vs. BERF with 64 QAM mapping. This time the IFFT size is set to 64 and 128 while maintaining the same

number of information bearing subcarriers, i.e. the data is therefore critically sampled (almost) and oversampled by a factor of 2 respectively. The other variation is the inclusion of a HPA with IBO. The HPA follows the Rapp model of (3.34) with $p=3$. This allows us to see the effect of peak regrowth on the BERF with and without oversampling.

In Figure 7.6 ($os=1$) even with an IBO of 4dB above the baseband clipping level ($IBO=CL+4dB$) peak regrowth still causes a small amount of saturation in the HPA, degrading the BERF. With no extra IBO in the HPA ($IBO=CL$) the BERF is between 10^{-2} and 10^{-3} at $CL=6dB$ while with a LPA the BERF is below 10^{-4} at 6dB baseband clipping, a 1.5 order of magnitude improvement.

In Figure 7.7 ($os=2$) the performance is better for all IBO across the board. Some of the clipping noise falls into the null bins and is subsequently filtered away while $os=1$ systems would cause this noise to fold back into the inband subcarriers. For no extra IBO in the HPA the 64 point IFFT has a BERF between 10^{-2} and 10^{-3} at 6dB baseband clipping (Figure 7.6) while the 128 point IFFT has a BERF just above 10^{-3} at the same clip level, an improvement of half a magnitude. Note in Figure 7.7 that for the curve $IBO=CL+4$ to the LPA curve ($IBO=CL+\infty$) there are no errors occurring in over 3 million transmitted bits at 7dB clipping level.

In order to further highlight the effect of oversampling, the CCDF in Figure 7.8 is also shown for the case described in Figures 7.6 and 7.7, showing the peak regrowth under critically and oversampled conditions. In this case the baseband clip level is set at 5dB, peak regrowth for the critically sampled case is extreme with almost 5dB peak regrowth at $\Pr(\zeta > \zeta_0) = 10^{-4}$. Peak regrowth is 3dB (2dB less) for the oversampled case ($os=2$) at $\Pr(\zeta > \zeta_0) = 10^{-4}$. Results not shown here indicate that the harder the clip level the more extreme the peak regrowth after filtering.

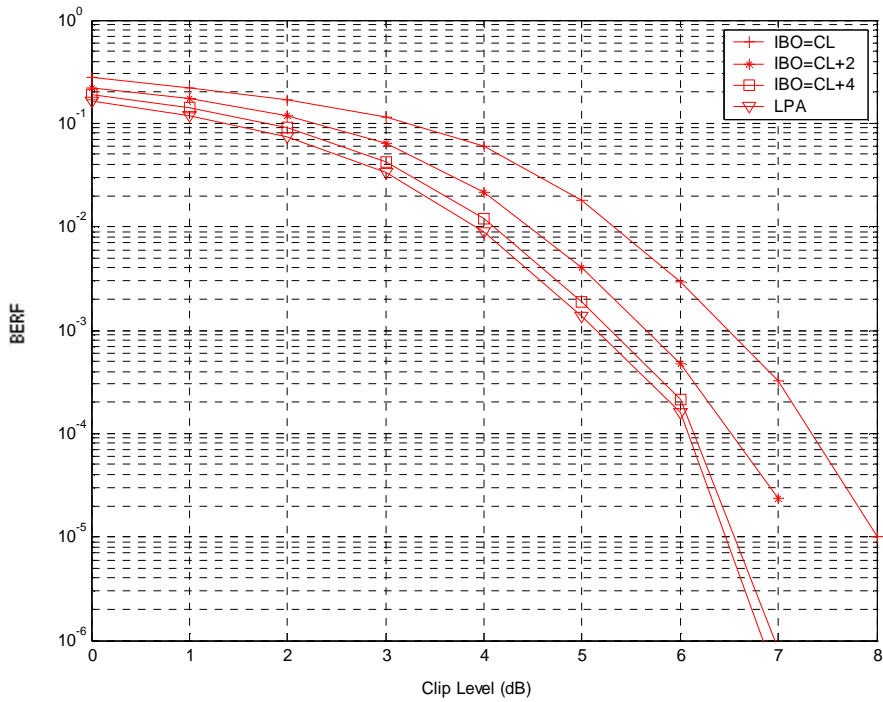


Figure 7.6: Baseband clip level vs. the BERF with varying IBO in HPA. 64 QAM symbols, 64 point IFFT ($os=1$), RRCF with 128 taps and $\alpha=0.15$. $p=3$ in HPA. AWGN=0.

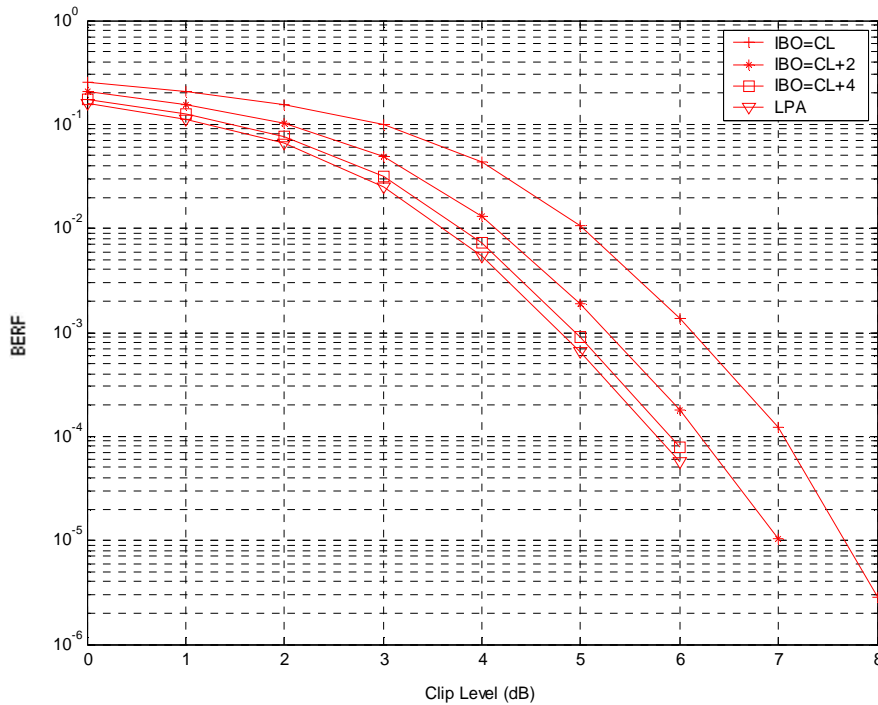


Figure 7.7: Baseband clip level vs. the BERF with varying IBO in HPA. 64 QAM symbols, 128 point IFFT ($os=2$), RRCF with 128 taps and $\alpha=0.15$. $p=3$ in HPA. AWGN=0.

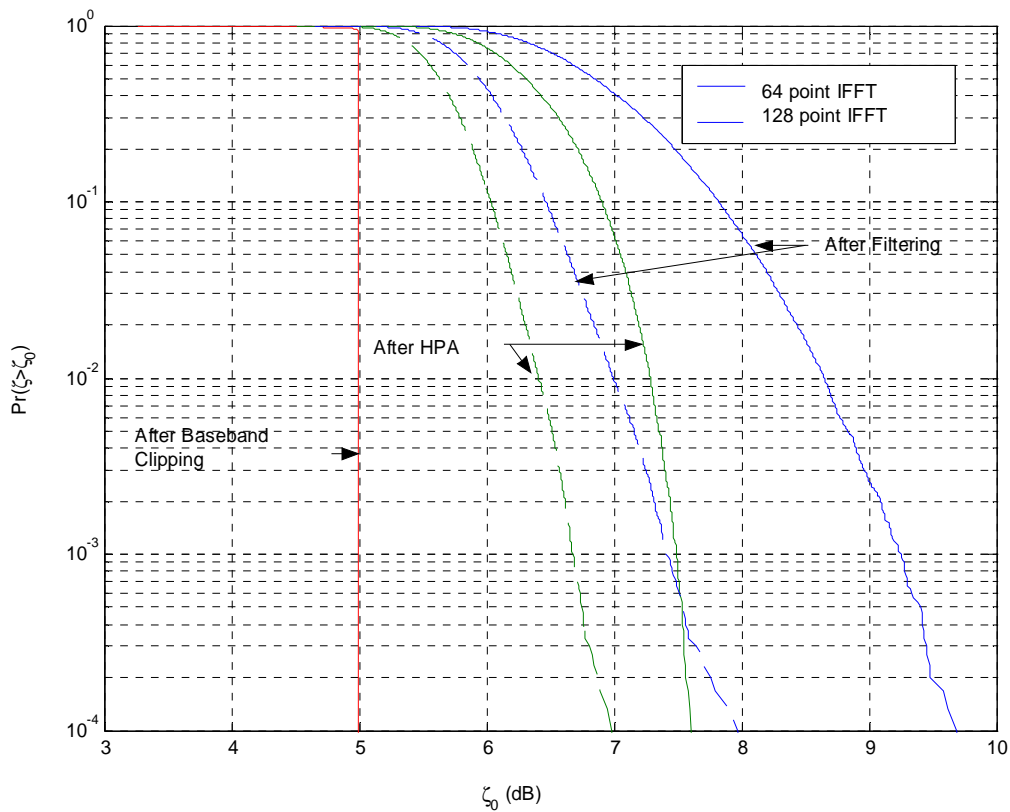


Figure 7.8: Simulated CCDF clipped in baseband at 5dB, IBO in HPA set to 8dB for 64 and 128 IFFT.

Effect of constellation size on the BERF.

Figure 7.9 shows the effect of changing the mapping constellation M with an oversampling factor of 2 in conjunction with a LPA. Although 4 QAM was simulated, it is extremely impervious to clipping with no detected errors at 0dB and above. 16 QAM also has rather robust performance in the presence of clipping with no errors being detected above 4dB clipping at 10^{-5} probability. 64 QAM clipping has performance around 2 magnitudes worse at equivalent clipping levels to 16 QAM.

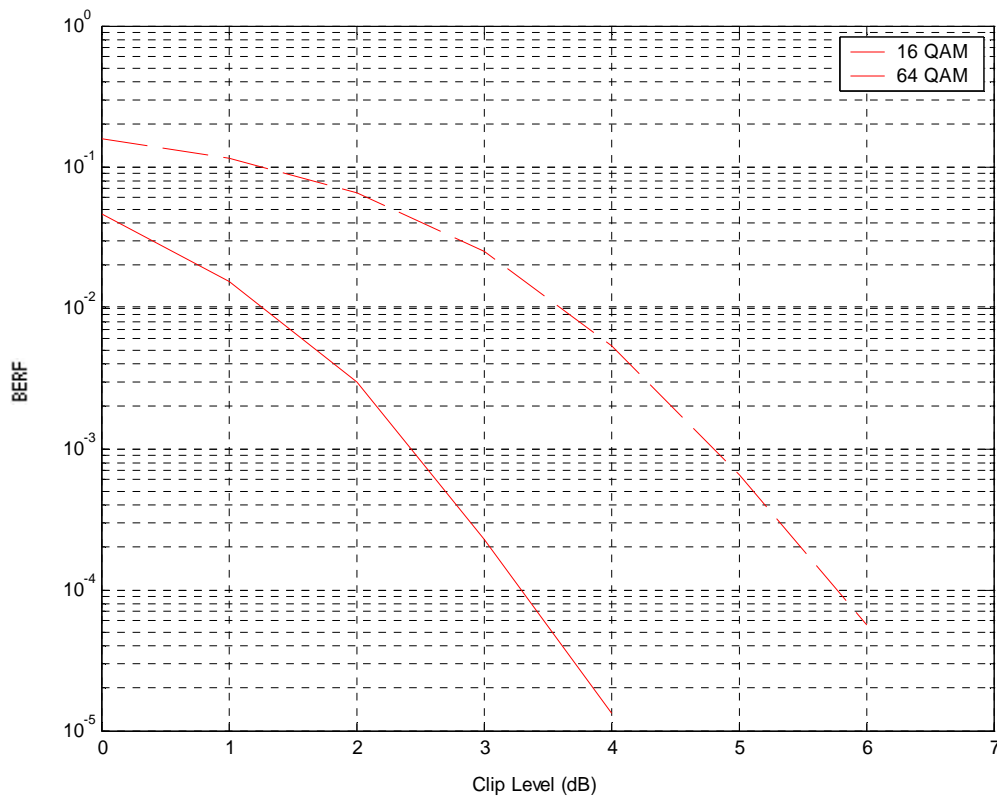


Figure 7.9: Baseband clip level vs. the BERF with varying M -ary constellations. 128 point IFFT ($os=2$), RRCF with 128 taps and $\alpha=0.15$. AWGN=0.

Effect of changing P in HPA

The model used to simulate the HPA is the SSPA described in Section 3.4.1. Varying the value of p in the SSPA controls the input to output curve of the amplifier as shown in Figure 3.14. Figure 7.10 demonstrates the effect of changing p on the BERF, the saturation level of the SSPA is set equal to the baseband clipping level. Here it is seen that $p=1$ has an extreme effect on the BERF. $P=3$ causes a magnitude of degradation over the absolutely linear region of $p=1000$. As $p=3$ is a practical value used in many designs [40] it will be used in all further simulations.

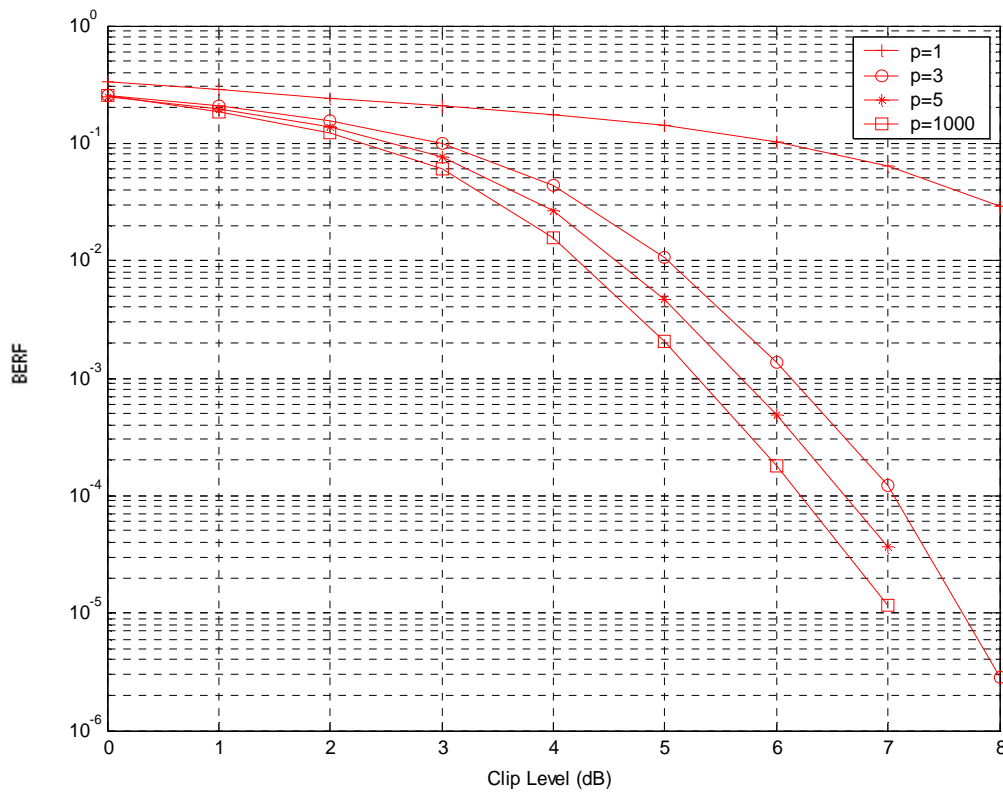


Figure 7.10: Baseband clip level vs the BERF with varying p in the SSPA. 128 point IFFT ($os=2$), RRCF with 128 taps and $\alpha=0.15$. HPA backoff set equal to baseband clipping level. AWGN=0.

This section provided a description and simulations of an OFDM system with baseband clipping. The effects of oversampling the IFFT, filter parameters, HPA parameters, and mapping type were simulated to see their effect on the baseband CL vs. the BERF. It can be concluded that a good set of parameters for further analysis of an OFDM system are:

- Oversampling factor of 2 in the IFFT.
- RRCF with 128 filter taps and a roll off factor of 0.15.
- A SSPA with $p=3$.

7.2 New Sector Clipping method

A new technique for clipping developed by the author which reduces hardware complexity is *Sector* clipping [3]. *Sector* clipping avoids magnitude estimates which require hardware multiplications to perform corrective scaling. The decision to clip is based on the I and Q values in conjunction with comparisons between them, and so divides the clipping region into different ‘sectors’. Figure 7.11 shows the I Q plane of *Sector clipping* with the clipping regions clearly identified. The new method requires only comparators and can be implemented in hardware as either an iterative (to reduce complexity) or parallel structure (to increase speed). The number of sectors can vary from 2 (square clipping) to 5 or more, although no discernable improvement in performance is seen above this number. Note that increasing the number of decisions beyond 5 Sector will clipping increase the complexity as much as multiplications.

As seen in Figure 7.11, *Sector* clipping not only introduces extra amplitude distortion over conventional clipping, but also phase distortion as data outside the clipping regions is not reduced in line with the origin. The symmetry of *Sector* clipping can be exploited to further reduce hardware complexity, the data can be ‘folded’ into the first octant by removing the sign bits (making it positive) and making the largest value of the complex signal the real component, the clipping operation is then performed on the new value. Sign bits and the relative size of the real and imaginary components can then be used to extrapolate the original position of the clipped sample. As there are 3 unique sectors in Figure 7.11 this structure is known as 3 *Sector* clipping.

7.2.1 Theoretical Analysis of Clipping Techniques

In order to compare the performance of the various clipping techniques the Clip Level vs. SNR is mathematically derived for 3 cases: *Conventional* clipping, *Sector* clipping with 3 sectors, and *Square* clipping. *Square* clipping can be construed as a DAC with limited word length. Note that for the theoretical analysis, no oversampling, filtering, or amplifier is assumed.

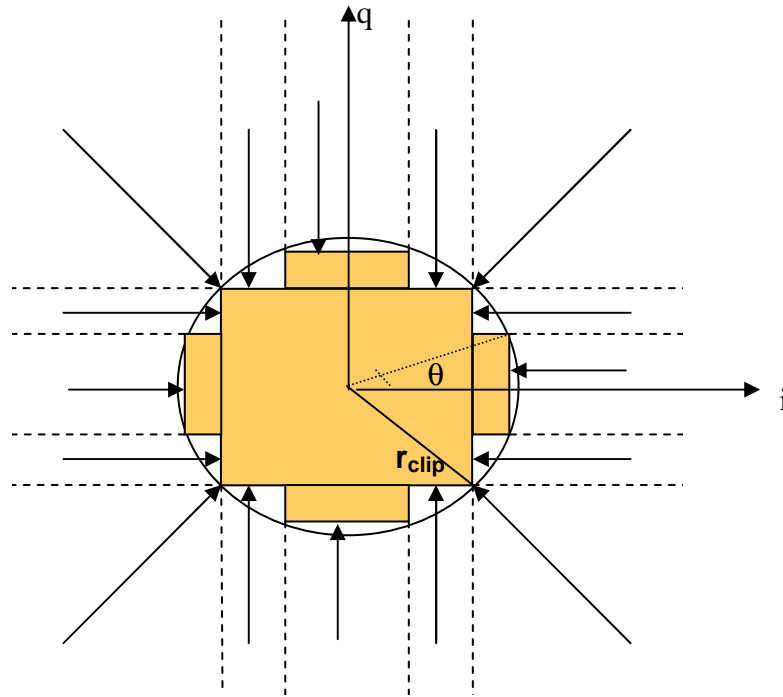


Figure 7.11: I Q diagram showing different sector clipping regions and the direction of data reduction for 3 Sector Clipping.

7.2.1.1 SNR Analysis

The relation between the input and output of the clipping operation is expressed pictorially in Figure 7.11 and can be used to find an expression for the SNR.

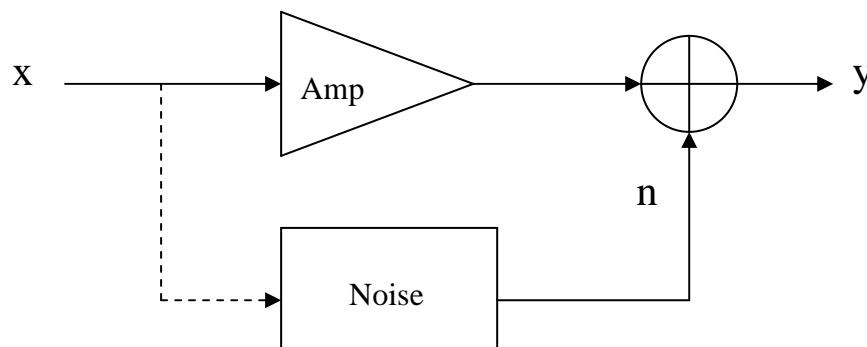


Figure 7.12: Input output relationship of clipping operation.

Mathematically, this relation between the input, x , and the output, y can be expressed as Bussgang's theorem

$$y = \alpha x + n \quad (7.2)$$

where x is the input signal, y is the output signal and α is chosen so that the input signal and the noise, n , is uncorrelated. Finding the 2nd moment of y (7.2) gives

$$\begin{aligned} E[yy] &= E[(\alpha x + n)(\alpha x + n)] \\ R_{yy} &= \alpha^2 R_{xx} + 2\alpha E[xn] + R_{nn} \end{aligned} \quad (7.3)$$

where R_{xx} is the autocorrelation of the input signal giving the input power, R_{yy} is the autocorrelation of the output signal giving the output power. As x is assumed to be uncorrelated to the noise the term $2\alpha E[xn]$ can be removed and (7.3) can be rearranged and solved for the noise power, R_{nn} .

$$R_{nn} = R_{yy} - \alpha^2 R_{xx} \quad (7.4)$$

Rearranging (7.2)

$$n = y - \alpha x \quad (7.5)$$

Taking the expected moments of (7.5) and then the correlation functions yields

$$\begin{aligned} E[nn] &= E[(y - \alpha x)(y - \alpha x)] \\ R_{nn} &= R_{yy} - 2\alpha R_{xy} + \alpha^2 R_{xx} \end{aligned} \quad (7.6)$$

Equating (7.4) and (7.6) and solving for α :

$$\begin{aligned} R_{yy} - \alpha^2 R_{xx} &= R_{yy} - 2\alpha R_{xy} + \alpha^2 R_{xx} \\ 0 &= 2\alpha^2 R_{xx} - 2\alpha R_{xy} \\ \alpha &= \frac{R_{xy}}{R_{xx}} \end{aligned} \quad (7.7)$$

The signal, S is equal to:

$$S = \alpha^2 R_{xx} \quad (7.8)$$

and the noise is given in (7.4), the SNR is then (7.9).

$$\frac{S}{N} = \frac{\alpha^2 R_{xx}}{R_{yy} - \alpha^2 R_{xx}} \quad (7.9)$$

To reduce mathematical complexity substitutions are made to factor out R_{xx} . The new SNR is given by (7.10).

$$\frac{S}{N} = \frac{\alpha^2}{\frac{R_{xy}}{R_{xx}} - \alpha^2} \quad (7.10)$$

The expressions for the correlation functions need to be defined for each of the clipping techniques, which are solved to find a closed form solution.

7.2.1.2 Conventional clipping

The definitions for the autocorrelation of the input, autocorrelation of the output and cross correlation for conventional clipping are respectively given below.

$$R_{xx(0)} = \int_0^{\infty} r^2 \cdot f(r) \partial r \quad (7.11)$$

$$R_{yy(0)} = \int_0^{r_{clip}} r^2 \cdot f(r) \partial r + \int_{r_{clip}}^{\infty} r_{clip}^2 \cdot f(r) \partial r \quad (7.12)$$

$$R_{xy(0)} = \int_0^{r_{clip}} r^2 \cdot f(r) \partial r + \int_{r_{clip}}^{\infty} r \cdot r_{clip} \cdot f(r) \partial r \quad (7.13)$$

where r is the input data (i.e. the magnitude of the data at the output of the IFFT), r_{clip} is the clipping level, and $f(r)$ is the probability distribution of the data, r , which is assumed to be Rayleigh distributed.

$$f(r) = \frac{r}{\sigma^2} e^{-\frac{r^2}{2\sigma^2}} \quad (7.14)$$

Note that for the Rayleigh assumption of the distribution of 'r' to hold the number of subcarriers is assumed to be greater or equal to 64 [39]. In order to reduce the mathematical complexity of the correlation functions they are normalized by the average input voltage, $\sigma\sqrt{2}$.

$$R = \frac{r}{\sigma\sqrt{2}} \quad (7.15a)$$

$$R_{clip} = \frac{r_{clip}}{\sigma\sqrt{2}} \quad (7.15b)$$

$$\partial R = \frac{\partial r}{\sigma\sqrt{2}} \quad (7.15c)$$

Substituting (7.15a, b, c) into (7.11), (7.12), and (7.13) yields the normalized expressions for R_{xx} , R_{xy} , and R_{yy} given in (7.16), (7.17), and (7.18).

$$R_{xx(0)} = 4\sigma^2 \int_0^\infty R^3 \cdot f(R) \partial R \quad (7.16)$$

$$R_{yy(0)} = 4\sigma^2 \int_0^{R_{clip}} R^3 \cdot f(R) \partial R + 4\sigma^2 \int_{R_{clip}}^\infty R_{clip}^2 \cdot R \cdot f(R) \partial R \quad (7.17)$$

$$R_{xy(0)} = 4\sigma^2 \int_0^{R_{clip}} R^3 \cdot f(R) \partial R + 4\sigma^2 \int_{R_{clip}}^\infty R^2 \cdot R_{clip} \cdot f(R) \partial R \quad (7.18)$$

where $f(R)$ is the normalized Rayleigh probability distribution of the data, R .

$$f(R) = e^{-R^2} \quad (7.19)$$

The normalised clip level is also required (7.20)

$$\begin{aligned} dB_{clip} &= 20 \log_{10} \left(\frac{r}{\sigma \sqrt{2}} \right) \\ dB_{clip} &= 20 \log_{10} (R) \\ R &= 10^{\frac{dB_{clip}}{20}} \end{aligned} \quad (7.20)$$

The evaluated correlation expressions of (7.16), (7.17), and (7.18) are shown in (7.21), (7.22), and (7.23). These are substituted into (7.10) to calculate the SNR at various clipping levels.

$$R_{xx(0)} = 2\sigma^2 \quad (7.21)$$

$$\frac{R_{yy(0)}}{R_{xx(0)}} = -e^{-R_{clip}^2} + 1 \quad (7.22)$$

$$\alpha = \frac{R_{xy(0)}}{R_{xx(0)}} = -e^{-R_{clip}^2} + 1 + \frac{\sqrt{\pi}}{2} R_{clip} - \frac{\sqrt{\pi}}{2} R_{clip} \cdot erf(R_{clip}) \quad (7.23)$$

The SNR vs. clipping level for conventional clipping reduces to (7.24)

$$SNR_{conv} = \frac{\left(-e^{-R_{clip}^2} + 1 + \frac{\sqrt{\pi}}{2} R_{clip} - \frac{\sqrt{\pi}}{2} R_{clip} \cdot erf(R_{clip}) \right)^2}{\left(-e^{-R_{clip}^2} + 1 \right) \left(\alpha = \frac{R_{xy(0)}}{R_{xx(0)}} = -e^{-R_{clip}^2} + 1 + \frac{\sqrt{\pi}}{2} R_{clip} - \frac{\sqrt{\pi}}{2} R_{clip} \cdot erf(R_{clip}) \right)^2} \quad (7.24)$$

A plot of the theoretical SNR vs. conventional clip level is shown in Figure 7.16.

7.2.1.3 Sector Clipping

In sector clipping the reduction in hardware complexity comes at a cost of introducing extra amplitude distortion and phase distortion as the components of the complex signal are not attenuated by the same scaling factor. This leads to more complex equations for R_{xx} , R_{xy} , and R_{yy} as the data must be represented in terms of its Cartesian co-ordinates.

A way to realize the transition from polar to Cartesian is to recognize that the joint probability of two independent, zero mean, quadrature shifted, Gaussian-distributed variables, x and y , with the same σ create a Rayleigh distribution (7.25).

$$f(x, y) = \frac{1}{\sigma\sqrt{2\pi}} e^{\frac{-x^2}{2\sigma^2}} \times \frac{1}{\sigma\sqrt{2\pi}} e^{\frac{-y^2}{2\sigma^2}} \quad (7.25)$$

$$f(x, y) = \frac{1}{2\pi\sigma^2} e^{\frac{-x^2-y^2}{2\sigma^2}}$$

3 sector clipping levels are defined relative to r_{clip} (7.26a, b, c) of the conventional clipping method. The clipping regions for 3 sector clipping are shown in Figure 7.13 showing the vectors of an unclipped signal and the resultant clipped sample.

$$l_0 = r_{clip} \sin \theta \quad (7.26a)$$

$$l_1 = \frac{r_{clip}}{\sqrt{2}} \quad (7.26b)$$

$$l_2 = r_{clip} \cos \theta \quad (7.26c)$$

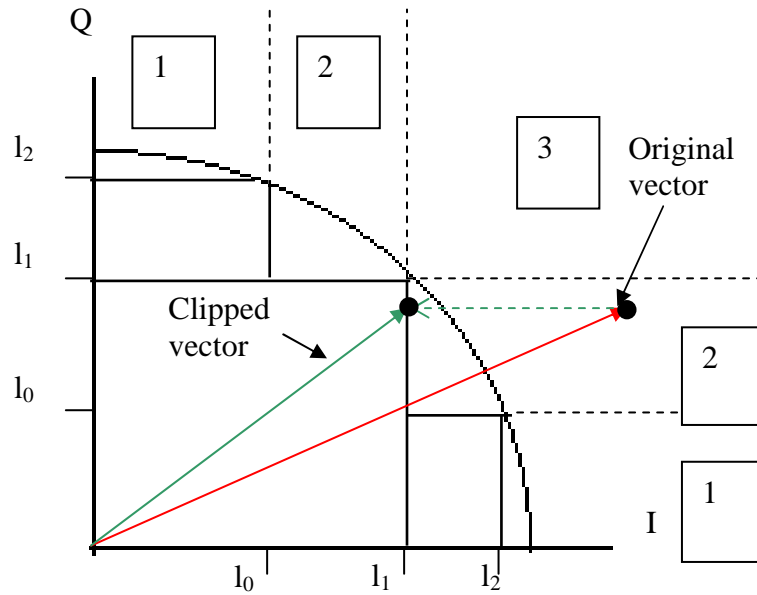


Figure 7.13: I Q diagram of 1st quadrant of a 3 Sector clipping system showing the vector of an unclipped and clipped sample.

The new sector clipping correlation equations for R_{xx} , R_{yy} , and R_{xy} are listed (7.27, 7.28, 7.29) respectively below. Due to symmetry, only the first quadrant is used

$$R_{xx(0)} = \int_0^{\infty} \int_0^{\infty} (x^2 + y^2) \cdot f(x, y) \partial x \partial y \quad (7.27)$$

The autocorrelation of the output equations are set out in (7.28) where the symmetry of the clipping regions is exploited. The limits of the integrals of each part (7.28) dictate what will happen at the output. Hence the first 2 parts of (7.28) do nothing to the data as they are inside the clipping region. The last 3 parts of (7.28) (1, 2, and 3 in Figure 7.13)) perform the attenuation as evidenced by the limits.

$$\begin{aligned}
 R_{yy(0)} &= 4 \int_0^{l_1} \int_0^{l_1} (x^2 + y^2) \cdot f(x, y) \partial x \partial y \\
 &+ 8 \int_{l_1}^{l_2} \int_0^{l_0} (x^2 + y^2) \cdot f(x, y) \partial x \partial y \\
 &+ 8 \int_{l_2}^{\infty} \int_0^{l_0} (l_2^2 + y^2) \cdot f(x, y) \partial x \partial y \\
 &+ 8 \int_{l_1}^{\infty} \int_{l_0}^{l_1} (l_1^2 + y^2) \cdot f(x, y) \partial x \partial y \\
 &+ 4 \int_{l_1}^{\infty} \int_{l_1}^{\infty} (l_1^2 + l_1^2) \cdot f(x, y) \partial x \partial y
 \end{aligned} \tag{7.28}$$

The cross correlation (7.29) follows the same form as (7.28) where the first 2 parts are inside the clipping regions. The last 3 parts of (7.29) show the translation of the input sample to the output. Again the symmetry of Figure 7.13 is exploited.

$$\begin{aligned}
 R_{xy(0)} &= 4 \int_0^{l_1} \int_0^{l_1} (x^2 + y^2) \cdot f(x, y) \partial x \partial y \\
 &+ 8 \int_{l_1}^{l_2} \int_0^{l_0} (x^2 + y^2) \cdot f(x, y) \partial x \partial y \\
 &+ 8 \int_{l_2}^{\infty} \int_0^{l_0} (xl_2 + y^2) \cdot f(x, y) \partial x \partial y \\
 &+ 8 \int_{l_1}^{\infty} \int_{l_0}^{l_1} (xl_1 + y^2) \cdot f(x, y) \partial x \partial y \\
 &+ 4 \int_{l_1}^{\infty} \int_{l_1}^{\infty} (xl_1 + yl_1) \cdot f(x, y) \partial x \partial y
 \end{aligned} \tag{7.29}$$

As in the normalized conventional clipping method, substitutions are made to remove σ and reduce the complexity of the correlation functions.

$$X = \frac{x}{\sigma\sqrt{2}} \tag{7.30a} \qquad Y = \frac{y}{\sigma\sqrt{2}} \tag{7.30b}$$

$$\partial X = \frac{\partial x}{\sigma\sqrt{2}} \tag{7.30c} \qquad \partial Y = \frac{\partial y}{\sigma\sqrt{2}} \tag{7.30d}$$

$$L_0 = \frac{l_0}{\sigma\sqrt{2}} \quad (7.30e) \quad L_1 = \frac{l_1}{\sigma\sqrt{2}} \quad (7.30f) \quad L_2 = \frac{l_2}{\sigma\sqrt{2}} \quad (7.30g)$$

Substituting (7.30) into (7.27), (7.28), and (7.29) yields the simplified expressions for the 3 sector clipping correlation functions. The normalized equation for $R_{xx(0)}$ is

$$R_{xx(0)} = 2\sigma^2 \int_{-\infty}^{\infty} \int_{-\infty}^{\infty} (X^2 + Y^2) \cdot f(X, Y) \partial X \partial Y \quad (7.31)$$

The normalized equation for α is

$$\begin{aligned} \alpha = \frac{R_{xy(0)}}{R_{xx(0)}} &= 4 \int_0^{L_1} \int_0^{L_1} (X^2 + Y^2) \cdot f(X, Y) \partial X \partial Y \\ &+ 8 \int_{L_1}^{L_2} \int_0^{L_0} (X^2 + Y^2) \cdot f(X, Y) \partial X \partial Y \\ &+ 8 \int_{L_2}^{\infty} \int_0^{L_0} (XL_2 + Y^2) \cdot f(X, Y) \partial X \partial Y \\ &+ 8 \int_{L_1}^{\infty} \int_{L_0}^{L_1} (XL_1 + Y^2) \cdot f(X, Y) \partial X \partial Y \\ &+ 4 \int_{L_1}^{\infty} \int_{L_1}^{\infty} (XL_1 + YL_1) \cdot f(X, Y) \partial X \partial Y \end{aligned} \quad (7.32)$$

The normalized equation for $R_{yy(0)}$ is

$$\begin{aligned} \frac{R_{yy(0)}}{R_{xx(0)}} &= 4 \int_0^{L_1} \int_0^{L_1} (X^2 + Y^2) \cdot f(X, Y) \partial X \partial Y \\ &+ 8 \int_{L_1}^{L_2} \int_0^{L_0} (X^2 + Y^2) \cdot f(X, Y) \partial X \partial Y \\ &+ 8 \int_{L_2}^{\infty} \int_0^{L_0} (L_2^2 + Y^2) \cdot f(X, Y) \partial X \partial Y \\ &+ 8 \int_{L_1}^{\infty} \int_{L_0}^{L_1} (L_1^2 + Y^2) \cdot f(X, Y) \partial X \partial Y \\ &+ 8 \int_{L_1}^{\infty} \int_{L_1}^{\infty} L_1^2 \cdot f(X, Y) \partial X \partial Y \end{aligned} \quad (7.33)$$

Where $f(X, Y)$ is given by (7.34)

$$f(X, Y) = \frac{e^{-X^2 - Y^2}}{\pi} \quad (7.34)$$

The normalized clipping levels are

$$\begin{aligned}
 dB_{clip} &= 20 \log_{10} \left(\frac{r}{\sigma \sqrt{2}} \right) \\
 dB_{clip} &= 20 \log_{10} (R) \\
 R &= 10^{\frac{dB_{clip}}{20}}
 \end{aligned} \tag{7.35}$$

The evaluated correlation expressions of (7.31), (7.32), and (7.33) are shown in (7.36), (7.38), and (7.40). These are substituted into (7.10) to calculate the SNR at various clipping levels.

$$R_{xx(0)} = 2\sigma^2 \tag{7.36}$$

α was calculated to be (7.37)

$$\begin{aligned}
 \alpha &= \frac{R_{xy(0)}}{R_{xx(0)}} = \left[2 \operatorname{erf}(L_1) \left(\frac{-L_1}{\sqrt{\pi}} e^{-L_1^2} + \frac{\operatorname{erf}(L_1)}{2} \right) \right] \\
 &+ 2 \left[\left(\operatorname{erf}(L_2) - \operatorname{erf}(L_1) \right) \cdot \left(\frac{-L_0}{\sqrt{\pi}} e^{-L_0^2} + \frac{\operatorname{erf}(L_0)}{2} \right) \right] \\
 &+ \frac{2L_2}{\sqrt{\pi}} e^{-L_2^2} \operatorname{erf}(L_0) + 2 \left[1 - \operatorname{erf}(L_2) \right] \left[\frac{-L_0}{\sqrt{\pi}} e^{-L_0^2} + \frac{\operatorname{erf}(L_0)}{2} \right] \\
 &+ \frac{2}{\sqrt{\pi}} \left[\left(1 - \operatorname{erf}(L_1) \right) \cdot \left(L_0 e^{-L_0^2} - L_1 e^{-L_1^2} + \frac{\sqrt{\pi}}{2} \operatorname{erf}(L_1) - \frac{\sqrt{\pi}}{2} \operatorname{erf}(L_0) \right) \right] \\
 &+ \frac{2}{\sqrt{\pi}} \left[L_1 e^{-L_1^2} \left(\operatorname{erf}(L_1) - \operatorname{erf}(L_0) \right) \right] + \frac{2L_1}{\sqrt{\pi}} e^{-L_1^2} \left(1 - \operatorname{erf}(L_1) \right)
 \end{aligned} \tag{7.37}$$

Which after expansion and reduction becomes

$$\alpha = \frac{R_{xy(0)}}{R_{xx(0)}} = \operatorname{erf}(L_2) \operatorname{erf}(L_0) - \operatorname{erf}(L_1) \operatorname{erf}(L_0) + \operatorname{erf}(L_1) \tag{7.38}$$

The normalized autocorrelation of the output, $\frac{R_{yy(0)}}{R_{xx(0)}}$ was derived to be (7.39)

$$\begin{aligned}
 \frac{R_{yy(0)}}{R_{xx(0)}} &= 2\operatorname{erf}(L_1) \left(\frac{-L_1}{\sqrt{\pi}} e^{-L_1^2} + \frac{\operatorname{erf}(L_1)}{2} \right) \\
 &+ 2 \left[\left(\operatorname{erf}(L_2) - \operatorname{erf}(L_1) \right) \left(\frac{-L_0}{\sqrt{\pi}} e^{-L_0^2} + \frac{\operatorname{erf}(L_0)}{2} \right) \right] \\
 &+ 2\operatorname{erf}(L_0) \left[\frac{-L_2}{\sqrt{\pi}} e^{-L_2^2} + \frac{\operatorname{erf}(L_2)}{2} + \frac{L_1}{\sqrt{\pi}} e^{-L_1^2} - \frac{\operatorname{erf}(L_1)}{2} \right] \\
 &+ 2L_2^2 \operatorname{erf}(L_0) (1 - \operatorname{erf}(L_2)) + 2(1 - \operatorname{erf}(L_2)) \left(\frac{-L_0}{\sqrt{\pi}} e^{-L_0^2} + \frac{\operatorname{erf}(L_0)}{2} \right) \\
 &+ 2 \left[(1 - \operatorname{erf}(L_1)) \left(\frac{-L_1}{\sqrt{\pi}} e^{-L_1^2} + \frac{\operatorname{erf}(L_1)}{2} + \frac{L_0}{\sqrt{\pi}} e^{-L_0^2} - \frac{\operatorname{erf}(L_0)}{2} \right) \right] \\
 &+ 2L_1^2 \left[(1 - \operatorname{erf}(L_1)) (\operatorname{erf}(L_1) - \operatorname{erf}(L_0)) \right] + 2L_1^2 \left[(1 - \operatorname{erf}(L_1))^2 \right]
 \end{aligned} \tag{7.39}$$

Which after expansion and reduction becomes (7.40)

$$\begin{aligned}
 \frac{R_{yy(0)}}{R_{xx(0)}} &= 2\operatorname{erf}(L_0) \left[\frac{-L_2}{\sqrt{\pi}} e^{-L_2^2} + \frac{L_1}{\sqrt{\pi}} e^{-L_1^2} \right] \\
 &+ \operatorname{erf}(L_0) \left[\operatorname{erf}(L_2) - \operatorname{erf}(L_1) \right] \\
 &+ 2L_2^2 \operatorname{erf}(L_0) \left[1 - \operatorname{erf}(L_2) \right] - \frac{2L_1}{\sqrt{\pi}} e^{-L_1^2} + \operatorname{erf}(L_1) \\
 &+ 2L_1^2 \operatorname{erf}(L_1) \left[\operatorname{erf}(L_0) - 1 \right] + 2L_1^2 \left[1 - \operatorname{erf}(L_0) \right]
 \end{aligned} \tag{7.40}$$

The closed form solution is shown in (7.41).

$$SNR_{3Sec} = \frac{\left(erf(L_2)erf(L_0) - erf(L_1)erf(L_0) + erf(L_1) \right)^2}{\left(\begin{array}{l} 2erf(L_0) \left[\frac{-L_2}{\sqrt{\pi}} e^{-L_2^2} + \frac{L_1}{\sqrt{\pi}} e^{-L_1^2} \right] \\ + erf(L_0) [erf(L_2) - erf(L_1)] \\ + 2L_2^2 erf(L_0) [1 - erf(L_2)] \\ - \frac{2L_1}{\sqrt{\pi}} e^{-L_1^2} + erf(L_1) \\ + 2L_1^2 erf(L_1) [erf(L_0) - 1] \\ + 2L_1^2 [1 - erf(L_0)] \end{array} \right)^2 - \left(\begin{array}{l} erf(L_2)erf(L_0) \\ - erf(L_1)erf(L_0) \\ + erf(L_1) \end{array} \right)^2} \quad (7.41)$$

A block diagram showing 3 Sector clipping implemented with a LUT is shown in Figure 7.14. Note that the sign bits are removed in I_{in} and Q_{in} and attached back on at I_{out} and Q_{out} . A flowchart detailing the decision matrix in the algorithm is shown in Figure 7.15. From this the LUT in Figure 7.14 is derived and shown in Table 7.1, where it is seen that the LUT requires a 8 bit input and a $(N \times 2) + 2$ bit output. A plot of the theoretical SNR vs. 3 Sector clipping is shown in Figure 7.16. The latency of the structure in Figure 7.14 is low as the level comparisons are made in parallel and fed into the LUT. Further more when reviewing the truth table in Table 7.1 the inputs for '0' and L2 can be replaced with logic 0 and 1 respectively reducing the number of inputs to the LUT to 4 and by implication the size of the LUT.

Table 7.1: Truth Table for 3 Sector clipping

Input								Output			
I_{in}				Q_{in}				I_{clip}	Q_{clip}	Ctrl I	Ctrl Q
0	L_0	L_1	L_2	0	L_0	L_1	L_2				
X	X	1	X	X	X	1	X	L_1	L_1	1	1
X	X	X	1	1	0	X	X	L_2	Q_{in}	1	0
X	X	1	X	1	1	0	X	L_1	Q_{in}	1	0
1	0	X	X	X	X	X	1	I_{in}	L_2	0	1
1	1	0	X	X	X	1	X	I_{in}	L_1	0	1
For all other combinations data is passed through								I_{in}	Q_{in}	0	0

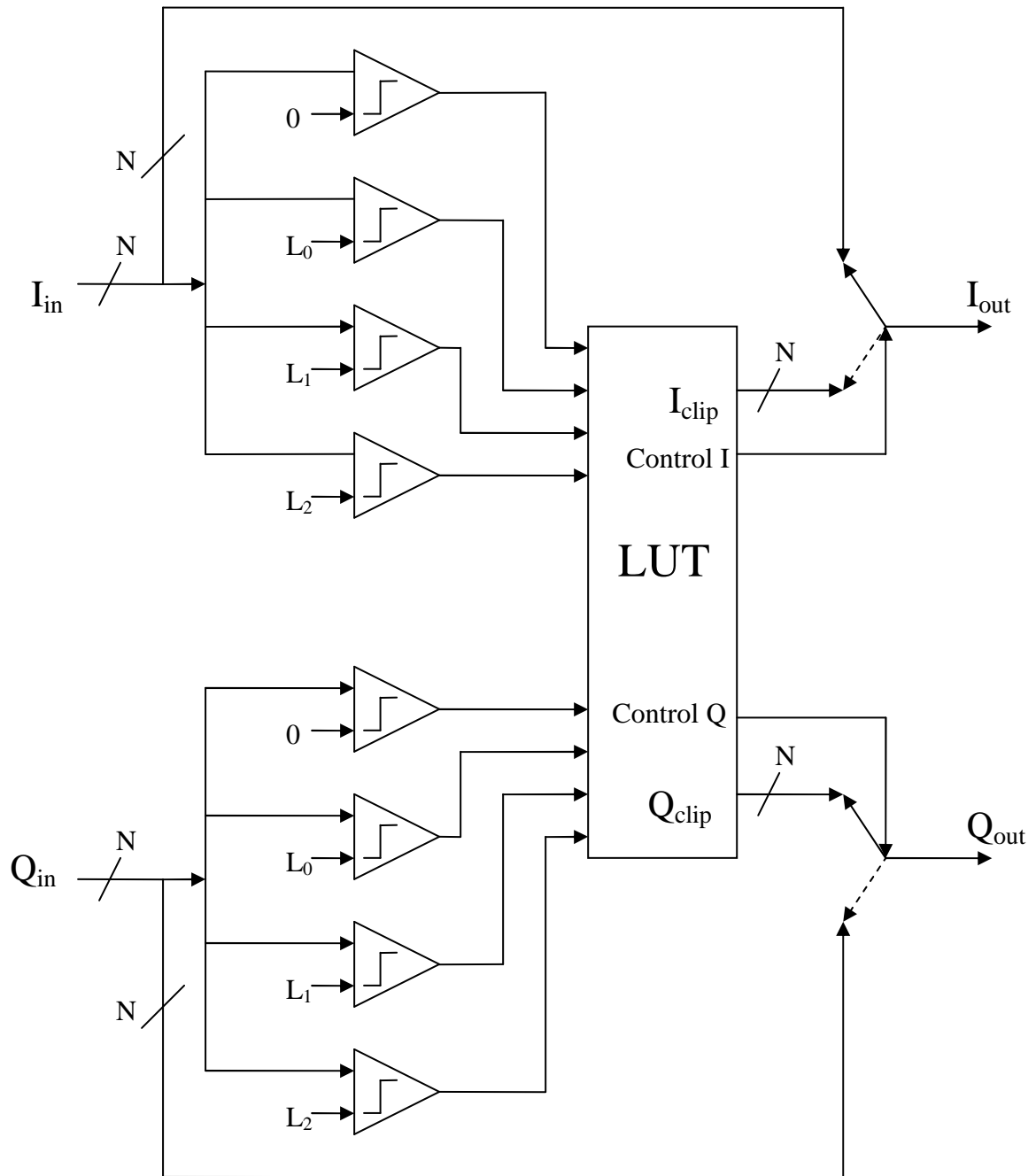


Figure 7.14: Block diagram of 3 Sector clipping.

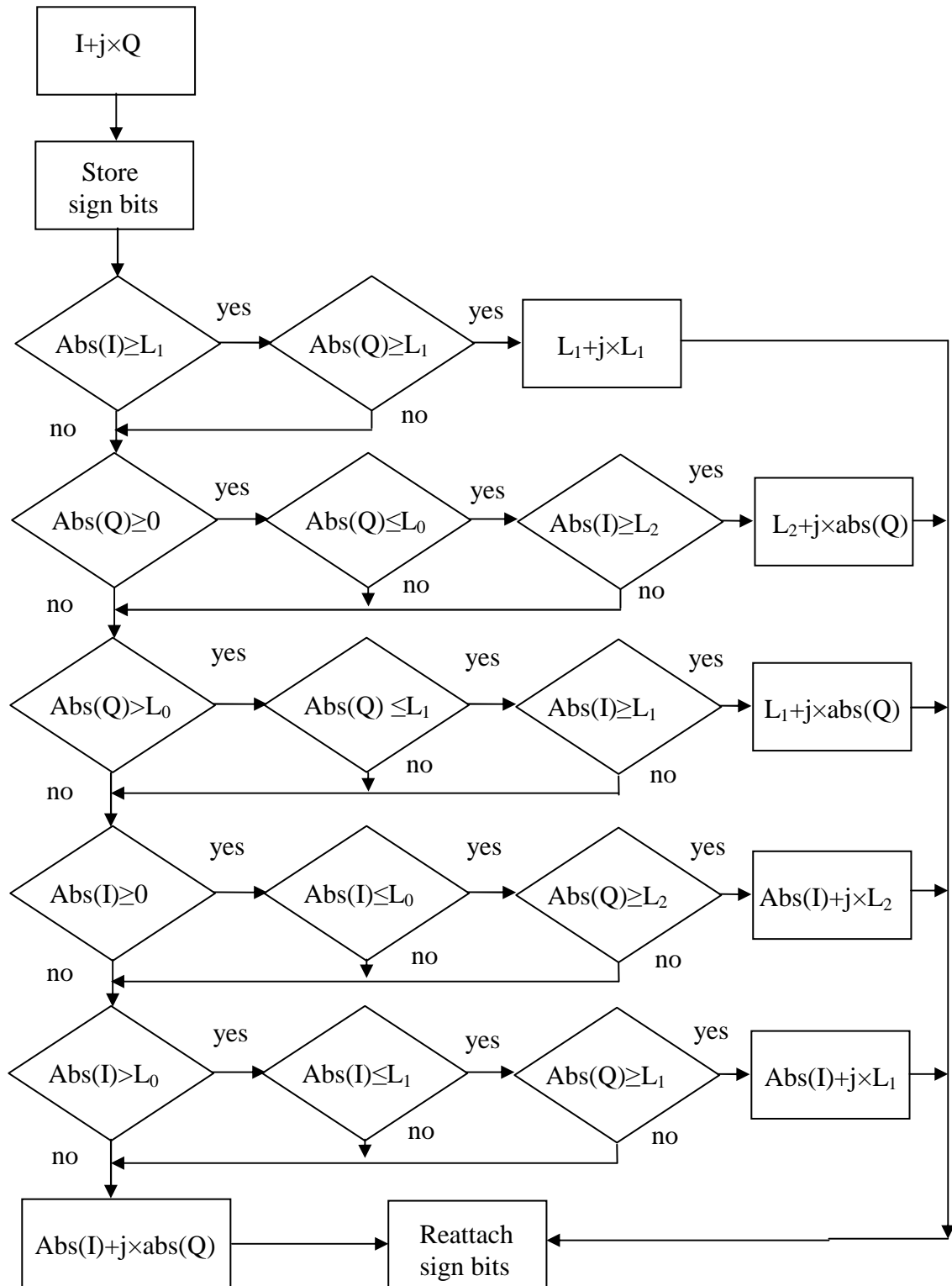


Figure 7.15: Flowchart for the LUT in Figure 7.14 (3 Sector clipping).

7.2.1.4 Square Clipping

Square clipping is the least complex form of clipping and is shown in the following theoretical results as a lower bound on the presented clipping techniques. The theoretical SNR for *Square* clipping can easily be found by using the same method as for *3 Sector* clipping and changing the limits on (7.32) and (7.33) where appropriate. That is by setting both I_0 and I_2 equal to I_1 in Figure 7.13. The equations are simpler to derive and can be construed as 2 sector clipping which is in fact Cartesian clipping.

7.2.1.5 Theoretical Results

The theoretical results for *Conventional*, *3 Sector*, and *Square* clipping SNR vs. clip level are shown in Figure 7.16 together with the equivalent simulated results. Note that for the simulated results no filtering, oversampling, or amplification is performed, the noise is measured after clipping. As expected *Conventional* clipping has the best performance and *Square* clipping the worst. *3 Sector* clipping has performance in the middle, but with greatly reduced complexity requiring only a few comparators and a simple LUT, making it only marginally more complex than square clipping. Generally *3 Sector* clipping suffers a 1dB penalty in SNR compared to *conventional* clipping levels above 0dB. In other words in order for *3 sector* clipping to achieve the same SNR as *Conventional* clipping the clip level needs to be set 1dB higher than the *Conventional* case. Also of note it is seen that sector clipping performance approaches the same SNR as *Square* clipping at clip levels below 0dB. This makes sense as harder clip levels reduce the size of regions 1 and 2 in Figure 7.13, making the corner sector the dominant clip region, just as in *Square* clipping. Therefore *3 Sector* and *Square* clipping share the same lower SNR bound of 2.439dB. *Conventional* clipping has a lower SNR bound of 5.634dB.

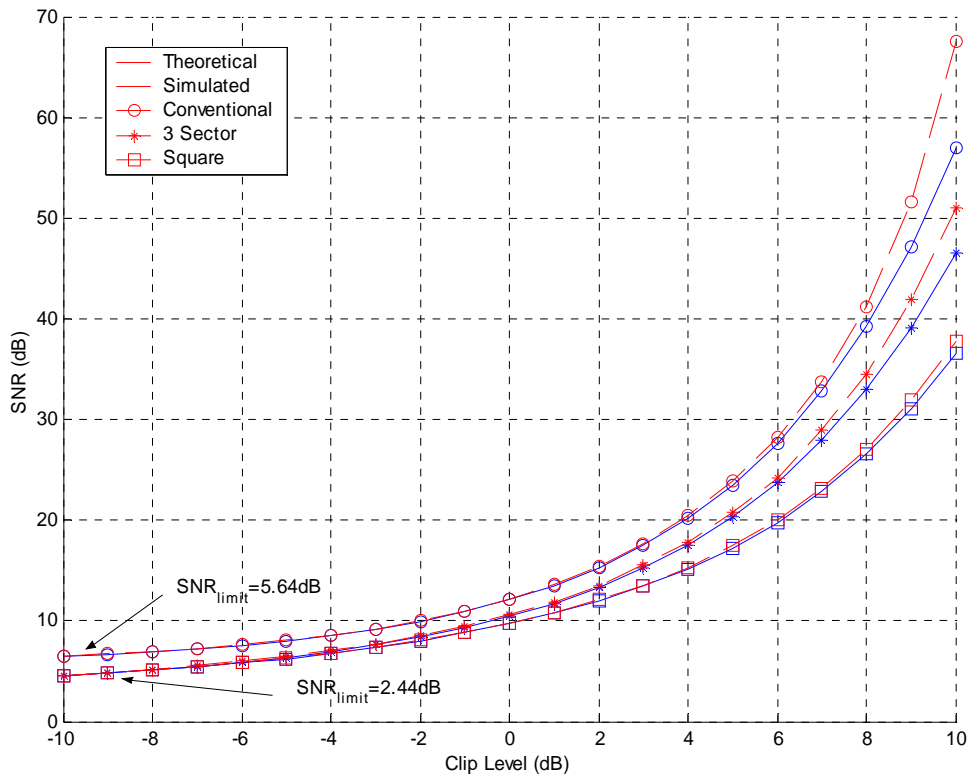


Figure 7.16: Theoretical Clip Level vs. SNR for *Conventional* (Standard), *3 Sector*, and *Square* Clipping. Theoretical (dashed), simulated (solid).

Comparing the simulated curves with the theoretical ones it is seen that they are well matched at clip levels below 6dB. At higher levels of clipping the simulated results have

slightly better SNR, this is due to the theoretical Rayleigh distribution assumption of the signal not holding at higher amplitude levels [89]. Simulated OFDM symbols have lower PDF values in the tail of the distribution.

Figure 7.17 plots the theoretical 3 sector clipping angle, θ (shown in Figure 7.11) vs. SNR for clip levels ranging from -10dB (at the bottom of Figure 7.16) to 10dB (at the top of Figure 7.16). The angle θ is varied from 20° to 40° . The choice of θ has no impact on harder clipping levels, but it does affect SNR performance at weaker levels (CL>5dB). It is seen that the optimum angle for θ is 27.5° , i.e. $\left(\frac{L_0}{L_2}\right) = \tan(27.5)$,

for all practical clipping levels as shown in Figure 7.17.

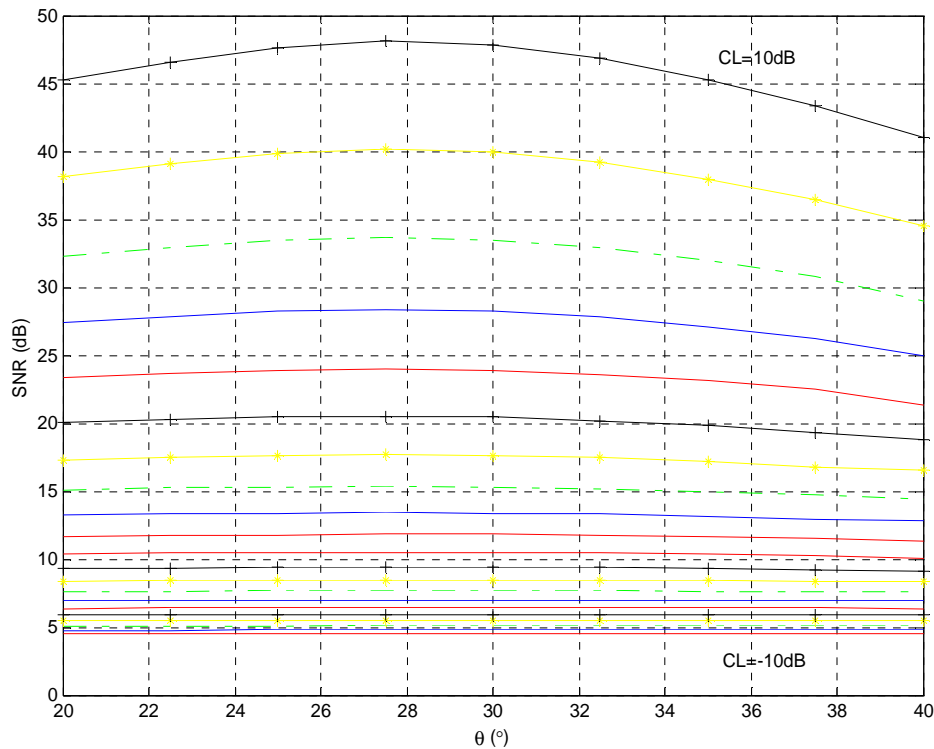


Figure 7.17: Clipping angle, θ (of Figure 7.11) vs. the SNR for 3 sector clipping, based on (7.41).

7.2.2 Extensions of Sector Clipping

3 Sector clipping can be extended to incorporate more sectors thereby improving performance. Figure 7.18 shows the I Q plot of the first quadrant of 4 and 5 Sector clipping. Figure 7.19 depicts simulated results for Sector Clipping with 3, 4, and 5 sectors as well as Conventional and Square clipping for comparison. Increasing the numbers of sectors from 3 to 4 improves the SNR by ~ 2 dB at a clipping level of 6dB. 5 sectors provides a further 0.5dB gain in SNR at the same clipping level. Generally, the SNR difference between the schemes increases with clipping level. The complexity increase for 4 and 5 sectors is minimal over 3 sector clipping requiring only a few extra comparators and a doubling of the LUT size.

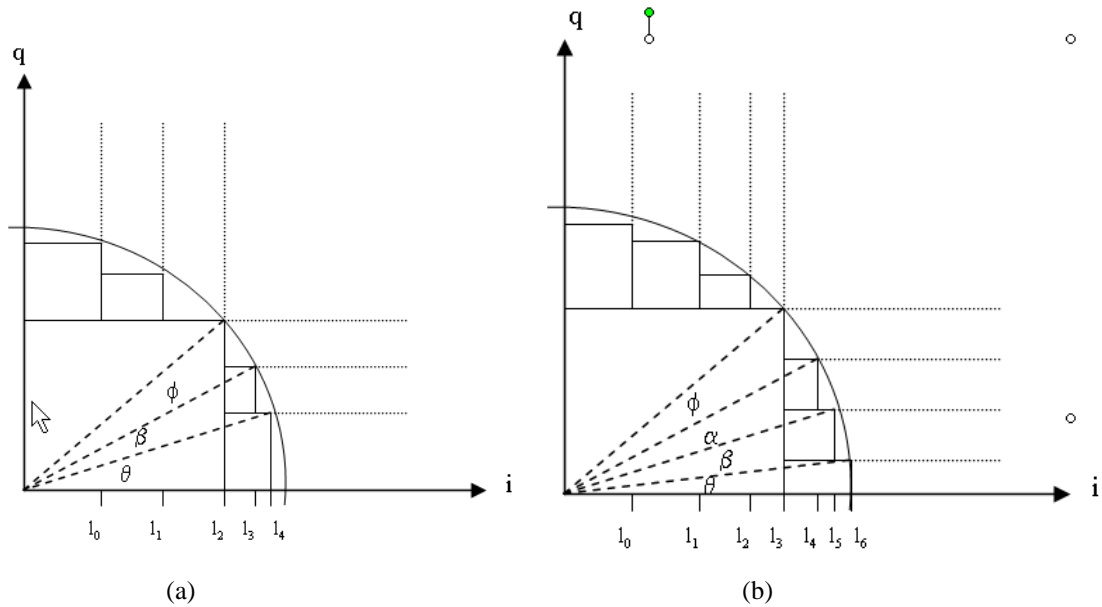


Figure 7.18: I Q diagram showing the 1st quadrant Sector clipping regions of a) 4 Sector clipping and b) 5 sector clipping.

The degradation in SNR for *Sector* clipping from optimal *Conventional* clipping is ~ 3 dB and the improvement in SNR over square clipping is ~ 4 dB at a clip level of 6dB. Results not shown here indicate that increasing the number of sectors above 5 shows no discernable improvement in the SNR. The choice of angles for 4 and 5 sector clipping has been found to be optimum when the angles which determine the sectors are equally spaced, i.e. for 4 sectors: $\theta=28.13^\circ$ and $\beta=39.75^\circ$; and 5 sectors: $\theta=11.25^\circ$, $\beta=22.5^\circ$, and $\alpha=33.75^\circ$.

This section detailed a new method for clipping OFDM symbols called *Sector* Clipping. The new method is very simple to implement requiring only a few extra comparators compared to *square* clipping, however its performance is closer to conventional clipping where traditionally more complex circuits are required.

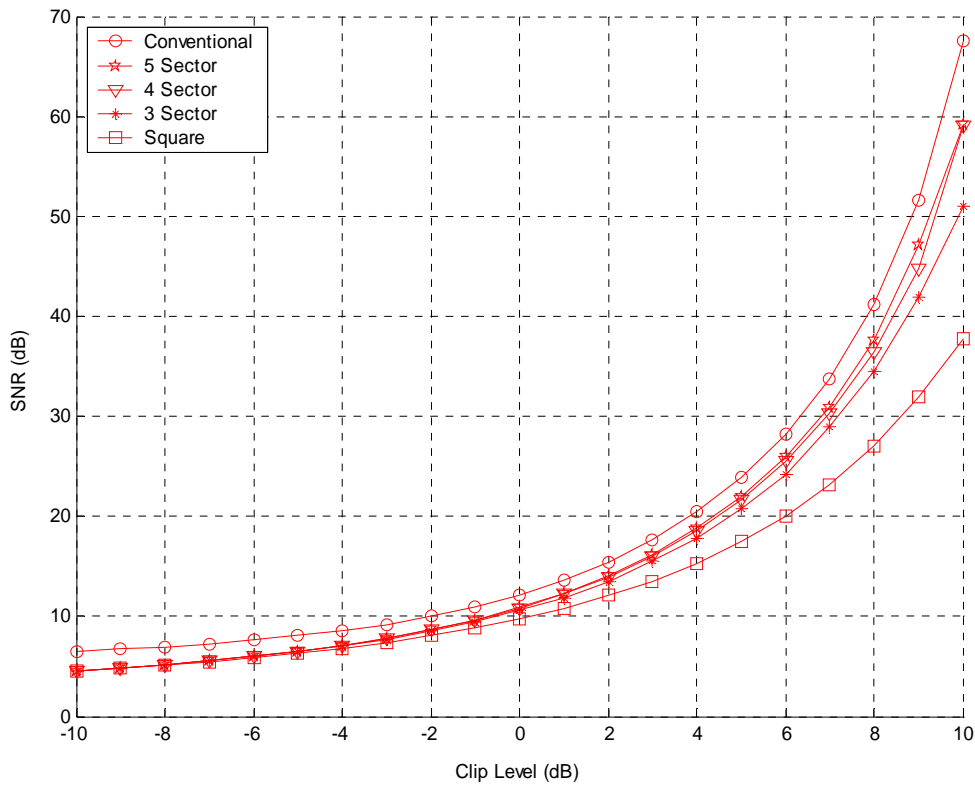


Figure 7.19: Simulated clip level vs. SNR for *Conventional*, *Square*, *3*, *4*, and *5 Sector* Clipping.

7.2.3 Hardware Implementation

3 Sector and *Square* clipping was implemented in digital form via Visual Hardware Design Language (VHDL). The two algorithms were then simulated using ‘Synopsys’ to ensure proper operation. Next the algorithms were compiled into ‘Verilog’ (VHDL code expressed in terms of gates, flip flops, etc.) code and simulated again in ‘Synopsys’. The ‘Verilog’ code was then exported into the ‘Cadence’ silicon design package, ‘Silicon Ensemble’, where routing and cell placement was performed with a 0.5μ standard cell and port library. After routing a ‘gds2’ file was produced which could then be sent to the foundry for production. However, this was not done, therefore the algorithm was only proved through hardware simulation. The design flow is summarized in Figure 7.20.

Figure 7.21 depicts the layout of the *3 sector* clipping algorithm with $N=8$ bit inputs. A gain table was included to allow 16 different Clipping levels (CL) set from -3dB to 12dB .

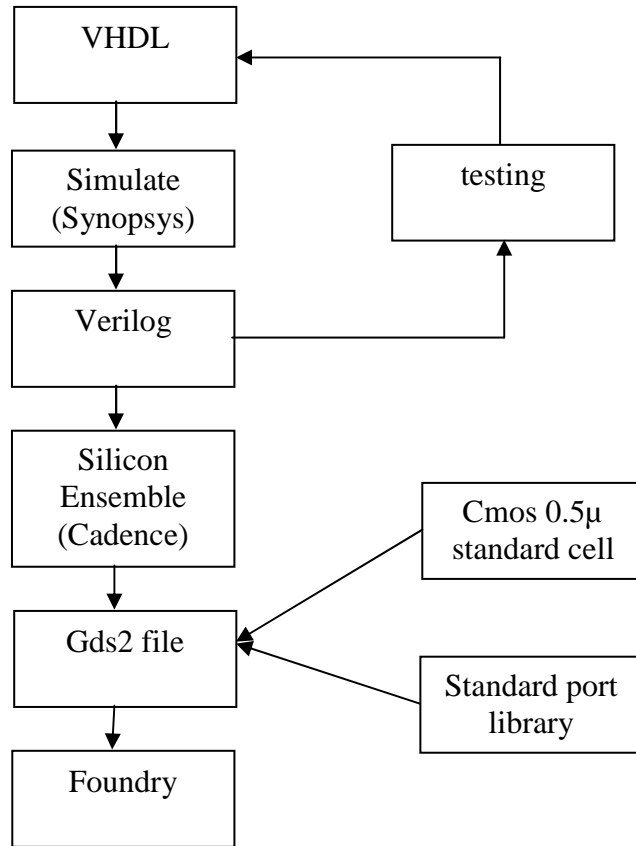


Figure 7.20: Design flow for silicon implementation of 3 sector clipping.

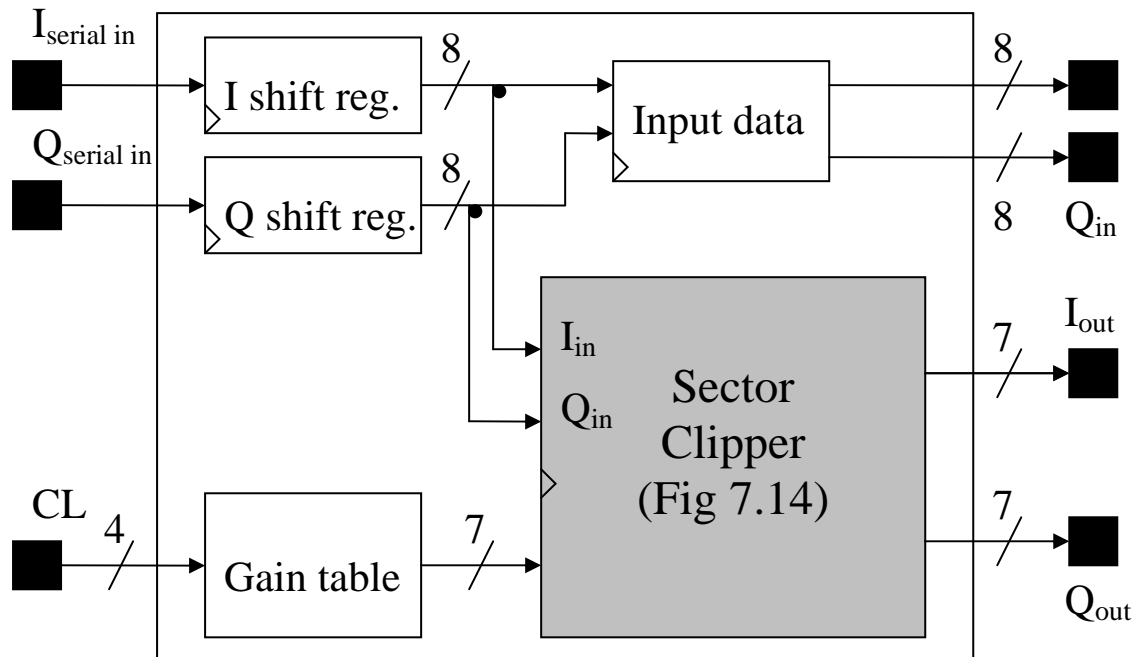


Figure 7.21: Block diagram of 3 Sector clipping implemented in VHDL.

Due to the clipping operation the Most Significant Bit (MSB) on each of the I and Q channels can be removed at the output. In order to save the number of input/output pins required, the I and Q input data is fed serially ($I_{in \text{ serial}}$ and $Q_{in \text{ serial}}$) into shift registers which then feed 8 bit words (I_{in} and Q_{in}) into the *3 Sector* clipping algorithm. The input data word is stored and output in parallel fashion for comparison to the clipped sample.

Table 7.2 shows a summary of various ‘Synopsys’ reports for the power consumption, delay path, and cell area of *Square* and *3 Sector* clipping. ‘System with buffer’ refers to the whole system shown in Figure 7.21 with the input and output buffers included. The buffers are necessary when the system is implemented as a stand alone device in silicon. In practice however the buffers are not necessary as only the clipping algorithm is implemented as a block in the whole OFDM transmitter.

Table 7.2: ‘Synopsys’ reports for *Square* and *3 sector* clipping. (Refer to Figure 7.21)

Hierarchy level	Report	Square clipping	3 sector clipping
System with buffer	Total cell area	13593.52 dbu	13827.55 dbu
	Total dynamic power	23.268mW	35.3874mW
System	Total cell area	357.16 dbu	591.1800 dbu
	Total dynamic power	11.5896mW	17.5455mW
Sector Clipper	Total cell area	110.37 dbu	385.38 dbu
	Total dynamic power	6.8317mW	8.7933mW
Gain table	Total cell area	62.70 dbu	131.08 dbu
	Total dynamic power	4.4682mW	8.3737mW
I and Q shift registers	Total cell area	37.36 dbu	37.36 dbu
	Total dynamic power	0.1893mW	0.1893mW

‘System’ again refers to Figure 7.21 without the input and output buffers. The cell area is greatly reduced in this case as the buffers take up a lot of space. The algorithm only takes up 4.27% of the total cell area for *3 Sector* clipping and only 2.62% for

Square clipping. The clipping algorithms themselves (‘Sector Clipper’ in Table 7.2) have an area of 385.38 dbu and 110.37 dbu for 3 *Sector* and *Square* clipping respectively, the power consumption is 8.7933mW and 6.8317mW for 3 *Sector* and *Square* clipping respectively. The 3 *Sector* Gain Table requires 50% more cells than *Square* clipping and the power consumption is doubled due to the extra clip levels required for sector clipping. The shift registers are the same in both systems.

Table 7.3 and 7.4 show the ‘Cadence’ reports for *Square* and 3 *Sector* clipping respectively. A 0.5 μ process with 3 metal layers was used. As is seen in the Application Specific Integrated Circuit (ASIC) view of 3 *Sector* clipping Figure 7.22 the size of the chip is determined by the input/output pads which are abutted to make the area as small as possible. This made the wire routing process easy as there was a lot of room to work with. The area of utilization (occupied chip area) is 74.78% in *Square* clipping and 75.62% for 3 *Sector* clipping, a small difference. Comparing the number of ‘CORE Rows’ and ‘CORE Cells’ for *Square* and 3 *Sector* clipping algorithms it is seen that *Square* clipping requires 22 rows and 148 cells while 3 *Sector* clipping requires 26 rows and 319 cells.

Table 7.3: ‘Cadence’ area utilization report on *Square* clipping

Type	Number	Length	Area
%_Row_Space			
CORE Rows	22	1205160	3012900000
CORE Cells	148	237380	593450000
19.70			
CORNERSITE_495 Rows	4	198000	9801000000
CORNERSITE_495 Cells	4	198000	9801000000
100.00			
IOPADSITE_495 Rows	4	420000	20790000000
IOPADSITE_495 Cells	28	420000	20790000000
100.00			
Area of chip: 41699680000 (square DBU)			
Area required for all cells: 31184450000 (square DBU)			
Area utilization of all cells: 74.78%			

Table 7.4: 'Cadence' area utilization report on 3 Sector clipping

Type	Number	Length	Area
%_Row_Space			
CORE Rows	26	1693120	4232800000
CORE Cells	319	390060	975150000
23.04			
CORNERSITE_495 Rows	4	198000	9801000000
CORNERSITE_495 Cells	4	198000	9801000000
100.00			
IOPADSITE_495 Rows	4	420000	20790000000
IOPADSITE_495 Cells	28	420000	20790000000
100.00			
Area of chip: 41744615000 (square DBU)			
Area required for all cells: 31566150000 (square DBU)			
Area utilization of all cells: 75.62%			

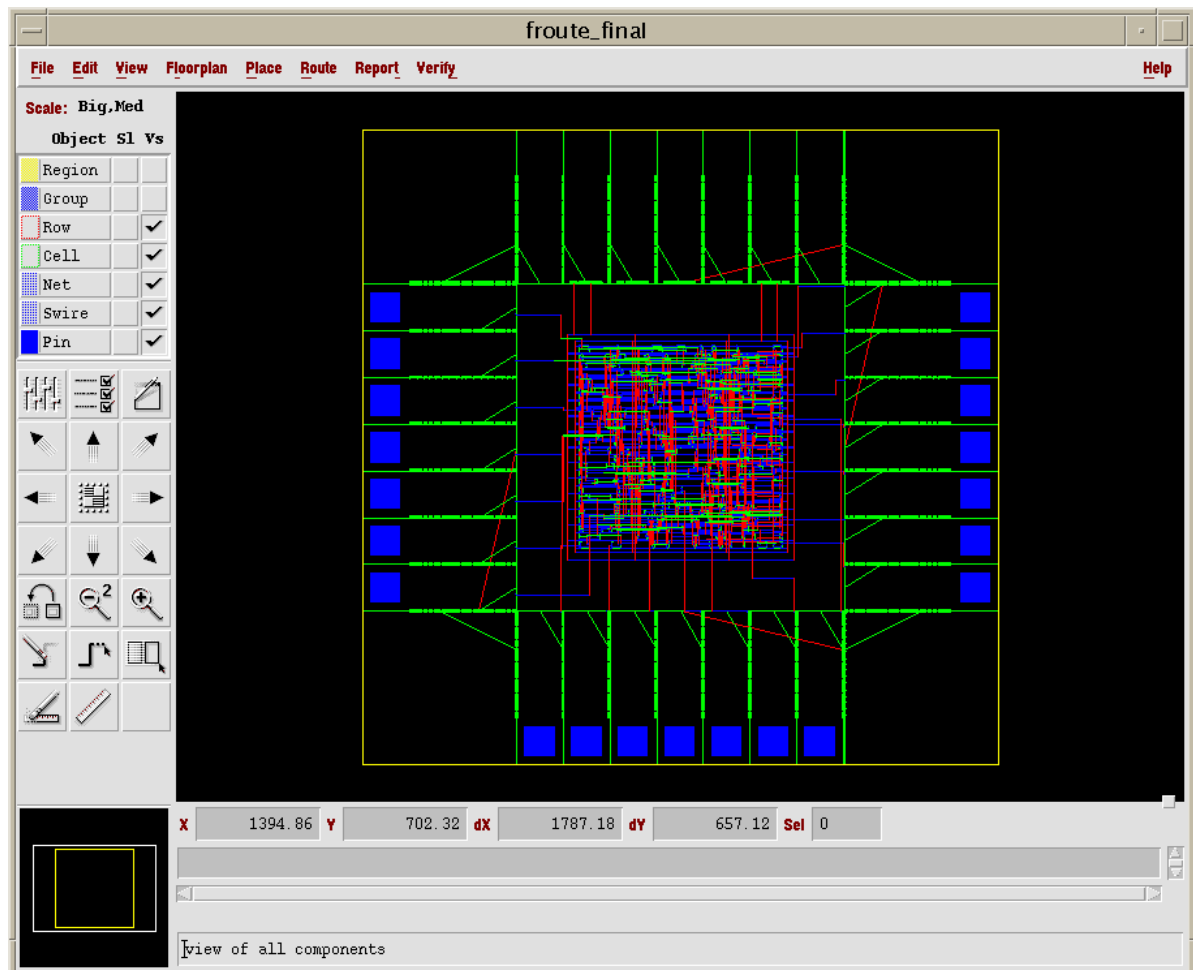


Figure 7.22: Application Specific Integrated Circuit (ASIC) view of 3sector clipping algorithm implemented in Silicon using 'Cadence Silicon Ensemble'. 0.5 μ process, 3 metal layers.

7.3 New Vector Subtraction clipping method

This section describes another new method called *Vector Subtraction* which is an enhancement of an existing algorithm [101] called the *Lucent* algorithm here, to clip samples. *Vector Subtraction* reduces complexity of the *Lucent* algorithm by removing the need for divisions, which are complex operations in hardware and add significantly to the complexity of the original algorithm.

7.3.1 Lucent Algorithm

The *Lucent* algorithm produces good estimates of the magnitude in K iterations. The *Lucent* algorithm works as follows, first the complex sample, $x = x_i + jx_q$ is folded into the first octant to give

$$x' = \max(|x_i|, |x_q|) + j \cdot \min(|x_i|, |x_q|) \quad (7.42)$$

x' is then rotated by a number, K , of fixed phase angles, θ_k , towards the real axis. The phase angle which returns the largest real part gives the closest approximation to the direction (phase) of the vector x' , and the magnitude of the real part, $|\hat{x}|$, is the closest approximation to the actual magnitude. The K phase values are spaced in the octant as

$$\theta_k = \pi l_k / 16K \quad (7.43)$$

where $l_k = \{1, 3, 5, \dots, 2K - 1\}$. For all K values of θ_k the magnitude estimate is given by

$$|\hat{x}| = \max_{\theta_k} \left(\text{Re} \left(x' \cdot e^{-j\theta_k} \right) \right) \quad (7.44)$$

After the magnitude has been estimated, any samples exceeding the clipping threshold, $|x_{clip}|$, are multiplied by a scaling factor (which reintroduces complexity that was mitigated by the iterative magnitude estimator), the clipped output signal is given by

$$x_{out} = \begin{cases} \left(\frac{|x_{clip}|}{|\hat{x}|}\right) x & |\hat{x}| > |x_{clip}| \\ x & |\hat{x}| \leq |x_{clip}| \end{cases} \quad (7.45)$$

The only error in this technique is a slight under estimate of $|\hat{x}|$ which reduces as K increases. The scheme has many similarities to the CORDIC [102] method, but gives better estimates of the magnitude at low values of K. The scaling operation requires a division which is a complex hardware operation and can be avoided by using the new *Vector Subtraction* technique described below.

7.3.2 Vector Subtraction

The process of finding the magnitude estimate, $|\hat{x}|$, is the same as [101] described in (7.44), but the scaling operation is replaced by a subtraction. First, the overshoot, o_s , is calculated

$$o_s = |\hat{x}| - |x_{clip}| \quad (7.46)$$

and then subtracted from the signal, x' . However the phase of the main signal is not known therefore the best estimate of the phase is used, this is $\theta_{k,max}$. The overshoot, o_s , is rotated by $e^{j\theta_{k,max}}$ giving the correction vectors y_i and y_q .

$$y = y_i + jy_q = o_s e^{j\theta_{k,m}} \quad (7.46a)$$

The correction vectors are octant adjusted prior to subtraction from the original signal, x .

$$x_i'' = x_i \pm (y_i, y_q) \quad (7.47)$$

$$x_q'' = x_q \pm (y_q, y_i) \quad (7.48)$$

The addition/subtraction of y_i and y_q can be extrapolated from the maximum and minimum values of x_i , x_q and the sign bits of the original data. A block diagram of *Vector Subtraction* is shown in Figure 7.23.

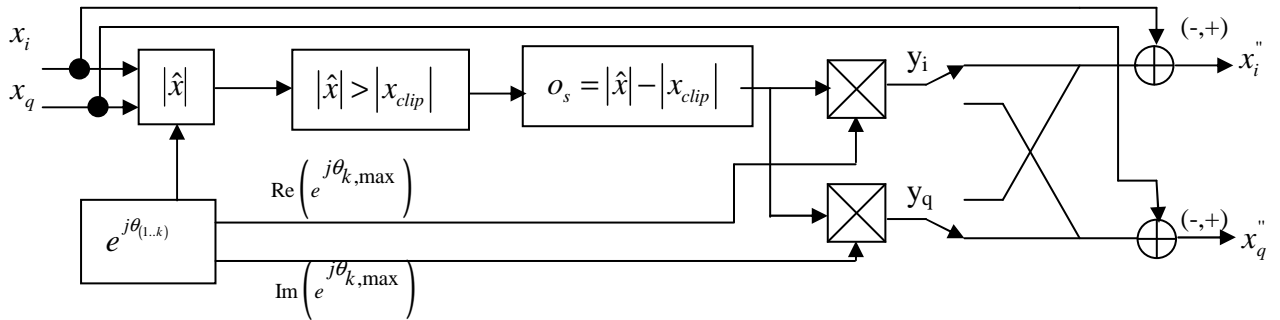


Figure 7.23: Block diagram of new *Vector Subtraction* scaling operation.

Figure 7.24 shows the I Q diagram for *Vector Subtraction* with $K=2$ iterations corresponding to phases of $\pi/16$ and $3\pi/16$. The vector x' is closest to the $\pi/16$ vector. Note that the clipped value, x'' , has an additional phase error compared to the *Lucent* method. It has both amplitude and phase error compared to the ideal clipped value.

Figure 7.25 and 7.26 show the CCDF of the *Lucent* algorithm [101] and the new *Vector Subtraction* variation respectively where 1000 OFDM symbols ($N=64$) are clipped at 5dB. Here it is seen that a slight underestimate in the magnitude means that samples are not always clipped back to the desired level. This is a function of the number of iterations in the algorithm with 1 iteration underestimating the magnitude by 0.7dB and 1.2dB to pass through in the *Lucent* algorithm and *Vector Subtraction* respectively. This problem is exacerbated in *Vector Subtraction* where the new scaling operation magnifies the error in the magnitude estimate.

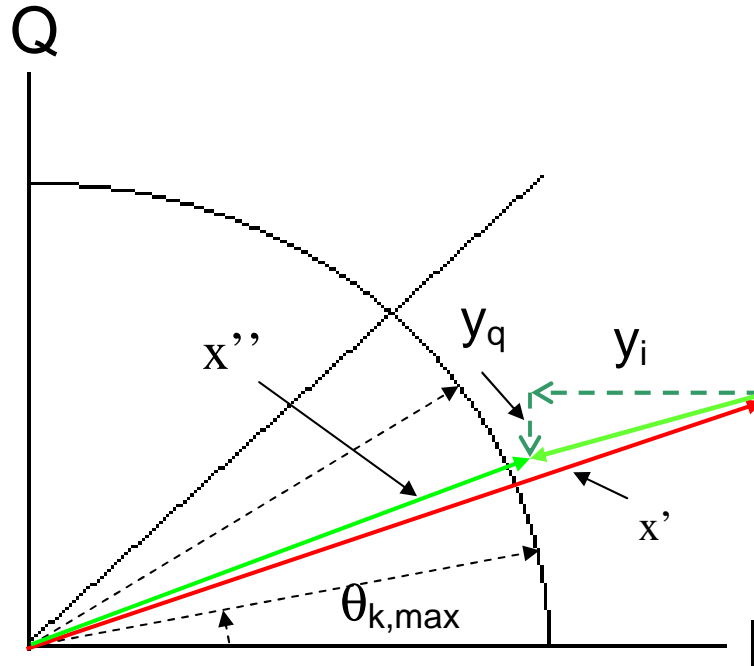


Figure 7.24: IQ plane for the new *Vector Subtraction* method showing vector, x' being clipped to x'' .

The amount of error in the magnitude estimate increases with the decrease in clipping level for *Vector Subtraction* with clipping under 3dB requiring a prohibitive amount of backoff. This is not an issue with the *Lucent* patent where the magnitude estimate error is constant irrespective of clip level. The upshot of this is that the clip level will need to be backed off to avoid saturation of the amplifier. Alternatively more than 1 iteration can be used making the error in the magnitude estimate small. This small error can normally be neglected as filtering will cause substantial peak regrowth anyway.

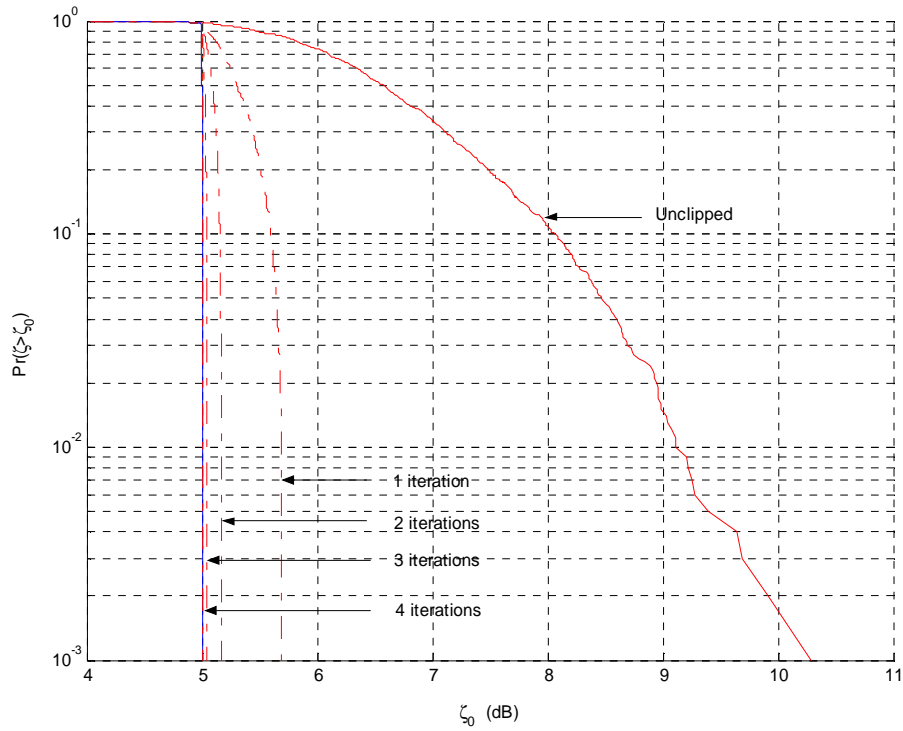


Figure 7.25: Simulated CCDF for *Lucent* patent [101] for various iterations clipped at 5dB showing the leakage of under clipped samples.

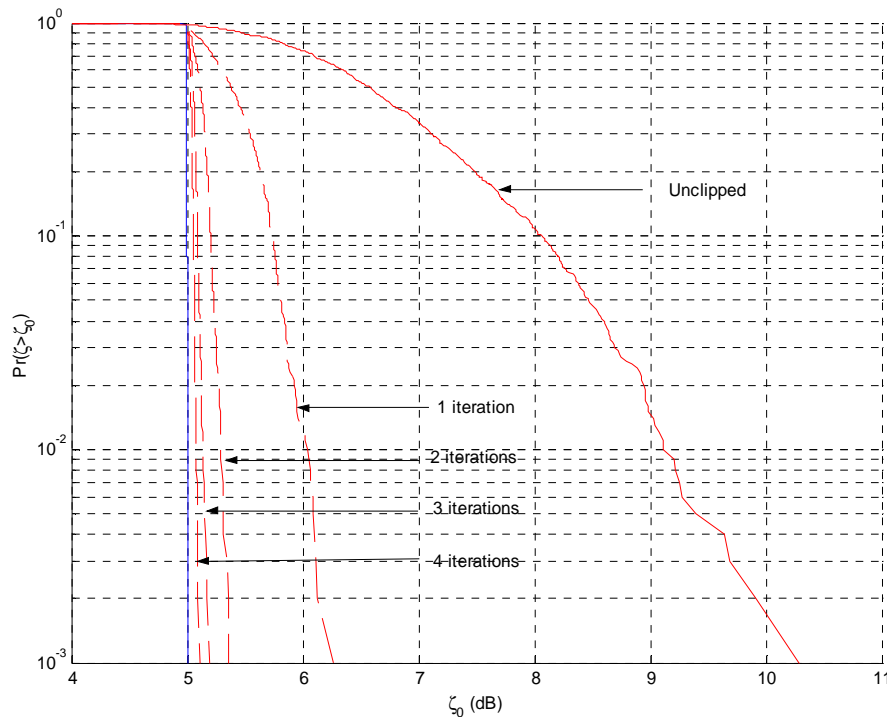


Figure 7.26: Simulated CCDF for *Vector Subtraction* for various iterations clipped at 5dB showing the leakage of under clipped samples.

The simulated clip level vs. SNR results are shown in Figure 7.27 and 7.28 for the *Lucent* algorithm and *Vector Subtraction* method respectively. Note that the clip level is adjusted depending on the iteration and clipping method according to the CCDF results of Figures 7.25 and 7.26, for example the *Lucent* patent with 1 iteration requires the clip level to be set to CL-0.7. This ensures that the samples will not saturate the HPA if it were present.

When 2, 3, or 4 iterations are used, both the *Lucent* patent and *Vector subtraction* have very similar performance to the conventional clipping method. 1 iteration results in a 5dB degradation from the optimum clipping method for the *Lucent* algorithm while 1 iteration in *Vector Subtraction* results in a more serious degradation across the board, making it impractical; In fact its performance goes below that of *Square* clipping for clip levels below 4dB. The reason for this is the increasing amount of back off required at harder clip levels to avoid saturation of the amplifier.

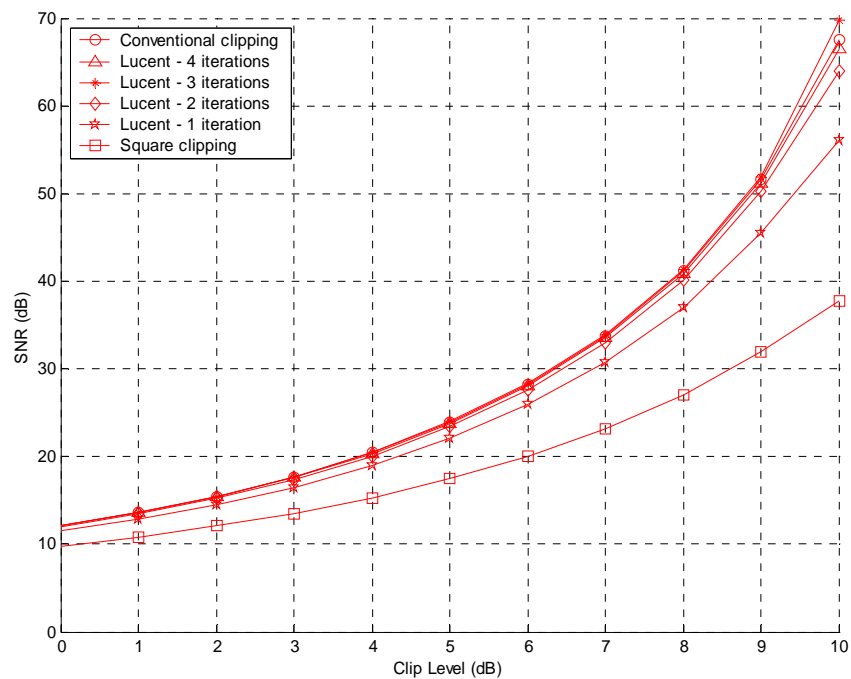


Figure 7.27: Simulated clip level vs. SNR for *Lucent* clipping technique with varying iterations, as well as *Conventional* and *Square* clipping.

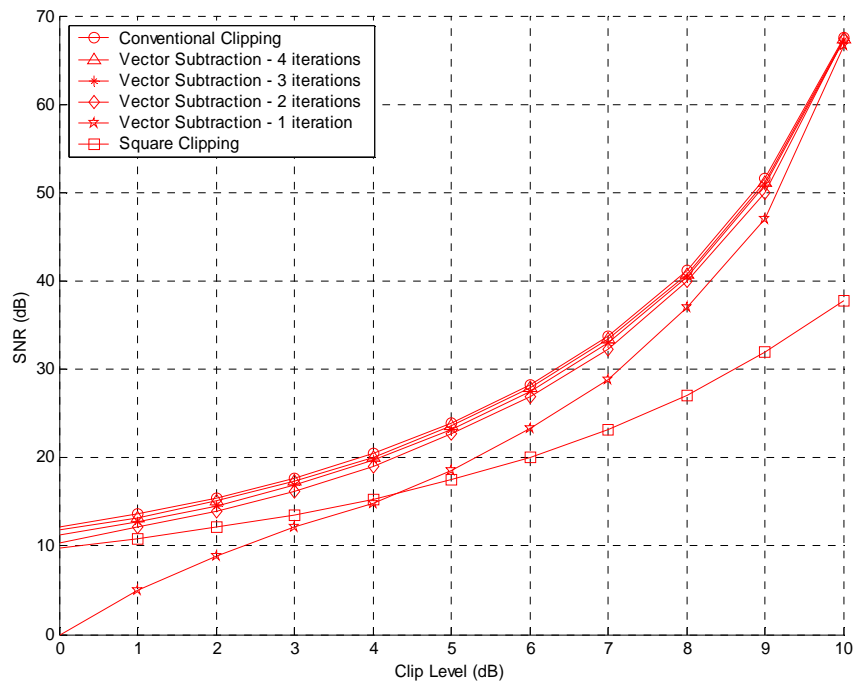


Figure 7.28: Simulated clip level vs. SNR for *Vector Subtraction* clipping with varying iterations, as well as *Conventional* and *Square* clipping.

7.4 Comparison of new and existing clipping methods

The previous sections described new low complexity clipping algorithms and evaluated them both theoretically and through simulation. Section 7.4.1 analyses their performance in the OFDM system described in Section 7.1. Section 7.4.2 compares them in terms of their complexity by comparing hardware operations. The mapping type used in the following simulations is 64 QAM, the number of taps in the RRCF is 128 with a roll off factor of 0.15, the oversampling rate in the IFFT is set to 2. A LPA is used initially and later simulations use a HPA ($P=3$) with increasing backoffs. *Conventional* and *Square* clipping are also shown as a reference.

7.4.1 BERF

Figure 7.29 shows the baseband clipping vs. BERF for 3, 4, and 5 *Sector* clipping where it is seen that increasing the number of sectors to 4 provides an improvement of 1 and a half magnitudes over *Square* clipping at 4dB clipping. Increasing the number of sectors to 5 provides a more modest decrease in the BERF beyond 4 *Sector*

clipping at 4 dB clipping. 5 sector clipping is 1 magnitude worse than conventional clipping at 4 dB clipping. At 5 dB clipping *Conventional*, 4, and 5 Sector clipping have a BERF below 10^{-6} . Note that *Sector* clipping over clips the data therefore performance after a HPA with a limited backoff may be better due to the extra regrowth allowed. This will be explored further later in this section.

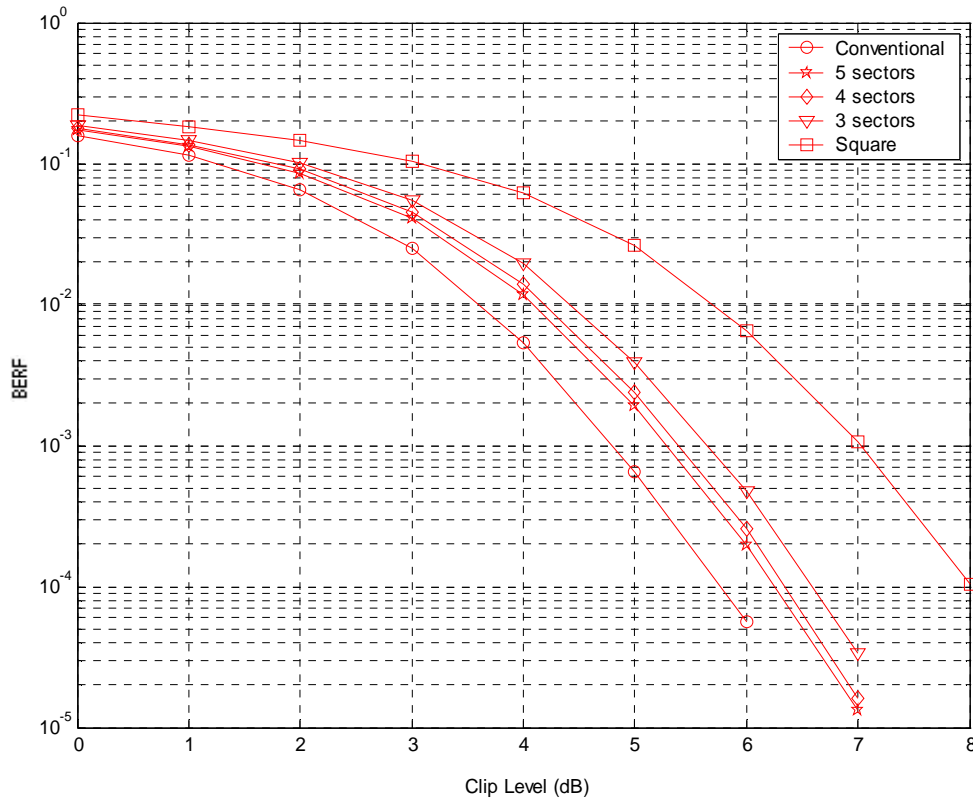


Figure 7.29: Simulated 3, 4, and 5 Sector, *Conventional* and *Square* clipping vs. BERF with a LPA. 64 QAM symbols, 128 point IFFT ($os=2$), RRCF with 128 taps, and $\alpha=0.15$. AWGN=0.

Figure 7.30 shows baseband clipping vs. BERF for *Vector Subtraction* with 1, 2, 3, and 4 iterations. Performance is nearly the same for all methods, however curiously 1 iteration has the best performance while conventional clipping has the worst. This can be explained by reviewing Figure 7.25 where it seen that *Vector Subtraction* under clips some samples which would lead to saturation of the amplifier had it not been a LPA.

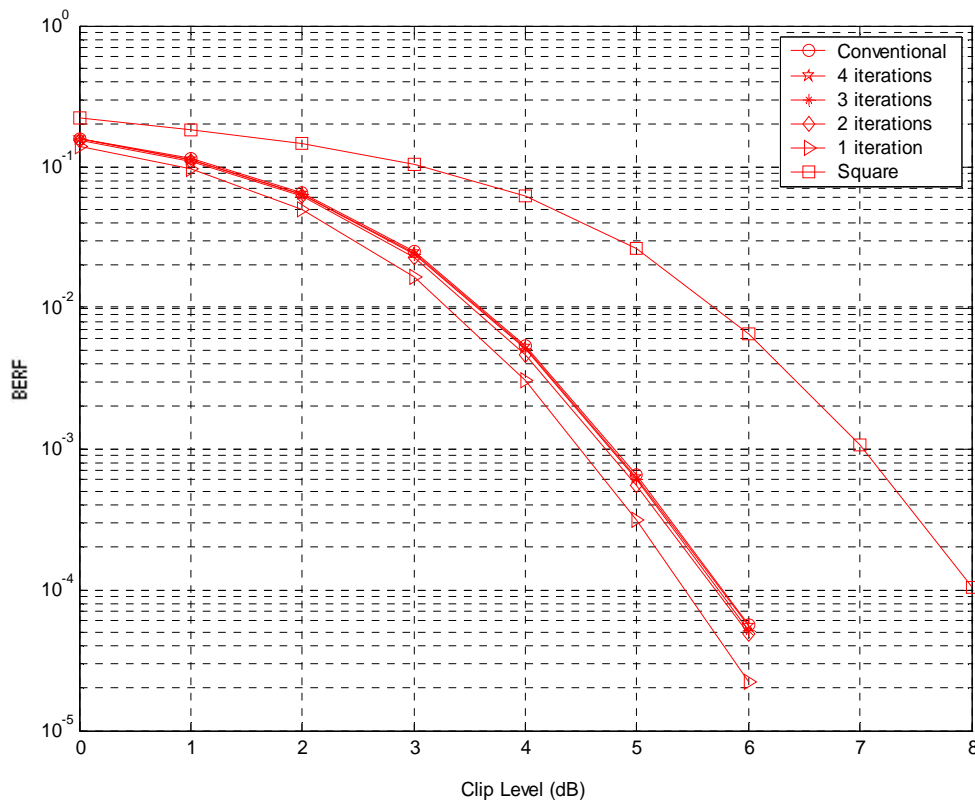


Figure 7.30: Simulated *Vector Subtraction* (1, 2, 3, and 4 iterations), *Conventional* and *Square* clipping vs. BERF with a LPA. 64 QAM symbols, 128 point IFFT ($os=2$), RRCF with 128 taps, and $\alpha=0.15$. AWGN=0.

Figure 7.31 shows baseband clipping vs. BERF for the *Lucent* algorithm [101] where it is seen that the performance of all iterations is almost the same as *Conventional* clipping. Again 1 iteration has slightly better performance than the other methods due to the under clipping of some samples as seen in Figure 7.25. *Vector Subtraction* has an almost identical performance to the *Lucent* method except for the trivial case of 1 iteration.

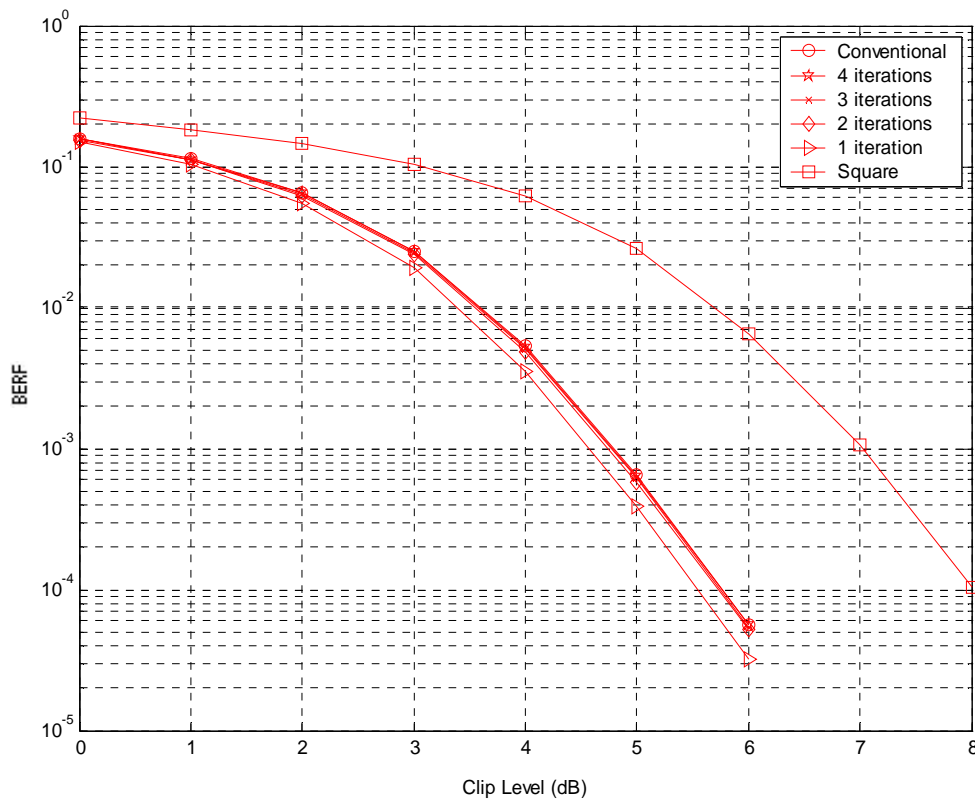


Figure 7.31: Simulated *Lucent* [101] clipping (1, 2, 3, and 4 iterations), *Conventional* and *Square* clipping vs. BERF with a LPA. 64 QAM symbols, 128 point IFFT ($os=2$), RRCF with 128 taps, and $\alpha=0.15$. AWGN=0.

This section simulated the performance of the new and existing clipping algorithms in an OFDM environment with a LPA. The rest of this section uses a HPA with different IBO's relative to the baseband clipping level. Note that *Sector* Clipping overclips the signal in some instances while *Vector Subtraction* and the *Lucent* algorithm under clip the signal which explains the higher BERF's of the *Sector* clipping when the HPA is taken into account.

Changing HPA backoff

Figures 7.32, 7.33, and 7.34 show baseband clipping vs. BERF for 3, 4, and 5 *Sector* clipping, respectively, with increasing backoff in the HPA. Increasing the IBO in the HPA improves the BERF in all cases.

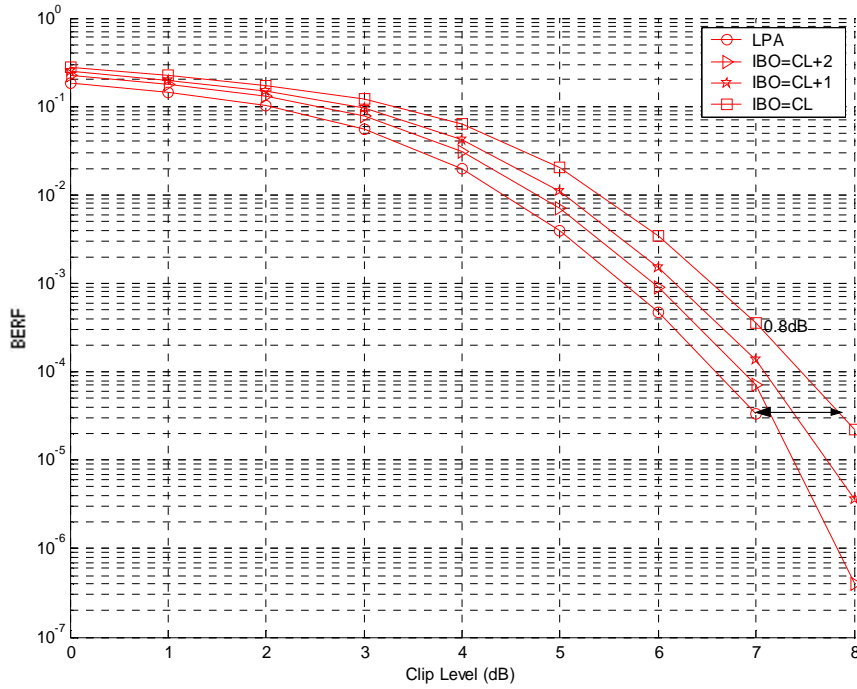


Figure 7.32: Simulated 3 Sector clipping, vs. BERF with varying IBO in HPA. 64 QAM symbols, 128 point IFFT ($os=2$), RRCF with 128 taps and $\alpha=0.15$. AWGN=0.

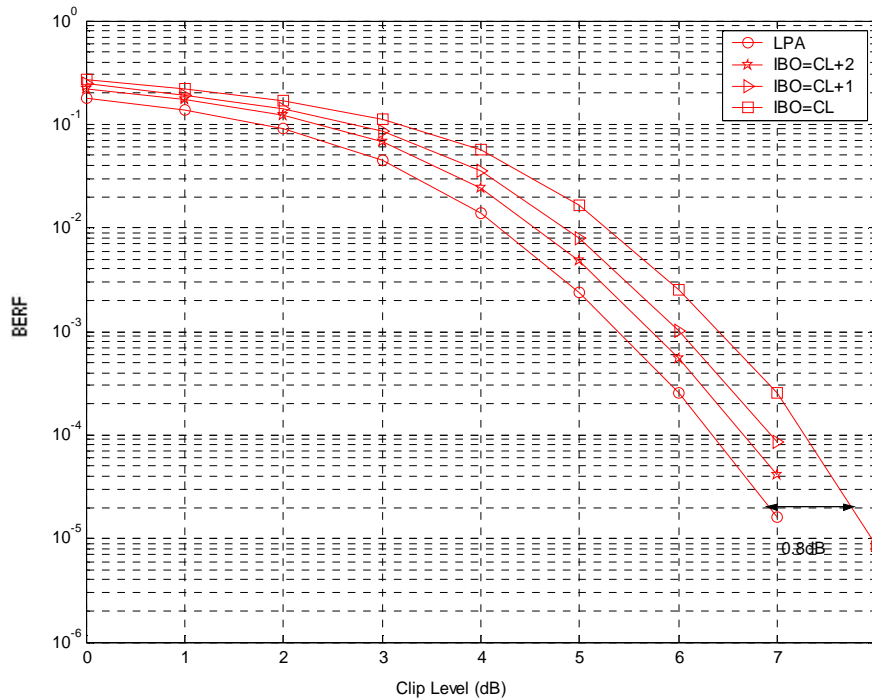


Figure 7.33: Simulated 4 Sector clipping, vs. BERF with varying IBO in HPA. 64 QAM symbols, 128 point IFFT ($os=2$), RRCF with 128 taps and $\alpha=0.15$. AWGN=0.

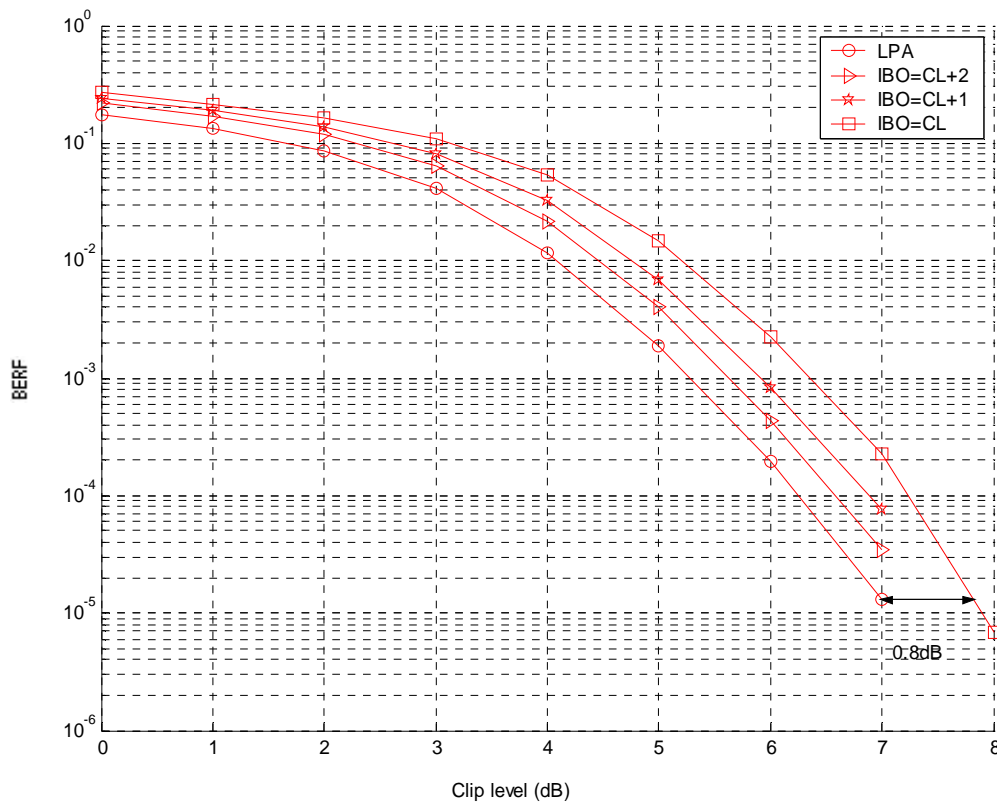


Figure 7.34: Simulated 5 Sector clipping, vs. BERF with varying IBO in HPA. 64 QAM symbols, 128 point IFFT ($os=2$), RRCF with 128 taps and $\alpha=0.15$. AWGN=0.

Comparing Figures 7.32 and 7.34, 5 Sector clipping is just under 1 magnitude better in terms of the BERF than 3 Sector clipping at 5dB baseband clipping with an IBO of 2dB above the baseband clip level (i.e. IBO=7dB). At an IBO=CL+2 the BERF is within 1 magnitude of the LPA at 5dB clipping for all methods and within half a magnitude at 4dB clipping. 1 dB of additional baseband backoff is required for 3 and 4 Sector and slightly more for 5 Sector clipping to maintain the same BERF as an LPA at a BERF= 10^{-4} with no additional IBO in the HPA.

The non-linear characteristics of a HPA adds another source of distortion to the transmitted signal. Figures 7.32 to 7.34 show that this additional distortion is equivalent to a 0.8dB change in the CL (at BERF= 10^{-4}) when the HPA saturation level is equal to the

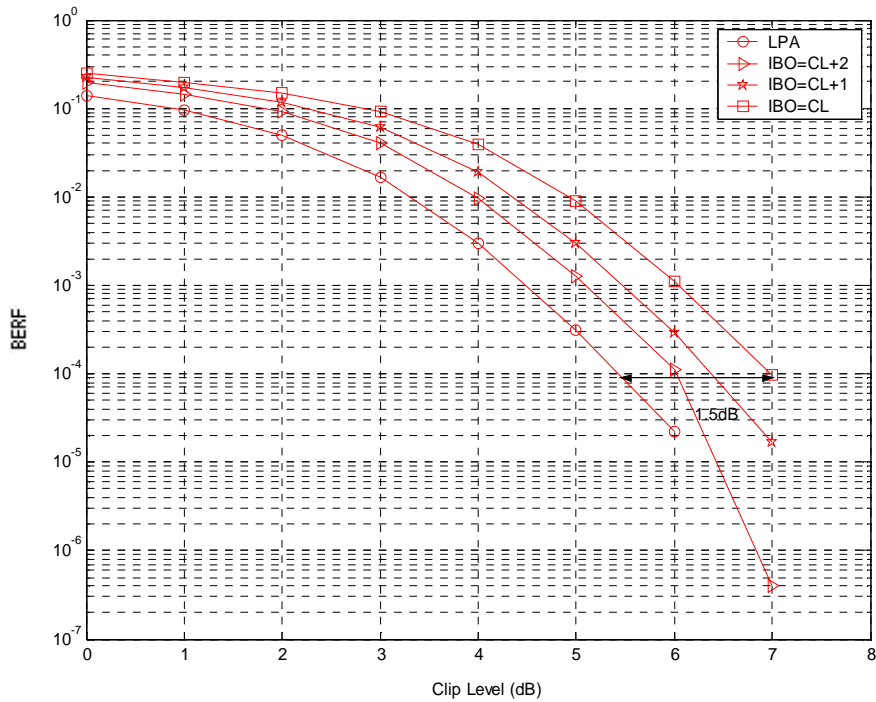


Figure 7.35: Simulated *Vector Subtraction* (1 iteration), vs. BERF with varying IBO in HPA. 64 QAM symbols, 128 point IFFT ($os=2$), RRCF with 128 taps and $\alpha=0.15$. AWGN=0.

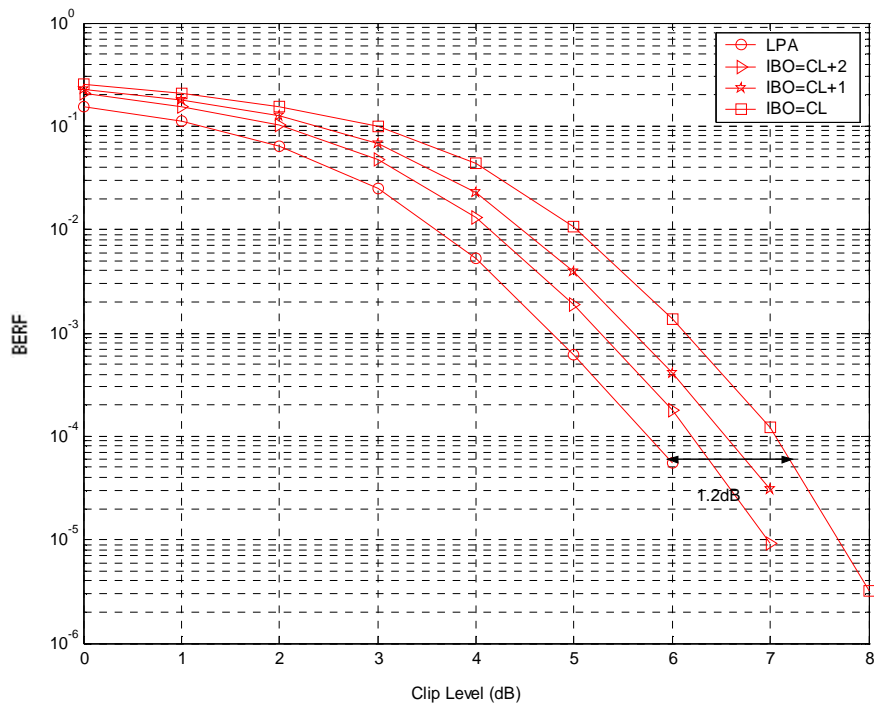


Figure 7.36: Simulated *Vector Subtraction* (4 iterations), vs. BERF with varying IBO in HPA. 64 QAM symbols, 128 point IFFT ($os=2$), RRCF with 128 taps and $\alpha=0.15$. AWGN=0.

clipping level (IBO=CL). Obviously, as the amplifier is backed off, IBO=CL+2, then the additional distortion is reduced.

Figures 7.35 and 7.36 show baseband clipping vs. BERF for *Vector Subtraction* with 1 and 4 iterations, with increasing backoff in the HPA. Increasing the IBO improves the BER in all cases. There is little difference between 1 and 4 iterations when $HPA=CL$ but this increases with the larger IBO in the HPA. However 1 iteration outperforms 4 iterations for all HPA backoffs. This is due to the underestimation of the magnitude reducing the clipping distortion. At an amplifier backoff of $HPA=CL+2$ the BERF is within 1 magnitude of LPA performance at 5dB clipping for all methods and within half a magnitude at 4dB clip level. When no extra backoff is allowed in the HPA above the baseband clip level the performance of 1 and 4 iterations is almost the same, with an additional backoff of 2dB in the HPA ($HPA=CL+2$) 1 iteration outperforms 4 iterations by 0.2 dB at a $BERF=10^{-4}$.

Figures 7.37 and 7.38 show baseband clipping vs. BERF for the *Lucent* patent with 1 and 4 iterations respectively, and increasing backoff in the HPA. As with the 2 previous methods increasing the IBO improves the BERF. In Figure 7.37 (1 iteration) at a baseband clip level of 6dB there is a difference of 1.5 magnitudes between $HPA=CL$ and a LPA. Under the same conditions the difference is under 2 magnitudes for Figure 7.38 (4 iterations). When no extra backoff is allowed in the HPA both 1 and 4 iterations have approximately the same performance. The performance of 4 iterations is slightly worse for $IBO=CL+1$ and $IBO=CL+2$.

For comparison *Square* clipping with different backoffs in the HPA is plotted in Figure 7.39. Here it is seen that like *Sector* clipping *Square* clipping is more robust against a reduction in the amplifier backoff with only half a magnitude in difference between a LPA and a HPA with no additional IBO ($IBO=CL$).

Comparing the 3 methods it is interesting to note that *Sector* clipping has the least increase in BERF from $IBO=CL$ to LPA with a difference of 1.2, 1.5, and 1.5 magnitudes

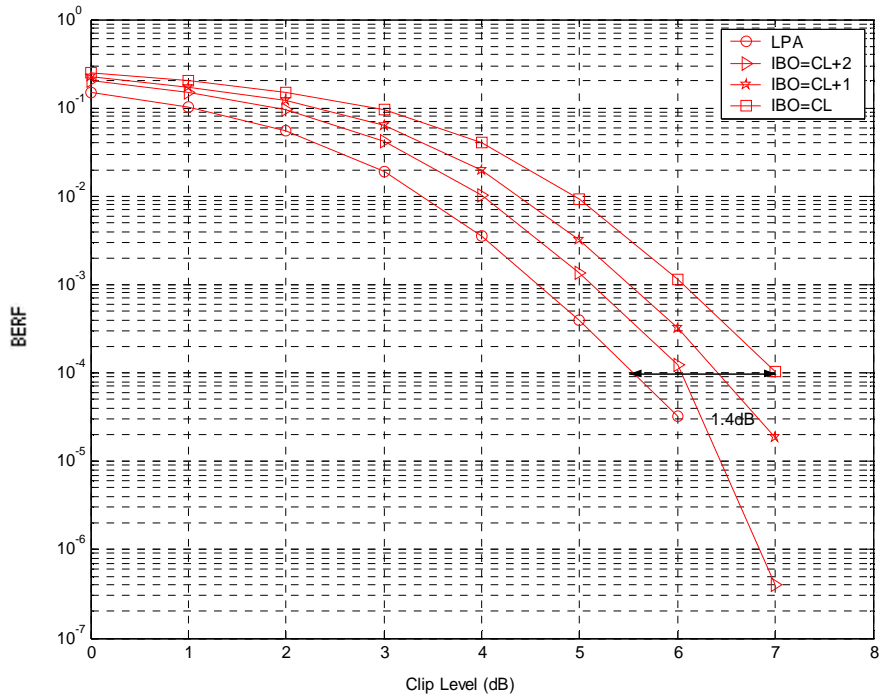


Figure 7.37: Simulated *Lucent* clipping (1 iteration), vs. BERF with varying IBO in HPA. 64 QAM symbols, 128 point IFFT ($os=2$), RRCF with 128 taps, and $\alpha=0.15$. AWGN=0.

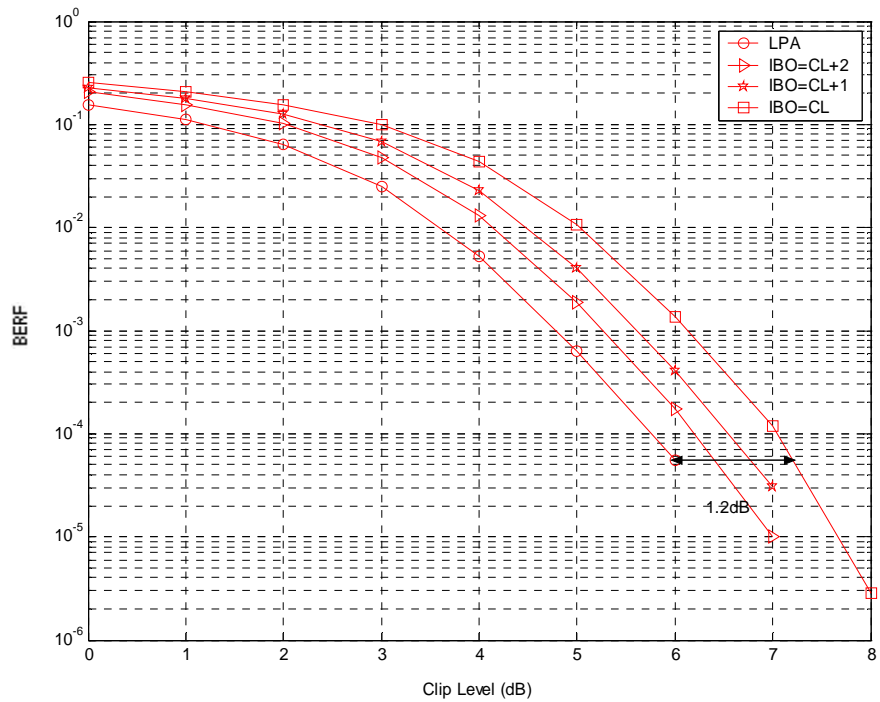


Figure 7.38: Simulated *Lucent* clipping (4 iterations), vs. BERF with varying IBO in HPA. 64 QAM symbols, 128 point IFFT ($os=2$), RRCF with 128 taps, and $\alpha=0.15$. AWGN=0.

for 3, 4, and 5 *Sector* clipping respectively. *Vector Subtraction* has a difference of 2.5 and 2 magnitudes for 1 and 4 iterations respectively, while the *Lucent* algorithm has a difference of 2.2 and 2 magnitudes.

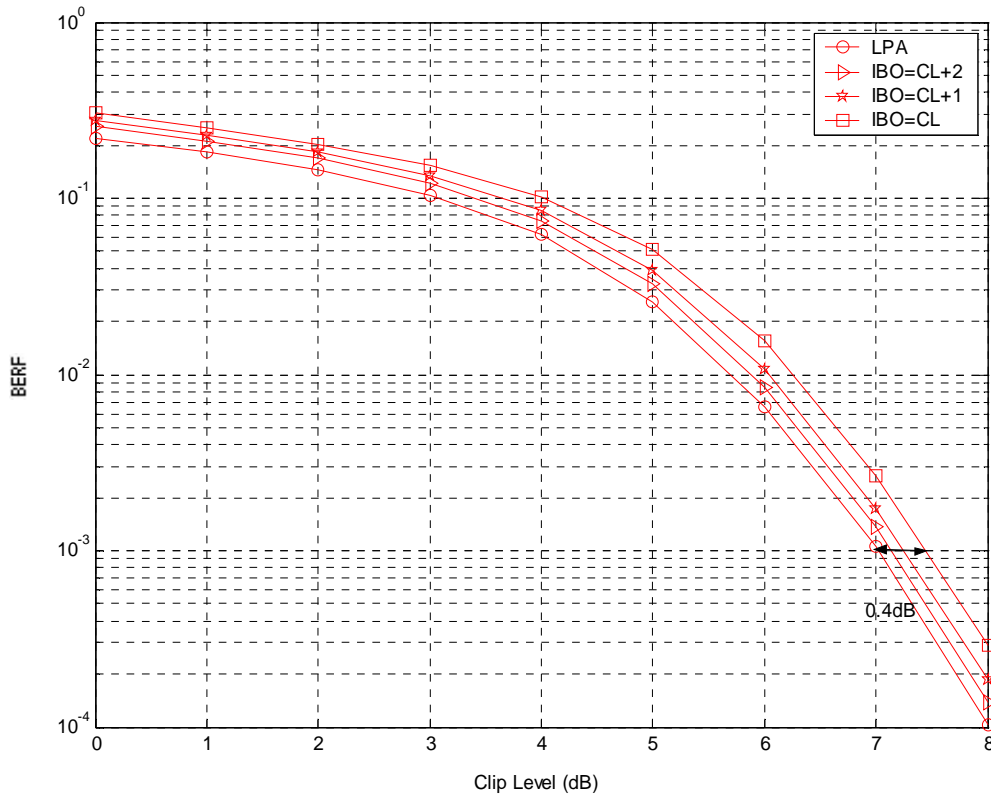


Figure 7.39: Simulated *Square* clipping vs. BERF with varying IBO in HPA. 64 QAM symbols, 128 point IFFT ($os=2$), RRCF with 128 taps, and $\alpha=0.15$. AWGN=0.

Table 7.5 compares the baseband clip level for the aforementioned clipping techniques required to maintain a BER of 10^{-4} for different backoffs in the HPA. For 3 and 4 *Sector* clipping decreasing the difference from a LPA to no additional backoff in the HPA (IBO=CL) comes at a cost of around an additional 1dB increase in the baseband clip level to maintain the same BERF= 10^{-4} , and a 1.1dB increase for 5 *Sector* clipping. For *Vector Subtraction* and the *Lucent* clipping method the increase required is around 1.5dB for 1 iteration and 1.3 dB for 4 iterations. *Conventional* (Figure 7.6) clipping requires a 1.2dB increase in clipping level and *Square* clipping only requires an extra 0.4dB to maintain the same BERF.

Reviewing the results in terms of performance at a set HPA backoff it is seen that for 3 *Sector* clipping there is an additional 0.4dB of extra baseband clipping backoff

required than for 5 Sector clipping with no additional backoff in the HPA, and an additional 0.6dB required under LPA conditions. Note that for 3 and 4 Sector clipping an extra backoff of 2dB in the HPA is sufficient to provide near optimal results (i.e. under LPA conditions), however for 5 Sector clipping an extra backoff of 3dB is required to approach the LPA results. Performance of *Vector Subtraction* and the *Lucent* method for both 1 and 4 iterations have similar performance at a set amplifier backoff, interestingly 1 iteration slightly outperforms 4 iterations. Underestimation of the amplitude must therefore dominate y^{je} phase error in the two schemes.

Table 7.5: Baseband clip level required to maintain a BER= 10^{-4} at varying IBO in HPA.

Baseband clip level required for BER= 10^{-4} at relevant HPA backoff				
HPA backoff	CL	CL+1	CL+2	LPA
Sector Clipping				
3 sectors (Fig 7.32)	7.5 dB	7 dB	6.9 dB	6.6 dB
4 sectors (Fig 7.33)	7.3 dB	7 dB	6.7 dB	6.3 dB
5 sectors (Fig 7.34)	7.2 dB	6.9 dB	6.6 dB	6.1 dB
Vector subtraction				
1 iteration (Fig 7.35)	7 dB	6.4 dB	6 dB	5.5 dB
4 iterations (Fig 7.36)	7 dB	6.6 dB	6.2 dB	5.8 dB
Lucent				
1 iteration (Fig 7.37)	7 dB	6.4 dB	6.1 dB	5.6 dB
4 iterations (Fig 7.38)	7 dB	6.6 dB	6.2 dB	5.8 dB
Conventional				
Conventional (Fig 7.7)	7 dB	-	6.2 dB	5.8 dB
Square				
Square (Fig 7.39)	8.4 dB	8.2 dB	8.1 dB	8 dB

7.4.2 PSD results

The PSD after the HPA and receiver filtering is shown in the following figures. The filter used is the same as the previous simulations, i.e. Matched RRCF, $\alpha=0.15$, 128 filter taps and the HPA is a SSPA with $p=3$. As in Section 3.4.2 the PSD is measured for each OFDM block and then averaged over many blocks.

In Figures 7.40 and 7.41 the baseband clip level is set at 0dB and 5dB respectively and the amplifier backoff is set at increasing levels above this clip level (IBO=CL, CL+1, CL+2, CL+3, CL+4, and a LPA). Baseband clipping at 0dB results in a large amount of both in band and out of band distortion (ACI). With no additional backoff in the HPA (IBO=CL) the ACI is only 18dB below the signal power and the inband distortion is 3dB below the LPA case. Increasing the IBO by 1dB (IBO=CL+1) results in spectral splatter 20dB below the signal power and an inband distortion of 2.5dB. With IBO=CL+2 the ACI is 22dB below the signal power and the inband distortion is 1.5dB. An IBO level set at CL+3 results in 23dB ACI and 1.3dB inband distortion. Even with a backoff of 4dB in the amplifier (IBO=CL+4) 24dB in ACI is present and the inband distortion is 1dB below the LPA case.

In Figure 7.41 the baseband clip level is set at 5dB and the amplifier backoff is set at increasing levels above the clip level as in Figure 7.40. Here it is seen that there is much less distortion, both in band and out of band. There is only 0.5dB difference in inband distortion between no additional IBO in the HPA and a LPA, and the ACI is 24dB for the IBO=CL case, and for higher backoffs is almost non existent.

These PSD results of 7.40 and 7.41 show that harder clipping in the baseband results in greater peak regrowth which leads to heavier saturation of the amplifier, hence the greater ACI and in band distortion. The inband distortion leads to a worse BERF as the difference between signal power and noise is reduced, i.e. SNR is reduced. The out of band distortion will lead to interference with adjacent channels.

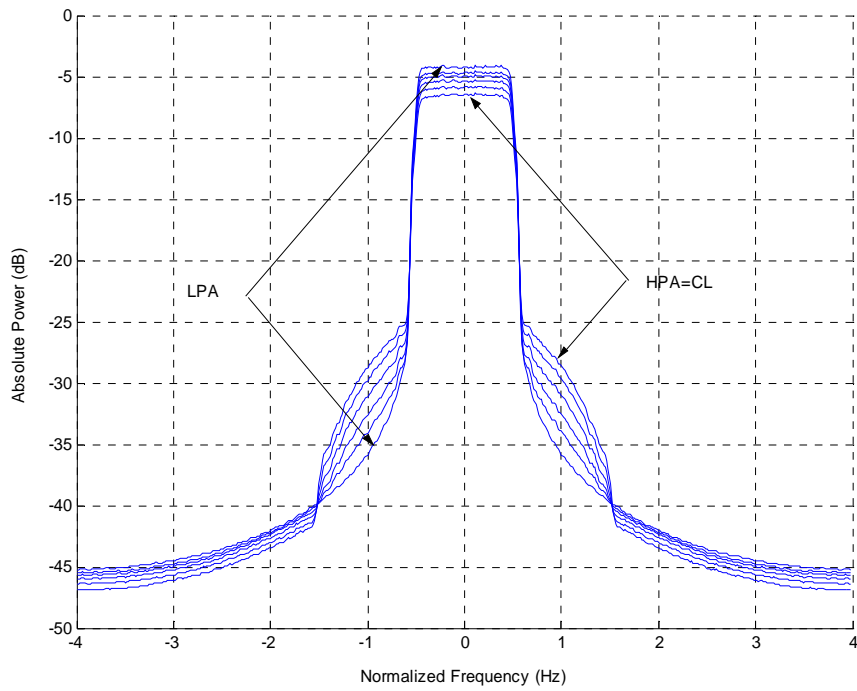


Figure 7.40: PSD; 0dB clipping in baseband with increasing amplifier backoffs (HPA=CL, CL+1,CL+2,CL+3,CL+4, LPA). RRCF, alpha=0.15, 128 taps.

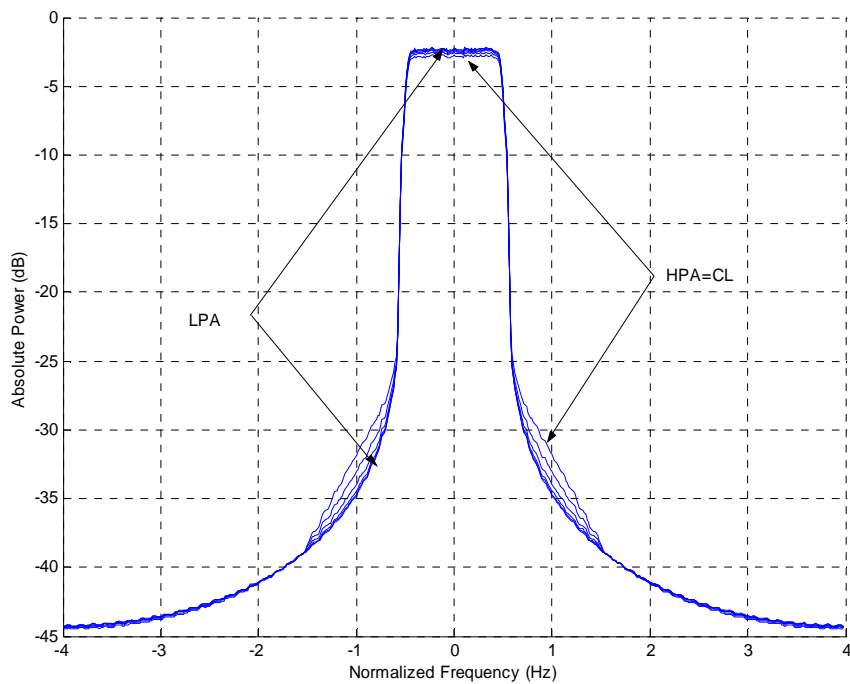


Figure 7.41: PSD; 5dB clipping in baseband with increasing amplifier backoffs (HPA=CL, CL+1,CL+2,CL+3,CL+4, LPA). RRCF, alpha=0.15, 128 taps.

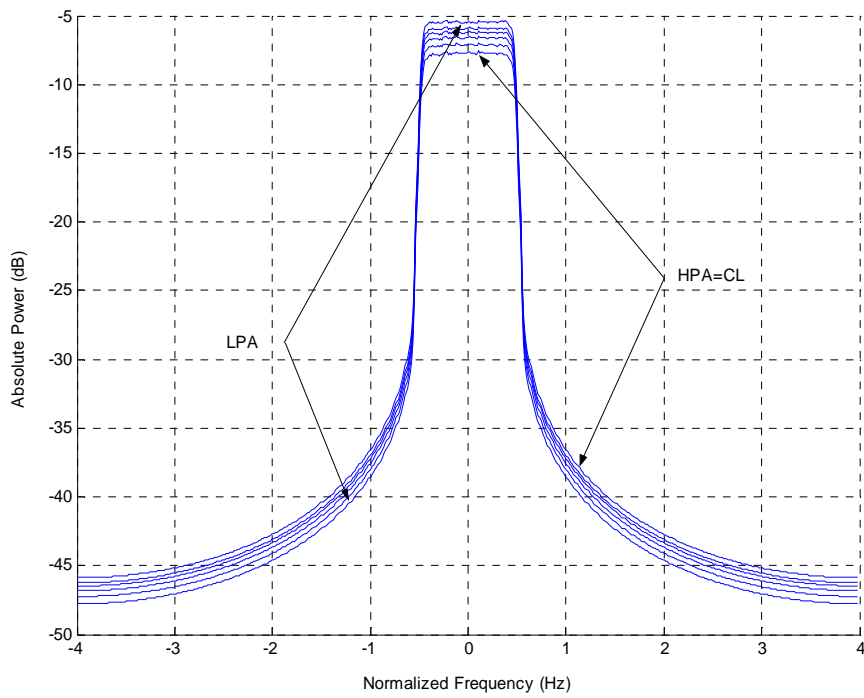


Figure 7.42: PSD; after 0dB clipping in baseband and receiver filtering, with increasing amplifier backoffs (HPA=CL, CL+1,CL+2,CL+3,CL+4, LPA). RRCF, alpha=0.15, 128 taps.

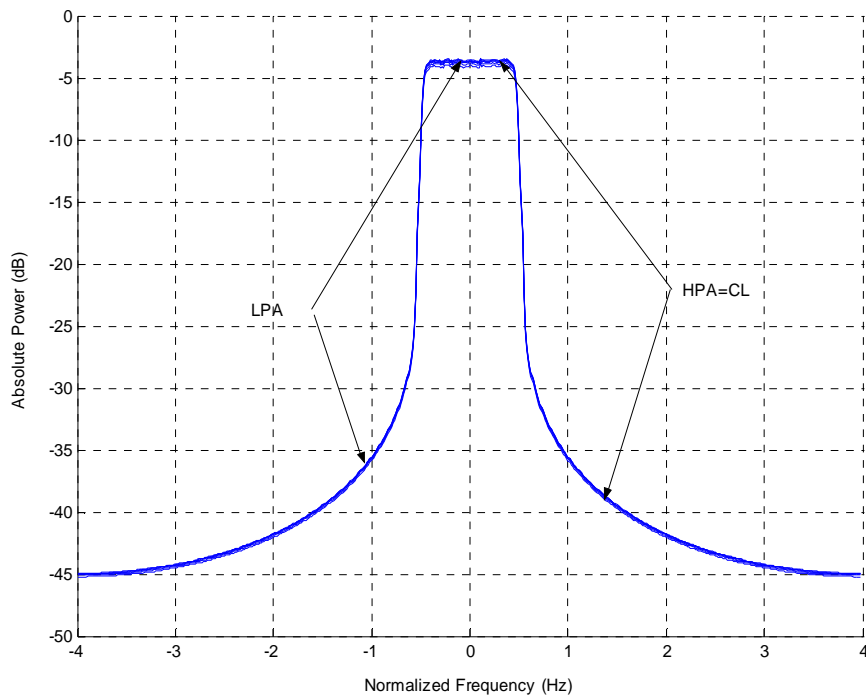


Figure 7.43 : PSD; after 5dB clipping in baseband and receiver filtering, with increasing amplifier backoffs (HPA=CL, CL+1,CL+2,CL+3,CL+4, LPA). RRCF, alpha=0.15, 128 taps.

Figures 7.42 and 7.43 show the PSD after receiver filtering for 0dB and 5dB baseband clipping respectively. Here as expected the out of band distortion is mitigated but the in band distortion remains.

7.5 New adaptive clipping method

Clipping after interpolation and filtering will ensure that the amplifier does not saturate eliminating AM to PM distortions in the amplifier, but results in ACI affecting adjacent channels. This effect can be compensated by putting the clipper before the filter as done earlier in this chapter. However, as shown clipping and filtering can regrow peaks causing saturation of the amplifier resulting in an increase in the BERF.

This section introduces a new adaptive clip and filter algorithm, *Level Detection Algorithm (LDA)* first presented in [103] which overclips the signal at certain times avoiding the peak regrowth issue and sparing the amplifier from saturation. However *LDA* as presented in [103] requires the use of a conventional clipper which adds significantly to the overall complexity and latency of the algorithm. Latency is an important issue in *LDA*, therefore *Vector Subtraction* is very useful in this algorithm. In this section *Vector Subtraction* with 2 iterations is used in place of the conventional clipper in *LDA* and their performance is compared through simulation. *Vector Subtraction* has the advantage of providing good estimates of the error magnitude with low latency, and low complexity, both of which are important in *LDA*.

LDA uses an extra matched filter before the standard pulse shaping filter to predict the response of the signal from which the amount of compensation required can be calculated. A block diagram showing the *LDA* algorithm is shown in Figure 7.44 with a more detailed view of the filtering operation shown in Figure 7.45. The input data is modeled as a complex Gaussian process which describes accurately either an OFDM ($N > 64$) or CDMA distribution of data where the algorithm could be implemented. The input data is interpolated to form the signal, $x(n)$, (Figure 7.46a) and then fed to 2 identical filters. The first filter is used for peak detection and for generation of the correction vector, $v(n)$. The suitably delayed correction vector is subtracted from the signal, x , before being passed to the second filter, and on to the

rest of the transmission chain. The filter used is a linear phase RRCF, in order to compensate for the group delay of the filter the subtraction point is set at the centre of the first filter's delay line. This reduces the potential for additional peaks by including the latter half of the smeared $v(n)$ waveform in the output estimate $y(n)$.

The clipping processor compares the amplitude of the first filter output with the Clipping Level (CL) threshold to detect peaks. When the filter output magnitude, $|y(n)|$, exceeds the CL as shown in (Fig 7.46b) the correction vector, $v(n)$ is subtracted from the second filter input. The correction vectors (Figure 7.46c) show the positions where the correction takes place at $n-1$, n , and $n+1$.

Figure 7.47 shows the I Q diagram for LDA showing how the vector, $v(n)$, is calculated based on the filter input samples. The correction required at the filter output to stop saturation at the amplifier is $\alpha(n)$ which is in phase with $y(n)$ and has amplitude

$$|\alpha(n)| = |y(n)| - CL \quad (7.49)$$

When the correction vector $v(n)$ is added to the centre of the filter delay line, $\alpha(n)$ will be

$$\alpha(n) = h_0 v(n) \quad (7.50)$$

where h_0 is the central filter tap value. Combining (7.49) and (7.50) gives $v(n)$ as

$$v(n) = \left(1 - \frac{CL}{|y(n)|}\right) \left(\frac{y(n)}{|h_0|}\right) \quad (7.51)$$

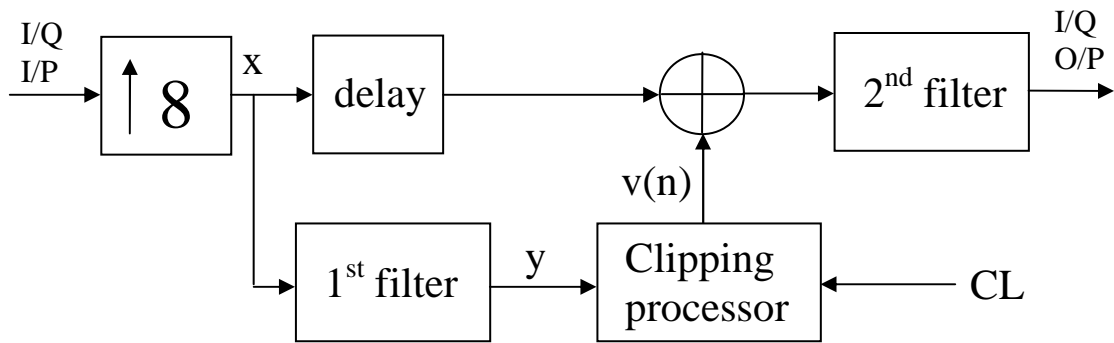


Figure 7.44: Block diagram of system with *Level Detection Algorithm (LDA)*.

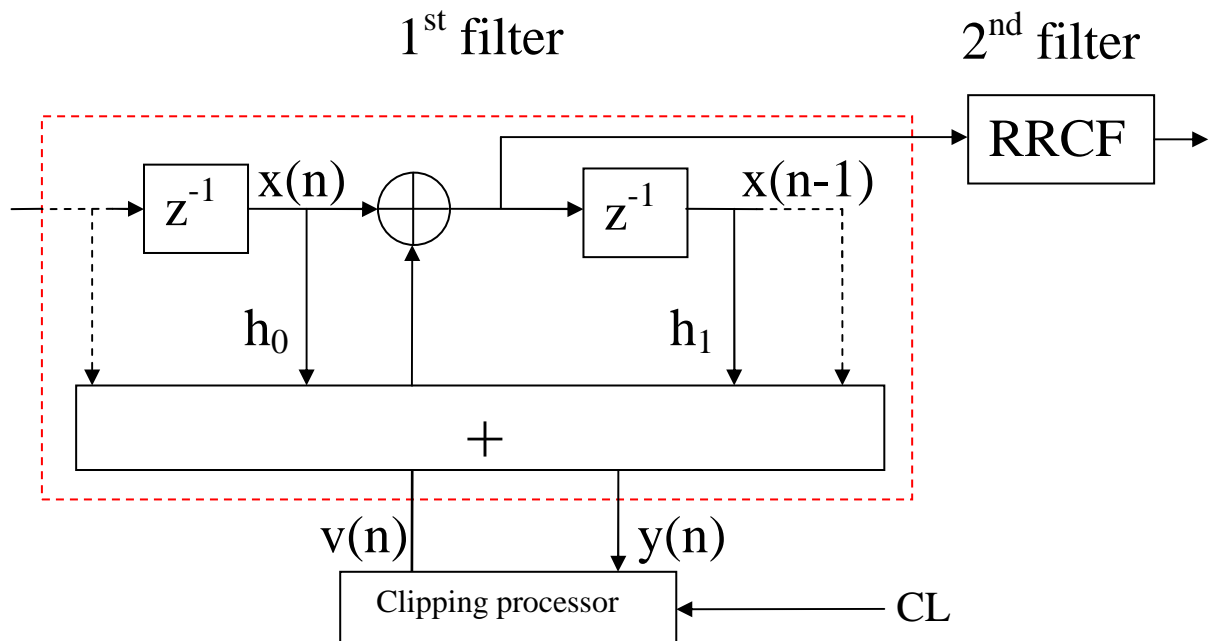


Figure 7.45: Detailed block diagram of the *LDA*.

A limitation with *LDA* is that the correction vector smears into other parts of the signal, which can introduce new peaks where none existed before. This problem is especially apparent when a number of peaks appear successively. To combat this problem the baseband clip level *CL* is set lower than the Amplifier Clip Level (ACL), the saturation level of the amplifier. The lower *CL* reduces the chance of regrown peaks saturating the amplifier.

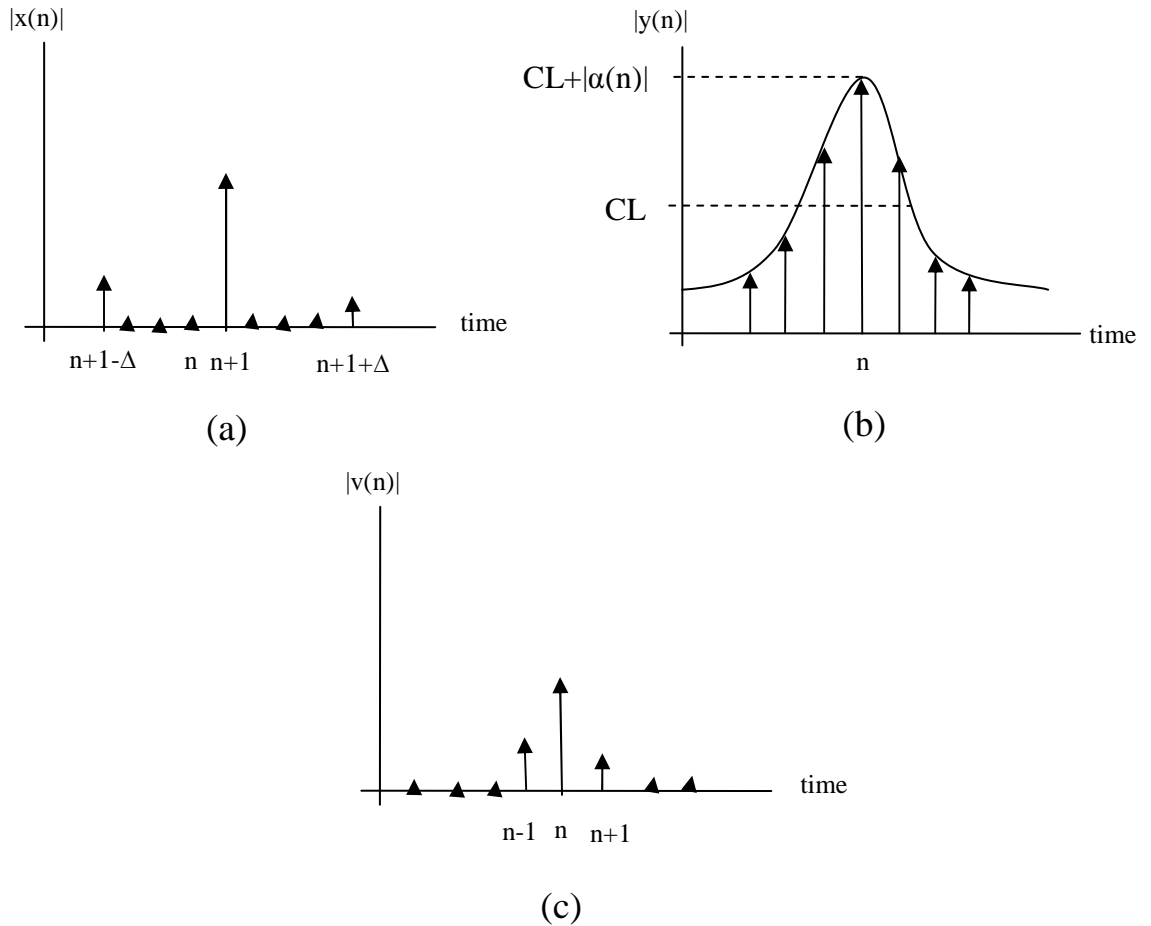


Figure 7.46: a) Amplitude of zero padded input to filter b) amplitude of filtered output c) *LDA* correction vectors.

In order to compare the performance of the *LDA* 2 parameters are used: the Clipping Error (CE) produced by the amplifier and the Mean Square Error (MSE) introduced by the compensation vector. The CE is the noise power of the clipped part in the amplifier, and is wideband and spread over many channels causing ACI. The MSE distortion introduced by the compensation filters is filtered by the second filter so no extra ACI is generated. The MSE introduces in band distortion that interferes with the desired signal.

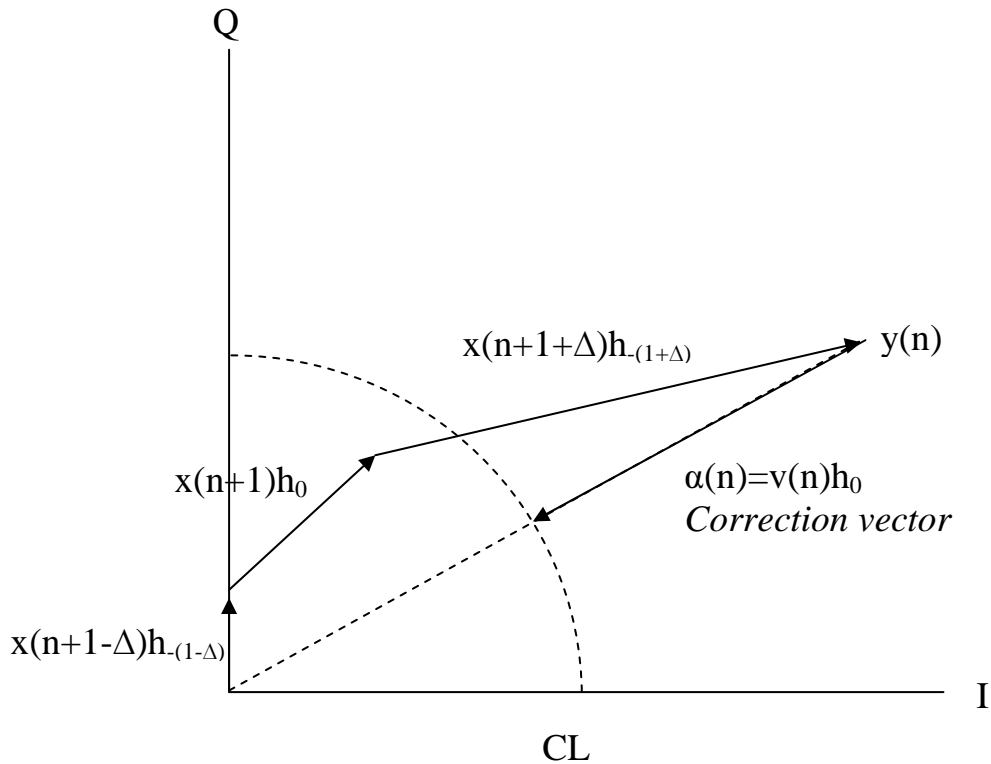


Figure 7.47: Vector representation of filtering with 3 active taps and the required correction vector to bring the output back to CL.

A block diagram of the simulation model used to evaluate *LDA* is shown in Figure 7.48. The interpolation factor is 8 and the RRCF has a roll off factor of 0.2. The HPA amplifier used in this case is just a linear limiter which saturates at ACL while the baseband clipper saturates at CL. A matched RRCF simulates the receiver filter and a decimator follows to sample the received data symbols. The measured clipped power is the average power of the difference between the amplifier input and output signals. Similarly, the MSE is the average power of the difference between the original data samples and the received ones.

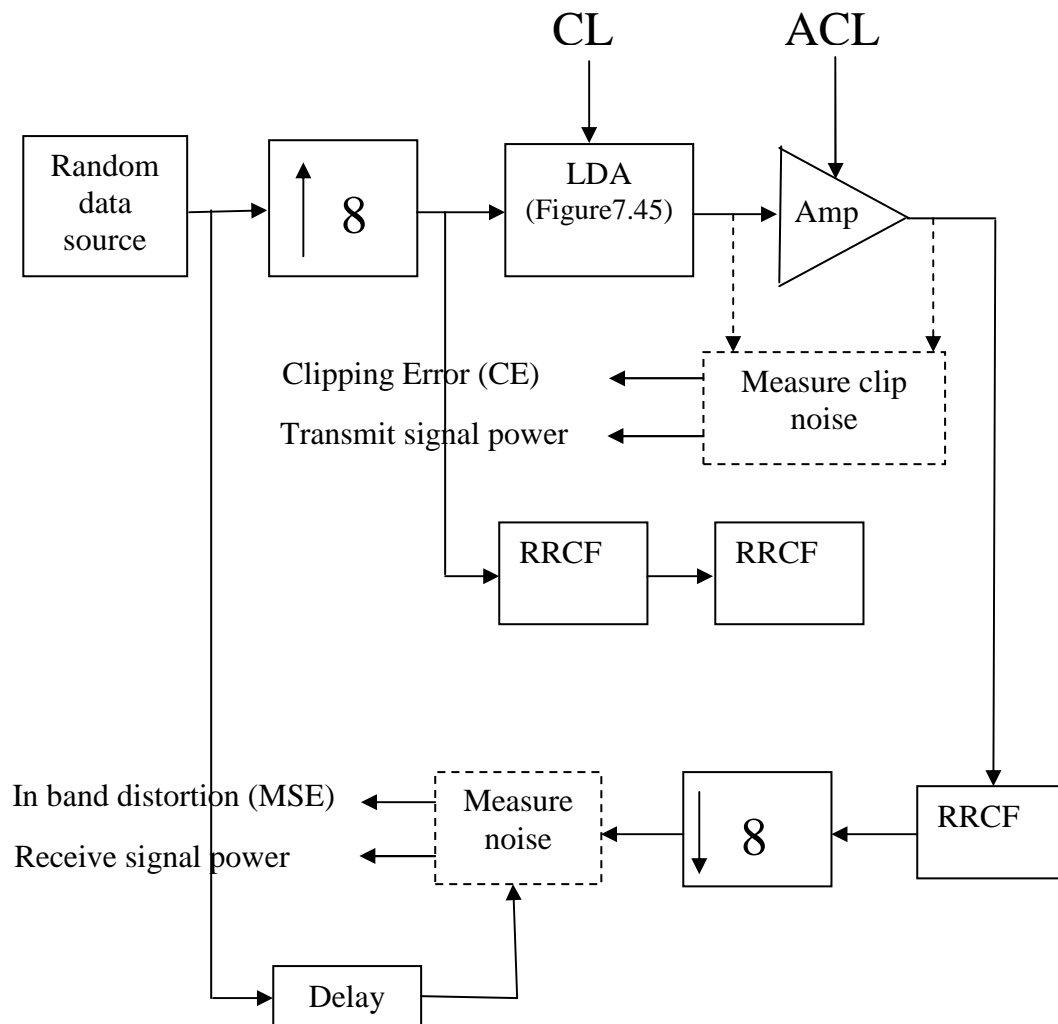


Figure 7.48: Block diagram of the simulation model used to evaluate LDA.

Figures 7.49 and 7.50 plot the simulated CL versus the inband distortion at the receiver. The ACL is set at 5dB and CL is varied from 2 to 9dB in Figure 7.49, and in Figure 7.50 the ACL is set at 8dB and the CL is varied from 7 to 12dB. Curves are plotted for *Vector Subtraction* with 2 iterations and *Conventional clipping*, both of which are implemented in a 64 tap and 128 tap filter.

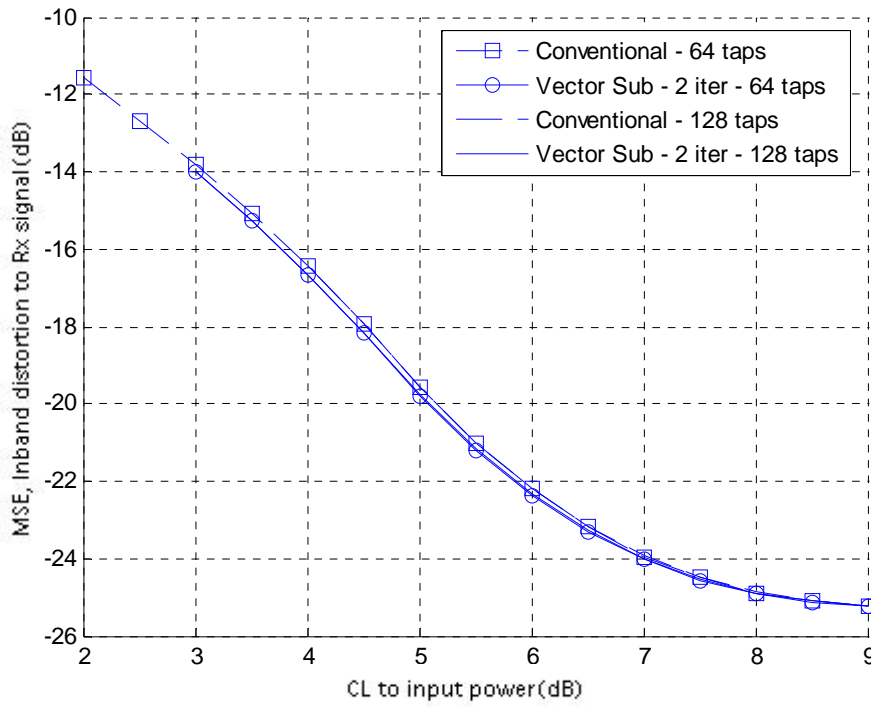


Figure 7.49: In band distortion for *Conventional* and *Vector Subtraction* (2 iter) with 64 and 128 taps in compensation filter. ACL=5dB.

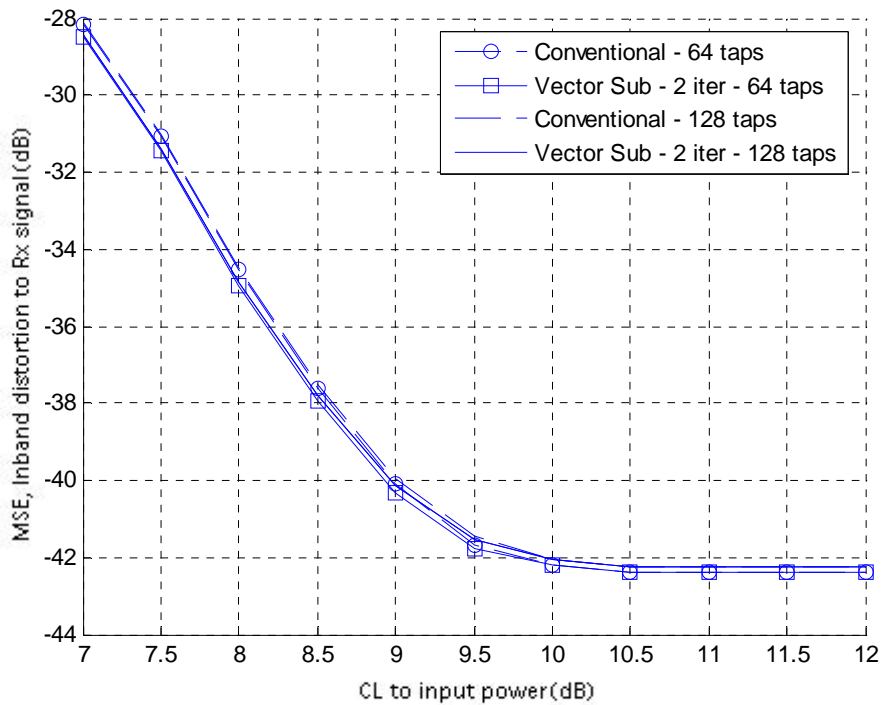


Figure 7.50: In band distortion for *Conventional* and *Vector Subtraction* (2 iter) with 64 and 128 taps in compensation filter. ACL=8dB.

In all cases when the CL is set below the ACL more inband noise is produced as the noise is dominated by the baseband clipping (CL). When the CL is set above the ACL the clipping noise is dominated by the amplifier and levels off at CL=9dB for ACL=5dB and at CL=10dB ACL=8dB. When the ACL=CL=5dB the inband distortion is 20dB below the received signal and when ACL=CL=8dB the inband distortion is around 35dB below the receive signal. Little variation is seen in performance between *Conventional* and *Vector Subtraction* with the 64 tap filter having slightly worse performance in the conventional case.

Figures 7.51 and 7.52 show the simulated results for the Clipping Error (CE) versus the inband distortion, or Mean Squared Error (MSE) for a constant ACL. The results are obtained by varying the CL and recording the two error sources (CE and MSE). When the CL is set larger than the ACL, all the clipping is performed by the amplifier and the most noise is produced as is evidenced by the top of the curves in Figures 7.51 and 7.52.

The bottom part of the curves in Figures 7.51 and 7.52 show noise produced when the CL is set smaller than the ACL, as a result clipping is mostly performed by the baseband clipper rather than the amplifier. The noise produced at the bottom of the curves is due to peak regrowth after baseband clipping saturating the amplifier. In the ACL=5dB case it is seen that at the top of the curves there is no discernable difference in performance between *Conventional* and *Vector Subtraction*, the number of taps also has a negligible effect on performance. At the bottom of the curves where the noise is due to peak regrowth there is a divergence in performance between *Conventional* and *Vector Subtraction* with *Conventional* clipping out performing *Vector Subtraction* by around 6dB from -55dB to -61dB in terms of the clipping noise. When the ACL is increased to 8dB the performance improves across the board as expected. Again *Conventional* clipping outperforms *Vector Subtraction* by at least 1dB, with *Vector Subtraction* displaying -64dB of noise and *Conventional* clipping displaying no noise below -65dB. The number of taps in the filter has a negligible effect. The amplifier CE is low enough for *LDA* with *Vector Subtraction* to meet the *ACI* specifications of most standards.

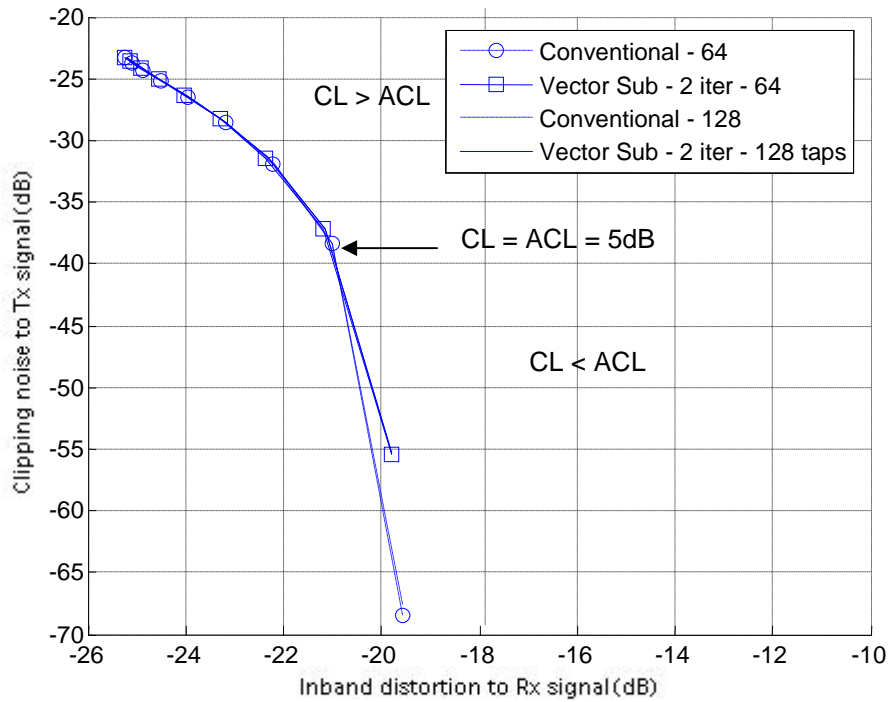


Figure 7.51: Clipping error vs. in-band distortion. Performance curves for *LDA* using *Conventional* clipping and *Vector Subtraction* with 2 iterations. Compensation filter has 64 and 128 taps. ACL=5dB.

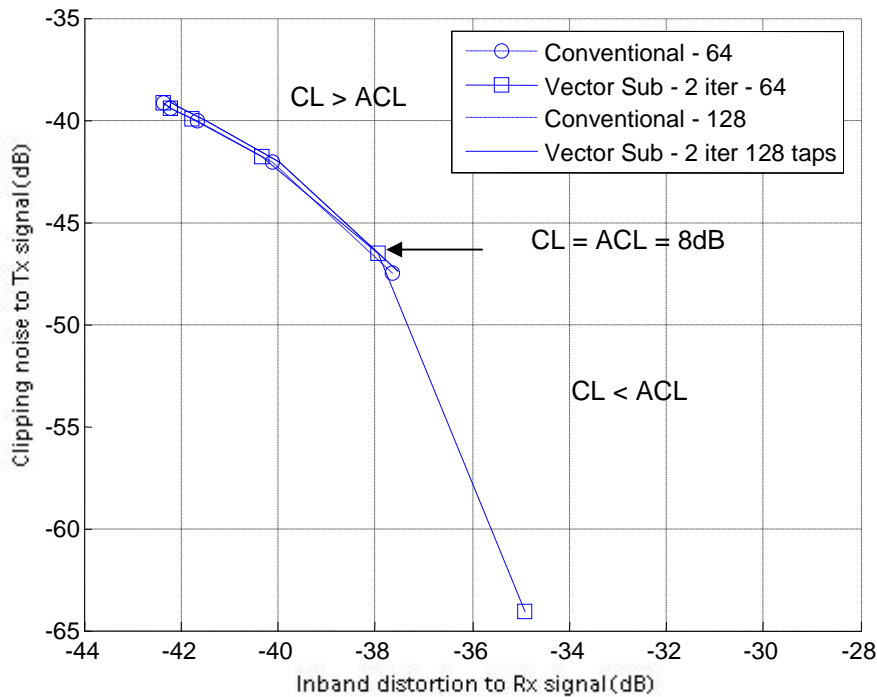


Figure 7.52: Clipping error vs. in-band distortion. Performance curves for *LDA* using *Conventional* clipping and *Vector Subtraction* with 2 iterations. Compensation filter has 64 and 128 taps. ACL=8dB.

7.6 Conclusion

This chapter presented new low complexity clipping methods for OFDM. Initially a Monte Carlo OFDM transceiver simulation model was used to establish the basic parameters on which the new clipping algorithms were tested. Various parameters such as the mapping type, the amount of oversampling in the IFFT, the baseband clip level, the number of taps in the pulse shaping filter, and the HPA backoff were varied to quantify their affect on the BERF. In this chapter the BERF was plotted against the clipping level with the noise set to zero, this meant that all the errors produced were due to clipping noise alone. Good parameters for further simulation were found to be oversampling the IFFT by a factor 2, a RRCF with 128 filter taps for a rolloff factor of 0.15, and a SSPA with $p=3$. The effect of filtering after clipping was also studied, it was shown through simulation how peak regrowth was more severe the harder the signal is clipped in the baseband. The peak regrowth could be countered to a certain degree by oversampling the IFFT by a factor of 2, oversampling beyond this point provided little discernable improvement. QPSK mapping was shown to be extremely robust to clipping, therefore making hard clipping a viable alternative at lower data rates.

In Section 7.2 *Sector* clipping was introduced as a low complexity alternative to conventional clipping. Theoretical analysis of *Conventional*, *Sector*, and *Square* clipping SNR was shown to be in good agreement with the simulated results. At higher clip levels the theoretical and simulated results diverged as the theoretical SNR used the assumption that the clipping noise was Gaussian in nature. This was shown to be untrue at higher clip levels where the clipping noise is more impulsive in nature, hence the divergence in results. Both 3 *Sector* and *square* clipping were implemented in silicon using a 0.5μ , 3 metal layer process. Reports generated by Synopsys and cadence proved that the complexity increase of the *Sector* clipping algorithm was small compared to *Square* clipping with the advantage of having much better SNR properties. Sector clipping was expanded to include more sectors thereby improving performance. 4 and 5 Sector clipping provided a marginal improvement over 3 sector in terms of the BERF with a minor increase in complexity.

Section 7.3 introduced another low complexity enhancement to an existing Lucent algorithm. An iterative method similar to the CORDIC algorithm to calculate the magnitude of a complex sample. The variation called *Vector Subtraction* further reduced complexity by the removal of a complex multiplication for the price of 2 extra additions and a comparison operation. Its performance was found to be as good as conventional clipping with only 2 iterations.

Section 7.4 compared simulated BERF results of the *Sector*, *Square*, *Lucent*, *Vector Subtraction*, and *Conventional* clipping under various backoffs in the HPA. It was shown that while the *Vector Subtraction* and *Lucent* algorithms have better performance across the board, *Sector* clipping was more tolerant to harder backoff levels in the HPA. The PSD results for conventional clipping at 0dB and 5dB at various HPA backoffs was shown. While the inband distortion remains in both clipping modes the ACI present at 0dB is up to 17dB below the signal power while ACI is almost non-existent at 5dB baseband clipping. As most WCDMA and OFDM standards require an ACI of 20dB below the signal power it was shown that even with hard clipping the ACI specifications are met.

For a baseband clipping system with 16 QAM mapping, an IFFT with an oversampling factor of 2, a pulse shaping RRCF with 128 taps and $\alpha=0.15$, to maintain a BER of 10^{-4} clipping at 3.8 to 4dB above the average signal power with a HPA with backoff 2dB above the baseband clip level is recommended. In this situation the HPA must have a peak power some 6dB above the average signal power.

Finally in Section 7.5 *Vector Subtraction* with 2 iterations was implemented into an existing adaptive clipping system which required the clipping operation to take place within the filter. A low latency magnitude estimate was therefore required. Simulated results showed that *Vector Subtraction* had similar performance to conventional clipping in this algorithm but with less latency and complexity.

Chapter 8

Conclusion

This thesis analysed and proposed new methods to deal with the PAPR in OFDM. Initially Chapter 2 introduced the theory and principles behind OFDM and detailed scenarios where it is used. Chapter 3 identified contributing factors to the PAPR, these were that peaks are a function of the IFFT operation, where in phase waveforms add to create a large peak. The general distribution of OFDM samples was shown to have a Rayleigh distribution. The number of subcarriers, and to a lesser degree the mapping type were also shown to contribute to the PAPR. Simulations of an OFDM system revealed how uncontrolled large peaks will saturate the HPA creating ACI and an increased BER at the receiver.

Chapter 4 began the literature review with an analysis of non distorted PAPR reduction techniques which included coding techniques, PTS, SLM, and Tone Reservation /Insertion. Coding introduced the most redundancy and became extremely complex at a higher number of subcarriers ($N > 64$), however later papers identified promising code sets such as second order Reed-Muller codes. PTS and SLM reduced the PAPR by producing a series of alternative transmit signals seeded from the same data source which are altered before the IFFT process so that they will have different PAPR properties. The waveform with the lowest PAR is chosen for transmission. These methods are complex and the amount of PAPR is not guaranteed. Tone Insertion/variation used peak reduction carriers which introduced redundancy and required some additional processing at the receiver.

Chapter 5 proposed two new low complexity variations to PTS, called Cyclic Shifted Sequences (CSS) and Time Inversion (TI). CSS and TI were shown to be less complex than PTS when the number of phase rotations was greater than 4.

Combining shifts of CSS and TI with non complex phase rotations of standard PTS allowed a whole IFFT operation to be removed at the expense of some extra non complex operations. CSS and TI were shown to display less peak regrowth after pulse shaping filtering. Oversampling at the IFFT by a factor of 2 was shown to improve the performance of PTS, CSS, and TI bringing the discrete and filtered CCDF to within 1dB of each other. These methods provided reduction in the CCDF of between 2 and 3dB at $\Pr(\zeta > \zeta_0) = 10^{-4}$.

Chapter 6 picked up the literature review again from Chapter 4 for distorted PAPR solutions. Distorted PAPR methods were defined here as methods which intentionally limit the excess peaks at the transmitter, usually in the baseband so that the HPA would not saturate. These papers revealed that a backoff of around 6dB is sufficient to maintain a respectable error rate for 4 and 16 QAM mapping. Other papers analysed the affect on the amplifier of saturation and the resultant in band and out of band distortion. Windowing was also examined which is the process of using a pulse shape to clip the signal and surrounding samples to give better spectrum properties. The gains in reduction in ACI were shown to be minimal when an acceptable amount of backoff in the HPA was used.

Chapter 7 presented the next set of new PAPR solutions where a series of low complexity and low latency clipping algorithms were proposed. This chapter started with a detailed Monte Carlo simulation of an OFDM transceiver where different stages of the transmission chain were modified to ascertain their effect on the BERF. The motivation behind clipping as a solution to the PAPR was that with an acceptable HPA backoff of around 6dB, clipping is a very rare occurrence affecting the BER negligibly. The first method, *Sector* clipping uses a rule base to perform the clipping operation. It was implemented in silicon and shown to have negligible extra complexity to square clipping but with much better performance. The rule base was extended up to 5 sectors where performance was close to conventional clipping. The second method used a variation of a CORDIC like magnitude estimator and was called *Vector Subtraction*. The complexity was further reduced by the removal of a multiplication at the expense of 2 additions and comparisons. *Vector Subtraction* was shown to have identical performance to conventional clipping with only 2 iterations. Finally *Vector Subtraction* with 2 iterations was implemented in a previously

proposed clip and filter algorithm where its low latency was important as the magnitude had to be found quickly as it was operating in a feedback loop on filter samples.

8.1 Future Work

The PAPR problem in OFDM is still an ongoing issue, especially for portable devices where the need to minimise the power amplifier linear range is paramount. The PTS/CSS/TI methods developed in this thesis to reduce the PAPR can be combined with other PTS techniques such as adaptive PTS and variations of the blind SLM techniques to further reduce complexity and the peak power. A hybrid system utilizing clipping techniques could also be added as a last stage so as to have an upper bound for the PTS signal.

Further enhancements of *Sector* clipping can be made where the error introduced by the phase distortion could be minimised so that only the amplitude distortion remains. All of the clipping techniques detailed in this thesis could be combined with coding techniques to further improve the BER performance. Code sets for larger numbers of subcarriers are an open ended problem and there is much ongoing research in this area.

Analysis of the proposed algorithms in a MIMO OFDM system is an area that has gained a lot of focus recently and analysis of the performance of the proposed techniques in such an environment would be valid.

The LDA algorithm with *Vector Subtraction* could be implemented in a complete OFDM transceiver and then implemented in hardware via a FPGA or silicon to ascertain whether the latency requirements can be met with the wider bandwidth systems now being proposed (40 MHz for 802.11n, and up to 100 MHz for 4G LTE).

Bibliography

- [1] G. Hill, M. Faulkner, and J. Singh, "Reducing the peak-to-average power ratio in OFDM by cyclically shifting partial transmit sequences," *Electronics Letters*, vol. 36, pp. 560-561, Mar 16 2000.
- [2] G. Hill, M. Faulkner, and J. Singh, "Cyclic Shifting and Time Inversion of Partial Transmit Sequences to Reduce the Peak-to-Average Power Ratio in OFDM," in *PIMRC*, London, 2000.
- [3] G. Hill, "Comparison of Low complexity clipping algorithms for OFDM," in *PIMRC*, Portugal, 2002.
- [4] M. L. Doelz, E. T. Heald, and D. L. Martin, "Binary Data Transmission Techniques for Linear Systems," *Proc IRE*, vol. 45, pp. 656-661, May 1957.
- [5] R. W. Chang, "Synthesis of Band Limited Orthogonal Signals for Multichannel Data Transmission," *Bell Syst. Tech. Jo.*, vol. 45, pp. 1,775-1,796, Dec 1966.
- [6] B. R. Saltzberg, "Performance of an efficient parallel data transmission system," *IEEE Transactions on Communication Technologies*, vol. COM-15, Dec 1967 1967.
- [7] S. Weinstein and P. Ebert, "Data transmission by frequency division multiplexing using the discrete fourier transform," *IEEE Transactions on Communication Techniques*, vol. COM-19, pp. 628-634, October 1971.
- [8] L. J. Cimini Jr, Ye, L., "Orthogonal Frequency Division Multiplexing for Wireless Channels," in *IEEE Global Telecommunications Conference GLOBECOM*, Sydney, Australia, 1998, p. 82.
- [9] C. H. Chang, C. L. Wang, and Y. T. Chang, "Efficient VLSI architectures for fast computation of the discrete fourier transform and its inverse," *IEEE Transactions on Signal Processing*, vol. 48, pp. 3206-3216, Nov 2000.
- [10] Y. Jung, Y. Tak, J. Kim, J. Park, D. Kim, and H. Park, "Efficient FFT algorithm for OFDM modulation," in *Electrical and Electronic Technology, 2001. TENCON. Proceedings of IEEE Region 10 International Conference on*, 2001, pp. 676-678 vol.2.
- [11] A. Sadat and W. B. Mikhael, "Fast Fourier Transform for high speed OFDM wireless multimedia system," in *Circuits and Systems, 2001. MWSCAS 2001. Proceedings of the 44th IEEE 2001 Midwest Symposium on*, 2001, pp. 938-942 vol.2.
- [12] A. D. S. Jayalath, "OFDM for Wireless Broadband Communications (Peak Power Reduction, Spectrum and Coding)," in *School of Computer Science and Software Engineering Melbourne: Monash University*, 2002, p. 257.
- [13] L. Hanzo, Webb, W., Keller, T., *Single and Multi-carrier Quadrature Amplitude Modulation*. Chichester: Wiley, 2000.
- [14] O. Edfors, Sandell, M., van de Beek, J.J., Landström, D., Sjöberg, "An Introduction to Orthogonal Frequency Division Multiplexing," Division of

- Signal Processing, Luleå University of Technology, Research Report TULEA 1996:16 1996.
- [15] R. Morrison, L. J. Cimini, Jr., and S. K. Wilson, "On the use of a cyclic extension in OFDM," in *Vehicular Technology Conference, 2001. VTC 2001 Fall. IEEE VTS 54th*, 2001, pp. 664-668 vol.2.
- [16] T. S. Rappaport, *Wireless Communications, Principles and Practice*. New Jersey: Prentice Hall, 1996.
- [17] S. Coleri, M. Ergen, A. Puri, and A. Bahai, "Channel estimation techniques based on pilot arrangement in OFDM systems," *Broadcasting, IEEE Transactions on*, vol. 48, pp. 223-229, 2002.
- [18] M. Morelli and U. Mengali, "A comparison of pilot-aided channel estimation methods for OFDM systems," *IEEE Transactions on Signal Processing*, vol. 49, pp. 3065-3073, Dec 2001.
- [19] W. G. Jeon, K. H. Paik, and Y. S. Cho, "Two-dimensional pilot-symbol-aided channel estimation for OFDM systems with transmitter diversity," *IEICE Transactions on Communications*, vol. E85B, pp. 840-844, Apr 2002.
- [20] J. Shentu and J. Armstrong, "Blind frequency offset estimation for PCC-OFDM with symbols overlapped in the time domain," in *Circuits and Systems, 2001. ISCAS 2001. The 2001 IEEE International Symposium on*, 2001, pp. 570-573 vol. 4.
- [21] F. Tufvesson, "Design of Wireless Communication Systems - Issues on Synchronization, Channel Estimation and Multi-Carrier Systems," in *Department of Applied Electronics Lund: Lund University*, 2000.
- [22] M. Faulkner, "OFDM: Overview," Melbourne, 2002.
- [23] A. G. Armada, "Understanding the effects of phase noise in orthogonal frequency division multiplexing (OFDM)," *IEEE Transactions on Broadcasting*, vol. 47, pp. 153-159, Jun 2001.
- [24] T. Pollet, M. Vanbladel, and M. Moeneclaey, "Ber sensitivity of ofdm systems to carrier frequency offset and wiener phase noise," *IEEE Transactions on Communications*, vol. 43, pp. 191-193, 1995.
- [25] ETSI, "Radio Broadcast Systems: Digital Audio Broadcasting (DAB) to mobile, portable and fixed receivers," ETSI final draft ETS 300 401, Nov 1994.
- [26] P. Shelswell, "The COFDM modulation system: The heart of digital audio broadcasting," *Electronic and Communication Engineering Journal*, vol. 7, pp. 127-135, June 1995.
- [27] J. Stott, "The DVB terrestrial (DVB-T) specification and its implementation in a practical modem," *International Broadcasting Convention*, pp. 255-260, 1996.
- [28] ETSI, "Digital Video Broadcasting (DVB); framing structure, channel coding, and modulation for digital terrestrial television (DVB-T)," European Telecommunications Standard Institute ETSI EN 300 744, Nov 1999.
- [29] ISO/IEC, "Information technology - generic coding of moving pictures and associated audio information: Part 2 video," ISO/IEC 13818, 2000.
- [30] J. Tellado-Mourelo, "Peak to Average Power Reduction for Multicarrier Modulation," in *Department of Electrical Engineering: Stanford University*, 1999.
- [31] H. Bolckei, D. Gesbert, and A. J. Paulraj, "On the capacity of OFDM-based spatial multiplexing systems," *Communications, IEEE Transactions on*, vol. 50, pp. 225-234, 2002.

- [32] S. H. Müller, R. W. Bauml, R. F. H. Fischer, and J. B. Huber, "Ofdm with reduced peak-to-average power ratio by multiple signal representation," *Annales des Telecommunications Annals of Telecommunications*, vol. 52, pp. 58-67, 1997.
- [33] C. Annis, "Central Limit Theorem," http://www.statisticalengineering.com/central_limit_theorem.htm, 2004.
- [34] C. Tellambura, "Phase optimisation criterion for reducing peak-to-average power ratio in ofdm," *Electronics Letters*, vol. 34, pp. 169-170, 1998.
- [35] H. Ochiai and H. Imai, "On the distribution of the peak-to-average power ratio in OFDM signals," *IEEE Transactions on Communications*, vol. 49, pp. 282-289, Feb 2001.
- [36] M. Sharif, M. Gharavi-Alkhansari, and B. H. Khalaj, "On the peak-to-average power of ofdm signals based on oversampling," *Communications, IEEE Transactions on*, vol. 51, pp. 72-78, 2003.
- [37] R. v. Nee, *OFDM for wireless multimedia communications*. Boston ; London: Artech House, 2000.
- [38] G. Wunder and H. Boche, "Upper bounds on the statistical distribution of the crest-factor in ofdm transmission," *Information Theory, IEEE Transactions on*, vol. 49, pp. 488-494, 2003.
- [39] S. Müller-Weinfurtner, "OFDM for Wireless Communications: Nyquist Windowing, Peak-Power Reduction, and Synchronization," in *Reihe Kommunikations- und Informationstechnik* Nürnberg: Universität Erlangen, 2000.
- [40] E. Costa, M. Midrio, and S. Pupolin, "Impact of amplifier nonlinearities on OFDM transmission system performance," *Communications Letters*, vol. 3, pp. 37-39, 1999.
- [41] E. Costa and S. Pupolin, "M-QAM-OFDM system performance in the presence of a nonlinear amplifier and phase noise," *IEEE Transactions on Communications*, vol. 50, pp. 462-472, Mar 2002.
- [42] C. L. Liu, "The effect of nonlinearity on a qpsk-ofdm-qam signal," *IEEE Transactions on Consumer Electronics*, vol. 43, pp. 443-447, 1997.
- [43] S. Merchan, A. G. Armada, and J. L. Garcia, "Ofdm performance in amplifier nonlinearity," *IEEE Transactions on Broadcasting*, vol. 44, pp. 106-114, 1998.
- [44] G. T. Zhou and J. S. Kenney, "Predicting spectral regrowth of nonlinear power amplifiers," *Communications, IEEE Transactions on*, vol. 50, pp. 718-722, 2002.
- [45] G. Santella and F. Mazzenga, "A hybrid analytical-simulation procedure for performance evaluation in m-qam-ofdm schemes in presence of nonlinear distortions," *IEEE Transactions on Vehicular Technology*, vol. 47, pp. 142-151, 1998.
- [46] X. Li and L. J. Cimini, "Effects of clipping and filtering in the performance of OFDM," *IEEE Communications Letters*, vol. 2, pp. 131-133, May 1998.
- [47] C. van den Bos, M. H. L. Kouwenhoven, and W. A. Serdijn, "Effect of smooth nonlinear distortion on OFDM symbol error rate," *IEEE Transactions on Communications*, vol. 49, pp. 1510-1514, Sep 2001.
- [48] M. Friese, "On the degradation of OFDM signals due to peak clipping in optimally predistorted power amplifiers," in *Globecom*, Sydney, Australia, 1998.

-
- [49] A. E. Jones, T. A. Wilkinson, and S. K. Barton, "Block coding scheme for reduction of peak to mean envelope power ratio of multicarrier transmission schemes," *Electronics Letters*, vol. 30, pp. 2098-2099, 1994.
- [50] T. A. Wilkinson and A. E. Jones, "Minimisation of the Peak to Mean Envelope Power Ratio of Multicarrier Transmission Schemes by Block Coding," in *VTC*, Chicago, USA, 1995.
- [51] A. E. Jones, "Combined Coding for Error Control and Increased Robustness to System Nonlinearities in OFDM," in *IEEE 46th VTC*, Atlanta, USA, 1996, pp. pp 904-908.
- [52] V. Tarokh and H. Jafarkhani, "An Algorithm for Reducing the Peak to Average Power Ratio in a Multicarrier Communication System," in *IEEE VTC*, Piscataway, NJ, USA, 1999, pp. pp 680-684.
- [53] ETSI, "Broadband Radio Access Networks (BRAN); HIPERLAN Type 2; Physical (PHY) layer," European Telecommunications Standards Institute ETSI TS 101 475 v1.1.1, 2000.
- [54] V. Tarokh and H. Jafarkhani, "On the computation and reduction of the peak-to-average power ratio in multicarrier communications," *Communications, IEEE Transactions on*, vol. 48, pp. 37-44, 2000.
- [55] P. W. J. VanEetvelt, S. J. Shepherd, and S. K. Barton, "The Distribution of Peak Factor in QPSK Multi-Carrier Modulation," in *Wireless Communications Netherlands: Kluwer Academic Publishers*, 1995, pp. 87-95.
- [56] S. Shepherd, J. Orriss, and S. Barton, "Asymptotic limits in peak envelope power reduction by redundant coding in orthogonal frequency-division multiplex modulation," *IEEE Transactions on Communications*, vol. 46, pp. 5-10, 1998.
- [57] D. Wulich, "Peak Factor in Orthogonal Multicarrier Modulation with Variable Levels," *Electronic Letters*, vol. 32, pp. 1859-1861, September 1996.
- [58] J. E. M. Nilsson, "Coding to control the signal waveform in M-ary PSK multicarrier communications," in *Radio Vetenskap och Kommunikation '96 (RVK)*, Luleå, Sweden, 1996, pp. pp 658-662.
- [59] K. G. Paterson, "Bounds on Envelope Power of Trace Codes for OFDM," Hewlett Packard Laboratories, Bristol HPL-98-176, October 1998.
- [60] C. Tellambura, "Upper bound on peak factor on n-multiple carriers," *Electronics Letters*, vol. 33, pp. 1608-1609, 1997.
- [61] C. Wulich, "Reduction of Peak to Mean Ratio of Multicarrier Modulation using Cyclic Coding," *Electronic Letters*, vol. 32, pp. 432-433, February 1996.
- [62] Y. Y. Zhang, A.; Chouinard, J.-Y.; Zhang, L., "OFDM peak power reduction by sub-block-coding and its extended versions," in *Vehicular Technology Conference, 1999 IEEE 49th*, 1999, pp. 695-699 vol.1.
- [63] S. Boyd, "Multitone signals with low crest factor," *Circuits and Systems, IEEE Transactions on*, vol. 33, pp. 1018-1022, 1986.
- [64] S. J. V. E. Shepherd, P.W.J.; Wyatt-Millington, C.W.; Barton, S.K., "Simple coding scheme to reduce peak factor in QPSK multicarrier modulation," in *Electronics Letters*. vol. 31, 1995, pp. 1131-1132.
- [65] R. D. J. van Nee, "OFDM codes for peak-to-average power reduction and error correction," in *Global Telecommunications Conference, 1996. GLOBECOM '96. 'Communications: The Key to Global Prosperity*, 1996, pp. 740-744 vol.1.

-
- [66] J. A. Davis and J. Jedwab, "Peak-to-mean power control and error correction for ofdm transmission using golay sequences and reed-muller codes," *Electronics Letters*, vol. 33, pp. 267-268, 1997.
- [67] J. A. Davis and J. Jedwab, "Peak-to-mean power control in OFDM, Golay complementary sequences, and Reed-Muller codes," *IEEE Transactions on Information Theory*, vol. 45, pp. 2397-2417, 1999.
- [68] A. E. Jones and T. A. Wilkinson, "Performance of Reed-Muller codes and a maximum-likelihood decoding algorithm for OFDM," *IEEE Transactions on Communications*, vol. 47, pp. 949-952, 1999.
- [69] A. G. Armada, V. Gil, and J. L. Garcia, "Improving Peak to Average power Ratio (PAR) and Probability of Error in OFDM-based WLAN," in *IST Summit*, United Kingdom, 2001.
- [70] A. J. Grant and R. van Nee, "Efficient maximum likelihood decoding of peak power limiting codes for OFDM," in *Vehicular Technology Conference, 1998. VTC 98. 48th IEEE*, 1998, pp. 2081-2084 vol.3.
- [71] I. Ochiai, M. P. C. Fossorier, and H. Imai, "On decoding of block codes with peak-power reduction in OFDM systems," *IEEE Communications Letters*, vol. 4, pp. 226-228, 2000.
- [72] B. S. Tarokh, H.R., "Construction of ofdm m -qam sequences with low peak-to-average power ratio," *Communications, IEEE Transactions on*, vol. 51, pp. 25-28, 2003.
- [73] K. Sathanathan and C. Tellambura, "Coding to reduce both par and picr of an ofdm signal," *IEEE Communications Letters*, vol. 6, pp. 316-318, 2002.
- [74] S. H. Müller and J. B. Huber, "A comparison of Peak Power Reduction Schemes for OFDM," in *Globecom '97*, Phoenix, USA, 1997.
- [75] S. H. Müller and J. B. Huber, "Ofdm with reduced peak-to-average power ratio by optimum combination of partial transmit sequences," *Electronics Letters*, vol. 33, pp. 368-369, 1997.
- [76] S. H. Müller and J. B. Huber, "A novel peak power reduction scheme for OFDM," in *IEEE Personal Indoor Mobile Radio Communications*, Helsinki, Finland, 1997, pp. 1090-1094.
- [77] S. H. Müller and J. B. Huber, "OFDM with Reduced Crest Factor," ETSI BRAN - European Telecommunications Standards Institute Broadband Radio Access Network, Ulm, Germany WG3 temporary document 25, 16 September 1997.
- [78] S. G. Kang, J. G. Kim, and E. K. Joo, "A novel subblock partition scheme for partial transmit sequence OFDM," *IEEE Transactions on Broadcasting*, vol. 45, pp. 333-338, 1999.
- [79] L. J. Cimini and N. R. Sollenberger, "Peak-to-average power ratio reduction of an OFDM signal using partial transmit sequences," in *ICC'99*, 1999.
- [80] L. J. Cimini and N. R. Sollenberger, "Peak-to-average power ratio reduction of an OFDM signal using partial transmit sequences," *Communications Letters*, vol. 4, pp. 86-88, Mar 2000.
- [81] C. Tellambura and A. D. S. Jayalath, "PAR reduction of an OFDM signal using partial transmit sequences," in *Vehicular Technology Conference, 2001. VTC 2001 Fall. IEEE VTS 54th*, 2001, pp. 465-469 vol.1.
- [82] H. Chen and G. J. Pottie, "An orthogonal projection-based approach for PAR reduction in OFDM," *Communications Letters*, vol. 6, pp. 169-171, May 2002.

- [83] R. W. Bauml, R. F. H. Fischer, and J. B. Huber, "Reducing the peak-to-average power ratio of multicarrier modulation by selected mapping," *Electronic Letters*, vol. 32, pp. 2056-2057, 1996.
- [84] H. Breiling, S. H. Muller-Weinfurtner, and J. B. Huber, "SLM peak-power reduction without explicit side information," *IEEE Communications Letters*, vol. 5, pp. 239-241, 2001.
- [85] A. D. S. T. Jayalath, C., "A blind slm receiver for par-reduced ofdm," in *Vehicular Technology Conference, 2002. Proceedings. VTC 2002-Fall. 2002 IEEE 56th*, 2002, pp. 219-222.
- [86] J. Tellado and J. Cioffi, "Peak Power Reduction of Multicarrier Transmission," in *Globecom 1998*, Sydney, Australia, 1998.
- [87] R. Dinis and A. Gusmao, "On the performance evaluation of OFDM transmission using clipping techniques," in *VTC'99*, 1999.
- [88] H. Nikopour and S. H. Jamali, "Effects of Cartesian Clipping Noise on the Performance of Orthogonal Frequency Division Multiplexing System: A Theoretical Approach," in *IEEE GLOBECOM 2002*, 2002, pp. 1254-1258.
- [89] A. R. S. Bahai, M. Singh, A. J. Goldsmith, and B. R. Saltzberg, "A new approach for evaluating clipping distortion in multicarrier systems," *IEEE Journal on Selected Areas in Communications*, vol. 20, pp. 1037-1046, Jun 2002.
- [90] G. Wunder and H. Boche, "The Impact of Nonlinear Devices on the Symbol Error Rate in Broadband OFDM Transmission," *?*, vol. *?*, 2002.
- [91] T. May and H. Rohling, "Reducing the Peak to Average Power Ratio in OFDM Radio Transmission Systems," in *VTC '98*, *?*, 1998, pp. 2474-2478.
- [92] J. Armstrong, "Peak-to-average power reduction for OFDM by repeated clipping and frequency domain filtering," *Electronics Letters*, vol. 38, pp. 246-247, Feb 28 2002.
- [93] D. Kim and G. L. Stuber, "Clipping noise mitigation for OFDM by decision-aided reconstruction," *Communications Letters*, vol. 3, pp. 4-6, 1999.
- [94] D. J. G. Mestdagh, P. M. P. Spruyt, and B. Biran, "Effect of Amplitude Clipping in DMT-ADSL Transceivers," *Electronic Letters*, vol. 29, pp. 1354-1355, 22nd July 1993.
- [95] D. J. G. Mestdagh and P. M. P. Spruyt, "A Method to Reduce the Probability of Clipping in DMT-Based Transceivers," *IEEE Transactions on Communications*, vol. 44, pp. 1234-1238, October 1996.
- [96] B. Come, R. Ness, S. Donnay, L. V. d. Perre, W. Eberle, P. Wambacq, M. Engels, and I. Bolsens, "Impact of Front-End Non-Idealities on Bit Error Rate of WLAN-OFDM Transceivers," in *Microwave Journal*, 2001, pp. 126-140.
- [97] J. Armstrong, H. A. Suraweera, S. Brewer, and R. Slaviero, "Effect of Rounding and Saturation in Fixed-Point DSP Implementation of IFFT and FFT for OFDM Applications," in *The Embedded Signal Processing Conference (GSPx 2004)*, Santa Clara, CA, USA, 2004.
- [98] S. Merchan, A. G. Armada, and J. L. Garcia, "OFDM performance in amplifier nonlinearity," *Broadcasting, IEEE Transactions on*, vol. 44, pp. 106-114, 1998.
- [99] R. v. Nee and A. d. Wild, "Reducing the Peak-to-Average Power Ratio of OFDM," in *Vehicular Technology Conference*, Ottawa, Canada, 1998, pp. 2072-2076.
- [100] S. B. Slimane, "Peak-to-average power ratio reduction of OFDM signals using broadband pulse shaping," in *IEEE VTC '02*, Canada, 2002, pp. 889-893.

- [101] R. S. Creighton, "System and method to reduce the peak-to-average power ratio in DS-CDMA transmitter," in *European Patent Application* Great Britain: Lucent Technologies (UK), 1999.
- [102] J. E. Volder, "The CORDIC Trigonometric Computing Technique," *IRE Trans. Electronic Computing*, vol. 8, pp. 330-334, Sept 1959.
- [103] R. Berangi and M. Faulkner, "Peak Power Reduction for Multi-Code CDMA and Critically Sampled Complex Gaussian Signals," in *IST 2001*, Iran, 2001.